Dissertation
submitted to the
Combined Faculties for the Natural Sciences and for Mathematics
of the Ruperto-Carola University of Heidelberg, Germany
for the degree of
Doctor of Natural Sciences

Put forward by
Diplom-Physiker Thomas König
Born in Pforzheim, Germany
Oral examination: 4/5/2011

Exploring Coherent Phenomena and Energy Discrimination in X-Ray Imaging

Referees: **Prof. Dr. Uwe Oelfke**
Prof. Dr. Wolgang Schlegel

Abstract

Conventional X-ray imaging is based on the generation of photons in materials that are selected for different applications according to their densities, dimensions, and atomic numbers. The photons produced in these targets are commonly detected by measuring the integrated amount of energy released in films or digital imaging systems. This thesis aims at extending these two paradigms.

First, it is shown that the use of single-crystalline, i.e. well-ordered targets, can significantly soften photon spectra created by megavoltage electrons when compared to usual targets. The reason for this is an effect called "coherent bremsstrahlung". It is shown that this type of radiation bears the potential of increasing the quality of megavoltage images and reducing radiation dose for image guided radiotherapy.

Second, new spectroscopic pixel detectors of the Medipix2 family operated with cadmium telluride sensors are characterised and thus potential benefits and difficulties for X-ray imaging are investigated. Besides describing in detail how to calibrate these detectors, emphasis is placed on determining their energy responses, modulation transfer functions, and detective quantum efficiencies. Requirements for photon counting megavoltage imaging are discussed. The detector systems studied are finally used to perform spectral computed tomography and to illustrate the benefits of energy discrimination for coherent scatter imaging.

Zusammenfassung

Herkömmliche Röntgenbildgebung basiert auf der Erzeugung von Röntgenstrahlung in Materialien, die abhängig vom Anwendungsgebiet hinsichtlich ihrer Dichte, Abmessungen und Ordnungszahlen ausgewählt werden. Die in diesen Targets produzierten Photonen werden überlicherweise dadurch detektiert, wieviel Energie deren Gesamtheit an einen Film oder ein digitales System abgibt. Die vorliegende Arbeit zielt darauf ab, diese beiden Paradigmen zu erweitern.

Zunächst wird gezeigt, dass durch die Verwendung von einkristallinen, d.h. wohlstrukturierten Targets, die von Megavolt-Elektronen erzeugten Photonenspektren wesentlich weicher sein können als durch konventionelle Targets. Verantwortlich dafür ist ein Effekt genannt "kohärente Bremsstrahlung". Es wird gezeigt, dass diese Art von Strahlung das Potenzial birgt, die Qualität von Megavolt-Bildern in der bildgeführten Strahlentherapie zu verbessern, bzw. die hierbei auftretende Strahlenbelastung zu reduzieren.

In einem zweiten Schwerpunkt werden neue spektroskopische Detektoren der Medipix2 Baureihe, betrieben in Verbindung mit Cadmium-Tellurid Sensoren, im Hinblick auf ihre Eignung zur Röntgenbildgebung charakterisiert. Neben der detaillierten Beschreibung der Inbetriebnahme dieser Detektoren wird ein Schwerpunkt auf die Bestimmung von Energieantwort, Modulationstransferfunktion und detektiver Quanteneffizienz gelegt. Darüber hinaus werden Anforderungen für photonenzählende Megavolt-Bildgebung diskutiert. Die Eignung der verwendeten Detektorsysteme in der spektralen Computertomographie wird beschrieben und abschliessend wird auf deren Vorteil in der kohärenten Streubildgebung eingegangen.

Contents

Chapter 1

Introduction

The aim of this thesis is to tackle two limitations of modern, absorptive X-ray imaging. The first limitation investigated is the poor soft-tissue contrast in megavoltage imaging, in which the imaging photons are generated by high energy (i.e. megavoltage) electrons in a medical linear accelerator. The main purpose of such a device is to provide high energy photons for the radiation therapy of cancer. However, with the advent of image guidance, the resulting photon spectra have been increasingly used to also obtain images of the patient. Unfortunately, these high energy photons are only weakly attenuated in human tissue, and hence the amount of radiation required to form a low noise image exceeds that of conventional, kilovoltage X-ray imaging by at least one order of magnitude. The inclusion of additional X-ray tubes into these linear accelerators to overcome this problem, however, requires additional calibration procedures and makes the devices also more expensive.

The idea that is pursued in this work is to increase the amount of low energy photons in these megavoltage spectra by replacing conventional amorphous or poly-crystalline bremsstrahlung targets with single-crystals. Their well defined structure gives rise to a phenomenon called "coherent bremsstrahlung", whose spectra, as will be shown in chapter 3, can exhibit a higher amount of kilovoltage photons if the incident electrons are aligned to one of the major axes of such a crystal. Furthermore, first theoretical indications will be presented that coherent bremsstrahlung could help to alleviate beam hardening when employed in the megavoltage regime.

The second major limitation that will be adressed is the fact that conventional computed tomography is unable to properly classify tissues, as it only reconstructs absorption coefficients rather than more specific parameters like electron densities or atomic numbers. Up to now, a method called dual source computed tomography has helped to solve this problem. It relies on the use of two separate X-ray tubes operated at different voltages, and thus performs some form of energy discrimination which provides the desired information.

The approach that is followed in this thesis to perform energy discrimination relies on the detector rather than on varying tube voltages. It is based on the principle of photon counting, which makes use of the generation of electron-hole pairs in semiconductor sensors by ionising radiation. Formerly, this was only possible for non-segemented detectors, but recent technological advances brought the development of pixelised versions of these kinds of devices. Unlike conventional, energy integrating panels, they no longer weight the importance of each photon by the amount of energy it carries. By counting individual photons, they also promise superior noise characteristics.

The detectors employed to achieve this goal are those of the Medipix2 family, which we at DKFZ chose to operate with cadmium telluride sensors. Chapter 4 is dedicated to characterising these detectors in detail, and will also give the fundamentals of energy discrimination, along with the charge transport properties of semiconductor sensors. Amongst other things, the spatial and

spectral resolution of these detectors will be determined for two pixel pitches (110 μm and 165 μm) and we will take a look at the feasibility of K-edge imaging with these devices.

Another coherence phenomenon will be encountered at the end of this thesis: coherent scattering. This is normally considered a source of image degradation in absorptive X-ray imaging, because together with Compton scattering, it contributes to a scatter background obscuring image details. In contrast to Compton scattering, however, coherent scattering is strongly emission angle specific, and even though the corresponding total cross-section is usually smaller, it can vastly exceed the Compton cross-section in certain angular intervals. The use of coherent scattering for imaging applications has been proposed about three decades ago, but it never became very popular. This is because the acquisition of images relies on a high enough energy resolution, which is not achievable with conventional, energy integrating imaging panels. With energy discriminating pixel detectors available to us, chapter 5 will finally demonstrate their use in coherent scattering for materials research.

Publications

Parts of this work have been published in the following articles:

Koenig, T. & Oelfke, U. (2010). Single crystal targets may improve soft-tissue contrast in megavoltage imaging by means of coherent bremsstrahlung, *Phys. Med. Biol.* **55**(5): 1327–1341.

Koenig, T., Zuber, M., Zwerger, A., Schuenke, P., Nill, S., Fauler, A., Fiederle, M. & Oelfke, U. (2011). A comparison of various strategies to equalize the lower energy thresholds of a CdTe Medipix2 Hexa detector for X-ray imaging applications, *J. Inst.* **6**(01): C01074.

Koenig, T., Zwerger, A., Zuber, M., Schuenke, P., Nill, S., Guni, E., Fauler, A., Fiederle, M. & Oelfke, U. (2010). On the energy response function of a CdTe Medipix2 Hexa detector, *Nucl. Instr. and Meth. A:* in press.

A patent application called “Method and Apparatus for Image Guided Radiotherapy” was published with the World Intellectual Property Organisation under the international publication number WO 2010/128034 A1 on 11/11/2010.

Chapter 2

Interactions of Energetic Charged Particles and X-Rays with Matter

2.1 Overview

This chapter aims at giving an overview of those processes relevant to medical physics that occur when charged particles (section 2.2) or X-rays (section 2.3) traverse matter. The effects detailed here are only those that will be of high relevance to the following chapters, while those that play a special role will be discussed directly where it is necessary. The properties of bremsstrahlung and pair production will be reviewed only briefly here, as they are considered in much more detail in chapter 3 and appendix B.

2.2 Charged Particles

2.2.1 The Collisional Stopping Power

The energy loss of charged particles moving through matter is commonly divided into two kinds of inelastic interactions: those involving the electrons present in the medium and those with atomic nuclei. These can be further split into radiative events, which lead directly to an emission of bremsstrahlung photons, and collisional events, in which emission of radiation only occurs through ionization, fluorescences and secondary bremsstrahlung in the target medium, and where radiation is mostly dissipated as heat. The influence of these effects is normally described by introducing the so-called mass stopping power, which is defined by:

$$\frac{S(T)}{\rho} \equiv -\frac{1}{\rho}\frac{\partial T}{\partial z}, \tag{2.1}$$

where $-\partial T/\partial z$ is the kinetic energy loss per unit path length and ρ represents the material density. The concept of the mass stopping power takes into account that the energy loss per single interaction is generally small and therefore models the slowing down process as being continuous expressed in terms of the derivative in (2.1). Determining this derivative for arbitrary particles is nontrivial and requires a precise understanding of the mechanisms involved.

2.2.1.1 Protons & Heavy Ions

For charged particles whose mass m_p is large comparable to the electron mass m, such as protons and heavy ions, both the nuclear as well as the radiative stopping power are usually neglectable

at energies typical in a medical context, and so the mass stopping power is almost completely determined by its collisional part, as given by the Bethe formula (Amsler 2008):

$$\frac{S_{coll}(T)}{\rho} = 4\pi r_e^2 m \frac{N_A Z Z_P^2}{M_u A \beta^2} \left[\ln\left(\frac{2m\beta^2}{I\,(1-\beta)^2} \right) - \beta^2 \right] \tag{2.2}$$

Here, T is the particle's kinetic energy in MeV, $\beta^2 = 1 - m_p^2/(T+m_p)^2$, m_p represents the projectile's and $m = 0.511\,\mathrm{MeV}$ the electron's rest mass, $r_e = 2.82 \cdot 10^{-13}\,\mathrm{cm}$ denotes the classical electron radius, $N_A = 6.022 \cdot 10^{-23}\,\mathrm{mol}^{-1}$ and $M_u = 1\,\mathrm{g\ mol}^{-1}$. A and Z are atomic mass and number of the target material, Z_p denotes the atomic number of the projectile. I is the mean ionisation potential of the target material and can be approximated by $I \approx 10\,\mathrm{eV} \cdot Z$ according to Bloch (1933).

With the nuclear stopping power being insignificant, protons and heavier ions interact almost exclusively with the medium's electrons, which are much lighter. As a consequence, the incident particles get deflected only slightly from their original path throughout their journey, and their range can be computed easily by

$$R(T) = \int_0^T \frac{1}{S(T')} dT' \tag{2.3}$$

and (2.2), which is again based on the above continuos slowing down approximation (CSDA) and thus often referred to as CSDA range.

2.2.1.2 Electrons

The collisonal stopping power for electrons is given by

$$\frac{S_{coll}(T)}{\rho} = \frac{N_A Z}{A} \frac{2\pi r_e^2 m}{\beta^2} \left[\ln \frac{\tau^2\,(\tau+2)}{2\,(I/m)^2} + (1-\beta)^2 \left(1 + \frac{\tau^2}{8} - (2\tau+1)\ln(2) \right) \right], \tag{2.4}$$

where τ is the electron's kinetic energy normalized to its rest mass. In contrast to ions, electrons get deflected from their original direction much easier due to their small mass. Because of this, the CSDA range is no longer a measure for the penetration depth of an electron beam in matter, but gives the range of electrons along their curved trajectories. The CSDA range therefore is only an upper boundary for the penetration depth that is very rarely reached.

Two examples for electron stopping powers in diamond ($Z = 6$) and tungsten ($Z = 74$) are given in Fig. 2.1. Both curves were obtained with a more sophisticated model than (2.4), which was described by Wambersie et al. (2007). In particular, the Sternheimer–Liljequist model was used to include inelastic scattering, i.e. radiative processes. The diamond curve actually represents the stopping power of amorphous carbon, with a density rescaled to that of diamond. This has to be considered an approximation, as scattering processes in a single-crystal are anisotropic (for details, cf. chapter 3).

Striking is the maximum of the energy deposition at the end of an electron's track. This is called the Bragg peak and typical for all charged particles traversing matter. In radiation therapy employing ions, one makes use of this behaviour in order to achieve a dose deposition that is more conformal to a target volume than it is possible with X-rays. Here, with electrons, we note that due to this Bragg peak, radiation damage is reduced if one deals with very thin targets, as the incident electrons are very likely to leave it again and therefore take most of their initial energy with them.

The collisional stopping power dominates over the radiative one for the energies typical for the phenomena considered in this thesis (Fig. 2.2). However, the radiative part is already large enough

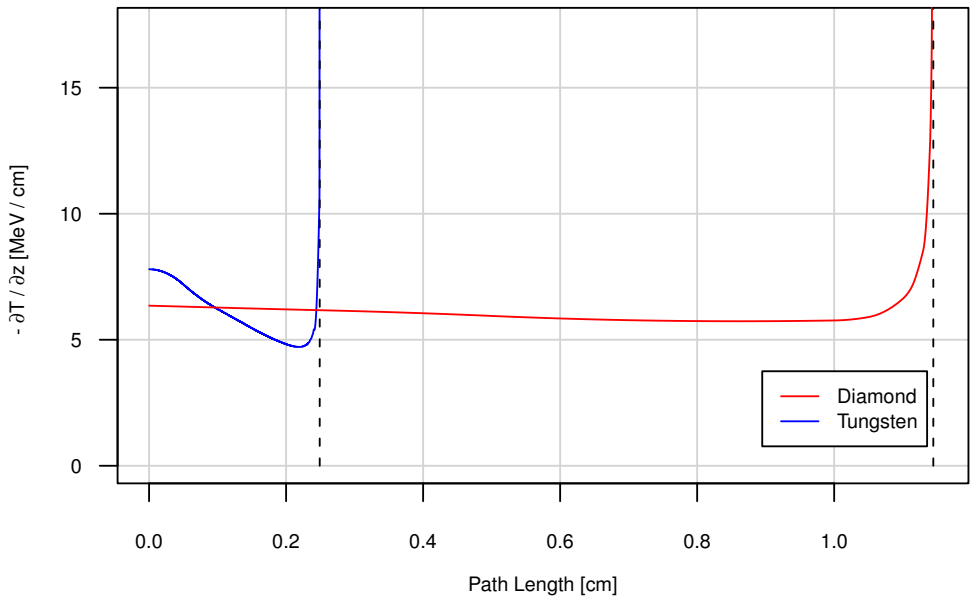

Figure 2.1 Comparison of the stopping powers of 7 MeV electrons traversing diamond (see text) and tungsten. The dashed lines represent the CSDA ranges.

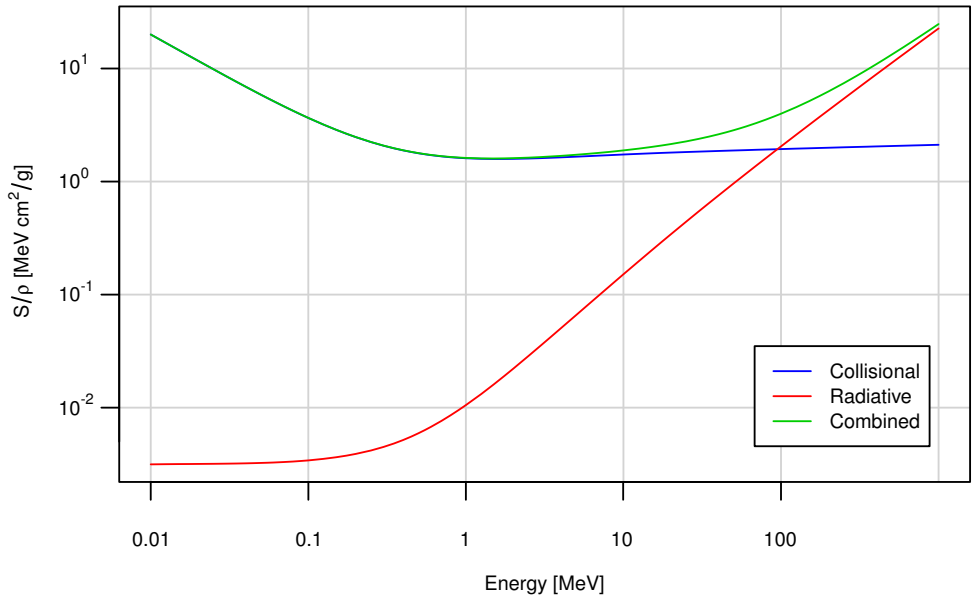

Figure 2.2 Comparison of the radiative and collisional mass stopping powers of electrons in amorphous carbon. The contribution of the radiative part to the total stopping power is negligible below 10 MeV, but still plays a role in X-ray generation even for very low electron energies. Above 100 MeV, it starts to dominate the collisional part. For tungsten, this point is located roughly at 50 MeV.

to facilitate the production of bremsstrahlung even for electrons in the keV range. We defer a detailed discussion of this phenomenon to chapter 3 and just state here that its cross-section is proportional to Z^2, where Z is the atomic number of the target.

In Fig. 2.3 we compare the angular scattering distributions for 5 MeV electrons in some materials that we will encounter as bremsstrahlung targets in chapter 3. It becomes clear here that for

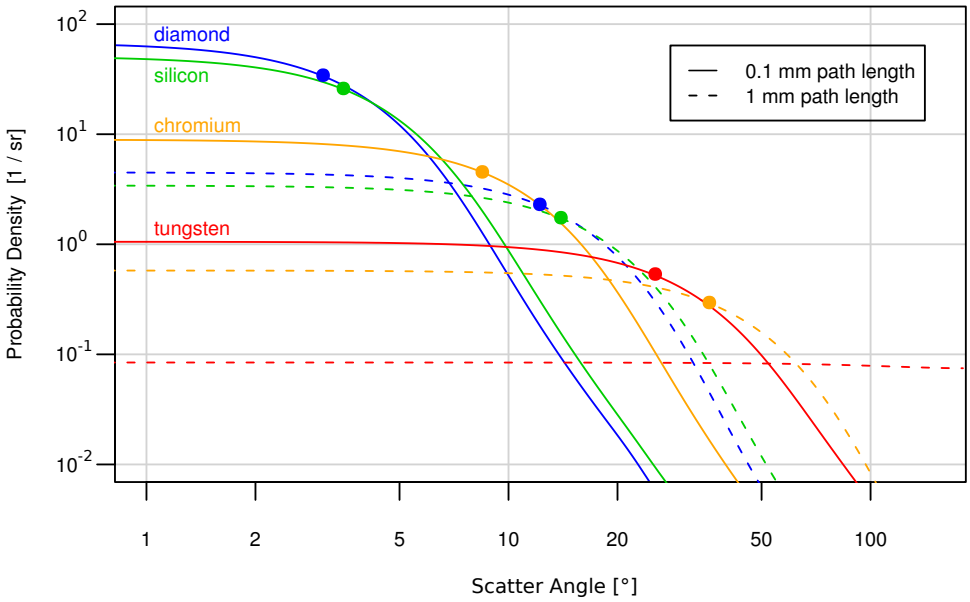

Figure 2.3 Probability density functions (PDFs) for the angular scattering distributions of 5 MeV electrons in various media. The dots give the positions at which the PDFs have dropped to 50% of their maximum value. The path lengths represent the lengths of individual trajectories rather than penetration depths.

increasing atomic numbers the electrons get scattered a lot more for a given path length.

2.3 X-Rays

2.3.1 The Attenuation Coefficient

X-rays interact with matter in a fundamentally different way than charged particles. Instead of having a finite range, they exhibit a finite interaction probability within a certain volume. Resulting is the Beer-Lambert law, which relates the transmitted intensity I to the original one I_0 by means of the attenuation coefficient μ:

$$I = I_0 \mathrm{e}^{-\mu \Delta x}. \tag{2.5}$$

Here, Δx represents the path length travelled by the photon in matter. μ is a function of the X-ray energy and is commonly divided by the material density to obtain the mass attenuation coefficient μ/ρ. In general, it has to include all photon interactions that are allowed for a given energy. For medical X-rays, these are the photoelectric effect, coherent and incoherent scattering, and for photon energies above 1.022 MeV also pair production. In the following sections, we will briefly review these effects.

2.3.2 Photoelectric Absorption

The photoelectric effect denotes the process of complete absorption of the incident photon by an electron bound to an atom, which is left in an excited state. The means by which an excited atom dissipates its excess energy is described in sidebar 4.1. Here, we will briefly review the main features of photoelectric absorption.

Modelling this process is probably one of the most difficult cases among all those described in this chapter. In fact, one has to consider the atomic shell, i.e. the main quantum number, of the electron involved in the process, plus the energy of the photon that is absorbed by it, both of which have to be described by the appropriate wave functions. As a consequence, many expressions exist for the interaction cross-section, and tabulated values are often used to avoid the complexity of evaluating different cross-sections for the various energy ranges and quantum numbers. Because of this, we just state the following relations for the absorption coefficient:

$$\mu_{ph} \sim Z^m \begin{cases} 1/k^3 \text{ for } k < 1\,\text{MeV} \\ 1/k \text{ for } k > 10\,\text{MeV} \ . \end{cases} \tag{2.6}$$

Here, k denotes the photon energy. What we can learn from these relationships is the fact that photoelectric absorption is particularly strong for low energies, where it also decreases rapidly with increasing energy. With $m \approx 3$ for low atomic numbers and $m \approx 4$ for large ones, we also conclude that photoelectric absorption is much more likely to happen in heavy elements, which illustrates the need for these materials in X-ray detectors (chapter 4).

When the photon energy exceeds the energy required to knock a particular electron out of its shell, the cross-section for photoelectric absorption experiences a sudden rise that interrupts the $1/k^3$ decrease. The ionisation energy required for this to happen rapidly increases with the atomic number Z. These absorption edges are thus particularly observed in heavy elements. This effect is employed in X-ray contrast agents, which are often used in combination with dual source or photon counting imaging (chapter 4).

2.3.3 Incoherent Scattering

Incoherent (or Compton) scattering denotes the process of a partial transfer of the incident photon's energy to the electron, resulting in both a secondary electron as well as an outgoing photon with reduced energy. Assuming the target electron is free and at rest, a simple consideration of the conservation of 4-momenta gives a relation between incident (k) and outgoing photon (k') energies as a function of the photon's scattering angle θ:

$$k' = \frac{k}{1 + \frac{k}{m}(1 - \cos\theta)} \ . \tag{2.7}$$

The corresponding cross-section for an unpolarized photon beam was derived by Klein & Nishina and is depicted in Fig. 2.4. It is given by (Salvat et al. 2001):

$$\frac{d\sigma_{\mathrm{KN}}}{d\Omega} = \frac{r_\mathrm{e}^2}{2}\left(\frac{k'}{k}\right)^2\left(\frac{k'}{k} + \frac{k}{k'} - \sin^2\theta\right) \ . \tag{2.8}$$

As can be seen, back- and forward scattering are equally likely for non-relativistic energies. In this case, k/m in (2.7) approaches zero, and we obtain the low energy limit of the Klein-Nishina cross-section, which was obtained classically for the scattering of electromagnetic waves at point charges by Thomson:

$$\frac{d\sigma_{\mathrm{T}}}{d\Omega} = \frac{r_\mathrm{e}^2}{2}\left(1 + \cos^2\theta\right) \ . \tag{2.9}$$

The scattering behaviour depicted in Fig. 2.4 is responsible for a degradation of X-ray image quality when large fields of view are used. With photon energies typically in the range of 40-120 keV, the mean squared scattering angle is generally large enough to create a dominant scatter component which lowers the contrast of the resulting images. This is especially relevant in cone beam computed tomography, but less so for fan beam geometries, where the X-ray beam is collimated in order to only image a thin slice of the object.

The energy of the secondary photon (2.7) has a minimum that is reached by setting $\theta = \pi$:

$$k'_{\min} = \frac{k}{1 + 2\frac{k}{m}} \ . \tag{2.10}$$

This lower boundary is commonly observed in X-ray spectrometry with low-Z sensor materials as a sharp rise if monoenergetic photons are employed and is therefore called the Compton edge. Sensors with higher Z, such as those made from CdTe discussed in chapter 4, have a much higher photoelectric cross-section, and the Compton edge can be neglected in those materials. As an example, for 60 keV photons the Compton edge is located at around 49 keV (for free electrons at rest).

The total Klein-Nishina cross-section can be obtained by integrating over the solid angle and gives a rather complicated expression. For this reason, we just give the high energy dependence of the corresponding mass attenuation coefficient:

$$\mu_{Co} \sim \frac{1}{k} \ \text{ if } k \gg m \ . \tag{2.11}$$

Note that the non-relativistic counterpart (2.9) does not depend on k.

The above assumptions do not hold for electrons bound to atoms. The Compton edge then exhibits a Doppler broadening due to the motion of the electrons around the atoms. Also, especially for high-Z electrons, the binding energy needs to be taken into account. This is usually treated in the so-called impulse approximation, and basically amounts to some multiplicative factors that have to be added to (2.8). These factors then also lead to the occurance of absorption edges, which are, however, not as pronounced as in the case of photoelectric absorption. Since a detailed treatment of the Compton profiles obtained using the impulse approximation will not be necessary for an understanding of the issues covered in this thesis, we will not go into any details here and refer interested readers to Salvat et al. (2001).

With the above considerations it becomes clear that incoherent scattering relies on the abundance of electrons present in the medium, that is on the electron density. Hence, in X-ray imaging incoherent scattering offers almost no contrast in biological tissues when compared with photoelectric absorption. In combination with its large angle scattering characteristics (Fig. 2.4), the Compton effect mainly contributes to image degradation in most cases.

2.3.4 Coherent Scattering

Coherent scattering (also called Rayleigh scattering) refers to the process of a photon being scattered elastically by the whole atomic charge cloud at once, i.e. no energy transfer is involved. Consequently, this case can be described by the Thomson cross-section (2.9). For a single atom, it now has to be multiplied by the square of the atomic form factor $F(q, Z)$ in order to account for the electronic charge distribution within the atom (sidebar 2.1), where q is the momentum transfer involved.

$$\frac{d\sigma_R}{d\Omega} = \frac{d\sigma_T}{d\Omega} F^2(q, Z) = \frac{r_e^2}{2} \left(1 + \cos^2\theta\right) F^2(q, Z) \ . \tag{2.12}$$

Here, the scattering angle θ and the momentum transfer q depend on each other according to

$$q = 2k \sin\frac{\theta}{2} \ . \tag{2.13}$$

Note that θ is again the *full* scattering angle here. Using (2.17) as given in sidebar 2.1, it is easy to see that for low values of q the coherent scattering cross-section is constant, whereas for large values it decreases with $1/k^4$, since $q \sim k$ (2.13). The above expressions neither take into account relativistic effects in heavy elements nor anomalous scattering that occurs when the photon energy is close to an absorption edge. For details on both effects, see Kane et al. (1986) and references therein.

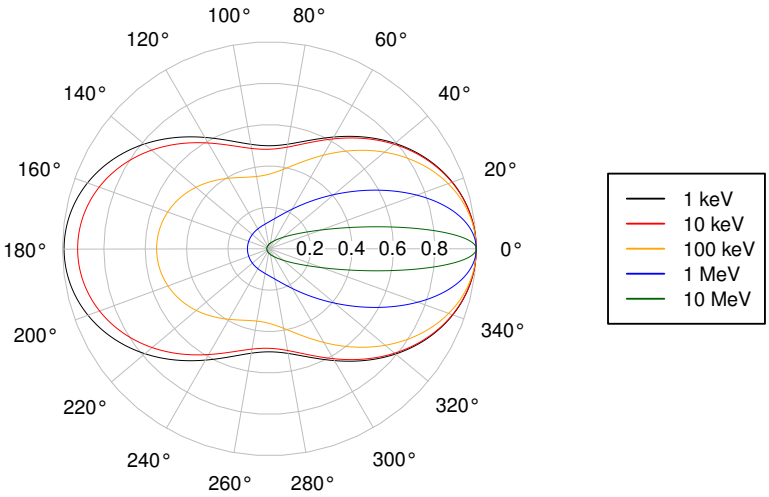

Figure 2.4 Angular dependence of the Klein-Nishina differential cross-section, normalised to unity at zero scattering angle.

2.3.5 Pair Production

In pair production, a photon interacts with an atomic nucleus or an electron to produce an electron-positron pair. Conservation of rest mass dictates a photon energy of at least 1.022 MeV for the process to happen. Pair production in the field of the atomic electrons is roughly one order of magnitude less likely than pair production in the field of the nucleus and will not be considered.

The nuclear pair production cross-section can be derived very similar to that of bremsstrahlung, and the kinematics of both processes share many common features. We will postpone a more detailed discussion of pair production to appendix B, where we will take a closer look on pair production in single-crystals, also called coherent pair production. Here, we again only state that the cross-section, and with it the mass attenuation coefficient, increases with Z^2.

2.3.6 Total Mass Attenuation Coefficients for Some Media of Interest

The above effects are most easily summarised using tabulated values such as those from the XCOM database maintained by the National Institute of Standards[1]. Fig. 2.5 shows the total mass attenuation coefficients for some materials that we will later refer to in this thesis. For water, we give the individual contributions of the various effects to the mass attenuation coefficient in Fig. 2.6.

In Fig. 2.7, a comparison of the mass attenuation coefficients of different soft tissues and bone is given. It shows the dilemma of modern X-ray imaging, where high soft tissue contrast can only be achieved with comparably low photon energies, which in turn can only be used for non-obese patients and those without metal implants.

Going to higher photon energies, contrast is mainly achieved through density variations, which again are small for soft tissues. So-called megavoltage imaging (which is relevant in radiotherapy and discussed in chapter 3) therefore offers only poor contrast and also requires a lot more radiation to achieve an acceptable noise level because of the generally lower mass attenuation coefficients in this high energy regime.

[1] http://www.nist.gov/pml/data/xcom/index.cfm

Sidebar 2.1 The Atomic Form Factor

The form factor represents a convenient way to handle the effect of average charge distributions on the outcome of scattering events. It is defined as the Fourier transform of the electron density $D(\boldsymbol{r}, Z)$, and can be expressed as follows for spherically symmetric atoms:

$$F(q, Z) = 4\pi \int_0^\infty D(r, Z) \frac{\sin(qr)}{qr} r^2 dr \ . \tag{2.14}$$

This means that the form factor only depends on the magnitude of the momentum transfer. Various semi-analytical methods exist in the literature to calculate $D(r)$. For ease of use, it is common to model the joint electron potential by a sum of three Yukawa potentials,

$$\phi_e(r, Z) = \frac{Ze}{r} \sum_{i=1}^{3} \gamma_i(Z) \mathrm{e}^{-\lambda_i(Z) r} \ , \tag{2.15}$$

which are fitted to the results obtained from these model calculations using the parameters $\gamma_i(Z)$ and $\lambda_i(Z)$. The models employed are usually either the Thomas-Fermi-Dirac (Bonham & Strand 1963) or the Hartree-Fock-Slater model (Salvat et al. 1987) and the corresponding fitting parameters are tabulated in the respective articles. The latter gives more accurate results, especially for high-Z materials (see figure below). Inserting the above expression into Poisson's equation then gives the radially symmetric electron density:

$$D(r, Z) = \frac{Z}{4\pi r} \sum_{i=1}^{3} \gamma_i(Z) \lambda_i^2(Z) \mathrm{e}^{-\lambda_i(Z) r} \ . \tag{2.16}$$

Combining (2.16) with (2.14), we obtain the final expression for the atomic form factor:

$$F(q, Z) = Z \sum_{i=1}^{3} \frac{\gamma_i \lambda_i^2(Z)}{\lambda_i^2(Z) + q^2}. \tag{2.17}$$

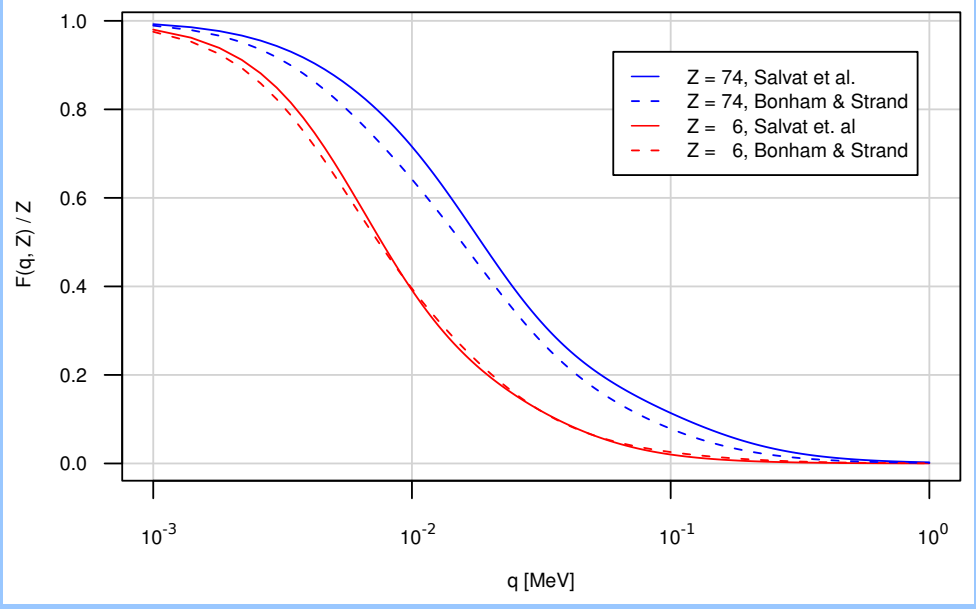

In X-ray scattering, the cross-section must be multiplied by $F^2(q, Z)$, hence large momentum transfers are suppressed. In electron scattering, such as bremsstrahlung (chapter 3), the relevant factor is $(Z - F(q, Z))^2$, and thus small momentum transfers are less likely to happen.

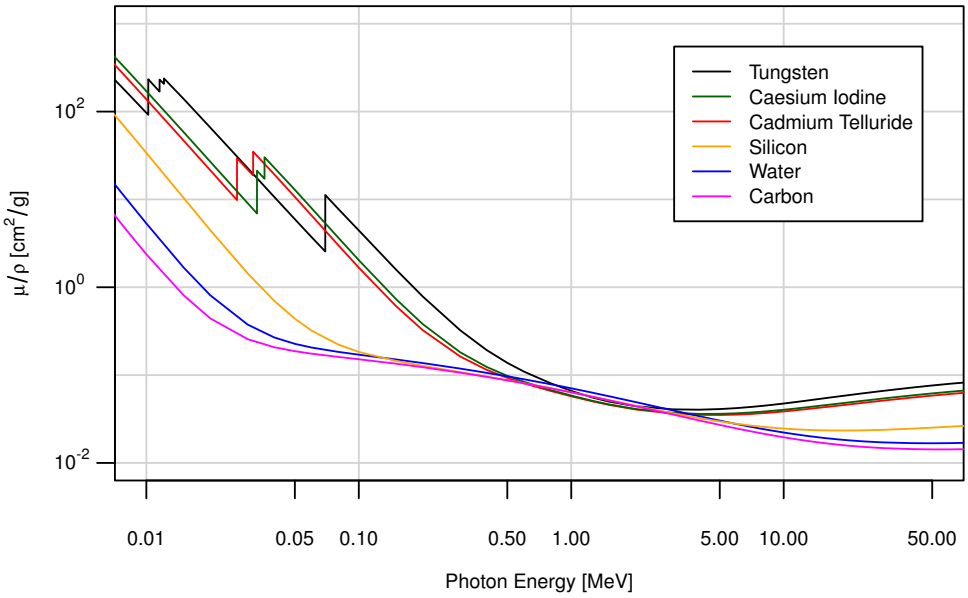

Figure 2.5 Total mass attenuation coefficients for various materials encountered in this work. Carbon ($Z = 6$), silicon ($Z = 14$) and tungsten ($Z = 74$) are discussed as possible targets for bremsstrahlung generation in chapter 3. Silicon also plays a role as the material the Medipix readouts discussed in chapter 4 are based on, and is a common sensor material for these detectors, too. Cadmium Telluride (CdTe) is another sensor material with much better absorption properties due to the high atomic numbers of cadmium ($Z = 48$) and tellurium ($Z = 52$), and is discussed extensively in the same chapter. Caesium iodine represents a common scintillator used in many flat panel detectors for X-ray imaging. Its mass attenuation coefficient is very similar to that of CdTe in the X-ray domain because of the similar atomic numbers ($Z = 55, 53$). It is, however, transparent to visible light. Last but not least, water is the most abundant material in the human body.

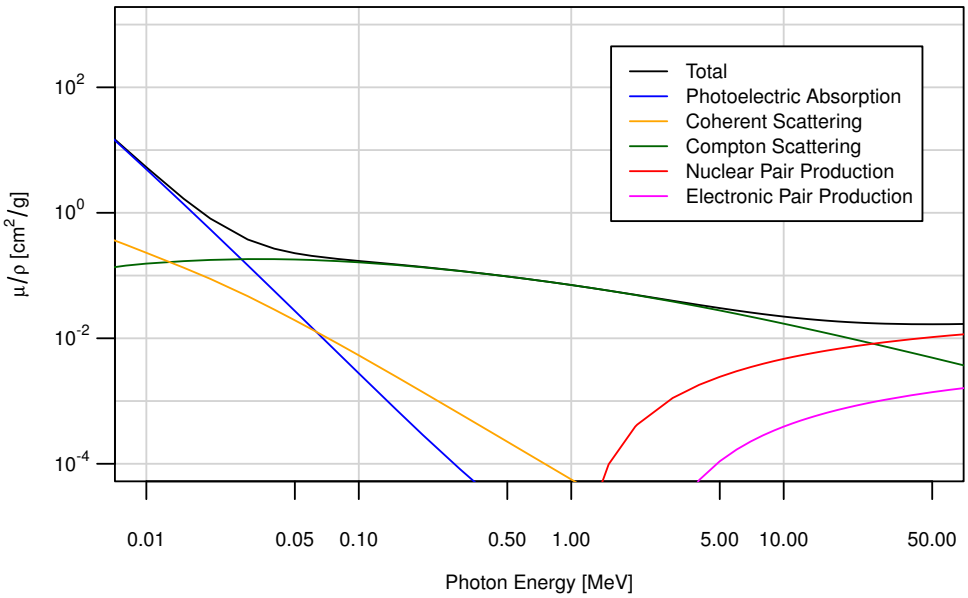

Figure 2.6 Total mass attenuation coefficient for water along with the contributions to it by the individual effects described in this chapter.

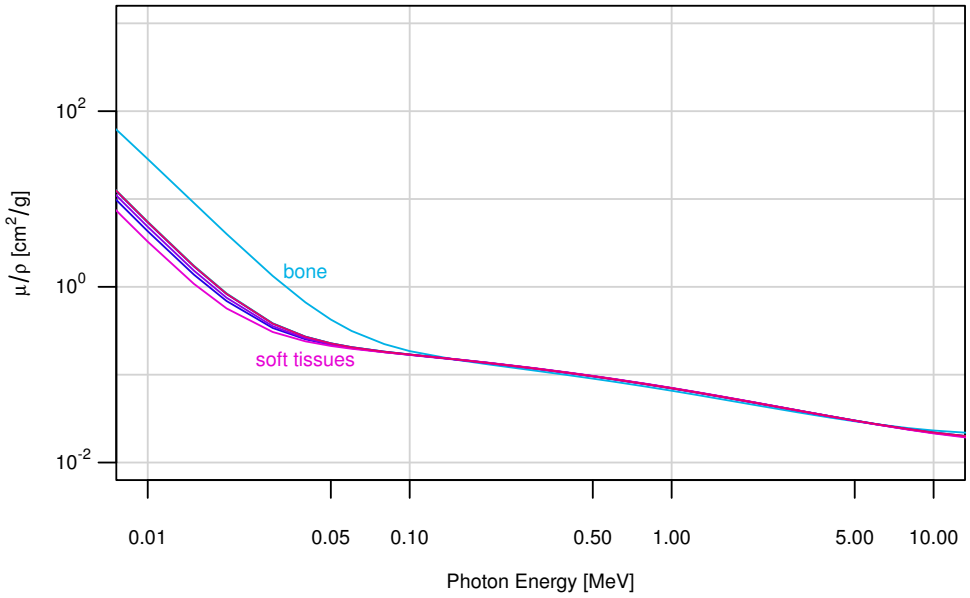

Figure 2.7 Total mass attenuation coefficients for various soft tissues and bone. Their relative differences almost vanish for higher energies.

Many more effects than those described exist, such as the nuclear equivalents to the scattering and absorption processes described above for electrons, along with the Delbrück effect, which is the process of Thomson scattering with virtual electrons or positrons in the nuclear field. All these effects are relatively unlikely and thus have no significant influence on the total mass attenuation coefficients shown.

2.4 Interactions with Extended Objects: When Single-Atom Cross-Sections Fail to Tell the Full Story

The considerations carried out in the preceeding sections were implicitly based on the so-called independent atom approximation, which assumes that the scattering caused by an extended object is the sum of the contributions by the individual atoms contained in it.

X-ray crystallography is a famous example where this assumption obviously fails. There, the incident beam is diffracted into many specific directions, rather than giving a more or less diffuse scatter image as would be expected from single atom Rayleigh scattering (2.12). This phenomenon is most commonly explained classically by interferences between the waves scattered by the various particles, which can interfere either constructively or destructively. A detailed consideration of the particle positions and the direction of the incident waves then gives the directions at which distinct intensity peaks can be observed.

This thesis will follow a different approach to this topic, which in the author's oppinion is conceptually more satisfying: the modelling of the scattering process as the scattering by the joint potential constituted by all the particles in the object. By introducing the atomic form factor (sidebar 2.1), we have already included such a line of thinking into the Rayleigh cross-section (2.12) in order to take the average electron distribution of an atom into our considerations. In fact, there is no reason why we should not follow the same approach to also include the distributions of the atoms themselves into the cross-sections.

There is also no reason why we should restrict ourselves to crystals as the objects to be treated in this manner. Their periodic ordering may give them a special role in human thinking, but there exists no physics-motivated argument why amorphous objects should not be modelled in the same way. Although aperiodic, they still possess a short-range order that can influence scattering amplitudes.

Analytically, the additional is goes as follows: Instead of the single atom potential, the joint potential made up by all the atoms enters the cross-section. Assuming identical atoms for simplicity here, this amounts to an additional factor in the cross-section:

$$d\sigma_j(\boldsymbol{q}) = \frac{1}{N}\left|\sum_{\boldsymbol{L}} \mathrm{e}^{i\boldsymbol{q}\cdot\boldsymbol{L}}\right|^2 d\sigma_s(\boldsymbol{q}) \ . \tag{2.18}$$

With $d\sigma(q)$, we here denote any differential cross-section expressed as a function of the momentum transfer $\boldsymbol{q}$, and N represents the total particle number. The reason that leads to this factor is that cross-sections are always computed in momentum space, which requires to Fourier transform the (in our case electrostatic) potential $V(\boldsymbol{r})$. Except for the atom which is placed at the origin, this causes to a phase factor according to the shift theorem depending on an atom's location $\boldsymbol{L}$, and consequently to a sum of phase factors for all the potentials. Since the matrix elements containing these potentials need to be squared, we arrive at the above expression.

The consequence is the so-called structure factor which we detail in sidebar 2.2. Sidebar 2.3 deals with the additional complexity that enters when individual atoms are not at rest with respect to the crystal coordinate frame.

Among all the phenomena considered previously, those that will require this treatment are coherent scattering, bremsstrahlung and pair production, since they are influenced by the position of the atomic nuclei. We will refer to the latter as coherent bremsstrahlung and coherent pair production (chapter 3). Being inelastic collisions, coherent in this context will denote strong emission angle specificity (as in the case of X-ray crystallography) and should not be mistaken for an elastic process.

Sidebar 2.2 The Structure Factor

Similar to the atomic form factor (sidebar 2.1) in the case of electron charge distributions, the structure factor is used to incorporate the positions of atomic nuclei into scattering cross-sections. As was shown by Überall (1956) and Palazzi (1968) in the context of coherent bremsstrahlung, the arrangement of atoms in a cubic lattice modifies the cross-section by an additional factor,

$$\frac{1}{N}\left|\sum_{\boldsymbol{L}} \mathrm{e}^{i\boldsymbol{q}\cdot\boldsymbol{L}}\right|^2_{\mathrm{cu.}} \approx \frac{(2\pi)^3}{v_0}\sum_{\boldsymbol{g}} \delta\left(\boldsymbol{q}-2\pi\boldsymbol{g}\right) = \frac{(2\pi)^3}{v_0}\sum_{\boldsymbol{\tau}} \delta\left(\boldsymbol{q}-\boldsymbol{\tau}\right), \tag{2.19}$$

where N is the number of unit cells in the crystal, $\boldsymbol{L}$ denotes a lattice vector, $\boldsymbol{g}$ is a vector of the reciprocal lattice (i.e. the Fourier transform of the crystal lattice) and v_0 the volume of a single unit cell. $\boldsymbol{q}_i$ represents the momentum transfer in the crystal coordinate frame. $\boldsymbol{\tau} = 2\pi\boldsymbol{g}$ will be used as a convenient abbreviation throughout this thesis. The approximation in (2.19) is valid for large numbers of unit cells, which is certainly justified for macroscopic crystals, and the δ-distribution associated with it effectively limits the momentum transfer to a vector of the reciprocal lattice (times 2π, a fact that we will omit for simplicity).

We can now think of a crystal basis more complex than the simple cubic one. In order to do this, we will add another cubic lattice to the one already existing, and we will shift this new lattice by the vector $\boldsymbol{u}$:

$$\sum_{\boldsymbol{L}} \mathrm{e}^{i\boldsymbol{q}\boldsymbol{L}} + \sum_{\boldsymbol{L}} \mathrm{e}^{i\boldsymbol{q}(\boldsymbol{L}+\boldsymbol{u})} = \sum_{\boldsymbol{L}} \mathrm{e}^{i\boldsymbol{q}\boldsymbol{L}}\left(1+\mathrm{e}^{i\boldsymbol{q}\boldsymbol{u}}\right) = \sum_{\boldsymbol{L}} \mathrm{e}^{i\boldsymbol{q}\boldsymbol{L}} \int \left[\delta\left(\boldsymbol{r}\right)+\delta\left(\boldsymbol{r}+\boldsymbol{u}\right)\right]\mathrm{e}^{-i\boldsymbol{q}\boldsymbol{r}}d\boldsymbol{r}\ . \tag{2.20}$$

Taking a look at the last step carried out in (2.20), we see that the Fourier transform of the unit cell (assumed to be a sum of δ-distributions here) has entered the equation. This Fourier transform is called the structure factor $S(q)$ and can - due to the linearity of the problem - be generally defined using the particle density per unit cell $n\left(\boldsymbol{r}\right)$:

$$S(q) = \int n\left(\boldsymbol{r}\right)\mathrm{e}^{-i\boldsymbol{q}\boldsymbol{r}}d\boldsymbol{r}\ . \tag{2.21}$$

Comparing (2.19) and (2.20) with (2.21), we see that it is the square of the structure factor $|S|^2 = SS^*$ that will be relevant for the computation of cross-sections. For an arbitrary unit cell with particle density $n\left(\boldsymbol{r}\right)$, we have to multiply (2.19) by this factor.

It is important to note here that the above considerations do not only apply to single crystals. Instead, $\boldsymbol{L}$ can represent the coordinate of any atom in 3D space. Therefore, we can rewrite the sum of complex exponentials in (2.20) according to

$$\sum_{\boldsymbol{L}} \mathrm{e}^{i\boldsymbol{q}\cdot\boldsymbol{L}} = \int \left[\sum_{\boldsymbol{L}} \delta\left(\boldsymbol{r}+\boldsymbol{L}\right)\right]\mathrm{e}^{-i\boldsymbol{q}\boldsymbol{r}}d\boldsymbol{r} = \int \rho(\boldsymbol{r})\mathrm{e}^{-i\boldsymbol{q}\boldsymbol{r}}d\boldsymbol{r}\ , \tag{2.22}$$

with overall particle density $\rho(\boldsymbol{r})$, and find for an amorphous body the spatial average

$$\frac{1}{N}\left\langle\left|\sum_{\boldsymbol{L}} \mathrm{e}^{i\boldsymbol{q}\cdot\boldsymbol{L}}\right|^2\right\rangle_{\mathrm{am.}} = \frac{1}{N}\int\int \left\langle\rho(\boldsymbol{r}\,')\rho(\boldsymbol{r}\,'+\boldsymbol{r})\right\rangle\mathrm{e}^{-i\boldsymbol{q}\boldsymbol{r}}d\boldsymbol{r}\,'d\boldsymbol{r} = \int G(\boldsymbol{r})\mathrm{e}^{-i\boldsymbol{q}\boldsymbol{r}}d\boldsymbol{r}\ , \tag{2.23}$$

where $G(\boldsymbol{r})$ is defined by the above equation and called the pair correlation function (Cuello 2008). It is proportional to the probability of finding an atom at a distance r from the reference atom. Thus, the left side of (2.23) is simply the Fourier transform of this pair distribution function, and for amorphous bodies often also called the structure factor.

The calculations performed above explicitly assume well-defined atom positions. Sidebar 2.3 gives details about how to include disturbances caused by finite temperatures and zero point motion due to the uncertainty principle.

Sidebar 2.3 The Debye-Waller Factor

Because of the uncertainty principle, an atom, that is a scattering centre, cannot be at rest, but always possesses a finite momentum, and so the location of all the atoms in a macroscopic body can never be known with an arbitrarily high precision. Vibrations induced by a finite temperature will even increase this effect. The question that arises then is how all this will influence the scattering behaviour of such an extended object. We will see below that this intrinsic motion will not cause a Doppler broadening as one might naively expect, but results in an attenuation of the scatter amplitudes depending on the temperature.

In order to see this, one has to compute the average of (2.18), which was done by various people, including Überall (1956), and which yields:

$$d\sigma_j(\boldsymbol{q}) = \frac{1}{N}\left\langle \left| \sum_{\boldsymbol{L}} \mathrm{e}^{i\boldsymbol{q}\cdot\boldsymbol{L}} \right|^2 \right\rangle d\sigma_s(\boldsymbol{q}) = \left[\mathrm{e}^{-q^2\langle u^2\rangle/3} \frac{1}{N} \left| \sum_{\boldsymbol{L}} \mathrm{e}^{i\boldsymbol{q}\cdot\boldsymbol{L}} \right|^2 + \left(1 - \mathrm{e}^{-q^2\langle u^2\rangle/3}\right) \right] d\sigma_s(\boldsymbol{q}) \ . \tag{2.24}$$

$\mathrm{e}^{-q^2\langle u^2\rangle/3}$ is called the Debye-Waller factor and contains the mean squared displacement of the atoms around their average positions. This means that due to the oscillations of the atoms, the cross-section splits up in two terms: one depending on $\mathrm{e}^{-q^2\langle u^2\rangle/3}$, and another one proportional to $1 - \mathrm{e}^{-q^2\langle u^2\rangle/3}$. The latter just represents the single atom cross-section with small momentum transfers q being attenuated, and is typically called the *incoherent* part of the cross-section. The first one contains the structure of the object's lattice (cf. sidebar 2.2) and is thus called the *coherent* part. Here, large momentum transfers are suppressed.
When dealing with mean squared displacments one needs to take care of which value is actually given in the literature. Very often values for *one* dimension can be found, which are related to the above through $\langle u^2\rangle/3 = \langle u_x^2\rangle$.

Naturally, in most scattering experiments one would like the coherent part to become as large as possible, and suppress the incoherent one, which can be achieved by lowering the temperature. Values for $\langle u^2\rangle$ or related quantities are usually tabulated. A compilation of values for some chemical elements was given by Peng et al. (1996).

It is interesting to note that the search for materials with low vibrational amplitudes can be limited to the search for hard materials. In order to see this, we relate $\langle u^2\rangle$ to the Debye temperature Θ_D (Peng et al. 1996),

$$\langle u^2\rangle = \frac{436.6\,\text{Å}^2}{A} \frac{T}{\Theta_D^2} \left[\Phi\left(\frac{\Theta_D}{T}\right) + \frac{\Theta_D}{4T} \right] \ , \tag{2.25}$$

where A denotes the atomic weight, T the temperature and Φ is the Debye integral (Peng et al. 1996). A numerical evaluation of the above relation teaches us that $\langle u^2\rangle$ decreases with Θ_D. Introducing the mean sound velocity c_s and the elastic modulus E, we find the following relation using textbooks on classical mechanics and solid state physics:

$$\Theta_D \sim c_s \sim \sqrt{E} \ . \tag{2.26}$$

Hence, scattering on hard materials will give a higher coherent fraction than on soft ones. Note that (2.25) is based on the Debye model, which is only accurate for simple cubic lattices.

Finally, we will close the discussion of the Debye-Waller factor by stating a neat observation made in this thesis: In order to calculate the average (2.25) for mixtures of atoms when only the overall Debye temperature Θ_D is known, choosing A as the harmonic mean of the individual atomic weights will give values that are quite close to the actual ones.

Chapter 3

Coherent Bremsstrahlung in Image Guided Radiotherapy: A Feasibility Study

3.1 Motivation & Overview

Previously based on X-ray tubes and radioactive sources, modern radiation therapy relies on the use of linear accelerators (LINACs, sidebar 3.1) that generate high energy bremsstrahlung with peak photon energies between 4 and 25 MeV. Along with the use of these devices comes the need for treatment monitoring and adaptation, which has led to the development of image guided radiation therapy (IGRT). IGRT is often based on anatomical X-ray images of the patient acquired in treatment position. Two basic technological imaging approaches integrated into LINACs are currently pursued.

First, diagnostic kilovoltage (kV) X-ray tubes together with oppositely mounted flat panel detectors (FPIs) are integrated with the LINAC (Jaffray & Siewerdsen 2000, Binder et al. 2005). The main advantage of this technology is the use of low-energy kV photon spectra that potentially allows a resolution of anatomical structures with a high soft tissue contrast. However, this imaging approach requires an additional kV X-ray source and the development of specific quality assurance procedures (Bissonnette et al. 2008). For instance, careful calibration of the imaging geometry with respect to the treatment beam is required. The second approach of IGRT imaging simply avoids these problems by directly using the megavoltage (MV) treatment beam for image acquisition (Ruchala et al. 2000, Mueller et al. 2000, Pouliot et al. 2005). However, these high energy photon spectra cannot provide soft-tissue contrast (Stützel et al. 2008).

Several ideas were pursued to overcome this limitation of IGRT with MV treatment beams. One of them made use of the fact that bremsstrahlung emitted from the target in a direction orthogonal to that of the electron beam exhibits softer energy spectra (Sarfehnia et al. 2007).

In a second and more popular attempt, the energy of the LINAC's electron beam was considerably lowered and the high-Z bremsstrahlung target, e.g. tungsten ($Z = 74$), was replaced with a low-Z target such as carbon ($Z = 6$) (Ostapiak et al. 1998, Flampouri et al. 2002, Faddegon et al. 2008) in order to avoid the absorption of kV photons already in the target itself.

Under the premise of megavoltage imaging, it would be desirable to use bremsstrahlung targets that exhibit an even more increased amount of kV photons in order to supplement the second approach. This would result in better image contrast at the same patient dose level.

Sidebar 3.1 Linear Accelerators in the Clinic

In radiotherapy, LINACs have replaced devices based on radioactive substances (such as ^{60}Co) in the 1980s. Their advantages are the ability to easily switch off the X-ray beam, and to control its energy as well as its intensity. In principle, they work like other linear accelerators known from high energy physics, but of course employ reduced energies (4-25 MeV on most of the machines). A high frequency electromagnetic wave is generated and propagates through a wave guide, where it is used to accelerate electrons emitted by an electron gun in the back of the device. The electrons pass a 270° bending magnet that is used to narrow the electron energy spectrum. The electrons eventually hit the bremsstrahlung target that in radiotherapy is made from a high-Z material to achieve a high photon flux.

The photon beam generated in the target passes an optional flattening filter that is used to create an isotropic emission profile across the field of view. This flattening filter has the shape of a cone and further removes low energy photons from the megavoltage beam. The beam then passes an additional y-shaped aperture and the so-called multileaf collimator. This device has a number of moveable tungsten leaves that can be controlled electronically in order to shape the radiation field to the requirements of the treatment plan.

The figure below shows an image of the treatment room at DKFZ. The "Siemens Artiste" LINAC can be seen in the foreground along with the patient couch. For megavoltage (MV) imaging, the tungsten target ($Z = 74$) used for therapy is replaced with a carbon target ($Z = 6$) in order to make the photon energy spectrum softer and more suitable for imaging (see main text). The MV imaging mode, also called "imaging beam line" (IBL), can be used to quickly obtain 2D projection images of patients, but also for acquiring cone beam CT scans. Up to now, the kilovoltage (kV) imaging system has not yet been included into this LINAC, but will later be available as an upgrade path.

In the background, there is the "Siemens Somatom Emotion", a CT scanner mounted on rails to enable an easy patient positioning. It acquires fan beam CT scans which are less affected by scatter than the cone beam images obtained with the LINACs kV system (chapter 2). It is used particularly to obtain images during the planning stage, where a good contrast is necessary to be able to distinguish soft tissues. Similar to the MV system, the kV part is intended as a tool for quickly assessing the patient's position immediately prior to or during treatment, yet at a lower dose and higher contrast. Due to the slow rotation of the LINAC, a fan beam acquisition is not an option here.

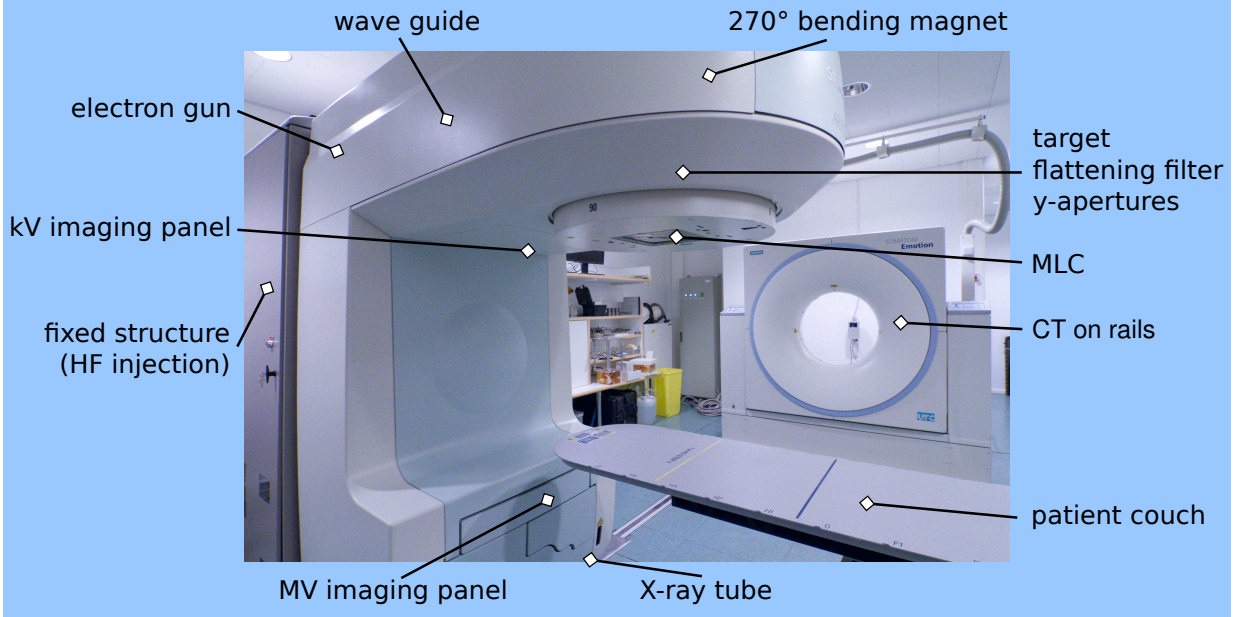

In this chapter, a new idea is introduced of how the photon energy spectrum obtained from a medical LINAC might be modified in order to improve its applicability for IGRT: the replacement of the standard bremsstrahlung target by a single-crystal. It is well known since the mid 1950s (Überall 1956) that these targets lead to an altered process for the creation of bremsstrahlung from charged particle beams, the effect of coherent bremsstrahlung (CB). CB is known to cause a series of strong low energy photon peaks in addition to the incoherent part of the photon energy spectrum when the incident electron beam hits the target at an angle close to one of the principal axes of the crystal lattice. Depending on the structure of the crystal, the electron phase space and irradiation geometry, one can theoretically create CB peaks at energies that correspond directly to the kV energy range we are interested in.

However, whether these promising theoretical features of CB can be realized for IGRT still has to be investigated. First, one has to note that currently CB is mainly used in high energy nuclear physics with GeV electron beams for experiments with 'tagged' photons (Palazzi 1968, Lohmann et al. 1994). Consequently, most theoretical papers describing CB refer to this energy range. Although there are various publications on low energy CB (Andersen et al. 1981, Sáenz & Überall 1982, Andersen & Laegsgaard 1988, Nasonov et al. 1998, Chouffani et al. 1999), this author could not find sources in the literature that provide a unified description of both coherent bremsstrahlung as well as its incoherent background. As will be shown further below, conventional expressions for incoherent bremsstrahlung cannot be used for reliable predictions as the cross-section is required in a form that allows the integration over the momentum transferred to the crystal lattice (cf. sidebars 2.1 - 2.3). Common expressions in the literature (Koch & Motz 1959) are not available in this form or only valid for ultra-relativistic electrons.

One of the main aspects of this chapter, therefore, is to provide a theoretical basis for the calculation of both relevant bremsstrahlung cross-sections. Furthermore, the developed framework will be used to review the most important physical aspects of CB, i.e. we will discuss the physical origin of CB peaks, the influence of specific crystal lattice properties on CB and the influence of the electron direction. This last property will turn out to be crucial when considering thick crystals, where CB from scattered electrons dominates the emission characteristics.

The present chapter is structued as follows: First, we will give an introduction into CB in section 3.2, including a historical overview and a discussion of the connection between CB and channelling radiation. Section 3.3 will introduce the relevant differential cross-sections, as derived in appendix A. In section 3.4, we will study the features of the CB cross-section for diamond, a very popular material for CB generation. Next, the influence of multiple scattering will be discussed in section 3.5. A comparison with other materials will be given in section 3.6. Section 3.7 will be dedicated to answering the question whether increasing the electron energy in combination with single-crystal targets can help to reduce the dose to the patient. The effect of target cooling on the CB intensities is investigated in section 3.8, which is followed by a discussion of beam stoppers and compound targets in section 3.9. Finally, the findings of this chapter will be summarised in section 3.10, and an effect related to CB, coherent pair production, will be briefly discussed in appendix B.

In this chapter, we will use the expressions "poly-crystalline" and "amorphous" targets as synonyms, because there is no notable difference in the bremsstrahlung spectra produced by these materials, and hence they will be treated using single-atom cross-sections. The reason why this is possible is detailed in section 3.4.4.

3.2 Introduction to Coherent Bremsstrahlung

3.2.1 Historical Overview

Although a variety of applications originated shortly after Wilhelm Conrad Röntgen's publication on the discovery of X-rays, it took another 39 years until the underlying process of bremsstrahlung was understood sufficiently by Bethe & Heitler (1934) on the basis of quantum electrodynamics. Despite the fact that the calculations presented in their work were based on the first order Born approximation, the resulting bremsstrahlung differential cross-section is still widely used to describe X-ray generation in the MeV regime and is nowadays known as the Bethe-Heitler formula.

Only one year later it was Williams (1935) who proposed an interference effect arising when the single particle potential of the Bethe-Heitler formula was to be replaced by a periodic one such as a crystal lattice. However, it took more than 20 years before an article by Überall (1956) presented first quantitative results based on the Bethe-Heitler formula using high-energy and small-angle approximations. Therein it was shown that the periodic spacing of the atoms in a crystal leads to a confinement of the momentum transfer to vectors of the reciprocal lattice, resulting in distinct peaks in the resulting bremsstrahlung spectra. Later it was Palazzi (1968) carrying out first experiments and correctly calculating the influence of different crystal structures, pointing out that diamond-type lattices were expected to produce an especially prominent coherent fraction in the bremsstrahlung process. Mozley & De Wire (1963) found that a narrowing of the CB peaks could be achieved by collimating the resulting photon beam, facilitating the production of quasi-monochromatic photons. This is called the Mozley - de Wire effect (sidebar 3.4).

3.2.2 Coherent Bremsstrahlung and Channelling Radiation

A close relation between CB and a phenomenon called channelling radiation (CR) was revealed by Andersen et al. (1981) in a derivation employing Bloch wave functions as the correct eigenfunctions of a periodic Hamiltonian (instead of plane waves, as used in the Born approximation).

This indeed represented a breakthrough in that CB and CR were originally considered two distinct phenomena. While CB was regarded as a bremsstrahlung process from the beginning, CR was used to refer to a number of anomalies occurring when charged particles were scattered by crystals (Gemmell 1974). In this case one can observe reduced stopping powers when the incident beam is aligned parallel to a major crystal direction, or anisotropic emission patterns when crystals are doped with radioactive atoms emitting alpha particles, for instance. These effects originate from the highly anisotropic transmissivity of crystals.

One example of a classical picture of channelling is an electron spiralling around a row of atomic nuclei when its momentum component transversal to this row is not large enough to let it escape from the atomic string potential (axial channelling, top of Fig. 3.1).

Assuming a high periodicity of the crystal along its trajectory, the particle will then only rarely experience a large angle deflection (de-channelling), while one travelling at random direction or through an amorphous body will change its original direction much quicker. A similar case occurs when the transversal momentum of the incident particle is increased in one direction, but kept small in the other one. Then its trajectory will be confined to a specific plane if it is negatively charged or to the space in-between adjacent planes, when it carries a positive charge (planar channelling). A very detailed overview of channelling from this perspective was given by Gemmell (1974).

The process of channelling naturally also leads to the emission of bremsstrahlung. Since channelled particles are bound to an external potential, their transverse momentum, defined as the

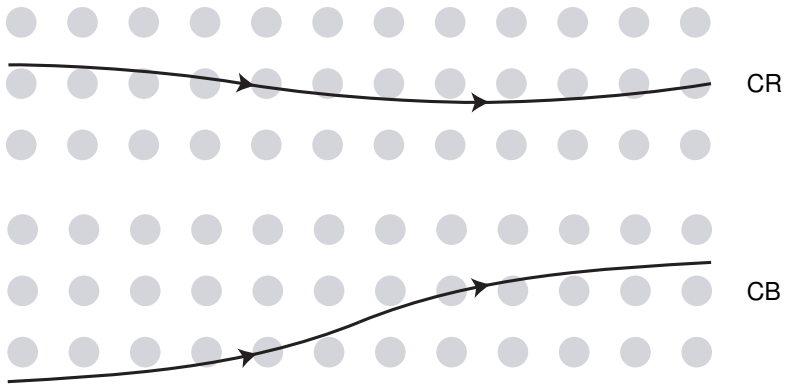

Figure 3.1 Classical pictures of the processes leading to channelling radiation (top) and coherent bremsstrahlung (bottom). When the component of a particle's momentum transverse to a major crystal axis is small enough, as in the case of axially channelled electrons, it is trapped along the string potential of that axis, and its transverse momentum is confined to discrete states. Transitions to lower states are then referred to as channelling radiation. As soon as the particle's momentum transverse to this major crystal axis is high enough to make the particle cross adjacent rows, coherent bremsstrahlung occurs.

momentum perpendicular to the respective crystal axis or plane, is confined to discrete states. Similar to CB, the respective bremsstrahlung spectra therefore also show characteristic spikes, corresponding to transitions between energy states of the crystal. However, in contrast to CB the calculation of these effects cannot be carried out in the Born approximation (sidebar 3.2), because the electrons can no longer be considered free.

Increasing the transverse momentum of an incident particle by slightly tilting its trajectory away from major crystal directions, thus exceeding a critical angle, will enable it to "jump" to adjacent atomic rows or planes, and now the particle can move "freely" within the crystal (bottom of Fig. 3.1). This critical angle, established by Lindhard (Gemmell 1974), is essentially $\psi_p \approx \sqrt{\pi n Z e^2 a / E_0}$ for relativistic electrons and planar channelling (cf. Table 3.1 on page 33 for an explanation of the symbols used here). In the case of 6 MeV electrons incident close to the

Sidebar 3.2 Coherent Bremsstrahlung in the Born Approximation
The Born approximation estimates cross-sections for scattering problems by treating the scattering potential as a small perturbation having only a weak influence on the incident and outgoing particles. Consequently, the cross-section for the scattering process can be approximated in first order perturbation theory by the expectation value of the scattering potential between plane wave initial- and final-states.
While popular applications of classical bremsstrahlung in amorphous targets mostly employ materials with high atomic numbers, e.g. tungsten ($Z = 74$) and gold ($Z = 79$), the effect of coherent bremsstrahlung is particularly pronounced mostly in light elements (Bilokon et al. 1983). Although this finding suggests to use the first order Born approximation (which becomes inaccurate for intermediate and high values of Z) to predict CB intensities, Shul'ga & Syshchenko (2007) found that second order terms become relevant for very small angles of incidence, close to the Lindhard critical angle (Gemmell 1974). We therefore have to assume that the predictions made by our following approach are expected to be valid only for angles sufficiently greater than the critical angle.

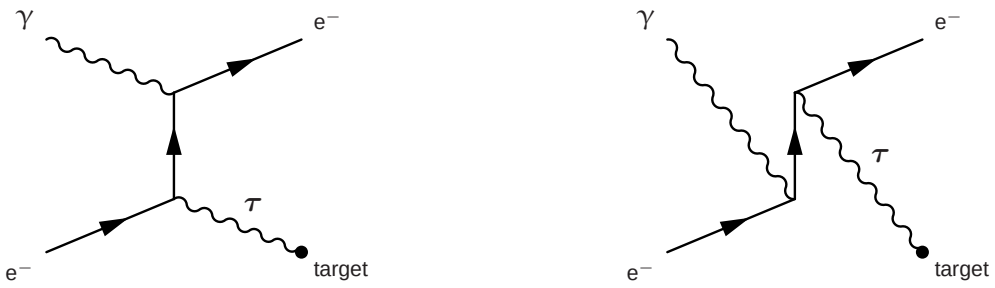

Figure 3.2 First-order Feynman diagrams for the generation of a bremsstrahlung photon γ by an electron e^-. In both cases, the target absorbs the 3-momentum $\boldsymbol{\tau}$, while the transferred amount of energy can be completely neglected due to the small electron mass.

110-direction of diamond this amounts to approximately 0.15°, and its value decreases for higher electron energies. The radiation occuring when this angle is exceeded is that of CB, the effect we will be dealing with in this chapter.

The results presented by Andersen et al. (1981) could explain well the coherent part of the bremsstrahlung spectra generated by 4 MeV electrons moving through a silicon crystal. They also proved that for increasing transverse momenta, as it is the case for CB, the Born approximation (sidebar 3.2) is valid unless the electron energies are smaller than roughly 1 MeV (distortions of the wave functions become important here).

Since the electron energies we are interested in produce channelling radiation in the low keV regime (about 10 keV, cf. Chouffani et al. 1999), we will neglect CR and concentrate on CB from now on. Also, we will not consider the production of parametric X-rays, which are briefly discussed in sidebar 3.3.

3.3 Analytical Forms of the Cross-Sections

3.3.1 Differential Cross-Sections

We consider the creation of a bremsstrahlung photon of 4-momentum $(k, \boldsymbol{k})$ from an electron that interacts with matter (Fig. 3.2) and neglect the contribution from electron-electron bremsstrahlung.

Sidebar 3.3 Parametric X-Rays
Parametric X-rays (PXRs) can be considered a special form of Cherenkov radiation, which is caused by charged particles moving through a medium with a speed greater than the phase velocity of light in that medium. In order for this radiation to occur, the medium's refractive index must be greater than one for the wavelengths considered. This is normally not the case in the X-ray domain, except for single-crystals.
Can PXRs help us to increase the amount of imaging photons? Unfortunately not, since the photon energies achievable with the electron energies considered here produce PXRs around 10 keV (Adishev et al. 2003). Higher photon energies are only possible if one increases the electron energy, and about 50 MeV would be necessary for our purposes. Also, the cone of the photons emitted has the same opening angle as that of bremsstrahlung ($1/\gamma$, see section 3.5). With electron energies as high as those required, this angle is too tiny to illuminate an area large enough for imaging.

E_0, E	Initial and final total electron energies
T_0, T	Initial and final kinetic electron energies
m	Electron rest mass
$\boldsymbol{p}_0, \boldsymbol{p}$	Initial and final electron (three-)momenta
$k, \boldsymbol{k}$	Energy and (three-)momentum of the emitted photon
θ_τ	Angle of $\boldsymbol{\tau}$ with respect to $\boldsymbol{p}_0$
a	Lattice constant
v_0	$= a^3$, volume of the fundamental unit cell
d	Distance between atoms in a row
n	Number of atoms per unit area in a plane
$\boldsymbol{\tau}$	Vector of the reciprocal lattice
Z	Atomic number of target material
ν	Number of atoms within an elementary cell
α	$\approx 1/137$: Fine structure constant
r_0	$= 2.82 \cdot 10^{-15}$ m $= 0.014291\text{MeV}^{-1}$ (classical electron radius)
$F(q^2, Z)$	Atomic form factor accounting for Coulomb screening
$\lvert S\rvert^2$	Structure factor of the crystal lattice under consideration
$p_\perp$	Transversal component of $\boldsymbol{p}$ with respect to $\boldsymbol{k}$
N	Number of unit cells in the crystal
$\langle u^2 \rangle$	Mean square displacement of the crystal atoms in three dimensions
ψ_i, ψ_o	Inner and outer collimation angles, $\psi_i < \psi_o \leq \pi$. A non-zero value for ψ_i corresponds to a ring-type aperture.
$\frac{d\sigma_{coh}}{dk}, \frac{d\sigma_{inc}}{dk}$	Differential cross-sections per unit cell with respect to photon energy for coherent and incoherent radiation

Table 3.1 Symbols and Constants. All quantities are given in natural units ($\hbar = c = 1$).

In the nuclear process, the initial 4-momentum $(E_0, \boldsymbol{p}_0)$ of the electron is reduced to $(E, \boldsymbol{p})$. The target, usually a macroscopic body, only absorbs a 3-momentum $\boldsymbol{\tau}$, while the respective energy transfer can be neglected due to its high mass. Consequently, energy and momentum conservation take the following form:

$$E_0 = E + k, \qquad \boldsymbol{p}_0 = \boldsymbol{p} + \boldsymbol{k} + \boldsymbol{\tau} \ . \tag{3.1}$$

The derivations of the coherent and incoherent cross-sections for this process are based on the Bethe-Heitler formula as given by expression (1BS) in Koch & Motz (1959), modified to account for the periodic crystal potential (Palazzi 1968). In particular, this implies that all the following analyses will be based on the first order Born approximation. One must then integrate over the 3-momentum of the final state electron $\boldsymbol{p}$ and the photon direction $\hat{k}$. This is done in appendix A without introducing any further approximations as to energy or angle. In this chapter, using the definitions listed in Table 3.1, we shall only give the resulting cross-sections *per unit cell* for coherent and incoherent production of bremsstrahlung from crystals (with all expressions in Planck units, i.e. $\hbar = c = 1$):

$$\frac{d\sigma_{coh}}{dk} = \frac{4\pi^2 r_0^2\, \alpha m^2}{p_0 v_0\, k^2} \sum_{\boldsymbol{\tau}'} |S|^2 \mathrm{e}^{-\tau^2 \langle u^2 \rangle /3}\ \frac{(Z - F(\tau^2, Z))^2}{\tau^4\, |\boldsymbol{p}_0 - \boldsymbol{\tau}|} \sum_{i=1}^{4} I_i\,(\boldsymbol{\tau}) \ , \tag{3.2}$$

$$\frac{d\sigma_{inc}}{dk} = \nu \frac{r_0^2\, \alpha m^2}{p_0 k^2} \int_{\tau_{min}}^{\tau_{max}} d\tau \int_{\theta_{\tau,min}(\tau)}^{\theta_{\tau,max}(\tau)} d\theta_\tau\ \sin\theta_\tau\ \left(1 - \mathrm{e}^{-\tau^2 \langle u^2 \rangle /3}\right) \frac{(Z - F(\tau^2, Z))^2}{\tau^2\, |\boldsymbol{p}_0 - \boldsymbol{\tau}|} \sum_{i=1}^{4} I_i\,(\boldsymbol{\tau}) \ . \tag{3.3}$$

The common physical origin of these cross-sections becomes clear by the fact that both can be described by four common terms I_i, which result from the integration over the directions of the final state particles:

$$\begin{aligned}
I_1 &= \frac{p_\perp^2 \left(4E_0^2 - \tau^2\right)}{\epsilon_b^2} \,, \\
I_2 &= \left(4E^2 - \tau^2\right) \left(-1 + \frac{2E_0}{\rho_b} - \frac{m^2 \left(E_0 - \eta_b\right)}{\rho_b^3}\right) \,, \\
I_3 &= \frac{2\left(4EE_0 - \tau^2 + 2k^2\right)}{\epsilon_b} \left[\left(E_0 - \epsilon_b\right) \left(\frac{E_0}{\rho_b} - 1\right) - \frac{\sigma_b}{\rho_b}\right] \,, \\
I_4 &= \frac{2k^2}{\epsilon_b} \left(\frac{p_\perp^2 - m^2}{\rho_b} + E_0 + \eta_b\right) \,.
\end{aligned} \tag{3.4}$$

These four contributions to the cross-sections are determined in terms of a set of purely kinematical variables:

$$\begin{aligned}
p_\perp^2 &= \left(\boldsymbol{p}_0 - \boldsymbol{\tau}\right)^2 - \left(E_0 - \epsilon_b\right)^2 \,, & \epsilon_b &= \frac{p_0^2 - \left(\boldsymbol{p}_0 - \boldsymbol{\tau}\right)^2}{2k} \,, \\
\sigma_b &= \boldsymbol{p}_0 \cdot \left(\boldsymbol{p}_0 - \boldsymbol{\tau}\right) \,, & \eta_b &= \frac{\sigma_b \left(E_0 - \epsilon_b\right)}{\left|\boldsymbol{p}_0 - \boldsymbol{\tau}\right|^2} \,, \\
\mu_b &= \sqrt{\frac{\tau^2 p_0^2 - \left(\boldsymbol{\tau} \cdot \boldsymbol{p}_0\right)^2}{\left|\boldsymbol{p}_0 - \boldsymbol{\tau}\right|^2} \left(1 - \frac{\left(E_0 - \epsilon_b\right)^2}{\left|\boldsymbol{p}_0 - \boldsymbol{\tau}\right|^2}\right)} \,, & \rho_b &= \sqrt{\left(E_0 - \eta_b\right)^2 - \mu_b^2} \,.
\end{aligned} \tag{3.5}$$

The interested reader may want to compare the coherent part (3.2) to the equations presented by Sáenz & Überall (1982). Unfortunately, this paper cannot serve as a reference for the derivation of reliable cross-section data. Obvious errors can be found in the reported cross-section (7), since the parameters (7d) depend on each other (compare ϵ_τ and ρ_τ, for instance). Furthermore, the units in the summation constraint (7e) are inconsistent.

We also would like to state that our incoherent cross-section (3.3) can be linked to a thin amorphous radiator by setting the temperature dependent term $\mathrm{e}^{-\tau^2 \langle u^2 \rangle / 3}$ to 0 and $\nu = 1$.

The energy range of the initial electrons considered by us requires the inclusion of the screening of the nuclear Coulomb potential by atomic electrons. This is accounted for by the atomic form factor F (sidebar 2.1), which for carbon we chose to be given by the work of Bonham & Strand (1963). Equation (3.3) incorporates arbitrary atomic form factors F at the expense of two numeric integrations (over τ and θ_τ).

3.3.2 Kinematical Constraints on the Target Momentum Transfer

So far, only the analytical structure of the cross-sections was specified in (3.2) and (3.3). However, the final calculation requires the knowledge of the kinematical constraints on the target momentum transfer $\boldsymbol{\tau}$. These depend on the range of photon emission angles that is naturally defined by the aperture of a given experimental setup. The defining inner and outer angles ψ_i and ψ_o are measured with respect to the direction of the incident electrons and are illustrated in Fig. 3.3.

For the coherent part of the bremsstrahlung spectrum the kinematically allowed momentum transfers $\boldsymbol{\tau}'$ in (3.2) refers to all $\boldsymbol{\tau}$ that fulfill the following condition:

$$\cos\left(\psi_o\right) \left|\boldsymbol{p}_0 - \boldsymbol{\tau}\right| \leq E_0 - \epsilon_b \leq \cos\left(\psi_i\right) \left|\boldsymbol{p}_0 - \boldsymbol{\tau}\right| . \tag{3.6}$$

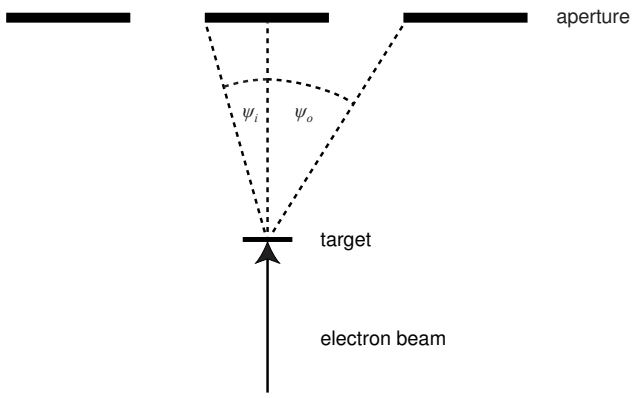

Figure 3.3 Illustration of the bremsstrahlung process as considered in this chapter: Electrons hit a target and the bremsstrahlung energy spectrum is then measured between the aperture angles ψ_i and ψ_o. Note that the aperture does not need to be implemented in an experiment, but purely serves here as a model to illustrate the emission angle specificity of CB.

In case of a crystal lattice, the $\boldsymbol{\tau}'$ correspond to vectors of the reciprocal lattice. The appearance of the collimation angles ψ_i and ψ_o here is a manifestation of the Mozley - de Wire effect, which is described in sidebar 3.4. There, also a reformulation of condition (3.6) is given that is necessary in order to carry out the numerical integrations for obtaining the incoherent part of the cross-section, along with some limitations that apply when identifying the above angles with the emission angles in the incoherent part.

Because of the Debye - Waller factor $\mathrm{e}^{-\tau^2\langle u^2\rangle/3}$ (sidebar 2.3), we can limit the summation over $\boldsymbol{\tau}'$ to small momentum transfers. An order of 20 τ values along each cartesian axis of the reciprocal lattice was determined to be sufficient for giving accurate results.

3.3.3 Critical Crystal Properties for the Calculation of Spectra

The fraction of coherent bremsstrahlung achievable for a given target crucially depends on two properties of the crystal that is used: the lattice structure and the thermal motion of its atoms at a given temperature as described by the Debye - Waller factor.

One can already infer from the above equations that peak intensities will be large for crystals having small unit cells v_0, as their size only enters the coherent cross-section (3.2) through $1/v_0$ (and the spacing of the reciprocal lattice points). Furthermore, the structure factor $|S|^2$ (sidebar 2.2) of the crystal lattice determines which vectors of a reciprocal lattice contribute to the cross-section. Labelling the vectors along the three dimensions of the reciprocal lattice by n_i, values for those lattices relevant in this thesis are given below:

$$|S_{\mathrm{bcc}}|^2 = \begin{cases} 4, & \text{if the sum of the } n_i \text{ is even,} \\ 0 & \text{otherwise;} \end{cases} \tag{3.14}$$

$$|S_{\mathrm{fcc}}|^2 = \begin{cases} 16, & \text{if all the } n_i \text{ are either even or odd,} \\ 0 & \text{otherwise;} \end{cases} \tag{3.15}$$

$$|S_{\mathrm{zb}}|^2 = \begin{cases} 16\left(Z_1+Z_2\right)^2/\overline{Z^2}, & \text{if all the } n_i \text{ are even and their sum is a multiple of four,} \\ 16\left(Z_1^2-Z_2^2\right)/\overline{Z^2}, & \text{if all the } n_i \text{ are even and their sum is a multiple of two,} \\ 16\left(Z_1^2+Z_2^2\right)/\overline{Z^2}, & \text{if all the } n_i \text{ are odd,} \\ 0 & \text{otherwise.} \end{cases} \tag{3.16}$$

Sidebar 3.4 The Mozley - de Wire Effect

The Mozley - de Wire effect is a purely kinematic effect that influences the coherent part of the cross-section (3.2) and was first described by Mozley & De Wire (1963). It refers to the behaviour of strong emission angle specificity as depicted in Figs. 3.5 and 3.8 and is a direct consequence of the Debye - Waller factor $\mathrm{e}^{-\tau^2\langle u^2\rangle/3}$, which suppresses any but very small momentum transfers in the coherent part. As a consequence, the integration over

$$\cos\theta_\gamma = \frac{(\boldsymbol{p}_0 - \boldsymbol{\tau})\cdot\boldsymbol{k}}{|\boldsymbol{p}_0 - \boldsymbol{\tau}|\,k} \tag{3.7}$$

carried out in Appendix A reduces to an integration over the angle between photon and initial electron directions and we can identify the two angles appearing in (3.6) as the inner and outer boundaries of the photon emission interval considered.

Unfortunately, the assumption $\tau \ll p_0$, does no longer hold for the incoherent part, which predominantly affects the high energy tail of the spectrum (as a numerical evaluation shows). Thus, for the incoherent part, ψ_i and ψ_o can no longer be identified with the collimation angles when k increases and the angular emission interval is chosen to deviate from the full solid angle, that is $\psi_i > 0$ or $\psi_o < \pi$. However, our comparisons with the cross-section by Schiff (1951) revealed that (3.6) gives still valid predictions if $\psi_i = 0$ and $\psi_o < \pi$ except for the very high frequency limit, where our cross-section will be larger than the one by Schiff for $\psi_o \lesssim 5^\mathrm{o}$ (for 5 MeV). This is not a severe drawback as the Born approximation in general is not valid at the high frequency limit, and it becomes less and less an issue when the electron energy increases. In the case of $0^\mathrm{o} < \psi_i < 5^\mathrm{o}$, our cross-section remains well usable up to a photon energy where it suddenly becomes imaginary, and this energy decreases with increasing ψ_i. Using our cross-section for the low-energy part of the spectrum remains easily possible, though, and it needs to be pointed out that the main reason for deriving the incoherent cross-section (3.3) was to be able to include the Debye - Waller factor, which influences the cross-section at the low-energy side only. If one is interested in more reliable estimates at the high frequency limit one should consider using the Schiff cross-section there.

With all that said, our approach of identifying ψ_i and ψ_o with the emission angles in the incoherent part can be somewhat "rescued" by introducing some case differentiations as given below, which only become relevant when deviating from the full solid angle as the emission interval:

$$\tau_{min} = p_0 - p - k \tag{3.8}$$

$$\tau_{max} = p_0 + p + k \tag{3.9}$$

$$\theta_{\tau,min}(\tau) = \arccos\frac{p_0^2 + \tau^2 - |\boldsymbol{p}_0 - \boldsymbol{\tau}|^2_{min}}{2p_0\tau} \tag{3.10}$$

$$\theta_{\tau,max}(\tau) = \arccos\frac{p_0^2 + \tau^2 - |\boldsymbol{p}_0 - \boldsymbol{\tau}|^2_{max}}{2p_0\tau} \tag{3.11}$$

$$|\boldsymbol{p}_0 - \boldsymbol{\tau}|_{min} = \begin{cases} k\cos\psi_o + \sqrt{k^2\cos^2\psi_o - 2kE_0 + p_0^2}, \text{ if } k^2\cos^2\psi_o - 2kE_0 + p_0^2 > 0 \\ k\cos\psi_o, \text{ if } k^2\cos^2\psi_o - 2kE_0 + p_0^2 < 0 \end{cases} \tag{3.12}$$

$$|\boldsymbol{p}_0 - \boldsymbol{\tau}|_{max} = \begin{cases} k\cos\psi_i + \sqrt{k^2\cos^2\psi_i - 2kE_0 + p_0^2}, \text{ if } k^2\cos^2\psi_i - 2kE_0 + p_0^2 > 0 \\ \text{undefined otherwise} \end{cases} \tag{3.13}$$

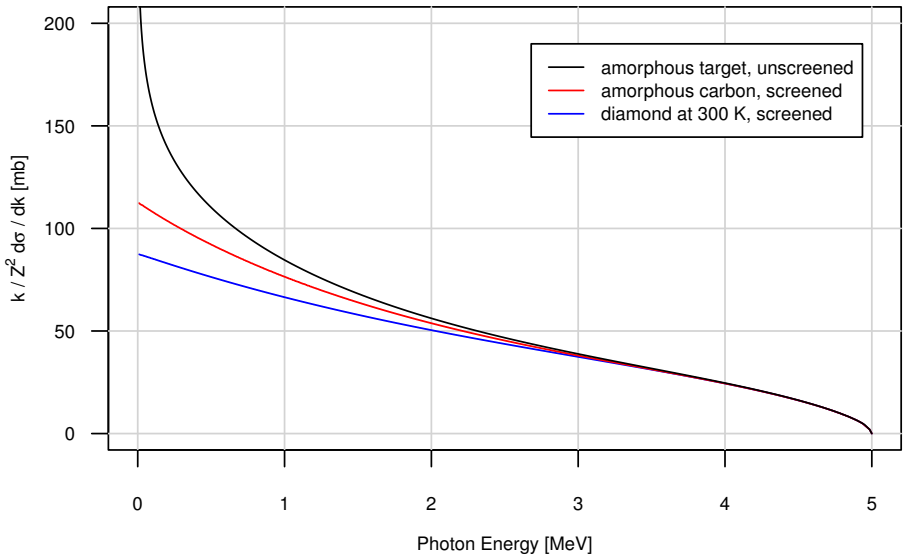

Figure 3.4 Intensity spectra of incoherent bremsstrahlung for two atomic arrangements at $T_0 = 5$ MeV in carbon. Both screening as well as thermal vibrations cannot be neglected at this energy.

Here, 'bcc' and 'fcc' denote (monoatomic) body and face centered cubic lattices, and 'zb' represents the (diatomic) zincblende lattice, which contains the diamond lattice as a special case for $Z_1 = Z_2$.

The second critical lattice feature is the Debye - Waller factor, that is, the contribution of each individual reciprocal lattice vector to the coherent and incoherent cross-sections is weighted by $\mathrm{e}^{-\tau^2\langle u^2\rangle/3}$ and $1 - \mathrm{e}^{-\tau^2\langle u^2\rangle/3}$, respectively. Naturally, the mean squared deviation of the atoms of the crystal from their equilibrium position $\langle u^2\rangle$ increases with increasing temperature, and so the bremsstrahlung intensities are shifted from the coherent to the incoherent part.

3.4 Cross-Section Features Using the Example of Diamond

Now, we will evaluate the cross-sections given above for diamond at a temperature of 300 K. Consequently, the value used for the mean squared displacement $\langle u^2\rangle$ in the Debye - Waller factor of carbon is 1407 $\mathrm{MeV}^{-2} = 5.48 \times 10^{-3}\text{Å}^2$ (Peng et al. 1996). It exhibits a comparatively weak temperature dependence, so diamond should be well suited for X-ray production.

3.4.1 Incoherent Bremsstrahlung

We shall begin with the incoherent part (3.3). Fig. 3.4 shows its shape for amorphous carbon and a diamond target. Due to the Debye - Waller factor, this background deviates from the well known Bethe Heitler cross-section predominantly at lower photon energies.

3.4.2 Coherent Bremsstrahlung

We will now consider the coherent part of the bremsstrahlung spectrum for a non-divergent electron beam perfectly aligned along the 110-direction of a diamond crystal. We have learned before that for a vanishing tilt angle the emission of CB gets replaced by CR, so this example is somewhat artificial. However, it will be very instructive in order to be able to unterstand the connection of the CB peaks to the vectors of the reciprocal lattice, hence we will discuss it here.

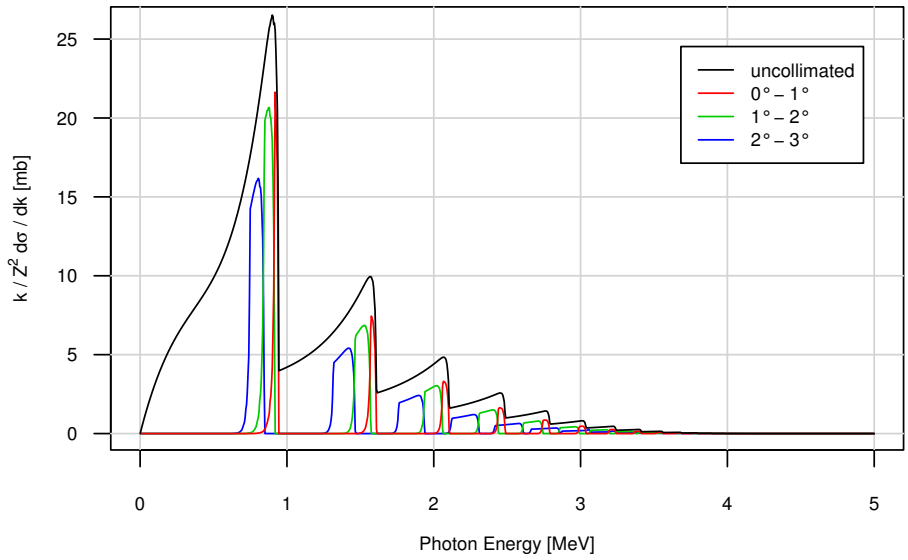

Figure 3.5 Intensity spectra of coherent bremsstrahlung for photons emitted at different angular intervals at $T_0 = 5$ MeV in a thin diamond crystal. The angles of emission for the resulting coherent radiation are given with respect to the axis of the incident beam. With the electrons aligned perfectly to the 110-direction, no peaks occur at the low end of the energy range. Notice that the CB peaks are highly emission angle specific (sidebar 3.4).

Fig. 3.5 shows the peaked nature of CB that arises in this case. It originates from the allowed discrete momentum transfers $\boldsymbol{\tau}$ to the crystal (3.2) in conjunction with energy and momentum conservation (3.1, 3.6). For a given electron beam of momentum $\boldsymbol{p}_0$ and an energy k of the emitted photon, these laws restrict $\boldsymbol{\tau}$ to values between two spheres in momentum space ("inelastic Ewald spheres") defined by the relations

$$(\boldsymbol{p}_0 - \boldsymbol{\tau})^2 = (p(p_0, k) \pm k)^2 \ , \tag{3.17}$$

which are equivalent to (3.6).

The sphere shell's two radii vary quite differently with increasing photon energy k (Fig. 3.6). Zooming into this figure, we cannot only observe a decreasing inner radius, but also a very slow decrease of the outer one (Fig. 3.7).

Apart from the conditions imposed by the momentum spheres, $\boldsymbol{\tau}$ can only take the discrete values provided by the reciprocal lattice of the crystal. These two conditions directly cause the sudden decreases in intensity at various positions within the photon spectrum. This happens when the outer sphere crosses a lattice point in the direction of $\boldsymbol{\tau}_{\parallel}$, and suddenly this point can no longer contribute to the cross-section.

This feature is illustrated in Fig. 3.7. For electron beams of sufficiently high energy, the permitted spherical region of momentum transfers appears as a rectangle at the scale of the reciprocal lattice vectors. The contributions of the successively spaced columns of transverse momenta are cut off more or less simultaneously, leading to the sudden decrease in intensity shown in Fig. 3.5. In this case, each of these so-called type-B peaks in the spectrum correspond to a single plane of the reciprocal lattice perpendicular to $\boldsymbol{p}_0$ (i.e. a column in Fig. 3.7). The comparably strong variation of the inner radius is responsible for the quasi-continuous increase of the spectrum at the low energy side of each peak.

Since the two radii are determined by (3.17), which implies (3.6), they are functions of the inner and outer collimation angles. Collimation, i.e. considering a specific angular emission interval,

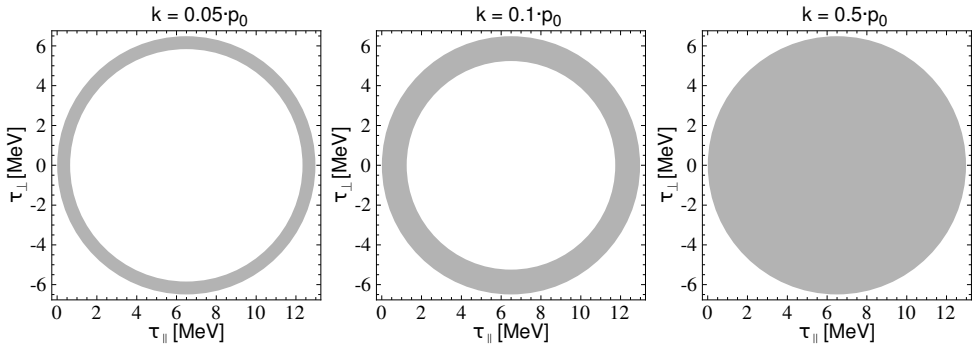

Figure 3.6 The shaded region contains the momentum transfers permitted by (3.6) for 6 MeV electrons. The thickness of the 'momentum-shell' increases with the photon energy until it reaches its maximum value at $k = p_0/2$, where it starts to shrink again.

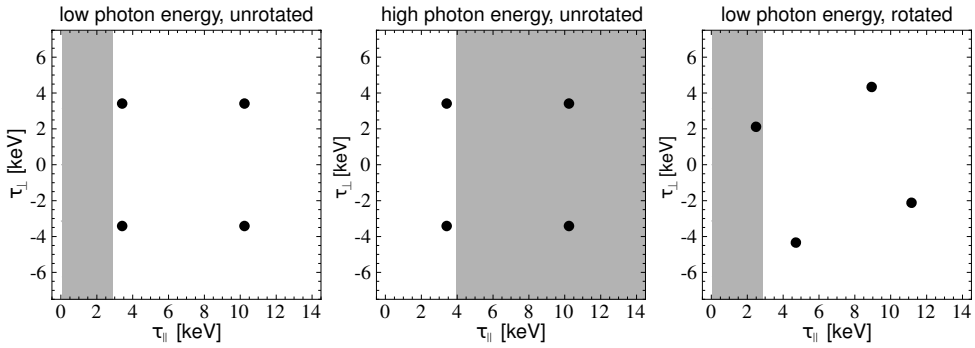

Figure 3.7 Reciprocal lattice of a diamond with the permitted momentum transfer region plotted in grey. The filled dots are the reciprocal lattice vectors permitted by the structure factor of diamond (3.14). Left: Zero tilt angle for a small value of the photon energy k. In the situation shown, none of the small lattice vectors participates in the momentum transfer. Middle: A further increase in k will cause the shaded region to pass the first plane of reciprocal lattice vectors. Right: A slight rotation of the crystal will lead to an increase in the cross-section even for small values of k.

will enlarge the inner sphere when ψ_o decreases, and shrink the outer one when ψ_i is raised. This gives a kinematical explanation of the Mozley - de Wire effect (sidebar 3.4).

The effect of rotating the crystal against the electron beam by a small angle is shown in Fig. 3.8, where the combined differential cross-section is shown (i.e. including both coherent and incoherent part). The resulting low energy peaks directly depend on the tilt angle and are termed type-A peaks according to Sáenz & Überall (1982). Note that for several higher photon energies the cross-section is actually *smaller* than for an amorphous target.

Linear accelerators used in a clinical environment usually exhibit an electron energy distribution that cannot be neglected in this context. In order to investigate the effects of this on the coherent part of the spectrum, we will assume a normally distributed electron energy spectrum with a mean energy of 5 MeV and a full width at half maximum (FWHM) of 10%. The results for such a source configuration are shown in Fig. 3.9, where it becomes clear that the excess amount of photons in the diagnostic energy range is well preserved.

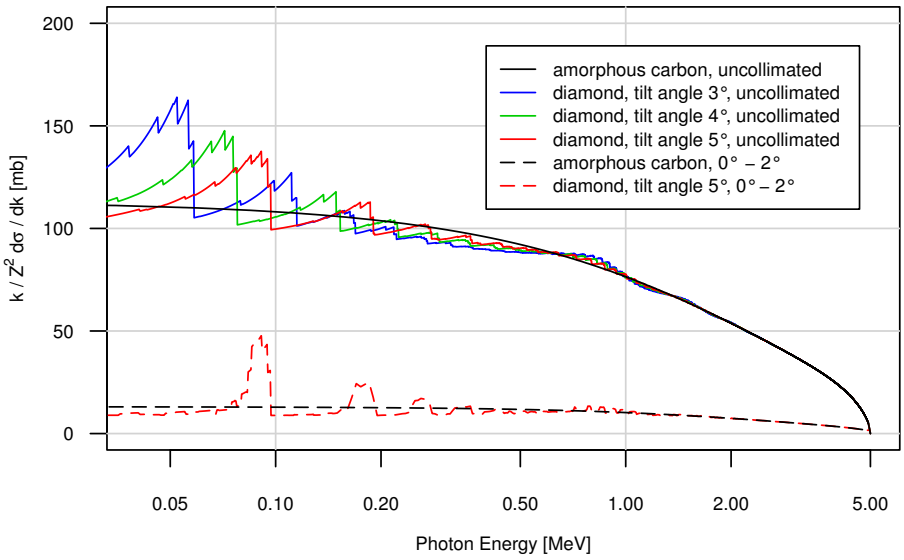

Figure 3.8 Combined photon spectra for electrons incident close to the 110-direction of carbon at $T_0 = 5$ MeV, rotated by various angles around the 100-direction. The peaks get more and more prominent when the size of the aperture is reduced (sidebar 3.4). Note that the multiplication of the differential cross-section by the photon energy k is for visualisation only. The relevant quantity for imaging are the photon fluences obtained without this factor, giving the low energy photons a higher weight than depicted.

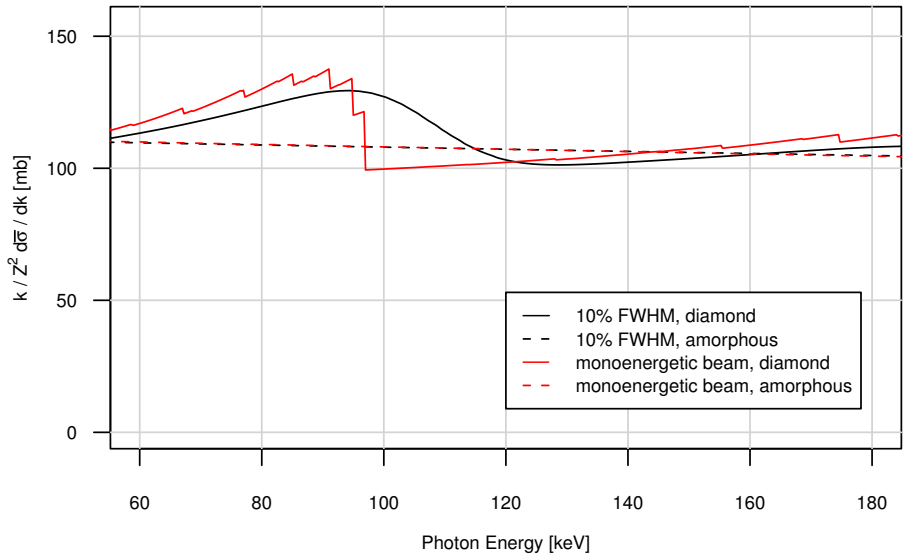

Figure 3.9 As in Fig. 3.8, but with a polychromatic electron beam of $T_0 = 5\,\mathrm{MeV}$ and a Gaussian energy distribution of 10% FWHM. The polychromatic spectra exhibit a baseline shift of about +13.8%, which was corrected in order to obtain comparable results.

3.4.3 Comparison with the Palazzi Cross-Section

With CB being a phenomenon known for years, cross-sections other than the one derived in this work were previously published. As a particularly well-known example we here compare our cross-section with the one derived by Palazzi (1968). It is based on the assumptions of ultrarelativistic electrons and small angles of photon emission. Furthermore, the sphere shell defined by (3.6) and

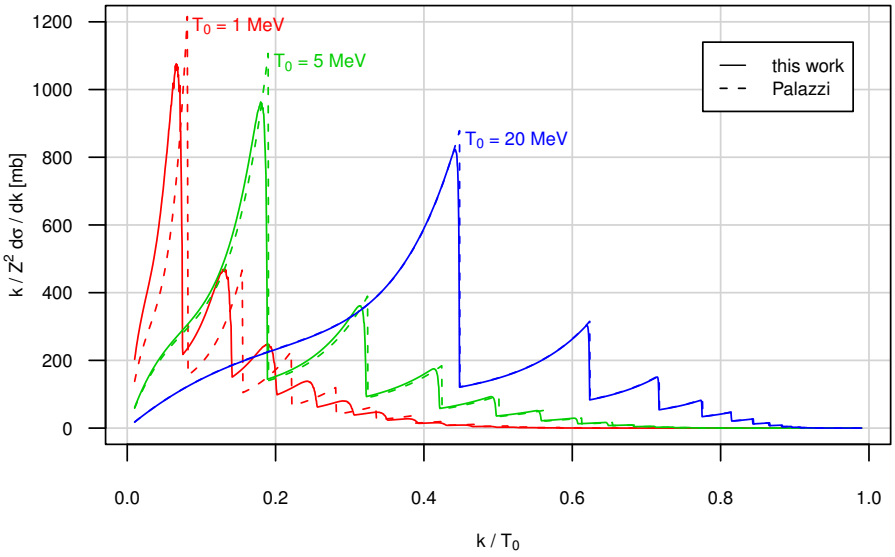

Figure 3.10 Comparison of the coherent part of the cross-section derived in this work with the one given by Palazzi (1968) for electrons incident along the 110-direction in diamond. The differences vanish with increasing electron energy T_0.

(3.17) (Fig. 3.6) is reduced to a rectangular box as indicated in Fig. 3.7, which is also only valid for ultrarelativistic electrons (remember $\tau \ll p_0$ here, sidebar 3.4). With the considerably shorter expressions of the Palazzi cross-section, it is interesting to see whether going through the trouble of carrying out the calculations given in appendix A was actually worth the effort.

A comparison of the two cross-sections is given in Fig. 3.10. It becomes obvious that for electron kinetic energies of $T_0 \lesssim 5\,\mathrm{MeV}$, the approximations stated are no longer justified. Especially the assumption $T_0 \gg m$ causes a heavy bias in the peak positions, and the reduction of the sphere shell to a rectangular box misses the round tips of the peaks. Note, however, that the Born approximation (sidebar 3.2) will get inaccurate for $T_0 \lesssim 1\,\mathrm{MeV}$ especially for heavier elements, and so the use of both cross-sections is probably no longer justified for these energies.

3.4.4 Coherent Bremsstrahlung from Amorphous Targets: A Contradiction?

Throughout this chapter, we have always used the single atom cross-section as a surrogate for the cross-section in amorphous targets. This approach has been followed very successfully since the discovery of bremsstrahlung and is nowadays extensively used in Monte Carlo codes. Readers familiar with section 2.4 and sidebar 2.2 will remember that even amorphous objects possess a structure factor different from 1. With this in mind, we recognise that it is not self-evident that we can model these targets by considering only the single-atom cross-section, and so the question arises why this actually works. The answer can be found by taking a look at amorphous structure factors like the one shown in Fig. 3.11. It shows an example for an AlSi alloy, reproduced from a figure by Cuello (2008), which implies some inaccuracies. However, for the sake of the following argument, only its general behaviour is important. For small momentum transfers, it is almost zero, and then shows an oscillating behaviour which is due to the short range order in the alloy. For higher momentum transfers the structure factor quickly reaches a value of one. Two things are important here: For each but the smallest momentum transfers this structure factor is the same as the one for a single atom. More importantly, the structure factor is radially symmetric. This is an important difference to the reciprocal lattice shown in Fig. 3.7. The reader might remember here that the CB peaks arise from the crossing of a reciprocal lattice vector by the outer radius

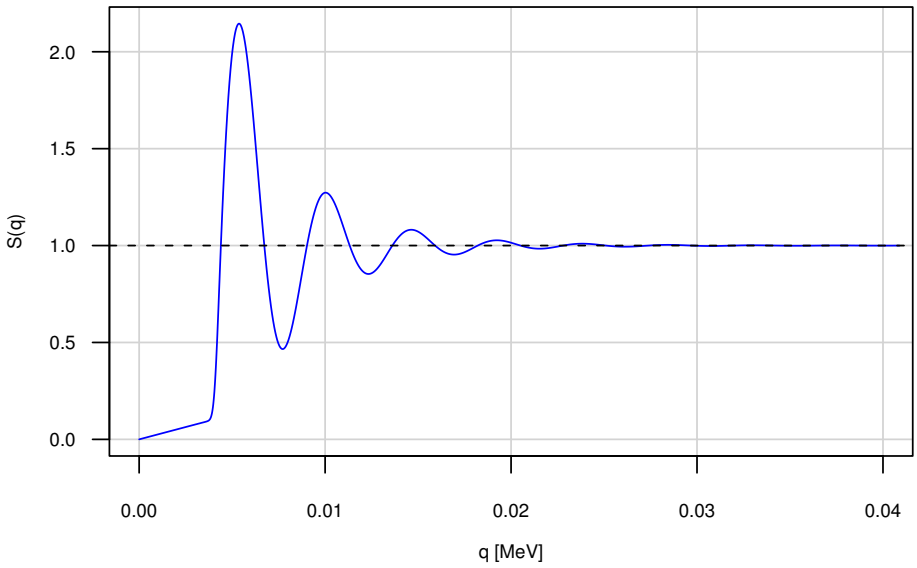

Figure 3.11 Amorphous structure factor of an AlSi alloy (see main text for explanations). The dashed line shows the structure factor of single nucleus (modelled as a delta function).

of the momentum shell in Fig. 3.6. This shell is centered on $\boldsymbol{p}_0$, whereas the amorphous structure factor is symmetric around the origin. This means, the peak structure shown in Fig. 3.11 cannot form any peaks in the photon spectra like the reciprocal lattice vectors of a single-crystal do. As a consequence, the numerical evaluation shows an absolutely tiny difference between the single atom and the amorphous cross-section, independent of the inter-atomic distance for the substance under consideration.

There does exist a coherent part in bremsstrahlung from amorphous targets, but the resulting spectra are virtually identical. Therefore, the single atom cross-section can be used in Monte Carlo simulations, simply because of the interplay of the bremsstrahlung kinematics with the radially symmetric structure factor.

We may now think of letting the two symmetry centres almost coincide for very low electron energies. This will indeed cause the outer radius of the momentum shell to cross the maxima and minima in the amorphous structure factor at every position almost simultaneously, and then we can again observe peaks for amorphous targets. The electron energies necessary for this, however, are in the sub-keV range and can thus not be treated in the Born approximation (and are of course of no interest in medical applications).

3.5 Multiple Scattering

So far, we have only discussed CB on a cross-section level. As the history of CB shows, this gives valid predictions for quasi-monoenergetic electron beams with a small divergence hitting a thin crystal in which multiple scattering can be neglected. While these well defined conditions are crucial in experiments depending on the polarization properties of CB, the only aspect we are interested in is the production of a higher amount of low-energy photons. Consequently, the question arises if this property will prevail when a clinical LINAC is employed.

We have shown before that CB peak positions depend on the direction of electron propagation (Fig. 3.8). Thus, both multiple-scattering in thick crystals as well as a finite beam divergence seem to represent limiting factors. In this section, we will take a closer look at the energy and

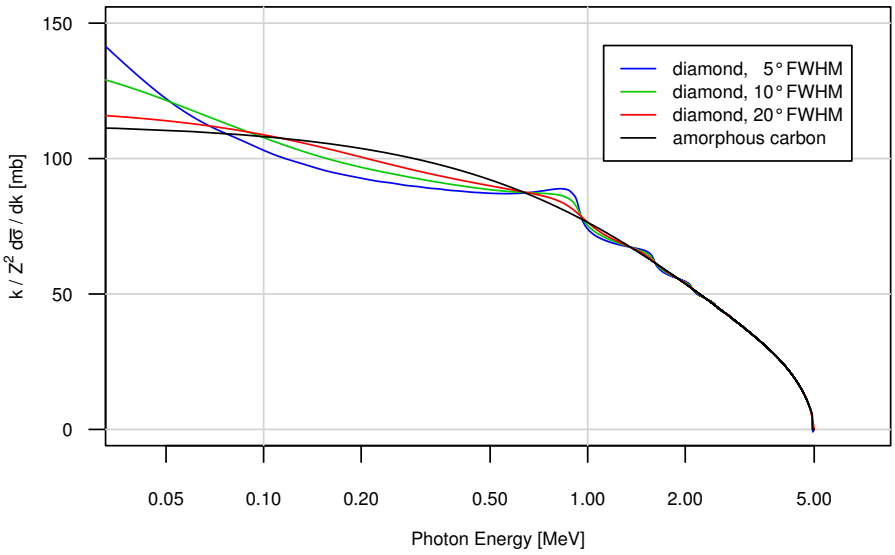

Figure 3.12 Comparison of photon spectra arising from different angular distributions of the incident electrons at $T_0 = 5$ MeV. The mean direction of propagation was chosen to be the 110-axis. Spectra corresponding to individual tilt angles were acquired by rotations around the 100-direction.

tilt angle dependence of the CB spectra, and relate these results to those of an amorphous target, where of course the direction of the electron beam does not matter.

Before we come to this, we first need to stress the importance of a field-of-view (FOV) that is large enough for diagnostic purposes. This means, whatever photon energy spectra leave the target, they must be emitted in an angle large enough to also provide sufficient photon fluences at the periphery of the patient. Otherwise, truncation artefacts can arise when performing computed tomography. In order to investigate this problem further, we introduce the characteristic angle of bremsstrahlung emission. A common estimate for this angle, which represents the most probable angle of emission, is $1/\gamma = m/E_0 = m/(T_0 + m)$, and hence it gets more and more narrow as the electron energy increases. A selection of these angles for values of T_0 between 1 and 8 MeV is given in Table 3.2. In a typical clinical setting one requires a FOV diameter of roughly 40 cm, and this means a characteristic angle of more than 10° is needed if one uses thin targets. This in turn has one of the following two consequences: If one decides in favour of such a thin target, where emission is dominated by $1/\gamma$, the kinetic energy of the electron beam must not be higher than 3 MeV, and a beam stopper has to be applied to remove the electrons exiting from the target (given a distance of 1 m between target and patient). If on the other hand a thick target is chosen, where multiple scattering influences the electron motion notably, the cross-section must exhibit features that will allow the electrons to travel with large angles (such as 5°) to a major crystal direction without losing too much of their ability to produce an excess amount of photons in the kV range.

To demonstrate that the second approach is not an easy undertaking we illustrate the averaged cross-section for various values of the electron angular distributions in Fig. 3.12. It clearly shows

T_0 [MeV]	1	2	3	4	5	6	7	8
$1/\gamma$	19.4°	11.7°	8.3°	6.5°	5.3°	4.5°	3.9°	3.4°

Table 3.2 Values for the characteristic angle of bremsstrahlung emission $1/\gamma$ as a function of the kinetic electron energy T_0.

that diamonds lose their ability to produce the desired amount of keV photons when the FWHM of the angular distribution exceeds 10°. We will now take a more detailed look into the dependence of the peak locations on the various parameters, such as crystal direction, electron energy and tilt angle.

In order to do this, we will divide the single-crystal spectra (including both parts of the cross-section) by those corresponding to an amorphous target for the same electron energy (a multiplication of the spectra by the factor k as done so far obviously cancels out here). Also, we will choose a more compact representation of the spectra by introducing a third dimension into our plots, that is, we will code these ratios as colours, leaving room for a tilt angle to be plotted on the y-axis. Since in general two tilt angles corresponding to polar and azimuthal directions exist, we will shorten our following discussions by always selecting the same values for both angles and calling this single value the tilt angle. While this actually only represents a single direction, it still gives an overview of the tilt angle dependence of CB for the various electron energies. All these figures will be based on an angular emission interval of 20°, i.e. $\psi_i = 0°$ and $\psi_o = 10°$, since the spectra comprising the full solid angle would give overly pessimistic results.

The corresponding plots for a reasonable choice of the angle around the electrons' directions of propagation ($\psi_i = 0$ and $\psi_o = 10°$) are shown in Figs. 3.13 - 3.15 for the three pincipal directions in diamond and various kinetic electron energies. The following observations can be made here:

- The peak positions shift to higher photon energies if the electron energy is increased (we noticed this above already).
- The intensity of the fraction of the type-A peaks that lie in the imaging window also increases with the electron energy.
- The peaked nature of CB leads to a redistribution of photon numbers especially around the type-B peaks, which is particularly visible for small tilt angles.
- The higher the electron energy, the greater the impact of the tilt angle, i.e. of multiple scattering, on the position of the type-A peaks.
- For high photon energies, there is literally no difference between the two target types within the energy range considered.

From the figures below it becomes also clear that it is the stopping of the electrons that will prohibit the use of thick targets to reach our goals, rather than multiple scattering. Despite the fact that scattering also degrades the quality of the overall spectra, we have to take into account the characteristic angle of bremsstrahlung emission (Table 3.2) when assessing the impact on image quality. As we have seen, this emission angle gets smaller and smaller for higher electron energies, meaning that electrons scattered by 10° or more produce photons that will not contribute significantly to the fluence that travels through the patient and eventually hits the detector. According to this line of thinking, the choice of the target thickness does not have to be overly influenced by multiple scattering, but by no means should it be that thick that the deceleration of the electrons will cause the minima preceeding the type-B peaks (dark blue areas) to dominate the spectra, which is the case for low energy electrons.

For our means, the 110-direction appears to be the best choice for diamond, as it seems to exhibit the best compromise between an additional amount of keV photons at low tilt angles and the corresponding decrease at higher angles, down to an electron energy of about 4 MeV. Below this energy, the above considerations become relevant.

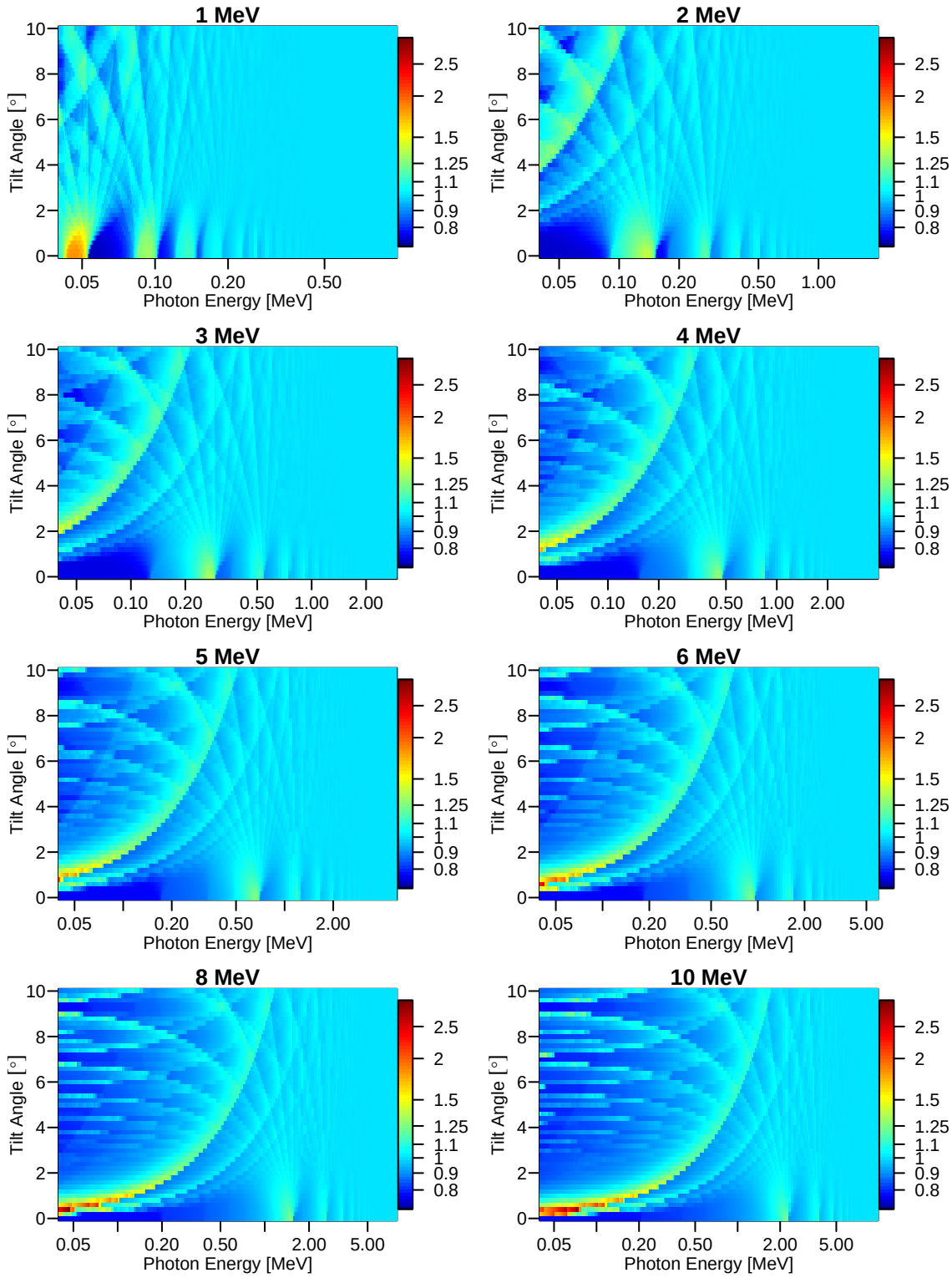

Figure 3.13 Relative enhancement and attenuation of CB from **diamond** when compared with bremsstrahlung generated in **amorphous carbon**. The colour scale shows the ratio of single-crystal and amorphous differential cross-sections for the kinetic electron energies given in the headings. The y-axes give the tilt angles with respect to the **100-direction**. The reader is advised to take the colour in the top right corners as a reference for a ratio of one.

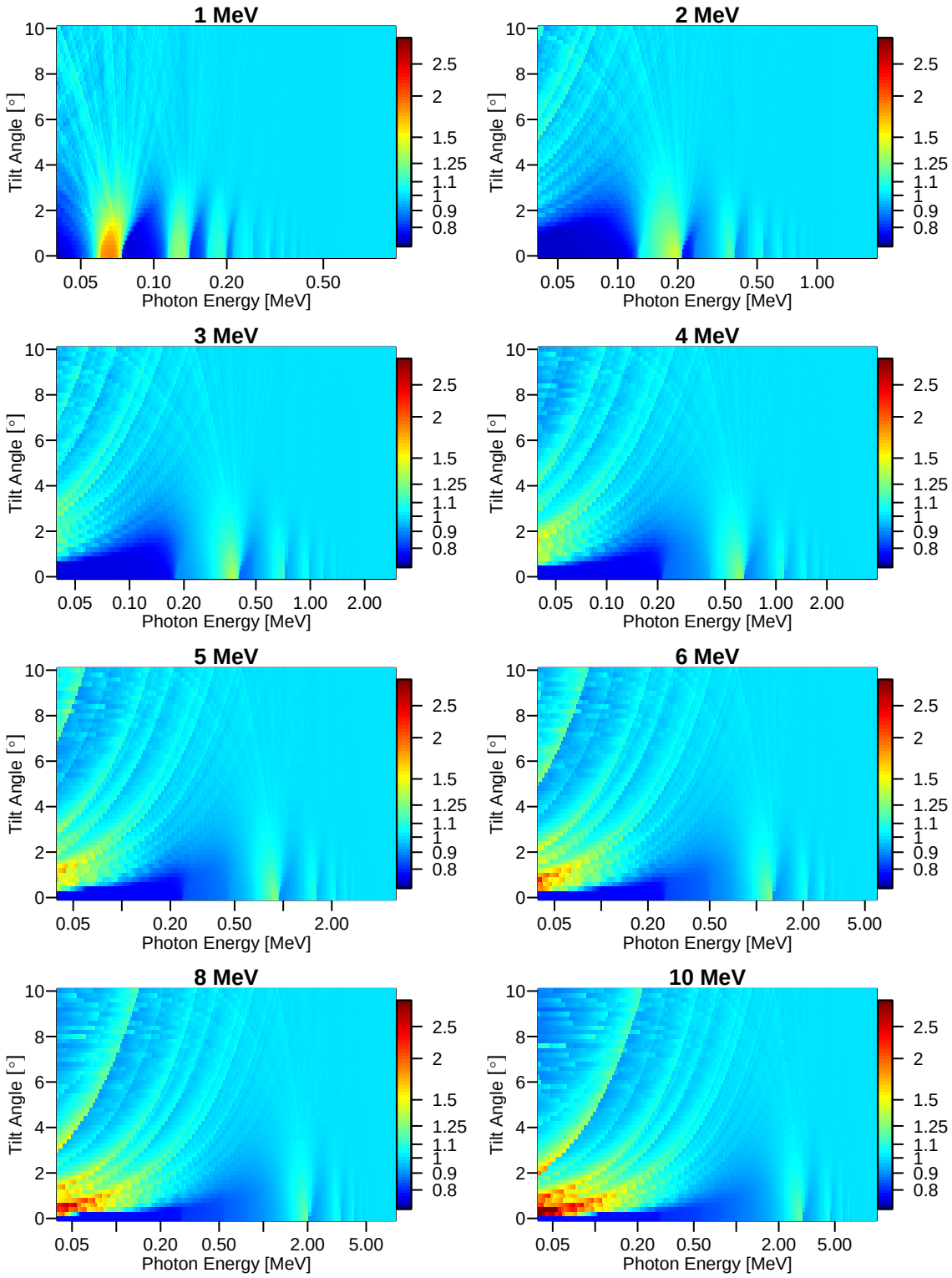

Figure 3.14 As in Fig. 3.13, but for the **110-direction**.

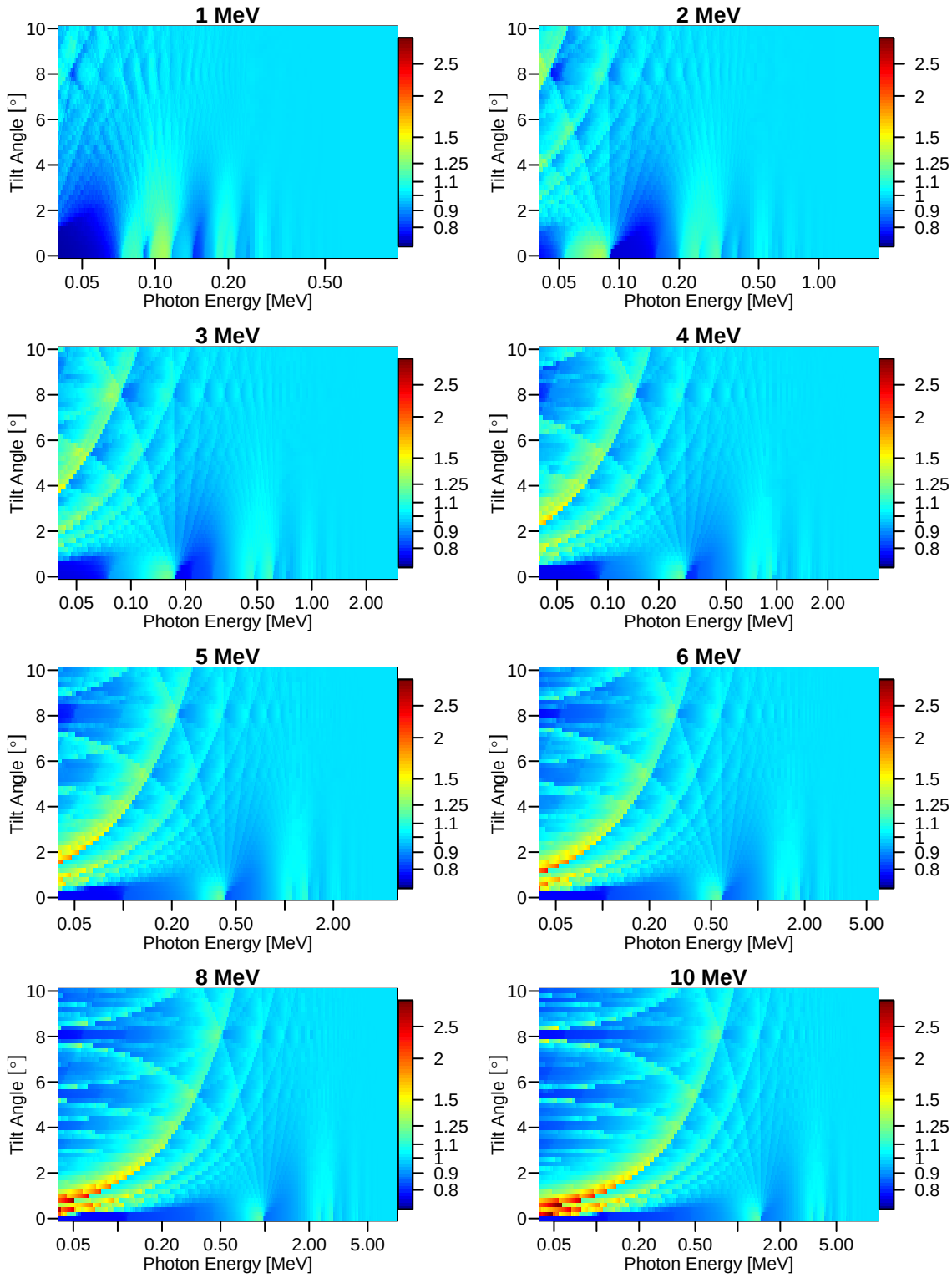

Figure 3.15 As in Fig. 3.13, but for the **111-direction**.

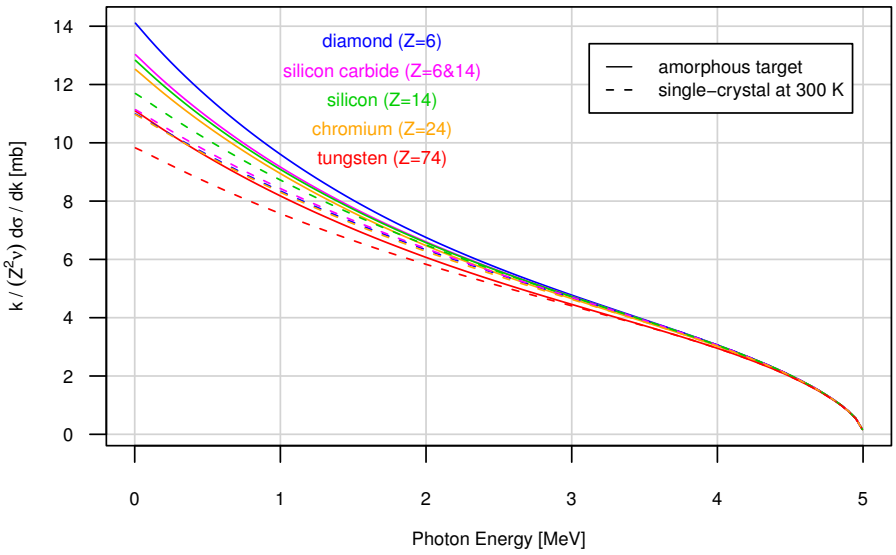

Figure 3.16 Comparison of the bremsstrahlung cross-sections for various amorphous targets (solid lines) and the incoherent parts of single-crystals (dashed lines). Note that the cross-sections shown here are per atom to incorporate the different numbers of atoms per unit cell.

3.6 The Search for Other Suitable Materials

Until now, we have extensively studied the properties of diamond as a bremsstrahlung target in IGRT. Indeed, it is a very common choice for the production of CB in high energy physics, as it exhibits a high particle density as well as a low thermal motion amplitude. Now, we will add some more substances to our considerations: boron nitride, silicon carbide, silicon, chromium and tungsten. Taking a look at their properties in Table 3.3, we find that with the exception of silicon, they also promise to produce a comparably prominent coherent fraction in their bremsstrahlung spectra. Silicon, on the contrary, is another common material used in high energy CB production experiments, also has a comparably low atomic number and is thus listed here for completeness.

What we would like to state first is the fact that boron nitride (BN) exhibits almost the same properties as diamond. The zincblende structure it crystallises in can be considered a generalisation to the diamond lattice for diatomic crystal bases, and also the other relevant parameters are very similar. Indeed, an evaluation of the cross-section shows that there are almost no differences in the CB spectra, with the exception of a small dislocation of the peaks due to the slighlty varying lattice constant. We can therefore treat BN as an alternative to diamond, but will not discuss it further here. The choice between the two materials will probably have to be based on criteria like market prices and availability, which goes beyond the scope of this thesis.

We can already learn a lot about the other materials by taking a look at their single-atom cross-sections, which are represented by the solid lines depicted in Fig. 3.16. What we can see there is that with increasing atomic number, screening (sidebar 2.1) suppresses the emission of low energy photons more and more, and one must not forget the strong Z-dependence caused by photoelectric absorption (section 2.3.2) either.

If one divides the cross-section by Z^2, as done in Fig. 3.16, the differences between the amorphous cross-sections are caused solely by the form factor $|1-F(q,Z)|^2$. In contrast to this, the incoherent parts of the single-crystal spectra (dashed lines) are also influenced by $1-\mathrm{e}^{-\langle u^2\rangle q^2/3}$. As a notable consequence, the incoherent parts of diamond, silicon carbide and chromium virtually coincide at room temperature, while the amorphous spectra significantly differ. This leads us to an interesting

question: Can the suppression of low and intermediate energy photons by the higher atomic number actually be complemented by CB peaks at just the right energy? In other words, can we remove a part of the intermediate energy photons - which we do not want - while maintaining the same keV fluence by using a single-crystal made from a higher-Z material?

The answer to this question is: yes in principle. In practice, the usual suspects like multiple scattering and electron deceleration spoil the game a little, but as we will see below, the situation looks quite good for both cubic silicon carbide, which also crystallises in the zincblende structure, and chromium, which has a bcc-lattice.

There are two application scenarios we need to distinguish here: The first one is finding a replacement for an amorphous carbon target, and consequently, we compute the ratio between the single-crystal spectra of silicon carbide or chromium and amorphous carbon. The resulting plots (Figs. 3.17 & 3.19) then give the differences to the gold standard polycrystalline graphite (which does not really differ from amorphous carbon). Indeed, we can get an enhancement here for small tilt angles down to electron energies of about 4 MeV, and we note that the desired attenuation of the intermediate energy photons is also achieved here. The latter observation is independent from the tilt angle as expected, as it is the screening of the nuclear field by the atomic electrons which is responsible for this behaviour. However, the spectra do get a bit harder for larger tilt angles, so there is probably a trade-off between image quality at the centre and the periphery of the FOV.

The second scenario arises when a low atomic number target like carbon is not desired. There are a few reasons why this could be the case. One is that the space in the target holder is limited, and therefore the thickness of the target may not be sufficient to prevent electron leakage. Also, the thickness of the carbon target may not be enough to prevent the very low energy photons below 40 keV from escaping. These photons get absorbed in the patient almost completely and therefore only cause an additional dose that does not come along with any improvements in image qualty. A higher-Z target can indeed deal with these problems, and thus we also take a look at the performance of silicon carbide and chromium compared with their amorphous counterparts. The resulting spectra are shown in Figs. 3.18 & 3.20. In contrast to the corresponding diamond spectra (Fig. 3.14), the decrease of the number of imaging photons below a ratio of 1 for larger tilt angles does not go as far. This, of course, comes along with a smaller increase for small tilt angles.

In the case of chromium we have to bear in mind the comparably high atomic number of $Z = 24$, for which one encounters already a very strong attenuation of the photons below 120 keV. For this reason, only targets thinner than about 1 mm are possible here. Note also that for bcc-crystals such as chromium, the 111-direction is the most promising.

Finally, tungsten has an atomic number of $Z = 74$, and so screening and photoelectric absorption are way too high for our purposes. Hence, we will not discuss it further here.

	lattice structure	$\sqrt{\overline{Z^2}}$	a [Å]	$\langle u_x^2 \rangle$[Å^2]
diamond	diamond	6	3.55	$5.5 \cdot 10^{-3}$
boron nitride	zincblende	6.1	3.61	$6.2 \cdot 10^{-3}$ *
silicon carbide	zincblende	10.8	4.36	$8.6 \cdot 10^{-3} / 8.4 \cdot 10^{-3}$
silicon	diamond	14	5.43	$18.8 \cdot 10^{-3}$
chromium	bcc	24	2.89	$9.7 \cdot 10^{-3}$
tungsten	bcc	74	3.16	$6.2 \cdot 10^{-3}$

Table 3.3 Some materials along with those parameters that are relevant for CB production. *: average value

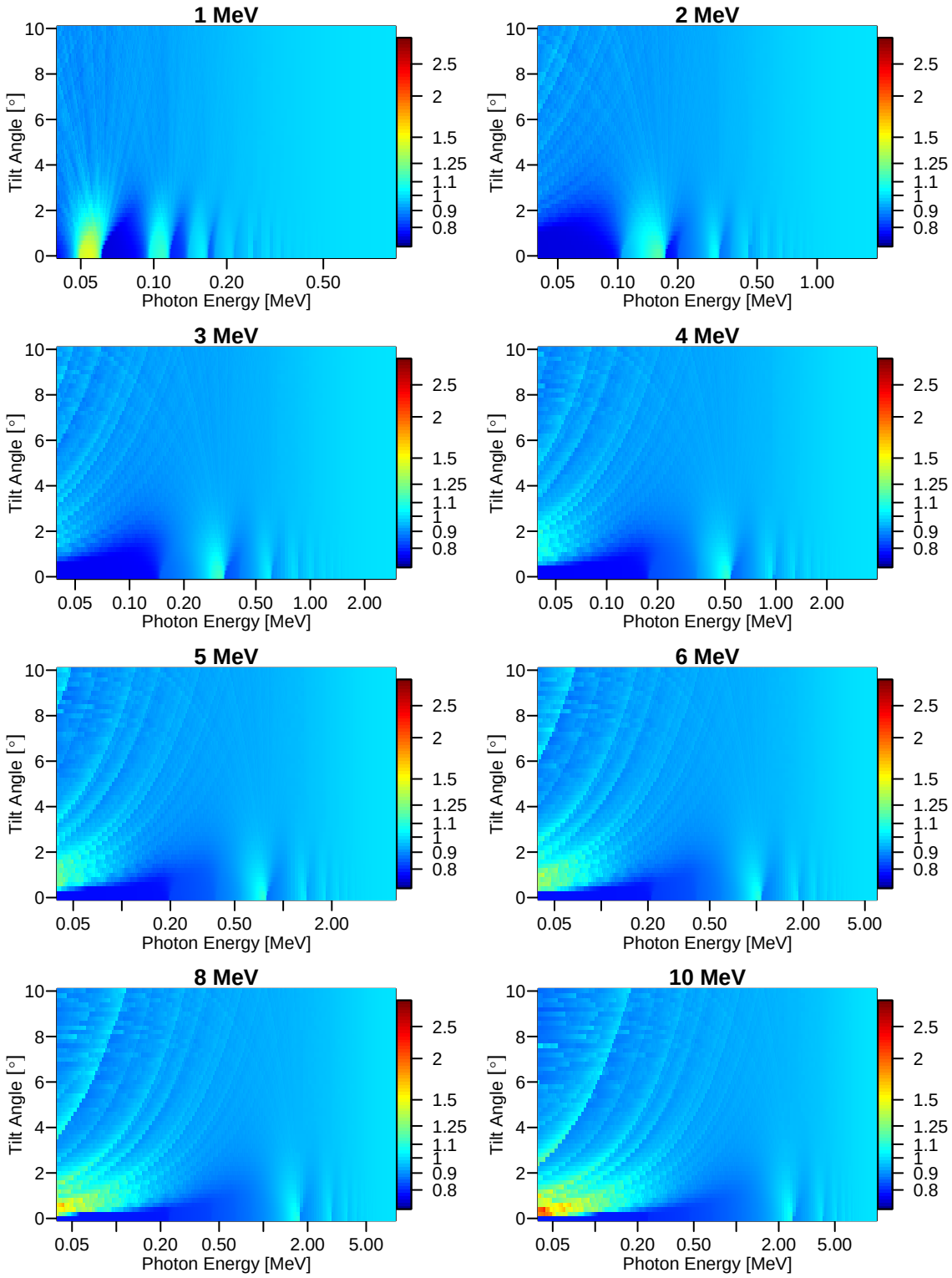

Figure 3.17 As in Fig. 3.13, but showing the ratios between single-crystal cross-sections in cubic **silicon carbide** for the **110-direction** and **amorphous carbon**.

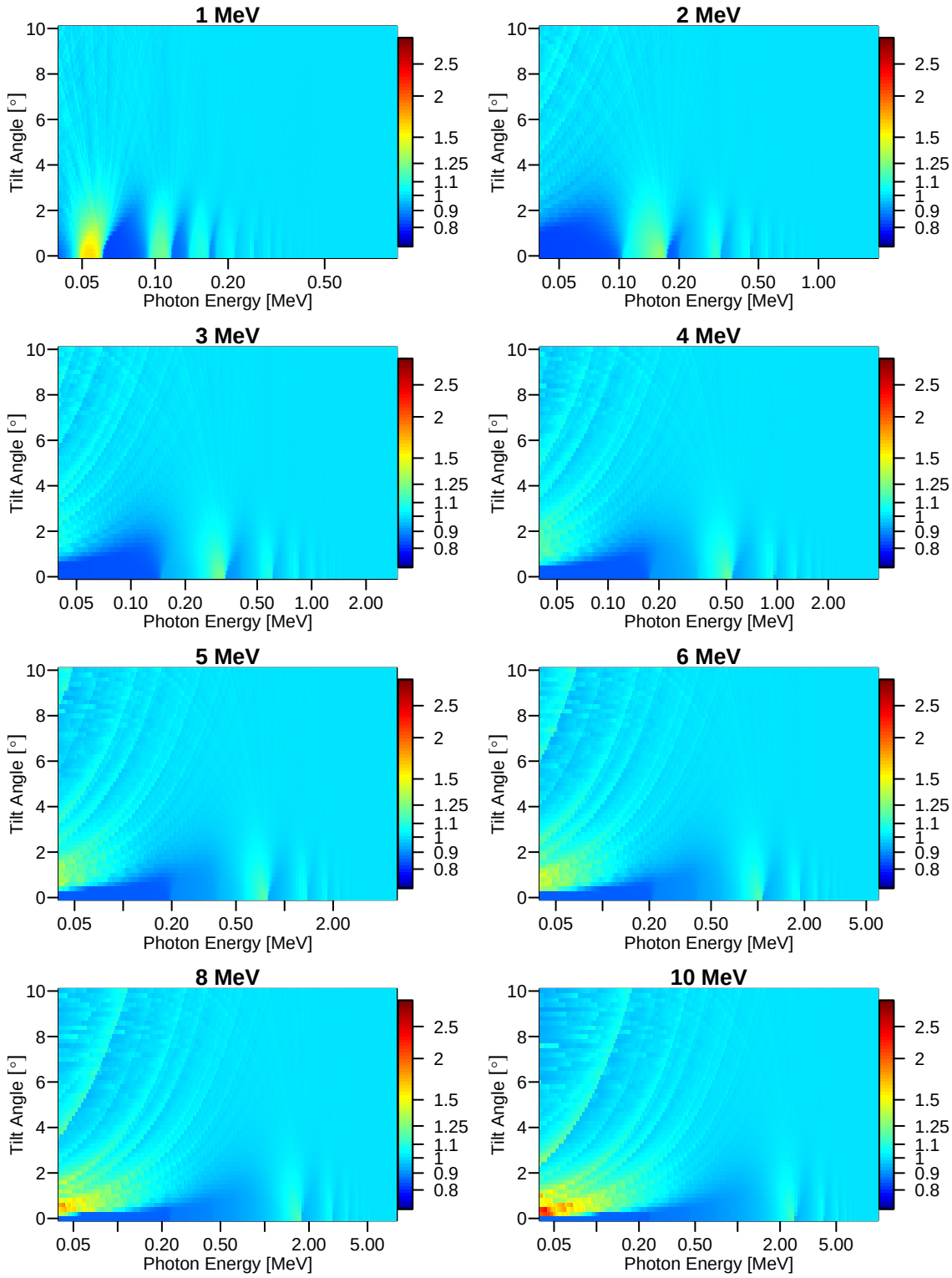

Figure 3.18 As in Fig. 3.17, but relating to **amorphous silicon carbide**.

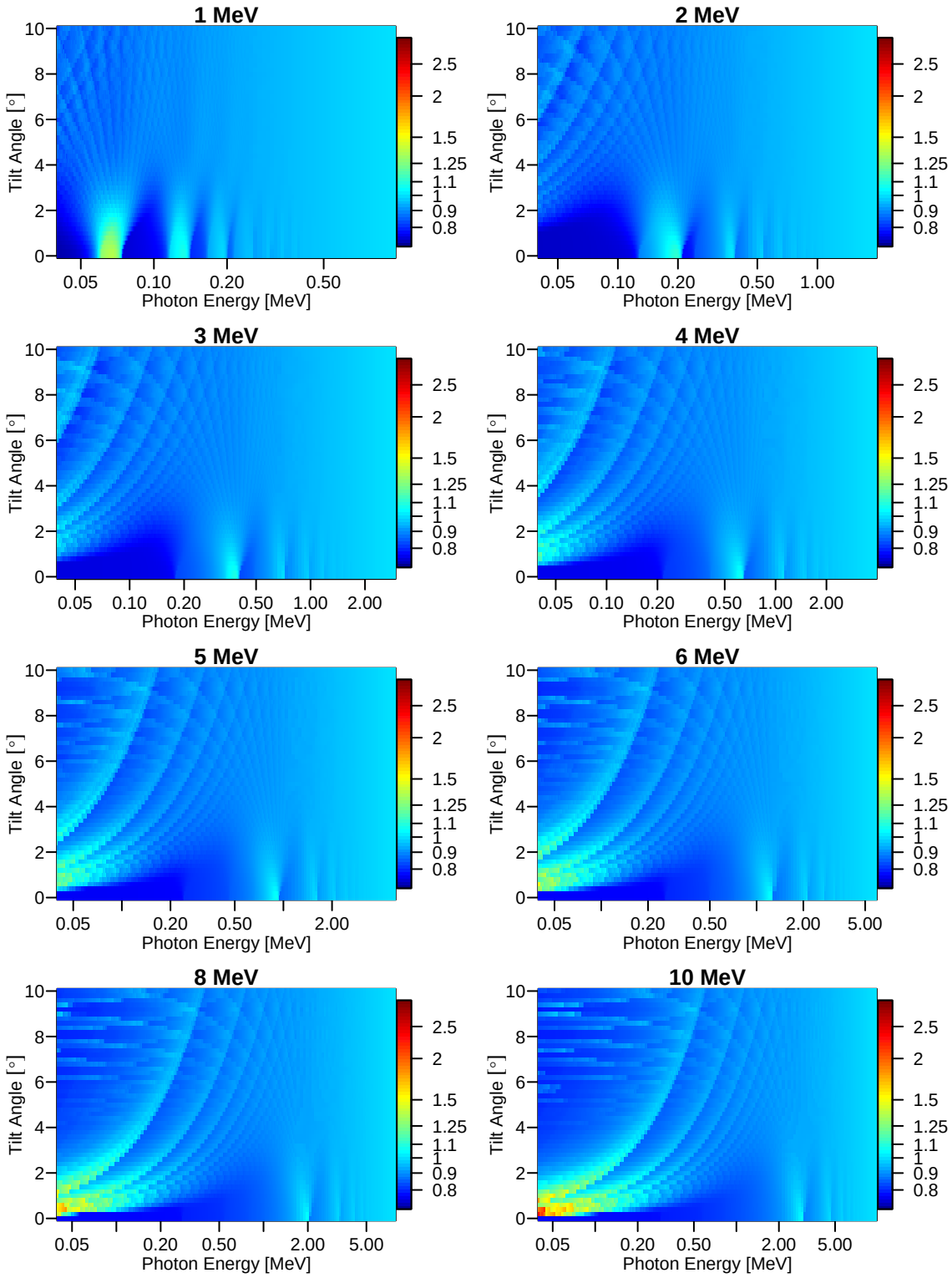

Figure 3.19 As in Fig. 3.13, but comparing the **111-direction** of a **chromium** single-crystal to **amorphous carbon**.

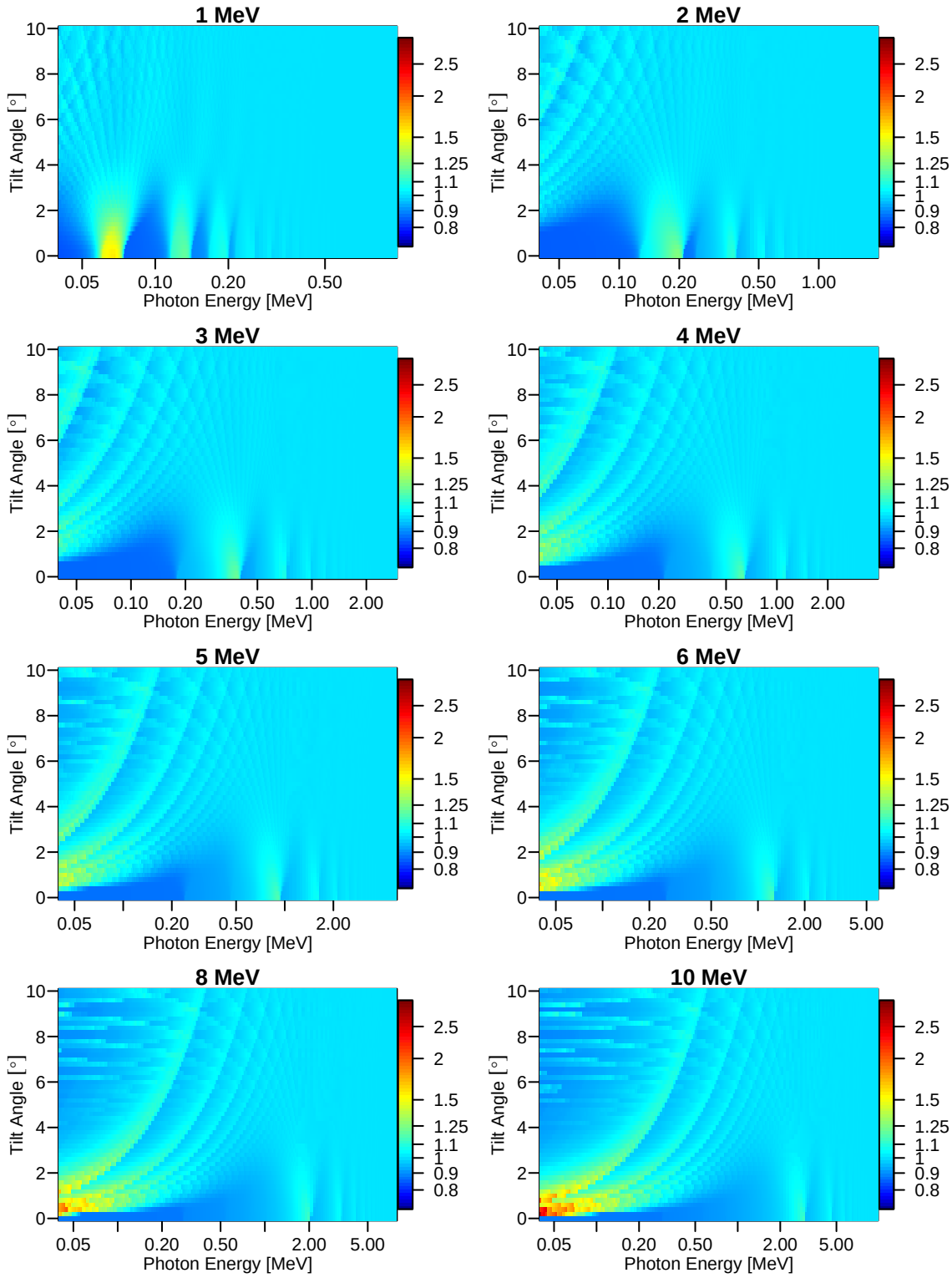

Figure 3.20 As in Fig. 3.17, but relating to **amorphous chromium**.

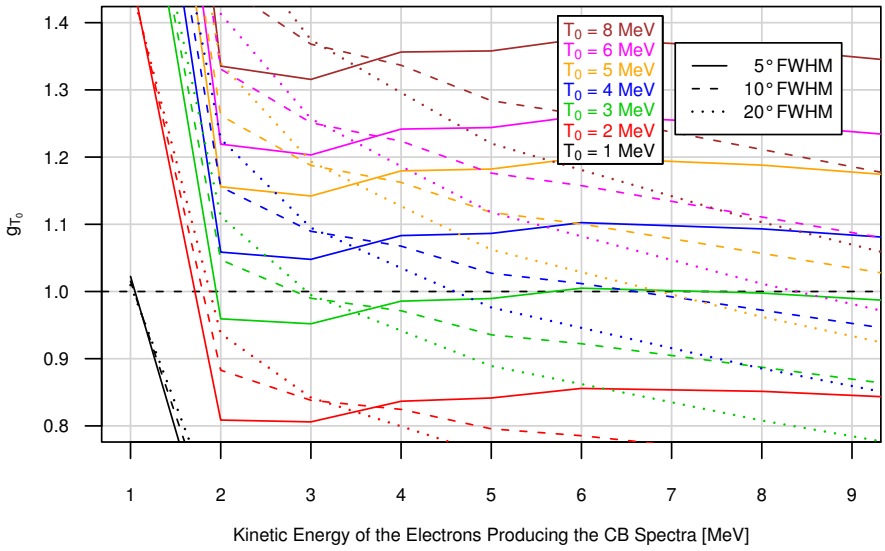

Figure 3.21 Values of g_{T_0}, as defined in (3.19), for various values of the kinetic energies of electrons impinging on **single-crystalline diamond** (x-axis) along the **110-direction** and **amorphous carbon** (the various lines, denoted by T_0 in the legend). The data shown here is to be interpreted as follows. Let us assume that we want to assess the performance of a 6 MeV beam creating bremsstrahlung in diamond. We then go to the value of 6 on the x-axis and find that this case significantly outperforms the same electron energy in amorphous carbon (represented by the pink lines), regardless of the electron beam's angular profile. The 5° and 10° curves even outperform 4 MeV electrons (blue lines) in the amorphous case. On the contrary, 2 MeV electrons (red lines) in diamond perform worse than the amorphous target.

The figures shown on the previous pages contain a lot of information, which makes it difficult to assess the suitability of all the various targets, crystal directions and kinetic energies to help us reach our goals of raising the amount of imaging photons in megavoltage spectra. We will now reduce the complexity of the problem by squeezing all this information into a single number, which we will use to rate the various parameter combinations with respect to each other. This quantity, g_{T_0}, will be defined based on the following two relations:

$$r = \frac{\#\text{ photons between 40 and 100 keV}}{\#\text{ photons above 100 keV}}\,, \tag{3.18}$$

$$g_{T_0} = \frac{r|_{\text{spectrum of interest}}}{r|_{\text{amorphous spectrum at } T_0 \text{ MeV}}}\,, \tag{3.19}$$

where # denotes "number of". Thus, we compare the amount of imaging photons, which we here define by the energy interval between 40 and 100 keV, to the amount of photons above 100 keV (which gives us r) and divide this by the corresponding number pertaining to an amorphous target which is hit by electrons with kinetic energy T_0. With this, we can spot beneficial combinations of the above parameters by simply looking for values of g_{T_0} which are greater than one. Rather than doing this for individual tilt angles, we will assume various (gaussian) angular distributions of the electron beam of 5°, 10° and 20° FWHM (stressing again that electrons with increasing tilt angles less and less contribute to the FOV). As before, we choose a full emission angle of 20°, which is of course defined around the individual direction of electron propagation rather than the initial beam direction. The results shown here should hence be treated with this in mind.

The results of these comparisons are shown in Figs. 3.21 through 3.25. A detailed description of how to read these figures is given in the caption of Fig. 3.21. What we find is a confirmation of

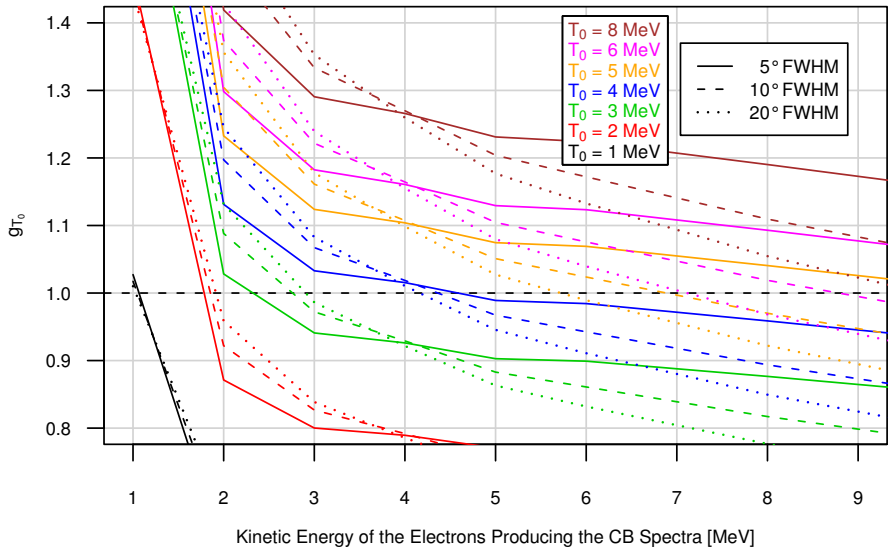

Figure 3.22 As in Fig. 3.21, but for a **silicon carbide single-crystal** compared with **amorphous silicon carbide**.

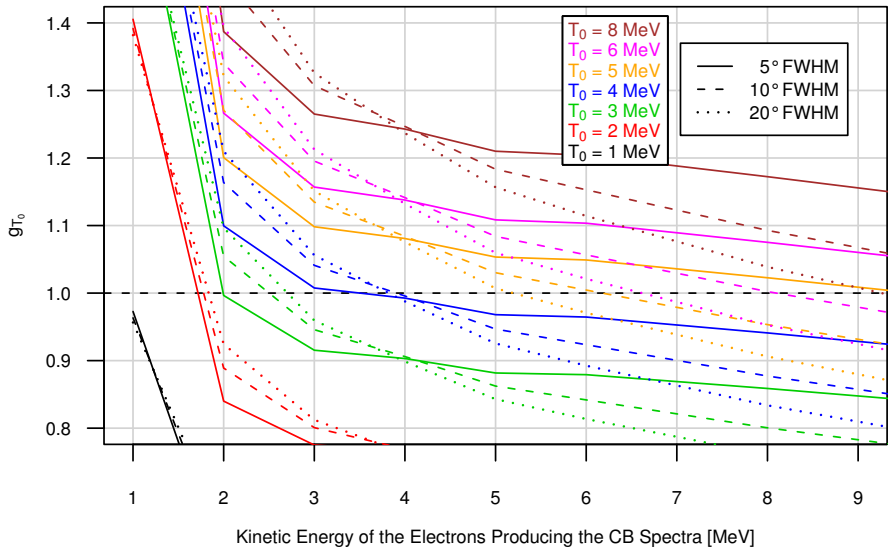

Figure 3.23 As in Fig. 3.21, but for a **silicon carbide single-crystal** compared with **amorphous carbon**.

two conjectures that arose from the discussion before. First, there is a minimum energy below which CB is not suitable anymore and even worse than conventional bremsstrahlung (about 4 MeV for diamond). This automatically translates to a maximum target thickness that must not be exceeded in order to not counteract the beneficial effects one gains from the higher energy electrons and implies a beam stopper. Second, an increase in the atomic number of the target is not necessarily detrimental (Figs. 3.23 & 3.25), because the increased screening of the nuclear charge by the atomic electrons partly removes unwanted photons at intermediate energies from the spectrum, while restoring the imaging fluence through the presence of CB. There is even a performance gain from single-crystal targets which is not to be underestimated, as it allows for a higher photon production efficiency and facilitates smaller targets, as already mentioned previously.

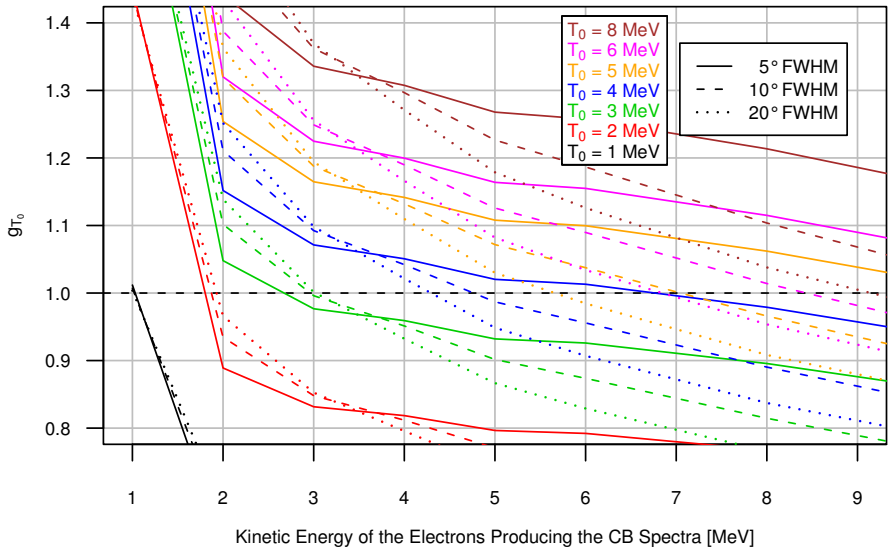

Figure 3.24 As in Fig. 3.21, but for a **chromium single-crystal** compared with **amorphous chromium**.

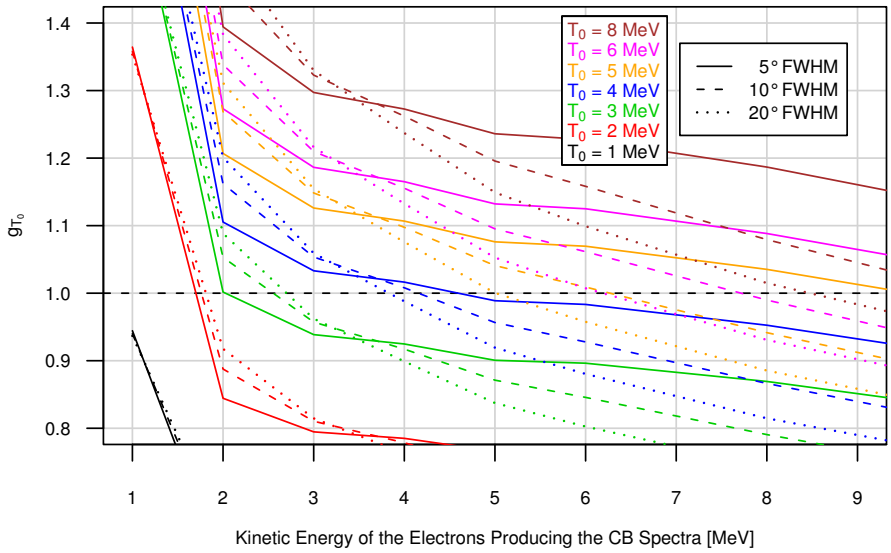

Figure 3.25 As in Fig. 3.21, but for a **chromium single-crystal** compared with **amorphous carbon**.

A careful treatment of all the multiple scattering and energy loss effects that we just discussed would of course have to be carried out using Monte Carlo (MC) simulations. As CB arises from an interaction of the incident electrons with the crystal *as a whole* rather than individual scattering centres, standard MC codes fail to simulate it (cf. section 2.4). To our knowledge, no CB MC code exists in the energy range considered, and so we have to rely on the cross-section analyses just carried out for the time being. Nonetheless, in the next section we will try to answer the question of whether we can expect dose savings from single-crystals when *increasing* the electron energy.

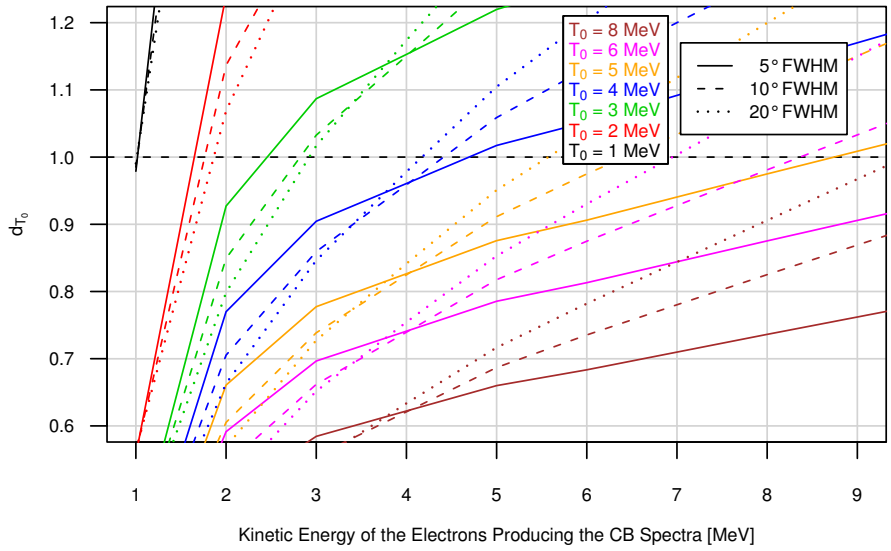

Figure 3.26 Values of d_{T_0}, as defined in (3.22), for various values of the kinetic energies of the electrons impinging on **single-crystalline diamond** (x-axis) along the **110-direction** and **amorphous carbon** (the various lines, denoted by T_0 in the legend). The data shown here are to be interpreted in the same way as explained in Fig. 3.21, but this time, values less than one indicate an improvement.

3.7 Can an Increased Electron Energy Lower the Patient Dose?

We will now perform a rough approximation for the dose in water according to the relation

$$D \approx \Phi \frac{\mu}{\rho} k \ , \tag{3.20}$$

where μ/ρ is the mass aborption coefficient and Φ denotes the photon fluence as given by the differential cross-section derived before. Following the approach introduced in the last section, we again consider the photons emitted into a 20° angular interval around the individual electron momenta and introduce a quantity that captures the amount of dose (similar to 3.20) instead of photon numbers:

$$r = \frac{\text{dose above } 100\,\text{keV}}{\text{dose between 40 and } 100\,\text{keV}} \ , \tag{3.21}$$

$$d_{T_0} = \frac{r|_{\text{spectrum of interest}}}{r|_{\text{amorphous spectrum at } T_0 \text{ MeV}}} \ . \tag{3.22}$$

This time, values less than one will indicate an improvement, that is, a higher ratio between imaging and unwanted "dose". The corresponding plots are shown in Figs. 3.26 - 3.30. The findings we obtain from them are quite encouraging: down to an energy of about 4 MeV, diamond (Fig. 3.26) performs superior to amorphous carbon. Even more important is that 6 MeV electrons here seem to beat 5 MeV electrons in an amorphous target. Considering only the values belonging to the narrowest electron angular distributions (i.e. the solid lines), which can be considered a proxy for electrons in broader distributions creating the dose at the centre of the FOV, we find that 8 MeV electrons in diamond even outperform 5 MeV electrons in amorphous carbon. Although this is no hard evidence (we are lacking a Monte Carlo tool here), this indeed suggests that an *increase* in the electron energy rather than a decrease can be beneficial to reduce patient dose if single-crystal targets are used. For the other two materials, silicon carbide and chromium, this effect is less

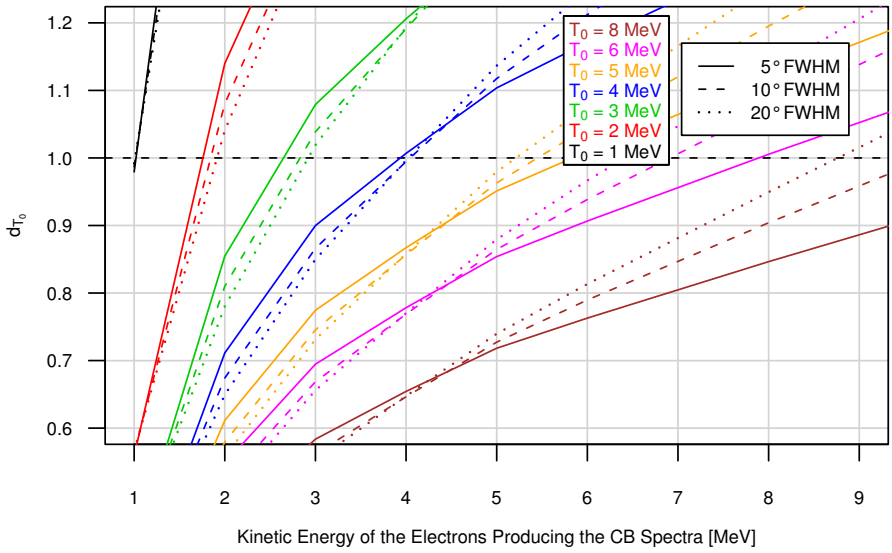

Figure 3.27 As in Fig. 3.26, but for a **silicon carbide single-crystal** compared with **amorphous silicon carbide**.

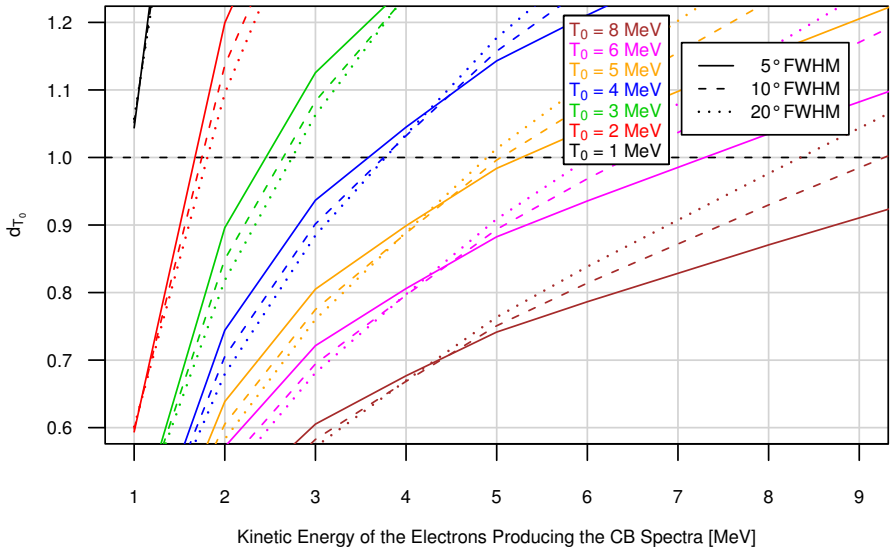

Figure 3.28 As in Fig. 3.26, but for a **silicon carbide single-crystal** compared with **amorphous carbon**.

pronounced, but one can still spot dose savings *even compared to carbon* when the same electron energy is used. For all materials, this goes down to about 4 MeV, where the amorphous targets start to become superior to the single-crystals.

The considerations carried out in this and the previous sections were based on the assumption that the photons between 40 and 100 keV are the ones desired. This criterion is of course rather artifical, because each imaging problem has its own requirements, depending on patient size and the anatomical region to be imaged. The choice we have made here is, however, a rather conservative one, as the following argument will show. In medical X-ray imaging, peak tube voltages of 120 or even 140 kvP are often used. The reason for this is not that one really

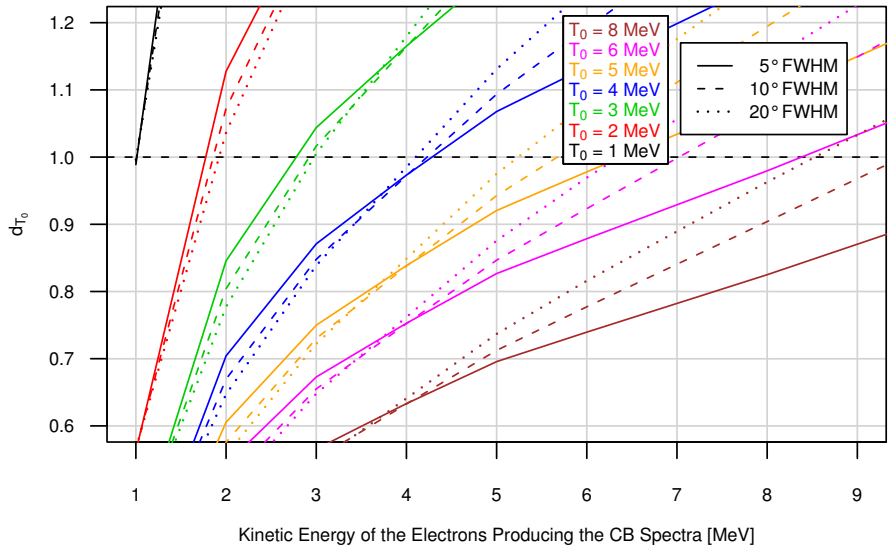

Figure 3.29 As in Fig. 3.26, but for a **chromium single-crystal** compared with **amorphous chromium**.

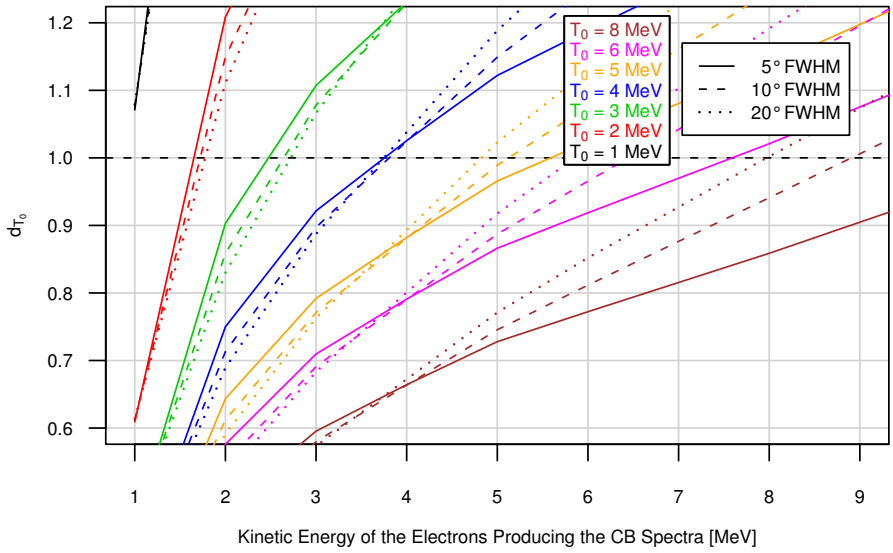

Figure 3.30 As in Fig. 3.26, but for a **chromium single-crystal** compared with **amorphous carbon**.

wants these rather high energy photons; they only deliver a comparably poor soft-tissue contrast (cf. Fig. 2.7). In fact, the voltage has to be chosen this high to create enough photons at the energy interval necessary for imaging. For instance, a 140 kVp setting in combination with a 2.5 mm aluminium filter has an average photon energy below 60 keV. From this, we see that our estimate is not an optimistic one, and the values shown above will of course become better as one allows a smaller upper limit for the photon interval desired.

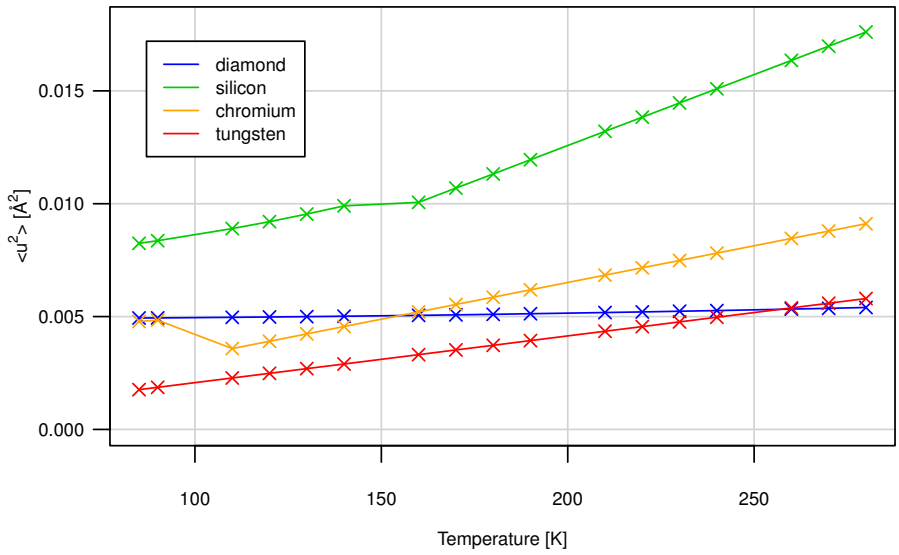

Figure 3.31 Mean squared vibrational amplitudes for various elements from values tabulated by Peng et al. (1996). They are based on phonon densities of states determined experimentally and are therefore more reliable than (2.25), especially at higher temperatures.

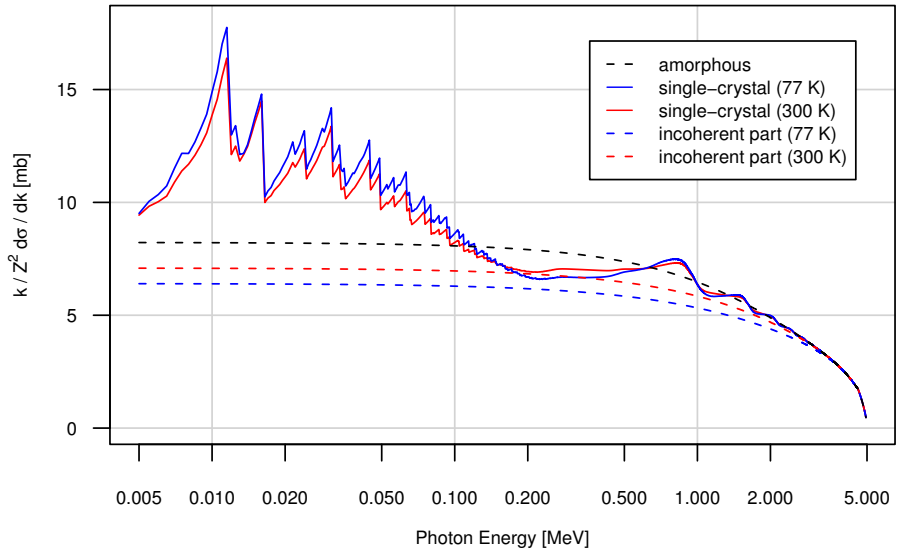

Figure 3.32 Temperature dependence of the spectra from single-crystalline chromium for 5 MeV electrons incident close to the 111-direction. The black line shows the amorphous cross-section for comparison.

3.8 Cooling the Target

The Debye - Waller factor (sidebar 2.3) is one of the quantities that influence the strength of the coherent part, and it depends on the mean squared vibrational amplitude $\langle u^2 \rangle$ of the atoms in the crystal, which naturally decreases with temperature. It is therefore interesting to see how a cooling of the target will affect the CB spectra. Before we do that, we take a look at the temperature dependence of $\langle u^2 \rangle$ for various materials in Fig. 3.31, where we find that there are huge differences at room temperature among the various materials.

Diamond, having the highest Debye temperature, shows only a very weak temperature depen-

dence, and thus a cooling does not help here. In other words, a heating of a diamond target due to extensive electron bombardment will also not have a significant impact. Silicon, however, has a very strong temperature dependence, and its $\langle u^2 \rangle$ in a cooled state is only as good as that of chromium at room temperature. Tungsten is very amenable to cooling, too, but also shows good values already at room temperature. However, with its high Z and strong screening, it is not suitable for IGRT, a finding which we have already stated above. Finally, chromium shows some temperature dependence and still has an acceptable Z.

Fig. 3.32 shows a comparison of some chromium spectra at 110 K and 300 K, and we see that while there is certainly a notable influence of the temperature on the kilovoltage component, the effect is probably not worth the associated costs in a clinical LINAC. For this reason, we will not consider target cooling further in this work.

3.9 Compound Targets

By now, it has become clear that the use of single-crystal targets in IGRT implies that the electron beam must not be fully stopped in the target. The reason for this is that the type-A peaks (which we propose to exploit here) move to lower energies when an electron loses its kinetic energy. These very low energy peaks have to be filtered out, and what remains is a spectrum that is in fact harder than those achievable with amorphous targets. Therefore, we need a target that will allow the electrons to escape at no less than 4 MeV. This is even more necessary for a chromium target, which has a comparably high attenuation of the imaging photons produced in it, and it therefore needs to be even thinner. For this reason, a beam stopper has to be used, which could be designed in a variety of ways.

One option would be to use a magnetic field to deflect the electrons by an angle of 90° or more, to stop these electrons in a low-Z medium such as beryllium and to shield its surroundings by a high-Z material to prevent the bremsstrahlung produced therein from escaping. Given the fact that medical LINACs already successfully apply a bending magnet, the deflection of the electrons leaving the target with reduced energies should not pose a major technical difficulty besides the requirement for additional space in the LINAC head. However, in addition to the costs that would be associated with this, another drawback arises here. The photon spectra exiting such a target basically lack the photons that otherwise would be produced by the continously decelerated electrons. While the photon spectra produced by the more energetic electrons are softer than in comparable amorphous targets, they lack all the photons from the slower electrons, which are of course of lower energy. Consequently, the resulting photon spectra are *harder* than with conventional targets. Another option appears therefore more promising.

This second option would apply the low-Z beam stopper directly after the actual single-crystal, and thus it would act as a second target producing bremsstrahlung. There is in fact no reason why the stopper should not be made from conventional target material like graphite, or in general by the amorphous counterpart of the material used. In other words: Make the spectra emitted by the electrons in the (say) upper third of the energy range softer, but do not touch the less critical ones. This could be achieved with all the single-crystal targets discussed above, or even a combination of them.

From the theory presented in this work there is no indication that an organic (i.e. low-Z) glue used to fix the various materials to each other would negatively affect the properties of the joint target. Because of this, there is reason to believe that the approach of designing such a compound target will be cheapest and most easy to implement in the context of IGRT.

The costs of the single-crystal are an issue that has not been investigated in this work. Along with this goes the question of how much radiation damage a single-crystal can handle before its

structure gets affected so severely that effectively it will not be different from a conventional target anymore, and if the replacement intervals are sufficiently long to justify the costs. In a compound target, however, the Bragg peak of the electrons would lie in the amorphous or poly-crystalline part, and so the majority of the radiation damage would be caused there and not in the crystal.

3.10 Discussion & Outlook

In this chapter, we developed a theory of coherent emission of X-rays in single-crystals in the first order Born approximation. It was specifically designed to be applied to electron energies down to about 1 MeV and complements previously published results.

Based on this theory, the use of single-crystals in medical LINACs was discussed and the potential of coherent bremsstrahlung to alter the X-ray spectra emitted by megavoltage electrons could be demonstrated: Employing single-crystal targets results in significantly softer X-ray spectra than achievable with conventional targets.

The ability of coherent bremsstrahlung to increase the amount of kilovoltage photons strongly depends on two parameters of the electrons producing these photons: their direction of motion and their energy. While the initial direction can be controlled by adjusting the crystal orientation, the electrons will scatter strongly once in the target and thus exhibit a very wide angular distribution, but only electrons travelling close to a major crystal direction will produce a significantly increased amount of kV photons. Since the emission of bremsstrahlung is strongly pointed in the direction of electron propagation, single-crystal targets are expected to create photon spectra that are softer within the central region of the field-of-view. This can be an advantage in computed tomography, where beam hardening is often a source of image degradation.

The energy loss of electrons in the target creates a problem that seems to be more critical than multiple scattering: the peaks move to lower and lower energies when the electron energy decreases, and the lowest electron energy that seems beneficial in the context of IGRT lies between 3 and 4 MeV. Below this energy, single-crystal targets perform worse than amorphous ones. As a viable solution to this problem, we propose the use of compound targets, which combine layers of one or more single-crystals with amorphous materials.

Our investigations to identify suitable target materials for the single-crystal parts of these compound targets lead to four promising candidates: boron nitride, diamond, silicon carbide and chromium. As low-Z components, boron nitride and diamond were found to behave very similarly, whereas the other two materials represent alternatives with higher atomic numbers. Surprisingly, both higher-Z targets, in their single-crystal manifestations, were observed to outperform amorphous carbon, which is the gold standard here. The effect is related to an increased screening of the nuclear charge by atomic electrons, which results in an attenuation of low and intermediate energy photons. In a single-crystal, the decrease at low photon energies can be compensated by the occurance of coherent bremsstrahlung, but the reduced photon numbers at intermediate energies are maintained, which is a desired property.

Albeit the conclusions presented here are somewhat speculative, they encourage to perform further studies in the author's opinion.

Chapter 4

From Greyscale to Colour: Energy Discrimination through Photon Counting

4.1 Motivation & Overview

Conventional digital X-ray imaging relies on measuring a signal proportional to the integrated amount of energy deposited in a pixel during exposure, which normally follows the conversion of X-ray photons into visible light in a scintillating material. During the last decade, this approach has been supplemented by direct conversion techniques based on pixelised semiconductor detectors. Attached to a sensor of choice, these devices are capable of counting individual photons and thus providing spectral resolution. Hence, the noise level of the readout electronics can be efficiently cut-off during image formation, which facilitates images that do not exhibit a dark current in the conventional sense. This property is usually referred to as "noise free", since - apart from the presence of defective pixels - the resulting images remain unexposed in the absence of radiation.

More important than the superior noise properties of photon counting detectors is their ability to discriminate photon energies. The interest in such devices dates back to the 1970s, when a paper by Alvarez & Macovski (1976) introduced the idea that energy discrimination could be used to separate photoelectric absorption and Compton scattering in the resulting images, hence providing information about the atomic number and electron density which cannot be obtained from conventional computed tomography. As a consequence, the classification of different tissue types can be performed more reliably. Since photon counting detector systems offering sufficient spatial resolution were unavailable by that time, the idea was implemented by performing energy discrimination on the source side, i.e. by choosing differerent X-ray tube voltages and filters to obtain X-ray spectra with comparably narrow bandwidths. This resulted in the development of so-called dual energy CT systems that are based on two X-ray tubes and which are nowadays available commercially for clinical use.

Only recently has the scientific community seen the development of commercial prototypes that allow energy discrimination in the detectors. Most notably, a paper by Schlomka et al. (2008) from Philips introduced the technology to a wider public and demonstrated the feasibility of K-edge imaging using a variety of contrast agents. In the meanwhile, other companies also revealed their dedication to this subject (Strassburg et al. 2011), yet most of these products have not left the prototype stage so far.

It was therefore a great opportunity for this author to work with the Medipix2 readout system

developed at CERN[1], which was provided to DKFZ in a collaboration with the Freiburg Materials Research Center (FMF) in Germany. The Medipix2 chips are renowned for their photon counting capabilities that are often used for X-ray imaging, featuring two energy thresholds.

Being a relatively new technology, the characteristics of the the Medipix2 readouts in conjunction with various sensor materials have been studied not to full extent yet. Much of this chapter is therefore dedicated to determining the imaging properties of two detectors employed at DKFZ. Before we come to that, we will give the necessary physical basics to understand the physics of semiconductor detectors in section 4.2. Then, the Medipix2 readout system will be described in section 4.3. We will continue by taking a close look on the charge carrier transport properties of cadmium telluride (CdTe), which is the sensor material used in the two detectors studied, in section 4.4, followed by a description of these detectors in section 4.5. After this, we are ready to discuss the threshold equalisation procedure that is necessary to make the response of each pixel more homogeneous across the chips in sections 4.6 and 4.7. This will be followed by a description of various energy calibration procedures in section 4.8. Bias voltage dependent energy response functions and modulation transfer functions of the two detectors are given in sections 4.9 and 4.10. In section 4.11, we will determine the detective quantum efficiencies (DQE) by measuring the average multiplicities of the two detectors, i.e. the mean number of pixels that respond to a single photon. We will go on by introducing a possible explanation of voltage dependent image artefacts in section 4.13. Finally, we will discuss spectral CT in section 4.15 and summarise this chapter in section 4.16.

4.2 The Physics of Semiconductor Detectors

Semiconductor radiation detectors are based on the conversion of the energy released in an ionising event directly into free electric charges, i.e. the creation of electron-hole pairs. These charges are accelerated towards a readout electronics by means of a bias voltage, where they are "counted". While we will detail the Medipix2 pixel cell in section 4.3, we will quickly review the relevant physics here.

4.2.1 The Effective Mass

Electrons excited into the conduction band leave a vacant position in the valence band, which is called a hole. Although this is simply a lack of an electron, it can be treated as a positive charge and thus also contributes to charge transport, i.e. conduction. Both electrons (negatively charged) and holes (positively charged) are no free particles within the semiconductor, yet they can be treated as such by introducing an effective mass $m^*_{n/p}$, which in the case of anisotropic crystals is a tensor (Hunklinger 2009). In analogy to the free electron dispersion relation $T(\boldsymbol{q}) = q^2/2m$, it is defined as:

$$\left(\frac{1}{m^*}\right)_{ij} = \frac{\partial^2 T(\boldsymbol{q})}{\partial q_i \partial q_j} \,. \tag{4.1}$$

With this, the classical equation of motion

$$a_i = \sum_j \left(\frac{1}{m^*}\right)_{ij} F_j \tag{4.2}$$

can be maintained, with a_i and F_j denoting the components of acceleration and force. Since the effective mass is a function of the wave vector $\boldsymbol{q}$, (4.2) implies that for a constant field strength

[1] http://medipix.web.cern.ch/MEDIPIX/

the acceleration varies among different electrons. This does not come as a surprise, as it simply describes a friction that depends on the electron momentum.

From (4.1) we see that it is the curvature of $T(\boldsymbol{q})$ that determines m^*, and hence it contains all the information on the interactions an electron experiences. An effective mass that is independent from $\boldsymbol{q}$ is encountered at the extrema of bands that can be described by a quadratic polynomial, since the curvature is constant there.

4.2.2 Intrinsic and Extrinsic Semiconductors

Semiconductors are characterised by a gap between valence and conduction band. They are rather loosely separated from the class of insulators by the width of the band gap, which is smaller for semiconductors and allows their use in technical devices at room temperature. Among the elemental semiconductors, silicon and germanium are probably those with the highest relevance, while a variety of compound semiconductors exist in technical applications, such as CdTe, which is employed in the detectors described in this chapter.

The width of the band gap only weakly depends on the temperature, but influences the so-called intrinsic conductivity of a semiconductor. The larger the band gap, the lower the chance that an electron will experience an excitation into the conduction band by thermal fluctuations. From textbooks on solid state physics (e.g. Hunklinger, 2009), we obtain the following relations for the charge carrier concentrations of electrons and holes:

$$n = 2\left(\frac{m_n^* k_B T}{2\pi\hbar^2}\right)^{3/2} \mathrm{e}^{-(E_C - E_F)/k_B T} \,, \tag{4.3}$$

$$p = 2\left(\frac{m_p^* k_B T}{2\pi\hbar^2}\right)^{3/2} \mathrm{e}^{(E_V - E_F)/k_B T} \,. \tag{4.4}$$

Here, k_B denotes the Boltzmann constant, T the temperature, E_C the minimum energy of the conduction band, E_V the maximum energy of the valence band and E_F the Fermi energy. Thus, the resistivity of a semiconductor decreases with temperature. Here, the effective masses can be considered those at the band extrema due to the exponential function and therefore assumed to be constant.

An intrinsic semiconductor is characterised by the absence of any dopants. Consequently, $n = p$ in this case, and the conductivity is very low. Extrinsic semiconductors are doped with very small concentrations of impurities. Choosing these dopants appropriately can introduce new allowed energy levels within the band gap. Depending on how these impurities bind to their neighbours, they might provide an additional electron that is rather loosely bound, i.e. located close to the minimum of the conduction band (called a donor), or they may offer an additional energy level not far away from the maximum of the valence band, accepting electrons (called an acceptor). In this case, the creation of electron-hole pairs is much easier, because only a small amount of energy is required to jump into these additional energy levels. Hence, the conductivity rises dramatically for extrinsic semiconductors.

4.2.3 Direct & Indirect Semiconductors

Direct and indirect semiconductors can be distinguished by the location of the maxima and minima of their valence and conduction bands. While for direct semiconductors these coincide in momentum space at $\boldsymbol{q} = 0$, they do not in the case of indirect semiconductors. As a consequence, electrons in direct semiconductors can be excited into the conduction band by photons much

more easily, as no momentum transfer is necessary (photons only carry a very small momentum). For indirect semiconductors, this implies that the momentum transfer necessary to create an excitation with the lowest possible energy must stem from an interaction with a phonon. This makes absorption in indirect semiconductors much more unlikely unless the energy of the incident photon is sufficiently high to enable direct absorption. For X-ray photons, this is generally the case.

4.2.4 The Mobility-Lifetime Product

A classical treatment of charge carrier transport in a semiconductor leads to an expression for the charge carrier speed $\boldsymbol{v}$ as a function of the applied electric field $\boldsymbol{\epsilon}$ and the mean time between collisions τ_{col}:

$$\boldsymbol{v} = \frac{-e\tau_{col}}{m^*}\boldsymbol{\epsilon} \equiv -\mu\boldsymbol{\epsilon} \ . \tag{4.5}$$

Here, we have introduced the mobility μ, which is simply a proportionality constant between the electric field applied and the speed of the charge carriers (for holes, the negative sign changes to a positive one).

With this, we get the current density $\boldsymbol{j}$,

$$\boldsymbol{j} = n\, e\, \mu\, \boldsymbol{\epsilon}, \tag{4.6}$$

where n represents the charge carrier density. Although this linear relationship is in good agreement with experiments, the classical approach cannot be right, because every electron has to find an unoccupied state to be left in after the scattering process. This is treated quantum mechanically in the so-called Sommerfeld model and described in many textbooks on solid state physics (Hunklinger 2009). As the only relevant quantity for us is the mobility μ, we will not go into any further details here.

The next important quantity is the lifetime of the charge carriers in the semiconductor. Remembering that these are simply electron-hole pairs, it is easy to see that recombination can occur. We denote the mean lifetime of a charge carrier by τ and obtain the mean carrier drift length λ according to Sellin et al. (2006):

$$\lambda = \mu\tau\frac{U}{d} \ . \tag{4.7}$$

Here, we have replaced the (homogeneous) electric field by $\epsilon = U/d$, where U ist the voltage applied and d the detector thickness. Obviously, λ depends on $\mu\tau$, which is called the mobility-lifetime product or simply $\mu\tau$-product, and can be considered independent of the voltage.

4.2.5 Signal Formation & Charge Collection Efficiency

Other than frequently assumed, a current can be measured in the readout electronics right at the moment of the electron-hole pair generation. The reason for this is charge induction, which is illustrated for a single charge in between non-segemented electrodes in Fig. 4.1. In a semiconductor, both electrons and holes contribute to this. Applying a bias voltage and hence separating the two charge types, the induced charge can be measured as a current directly after the ionizing interaction takes place and until all charges either have been collected or disappeared otherwise (by recombination or trapping).

Both induced charge and current can be computed with the help of Ramo's theorem for arbitrary geometries and electrode numbers. It is summarised as follows (Spieler 2006):

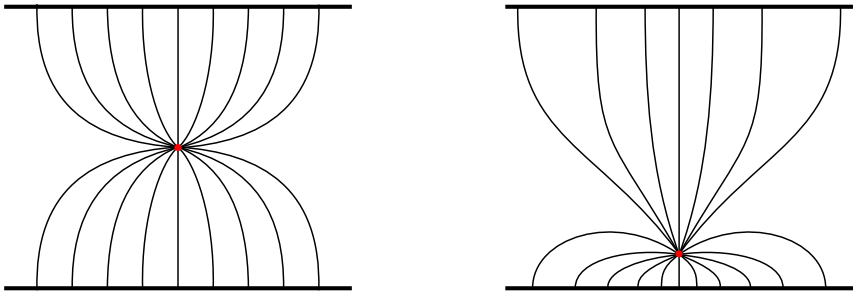

Figure 4.1 Schematic of the field lines emanating from a charge between two parallel plates. The closer the charge is to one of the plates, the more charge will be induced on the respective side, and the less on the opposite one (adopted from Spieler, 2006).

- If a charge q moves along an arbitrary path between positions $\boldsymbol{x}_1$ and $\boldsymbol{x}_2$, the net induced charge on electrode n is:

$$\Delta Q_n = q\left[\phi_n\left(\boldsymbol{x}_2\right) - \phi_n\left(\boldsymbol{x}_1\right)\right] \ . \tag{4.8}$$

  Here, $\phi_n\left(\boldsymbol{x}\right)$ is called the weighting potential. It can be computed by setting the potential of electrode n to 1 and all others to 0, and hence is a dimensionless quantity.

- The current I_n at electrode n can be computed in terms of a weighting field $\boldsymbol{E}_Q = -\boldsymbol{\nabla}\phi$:

$$I_n = -q\boldsymbol{v}\boldsymbol{E}_Q \ . \tag{4.9}$$

For the geometry shown in Fig. 4.1 as an example, we have $v = \mu E = \mu U/d$, $E_Q = 1/d$, and we obtain the current

$$I = q\mu\,\frac{U}{d^2} \ , \tag{4.10}$$

which is constant until all charges have been collected. The collection time $t_c = x/v = xd/\mu U$ to traverse the distance x to the electrode then gives us the induced charge

$$Q = It_c = qx/d \tag{4.11}$$

and thus

$$dQ = qdx/d \ . \tag{4.12}$$

For an electron-hole pair, the above equations are valid if one chooses the corresponding mobilities and distances, and from (4.11) we see that the induced charge depends on the location of the charge carriers.

Weighting fields for segemented electrodes like the pixel detectors described in this chapter are generally non-trivial to compute. Without going into details here, we just report that the weighting fields significantly differ from 0 only in the vicinity of a given electrode n (Spieler 2006). Hence, most of the charge will be induced when the moving charge is near this electrode. Neighboring electrodes, i.e. pixels, will see an induced charge, too, but since the moving charge does not terminate on them, the currents measured for them will eventually change sign, leading to zero total charge collected. Only the pixel receiving the charge will exhibit an integral charge that differs from zero.

In the presence of trapping at defects, which particularly happens for holes due to their lower $\mu\tau$-product, the induced charge is different from the results above if the integration time in the readout electronics is finite. Assuming $Q(t) = Q_0\mathrm{e}^{-t/\tau}$, $t = x/\mu E$ and using (4.12), we can easily

derive the Hecht equation (Spieler 2006) giving the charge collection efficiency (CCE) Q_s/Q_0 at interaction site x_0, which relates the signal charge Q_s to the original charge Q_0 through:

$$\frac{Q_s}{Q_0} = \frac{\mu_e \tau_e U}{d^2}\left(1 - \mathrm{e}^{\,d(d-x_0)/\mu_e\tau_e U}\right) + \frac{\mu_h \tau_h U}{d^2}\left(1 - \mathrm{e}^{\,dx_0/\mu_h\tau_h U}\right) \ . \tag{4.13}$$

Q_0 can be expressed as a function of the interaction energy E_i, the average energy W to create an electron-hole pair and the charge q of the charge carrier through

$$Q_0 = \frac{E_i}{W}\, q \ . \tag{4.14}$$

In general, W is about three times higher than the band gap (Alig & Bloom 1975).

Again, we see that the total collected charge depends on the position of the interaction when trapping cannot be neglected. As trapping is an event especially pronounced for holes because of their lower mobility, this can lead to an effect called hole-tailing in some materials, such as CdTe. In this case, the actual photopeak measured will exhibit a long tail at lower energies, which is exactly due to incomplete signal collection. For photons interacting close to the surface of the sensor, this will not play a major role for two reasons: The holes generated there do not have to travel very far if this side is chosen as the cathode. Also, the distance the holes have to traverse is rather well-defined. On the contrary, photons with higher energies - thus interacting all over the sensor volume - will show an increased hole-tailing effect, precisely because the induced current depends on the position of interaction.

One of the relevant terms in (4.13) is U/d^2, from which we learn that a doubling of the detector thickness cannot be compensated by a doubling of the voltage, but will require an increase by a factor of four in order to maintain a constant CCE. It is important to note here that the Hecht equation (4.13) does not incorporate any detrapping of charge carriers.

As we have seen above, for segmented readouts the weighting field is only significant close to the electrode that actually collects the charge. As a consequence, the smaller these electrodes are chosen, the smaller this relevant region will become. Thus, collecting electrons at the segmented electrode, hole tailing will become less and less a problem when the pixel size is reduced (Barrett et al. 1995).

4.2.6 Maximum Sustainable Photon Flux

The electric field within a semiconductor sensor can be severely affected when the rate of electron-hole pairs generated is so high that the drift time of the resulting charge carriers can no longer keep up, and hence the detector polarises. The generally linear relationship between count rate and photon flux then flattens above a critical value until eventually the count rate decreases and reaches zero, resulting in catastrophic device failure. This effect was detailed by Bale & Szeles (2008), who also gave an expression for the maximum sustainable photon flux for Cd(Zn)Te above which linearity breaks down:

$$\Phi^*_\gamma = \frac{\epsilon_0 W U^2}{e\, d\, \overline{k}\, \Lambda^2}\left(\beta - \frac{d}{\Lambda}\mathrm{e}^{-d/\Lambda}\right)^{-1} \frac{\mu_h \tau_h}{\tau_h + \tau_D} \ . \tag{4.15}$$

Here, ϵ_0 is the dielectric constant, e the elementary charge, Λ the mean free path for the average photon energy $\overline{k}$ of the incident X-ray spectrum and $\beta = 1 - \exp(-d/\Lambda)$. $\mu_h\tau_h$ is the mobility-lifetime product for holes, and τ_D denotes the inverse of the detrapping rate, i.e. the rate by which holes escape from acceptors. We find that $\mu_e\tau_e$ does not appear in this equation, since electrons move much faster than holes in CdTe.

From the Bale-Szeles equation (4.15) we can learn two things. Unlike in the case of the CCE (4.13), we now find a dependence on U^2/d, i.e. an increase in the detector thickness d can be easily compensated by a moderate increase of the bias voltage U. Also, through the dependence on τ_D we get

$$\Phi_\gamma^* \propto \mathrm{e}^{-\frac{E_A}{k_B T}} \ , \tag{4.16}$$

where E_A is the energy of the acceptor. An increased detrapping of holes from defects at higher temperatures therefore causes a quicker polarisation of the detector.

4.2.7 Charge Sharing

Charges moving towards the electrodes are being scattered inelastically, and hence the intial charge cloud more and more broadens with the distance travelled. Arriving at the electrodes, this charge cloud then may be shared among neighboring pixels, each measuring independent events of lower energies. This effect is called charge sharing and again leads to a low-energy tail of the photopeak. In contrast to hole-tailing, however, charge sharing increases when the pixel size is reduced.

Assuming a random walk of the charge carriers due to thermal diffusion (Spieler 2006), we can calculate the transverse standard deviation σ,

$$\sigma = \sqrt{2Dt} \ , \tag{4.17}$$

where t represents the drift time and D the diffusion constant, which is related to the mobility μ through the Einstein relation:

$$D = \frac{k_B T}{e}\mu \ . \tag{4.18}$$

With this, (4.5) and assuming an average electric field $\epsilon = U/d$, we obtain:

$$\sigma = d\sqrt{2\frac{k_B T}{eU}} \ . \tag{4.19}$$

Hence, the diffusion responsible for charge sharing is independent of μ in this approximation and thus the same for electrons and holes. For $d = 1\,\mathrm{mm}$, $T = 300\,K$ and $U = 400\,\mathrm{V}$, which are typical values for the detectors described below, we obtain $\sigma \approx 11\,\mu\mathrm{m}$ for the transverse diffusion, which increases to about $16\,\mu\mathrm{m}$ when the bias voltage is reduced to $200\,\mathrm{V}$.

In addition to this diffusion related part of charge sharing, the final shape of the charge cloud is further influenced by the inital photo- or Compton electrons, whose ranges increase with the photon energy. Also, no matter how small the diffusion, events occuring at pixel boundaries will always create signals registered by two or more pixels. The probability for this to occur again shrinks with the pixel size.

4.2.8 X-Ray Fluorescences

X-rays interacting in the sensor by means of photoelectric absorption (section 2.3.2) inevitably lead to the emission of characteristic X-rays (sidebar 4.1). The energies of these fluorescence lines, their yields and their mean free path lengths increase with the atomic number of the atom which emits them (Table 4.1). Depending on the pixel size, the resulting photons may or may not be detected in pixels that do not correspond to the pixel pertaining to the initial interaction site. In consequence, two events can be registered. One is created by the fluorescence photon, the other, called escape peak, by the photo-electron at the original site. While the fluorescence

material	Z	E_{K_α} [keV]	$1/\mu_{K_\alpha}$ [10^{-5} m]	η [%]
Si	14	1.74	1	4
Ge	32	9.89	5	55
Cd	48	23.17	11	87
Te	52	27.47	6	87

Table 4.1 Comparison of the K_α fluorescence energies, mean free path lengths $1/\mu$ (μ denotes the absorption coefficient here) and fluorescence yields η. The mean free path lengths for the Cd and Te fluorescences are in CdTe, and the smaller value of Te is due to an absorption edge of Cd. Data taken from Casnati et al. (1984) and Tlustos (2005).

photons possess well defined energies k_f, those of the escape peaks E_e depend on the energy of the incident photon k:

$$E_e = k - k_f \ . \tag{4.20}$$

Thus, the escape peaks will form a diffuse background rising towards low photon energies when broadband sources, such as X-ray tubes, are used.

The effects of both charge sharing as well as flurescences can be avoided either by choosing pixel sizes that are large enough to absorb most of the fluorescence photons or by using coincidence electronics in the pixels which will treat events in a certain neighbourhood as belonging to the same event if all of them occur on a very small timescale.

4.3 The Medipix2 Readout System

4.3.1 History

The Medipix collaboration was formed at CERN, where the development of pixel detectors started in the late 1980s for particle tracking purposes. The aim of designing the first Medipix chip was to develop a general purpose X-ray imaging detector with photon counting capabilities, although Medipix chips can be used for detecting a variety of particle species.

The Medipix1, as the first chip generation is nowadays called, was described by Campbell et al. (1998) and featured a pixel size of 170 µm × 170 µm. With pixels arranged on a 64 × 64 array, the total sensitive area covered 1.09 cm × 1.09 cm. It featured a leakage current compensation, working by detecting, inverting and feeding back leakage current into columns of pixels to compensate for the finite resistivity of sensor materials. Energy discrimination was achieved by an energy threshold which could be used to only count events above it (or, to be precise, to count only those events which created a minimum amount of charge at the input of a charge sensitive preamplifier, sidebar 4.2).

The Medipix2 chip was introduced only four years later (Llopart et al. 2002). Along with a pixel pitch reduced to 55 µm, it offered a second energy threshold which could be used to obtain an energy window. The leakage current compensation was enhanced to work individually for every pixel, and the charge sensitive preamplifier was modified to accept both positive and negative polarities as input signals, allowing operation with different sensor materials. The chip was designed to be buttable on three of its sides, allowing the assembly of larger detectors. A redesign of the Medipix2, the Mpix2MXR20 (Llopart 2007), was introduced later, offering better temperature stability, higher radiation hardness and a maximum counter depth increased from 8001 to 11810, among many more improvements. A variation of this detector, the Timepix chip (Llopart et al. 2007), adds the functionality of arrival time as well as time-over-threshold measurements.

Sidebar 4.1 Atomic Relaxations

While X-rays tend to choose tightly bound electrons as their interaction partner, charged particles favour outer shell electrons as they travel along their path. Generally, an ionisation in an inner shell is subsequently filled by electrons of outer ones. Two distinct effects of how the excess energy is dissipated generally contribute to this:

Emission of Auger electrons: Here, the energy gained from filling up a hole directly causes the emission of an electron from an outer shell. This emission creates an additional vacancy that successively travels outwards. It is also called a non-radiative process since no X-rays are observed during this process apart from the emission of secondary bremsstrahlung.

Emission of Characteristic X-rays: The transition to a lower state can also happen by means of directly emitting an X-ray photon. Its energy naturally depends on the type of transition and can be observed as a well-defined peak in X-ray spectrometry. It is also characteristic for the material, hence the name.

The figure below shows some examples for radiative transitions that happen between the various energy states. The notation on the left contains main, angular momentum and spin quantum numbers. The letters in the figure correspond to the famous Siegbahn notation which is used to label the various transitions according to their intensities. On the right, a different notation is used to refer to the different states. It is recommended (Jenkins et al. 1991) by the International Union of Pure and Applied Chemistry (IUPAC) to label transitions instead of using the Siegbahn notation, because it contains information about the origin of all the lines. As an example, the K_{α_1} transition is called K-L_3 according to this recommendation.

In principle, all these transitions are constrained by the well-known selection rules, for which the interested reader is referred to standard literature on atomic physics.

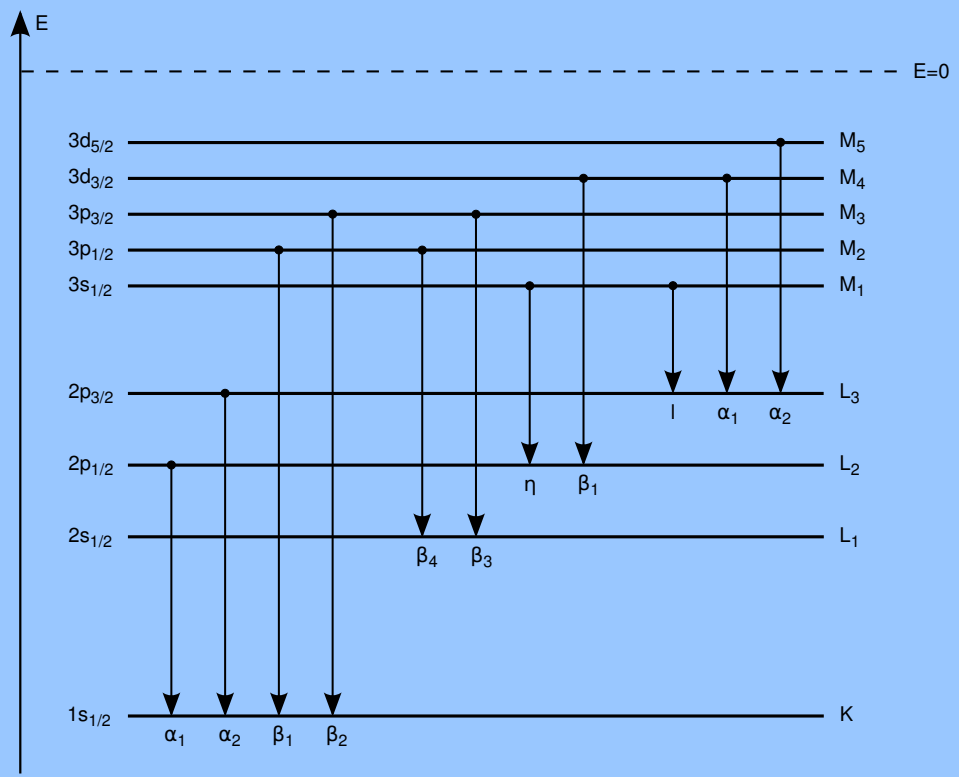

Figure adopted from Salvat et al. (2001).

The latter feature enables true spectroscopic imaging without the need for setting an energy window, yet at the cost of a maximum count number of one per pixel prior to readout.

Finally, the third generation of the Medipix chips was announced (Ballabriga et al. 2007) recently. Among many changes, it offers a charge summing mode to account for both charge sharing as well as X-ray fluorescences (sections 4.2.7 & 4.2.8). By combining pixels to larger networks, meta pixels up to a pixel pitch of 220 µm promise to effectively reduce the distortion of X-ray spectra by these two effects. At the time of writing, the Medipix3 had not exited the protype stage yet and therefore was not available for any of the measurements described in this chapter. Hence, all results were obtained with the Mpix2MXR20 architecture.

4.3.2 Pixel Cell

Below, we will describe the components present in each pixel relevant to energy discrimination. Detailed schematics were given by Tlustos (2005) and Llopart (2007), for instance. The behaviour of the elements listed here is controlled by the output of a variety of digital-to-analog converters (DACs), which can be controlled by the user and which we will refer to in uppercase letters below.

Preamplifier

The charge that has been created in an event and accelerated towards the pixels serves as an input to a charge sensitive preamplifier (sidebar 4.2), whose output voltage is proportional to the charge that has been accumulated. Both preamplifier gain and the rise time of the voltage output are adjusted using the PREAMP DAC, while its input DC level is controlled setting by GND. By varying FBK, the output DC level is chosen to adjust dynamic range and to equalise the response of individual chips in multi-chip assemblies to some extent. IKRUM limits the leakage current compensation and also determines the time the output pulse takes to return to zero.

Discriminators

The two energy thresholds of the Medipix2 are implemented by means of two identical discriminators, into which the output of the preamplifier is fed. Their output current, whose gain is controlled by DISC, is low if the input voltage is below the threshold voltages and high otherwise. Thus, the output of the two discriminators is related to the collected input charge, which is made use of in the Timepix chips. Low and high threshold voltages are controlled by 2x2 DACs responsible for coarse and fine-tuning ($\mathrm{THL_{coarse}}$, $\mathrm{THH_{coarse}}$, THL & THH). These thresholds are set globally for a chip rather than per pixel. Hence, in order to minimise threshold variation among the pixels and to compensate for inhomogeneous voltage distributions across a chip, each of the thresholds can be fine-tuned by a three bit DAC, which can be chosen individually for each pixel. The magnitude of how these DACs affect the threshold voltages is controlled by THS, which controls their dynamic range. Optimising the values of these DACs is called threshold equalisation and will be discussed in detail in section 4.6.

Double Discrimination Logic

The double discrimination logic (DDL) follows the two discriminators and offers two modes of operation: The single threshold mode, where $V_{\mathrm{THH}} < V_{\mathrm{THL}}$ and every event above the low threshold increments a counter, and the dual threshold or window mode, where $V_{\mathrm{THH}} \geq V_{\mathrm{THL}}$, and events resulting in voltages in-between the two thresholds are counted. The length of the

Sidebar 4.2 The Charge Sensitive Amplifier

A charge sensitive amplifier provides an output voltage that depends on the charge at the amplifier's input. The charge Q_s generated in the sensor with capacitance C_d is distributed among the charge Q_d remaining in the sensor and the charge Q_i flowing towards an inverting voltage amplifier with gain $-A$. Assuming an infinite input resistance, no current will pass the amplifier, and all of Q_i must end up at the feedback capacitance C_f, hence $Q_i = Q_f$. For the voltage difference at the amplifier, i.e. the voltage at C_f, we get $U_f = U_i - U_o = U_i(A+1)$, and thus the charge at the feedback capacitance is $Q_f = C_f U_f = C_f(A+1)U_i$. For the amplifier's voltage output per input charge we then obtain:

$$\frac{U_o}{Q_i} = \frac{AU_i}{C_f(A+1)U_i} = \frac{A}{C_f(A+1)} \approx \frac{1}{C_f} \,. \tag{4.21}$$

The component influencing this charge gain is therefore the feedback capacitance C_f. The ratio of the measured to the total charge generated Q_s is:

$$\frac{Q_i}{Q_s} = \frac{Q_i}{Q_d + Q_i} = \frac{C_f(A+1)U_i}{C_d U_i + C_f(A+1)U_i} = \frac{1}{1 + \frac{C_d}{C_f(A+1)}} \,. \tag{4.22}$$

Hence, in order to obtain a ratio that is close to 1, $C_f(A+1)$, called the dynamic input capacitance, must be large compared to the sensor capacitance.

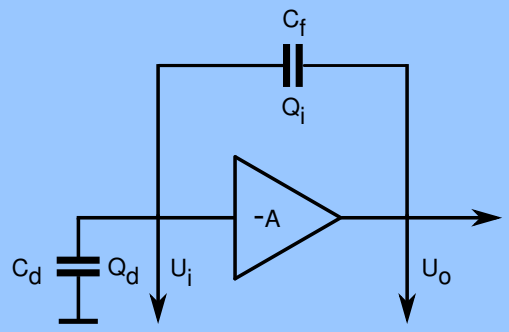

Figure and text adopted from Spieler (2006).

DDL's output pulse is controlled by DELAYN, which was again left at its default value for all of the following measurements. Resulting is a dead time is about 1 µs for a 60 keV photon.

For all the studies performed in this chapter, only the thresholds along with the FBK and THS DACs were chosen differently to their default values.

4.4 Cadmium Telluride as Sensor Material

CdTe is a direct semiconductor with a band gap of 1.56 eV at 300 K. Compared to Si (1.11 eV) and Ge (0.67 eV), this value is rather large, and therefore CdTe is often referred to as a wide-bandgap semiconductor or even a semi-insulator. This property is useful in radiation detectors, where it allows operation at room temperature. Among the materials listed above, it also offers by far the best absorption due to the high atomic numbers of Cd ($Z = 48$) and Te ($Z = 52$). Unlike Si and Ge, CdTe has been used far less in technical applications in the past and is therefore understood only poorly.

CdTe is characterised by a comparably low hole mobility. Characteristic values for the $\mu\tau$-products are $3{\cdot}10^{-3}\,\mathrm{cm}^2/\mathrm{V}$ for electrons and $2{\cdot}10^{-4}\,\mathrm{cm}^2/\mathrm{V}$ for holes (Spieler 2006). However, the high anode segmentation leads to an increased injection of free charge carriers into the sensor, interacting with the signal charge. Greiffenberg et al. (2011) determined values of $1.9 \cdot 10^{-3}\,\mathrm{cm}^2/\mathrm{V}$ and $7.5 \cdot 10^{-5}\,\mathrm{cm}^2/\mathrm{V}$, respectively, for a pixel pitch of 110 µm.

We will later see that a typical voltage to operate a 1 mm thick CdTe sensor is about 400 V. With this and (4.7), we obtain average drift lengths of about 7.6 cm for electrons and 0.3 cm for holes. Hole tailing should therefore not play a *dominant* role for sensors thinner than 3 mm. These values need to be contrasted to Si and Ge, for which $\mu\tau$-products greater than one can be measured for detector-grade single-crystals, amounting to drift lengths in the order of 100 m for both charge types.

The maximum photon flux Φ^* (4.15) requires the knowledge of the detrapping rate τ_D, which depends on the CdTe crystals employed. No generally accepted value exists which could give us a proper estimate of Φ^*[2], instead values are usually determined experimentally. Depending on the detector thickness, they usually range from 10^8 to $10^6\,\mathrm{mm}^{-2}\,\mathrm{s}^{-1}$.

The CdTe sensors used with the two detectors to be described below stem from wafers which are commercially available from a company named Acrorad (Uruma City, Japan). These single-crystals represent the state of the art of high resistivity, detector-grade material and are commercially available with a diameter of 75 mm and various thicknesses. The crystals were grown by the travelling heater method (THM), which offers the advantage of a low growth temperature that reduces the concentration of defects and increases homogeneity. Characterisation of these wafers at FMF obtained a homogeneous distribution of the resistivity with an average value of $5 \cdot 10^9\,\Omega{\cdot}\mathrm{cm}$ and a variation of less than 10 %. Tellurium inclusions were identified by infrared microscopy with an average diameter of less than 10 µm and a concentration of about $10^4\,\mathrm{cm}^{-3}$.

The quality of the CdTe sensors used on the detectors to be described below leads to visible defects on the resulting images. The size of these defects both depend on the magnitude of the bias voltage and the time it has been switched on. Hence, in order to obtain reproducible results, the bias voltage was applied at least four hours prior to measurements. Prior to lowering the bias voltage, it was switched off to avoid hysteresis effects that otherwise would have occured (section 4.13).

4.5 Features of the Medipix2 Readouts at DKFZ

The two Mpix2MXR20s employed at DKFZ at the time of writing were fabricated as so-called Quad and Hexa detectors. These are multi-chip arrays comprising 2×2 and 3×2 individual chips with sensitive areas of $2.8{\times}2.8\,\mathrm{cm}^2$ and $4.2{\times}2.8\,\mathrm{cm}^2$, respectively.

More important to these detectors than their size is the effective area of their pixels. Although the Medipix2 ASICs (application specific integrated circuits) offer a fixed pixel pitch of 55 µm only, larger pixels can be implemented in multiples of 55 µm by connecting only a subset of the pixels to the sensor. This must not be understood as an electronic binning of the pixels in some manner, but purely as an omission of the bump bonds necessary for a pixel to receive a signal from the sensor. Upon readout, these non-connected pixels still act as a separate entity, although they will show no signal (provided they are working properly). The pixel pitches achieved in this manner for the Quad and Hexa systems used are 110 µm and 165 µm, and the total numbers of connected pixels are 65,536 and 44,376, respectively. The two detectors therefore allow to study the effects of different pixel sizes on the energy response function (ERF), that is the response of the detector-sensor combination to monochromatic radiation.

[2]Private communication with Alex Fauler, FMF Freiburg.

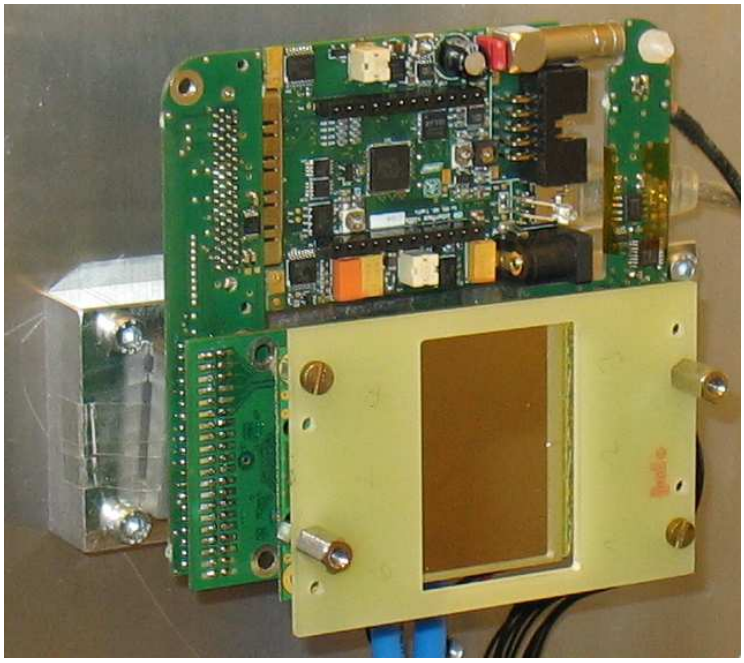

Figure 4.2 The Hexa detector with its CdTe sensor (bottom) and the USB interface (top).

A picture of the Hexa device and a sample X-ray image are shown in Figs. 4.2 & 4.3. It was the detector most extensively used for the following investigations due to its larger pixel pitch and sensitive area, and with the exception of a few cases, all results will be reported for this device only. It operates at a supply voltage of 2.5 V and an average current of 1.6 A, thus consuming about 4 W of power. The exact values for current and power depend on the count rate and therefore on the threshold values applied. The leakage current was measured to be around 70 µA for a bias voltage of 350 V, i.e. a little more than 10 µA per chip. This is about one order of magnitude less than what would be expected from the resistivity of $5 \cdot 10^9\,\Omega$·cm given in the previous section. The difference supposedly stems from the high anode segmentation, which implies an increased injection of free charge carriers into the CdTe sensor.

The two detector systems come with unique IDs which allow easy identification. These are N05-W0799 for the Quad and C05-W0460 for the Hexa detector. All measurements described below were performed using the Medipix USB interface (Vykydal et al. 2006) and the Pixelman software (Holy et al. 2006). The USB interface takes about 0.33 s to acquire frames from a single chip, which leads to considerable readout times for the multi-chip arrays used here. Faster versions have recently been introduced (Kraus et al. 2011), but were not available to DKFZ yet.

4.6 Low Threshold Equalisation

4.6.1 Recording Photon Spectra with the Medipix2

In principle, the window mode can be used to obtain spectroscopic information about the incident X-rays. However, the energy window must not be chosen too small as each pixel's response to radiation varies even after threshold equalisation. This means, the smaller the window size, the higher the chance that the voltage determining a pixel's upper threshold gets below the one defining the lower threshold. As a consequence, the pixel changes from dual to single threshold mode. This leads to a minimum window size of a few keV, which would be too much for a variety of tasks. For this reason, the recording of spectra with a high resolution, which is a requirement

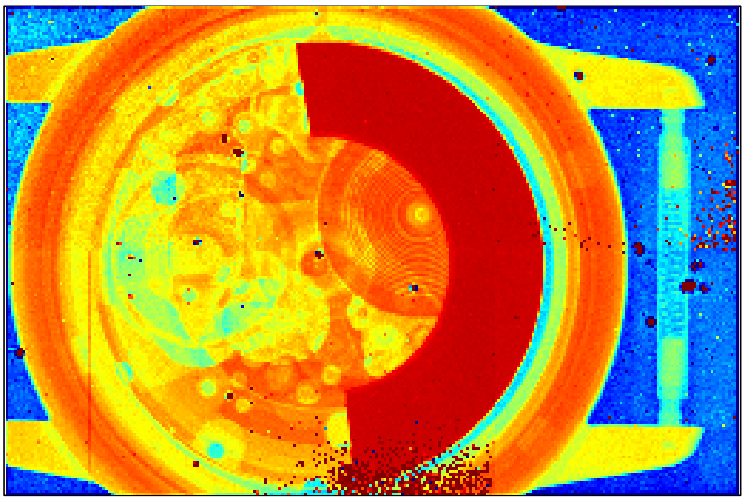

Figure 4.3 One of the first images acquired with the Hexa detector at DKFZ with the lower threshold set to about 80 keV, showing a metal watch ($U = 200$ V). The defective areas on the bottom and on the right are due to broken bump bonds. The red clusters (zero counts) distributed across the image are caused by defects in the CdTe sensor and grow with the bias voltage. All in all, these sensor defects seem well controlled. The spiral close to the centre shows aliasing. The rather noisy appearance in the upper left is due to an instability of chip 5, which tends to "forget" its threshold adjustment values when the supply voltage deviates from its required value even slightly (by about 50 mV).

for threshold equalisation, is done by scanning in single threshold mode across the energy range of interest, yielding an integrated spectrum. This spectrum is then differentiated to obtain the actual photon energy spectrum. Fig. 4.4 shows an example of this procedure.

As we are dealing with discrete data, the differentiation that we just spoke of is in fact a difference quotient implemented by the linear filter [-0.5 0 0.5], meaning that the filtered value at position THL will be the one at THL - 1 minus the one at THL + 1, divided by two.

Differentiating data is unfortunately very prone to noise, as we will now illustrate. Taking a look at Fig. 4.4, we find that the number of counts N_{THL} in the integral scan changes only slowly with the THL value. Assuming Poisson noise, we get a standard deviation of $\sqrt{N_{\mathrm{THL}-1}} \approx \sqrt{N_{\mathrm{THL}+1}} \approx \sqrt{N_{\mathrm{THL}}}$, and by means of error propagation we obtain a standard deviation of $\sqrt{2N_{\mathrm{THL}}}$ for the differential value, i.e. a signal that has about 41% more noise than the original one. Because this signal is only very small due to the small differences in the number of counts, the signal-to-noise ratio deteriorates dramatically upon differentiation.

We can see from the above argument that a subsampling of the data, i.e. choosing larger THL intervals, will result in a better SNR, simply because the count difference will be larger. Hence, as long as the sampling theorem remains acceptably fulfilled, we can obtain a better SNR by choosing larger steps. From our analyses, a sampling rate of 1 / keV (rather than 5 / keV which is possible using the default DAC values) is easiliy compatible with this requirement, and this greatly reduces acquisition times. It needs to be stressed that this comes without any additional lowpass filtering.

Understanding data acquisition now, we can take a look at the actual message of Fig. 4.4: the influence of the 3-bit adjustment values on the spectra recorded. Given that lower thresholds cannot be set for individual pixels, but only for whole chips, we need these bits to adjust each pixel's response in a way that will make them as homogeneous as possible across a chip. Before we discuss how these adjustments are done, we first take a look at how the dynamic range of the adjustment values has to be chosen to give optimal coverage.

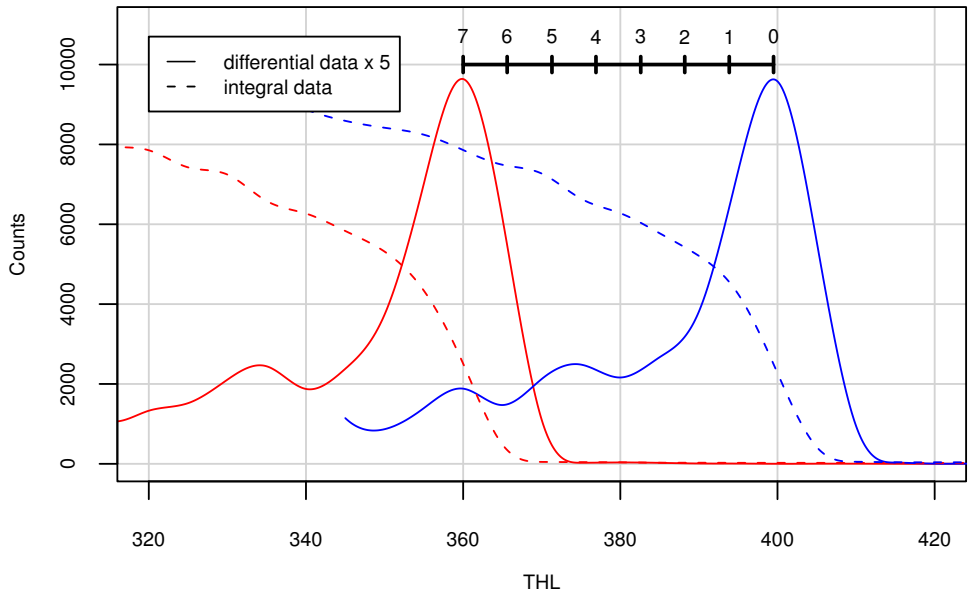

Figure 4.4 Single pixel spectra of an ^{241}Am source aquired in single-threshold mode by scanning the lower threshold DAC THL, and the resulting (negative) derivative showing the actual photon spectra. The two measurements belong to the extremes of the lower threshold adjustment values. As we will find out in section 4.8, five THL values roughly correspond to 1 keV.

4.6.2 Choosing the Optimal Dynamic Range

From Fig. 4.4 we learn that a decrease in adjustment value causes a shift of the spectra to higher THL values (when counting electrons, as in the case of CdTe sensors). The magnitude of this shift is determined by the value of the THS DAC: While it does not influence pixels with an adjustment value set to 7, the spectra of those with lower adjustment values will be shifted more and more the higher the THS value. Hence, the lower its value, the smaller the range covered by the eight possible adjustments. It is therefore necessary to determine the THS value that will result in the lowest possible deviation of peak positions after threshold equalisation. In principle, this can be done by a Pixelman plug-in. Unfortunately, due to a number of bugs this was only possible when equalising the lower thresholds using the noise edge rather than X-ray spectra. Thus, the way the optimal value of THS was determined at DKFZ was by means of a Monte Carlo simulation (algorithm 4.1).

Surprisingly, the THS value of 114 determined in this manner differed significantly from the 160 obtained by the Pixelman plugin using the noise edge. Further measurements revealed that this was indeed caused by the different physical origins of the signals used for threshold equalisation: The value of 114 gave better results (i.e. a lower residual threshold dispersion) for X-rays, while the value of 160 performed better with the noise edge. The reason for this behaviour was not clear to us.

4.6.3 Determining Adjustment Values

Having found a suitable THS value, we can finally determine the adjustment values. This can be done in a variety of ways:

- Adjusting the peak positions in the differential spectra, recorded from radioactive sources, characteristic X-rays of metal foils etc (spectral equalisation, algorithm 4.2).

Algorithm 4.1 Finding the Optimal THS Value

1. Let σ_0 and σ_7 be the experimentally determined standard deviations of the peak positions across a chip for adjustment values 0 & 7, and let $\overline{\mathrm{THL}}_7$ be the mean for adjustment value 7, excluding defective pixels. We now optimise the standard deviation σ_{opt} of the residual threshold dispersion by varying $\overline{\mathrm{THL}}_0$ and letting $\overline{\mathrm{THL}}_{\mathrm{opt}} = \left(\overline{\mathrm{THL}}_0 + \overline{\mathrm{THL}}_7\right) / 2$.
   (a) Randomly sample N pixels from two independent Gaussians $\mathcal{N}_0\left(\overline{\mathrm{THL}}_0, \sigma_0\right)$ and $\mathcal{N}_7\left(\overline{\mathrm{THL}}_7, \sigma_7\right)$.
   (b) Linearly interpolate the peak positions from step 2 to give each pixel's response at adjustment values 1-6.
   (c) For each pixel, choose the adjustment value that is closest to $\overline{\mathrm{THL}}_{\mathrm{opt}}$. Determine the resulting standard deviation σ_{opt} and return it.
2. Experimentally determine the THS value that gives the above $\overline{\mathrm{THL}}_0$.

Algorithm 4.2 Adjusting Low Thresholds via Peak Positions (Spectral Equalisation)

1. Let $\overline{\mathrm{THL}}_0$ and $\overline{\mathrm{THL}}_7$ be the experimentally determined average peak positions across a chip for adjustment values 0 & 7. Let $\overline{\mathrm{THL}}_{\mathrm{opt}} = \left(\overline{\mathrm{THL}}_0 + \overline{\mathrm{THL}}_7\right) / 2$, i.e. the desired value for each pixel's peak position.
2. Linearly interpolate the peak positions to give each pixel's response at adjustment values 1-6.
3. For each pixel, choose the adjustment values that are closest to $\overline{\mathrm{THL}}_{\mathrm{opt}}$.

- Finding the THL value where a pixel starts to record the noise present in its electronics. This assumes that the noise in each pixel is constant and can be considered a special case of spectral equalisation (performed by a Pixelman plug-in).

- By acquiring homogeneously illuminated frames and optimising the adjustment values such that the standard deviation of the count rate in the resulting frames is as low as possible (homogeneity equalisation, algorithm 4.3). This can be done much quicker than spectral equalisation, since no scans are necessary, but instead a number of frames averaged is sufficient for each of the settings.

While ideal detectors should produce the same adjustment values regardless of the method chosen, we will see later that manufacturing tolerances as well as sensor defects cause differences between the various procedures. An example of the results obtained when equalising the low thresholds by scanning over the K_α fluorescence of silver is shown in Fig. 4.5, where we find that the standard deviations of the peak positions can typically be reduced by a factor of 4. The residual threshold dispersion of 2.5 THL values roughly corresponds to 0.5 keV.

Algorithm 4.3 Adjusting Low Thresholds via Image Homogeneity (Homogeneity Equalisation)

1. Let $\overline{I}_0$ and $\overline{I}_7$ be the experimentally determined average intensities across a chip for adjustment values 0 & 7. Let $\overline{I}_{\text{opt}} = \left(\overline{I}_0 + \overline{I}_7\right) / 2$, i.e. the desired intensity for each pixel.
2. Linearly interpolate the intensities from step 2 to give each pixel's response at adjustment values 1-6.
3. For each pixel, choose the adjustment values that are closest to $\overline{I}_{\text{opt}}$.

4.6.4 Spatial Patterns in the Adjustment Values

When plotting adjustment values, no matter which method is used to obtain them, a dependence on the pixel position can be observed (Figs. 4.6 & 4.7). This led us to an inspection of the images acquired for the two extremes of the adjustment values (0 and 7), where we found a corresponding decrease of the mean count numbers. Interestingly, this was more pronounced for the measurements with the adjustment values set to 0. These, in turn, are influenced by the THS value set. Consequently, we believe that this effect is caused by a drop in the voltage supplying this and the THL DAC along the Medipix chips. As this observation was also made for the noise measurements with the bias voltage switched off, we can exclude the possibilty of sensor inhomogeneities as the cause for this. Also, a similar finding has already been reported by Procz et al. (2009) for a single Medipix2 chip with a silicon sensor.

4.6.5 Differences Among the Various Techniques and X-Ray Energies Used

We will now take a look at how important the differences are between the methods listed in section 4.6.3. Furthermore, we will investigate if there are significant changes if the energy of the X-ray photons is altered.

For the spectral alignment techniques, silver and tantalum foils were placed in front of a Siemens Powerphos X-ray tube operated at 120 kVp. The detector itself was arranged to be outside the primary beam to ensure that the recorded images would be dominated by the fluorescence photons. A bias voltage of 350 V was applied without an active high threshold. The noise measurements were performed with a Pixelman software plug-in. All the comparisons with these noise measurements were performed using the connected pixels only.

Homogeneity equalisation was performed for two different settings of the X-ray tube voltage, 40 kVp and 120 kVp, with the lower threshold being set to roughly 27 keV. 100 frames were averaged for each of the two settings in order to obtain a high SNR.

To determine whether the equalization procedures above differ significantly in their results, the crucial quantities are the adjustment values produced. Consequently, we compare the relative differences among them for the various strategies. Here, one has to bear in mind that even two measurements performed with the same method will not produce exactly the same adjustment values, as there is always some random component involved, caused by noise and a non-constant behavior of the pixels over time. In order to account for this, each measurement was also supplemented by an additional one as a reference.

The reason for this behavior was found to be related to readout rather than sensor, as it was also present in the noise measurements without the bias voltage turned on (and thus without

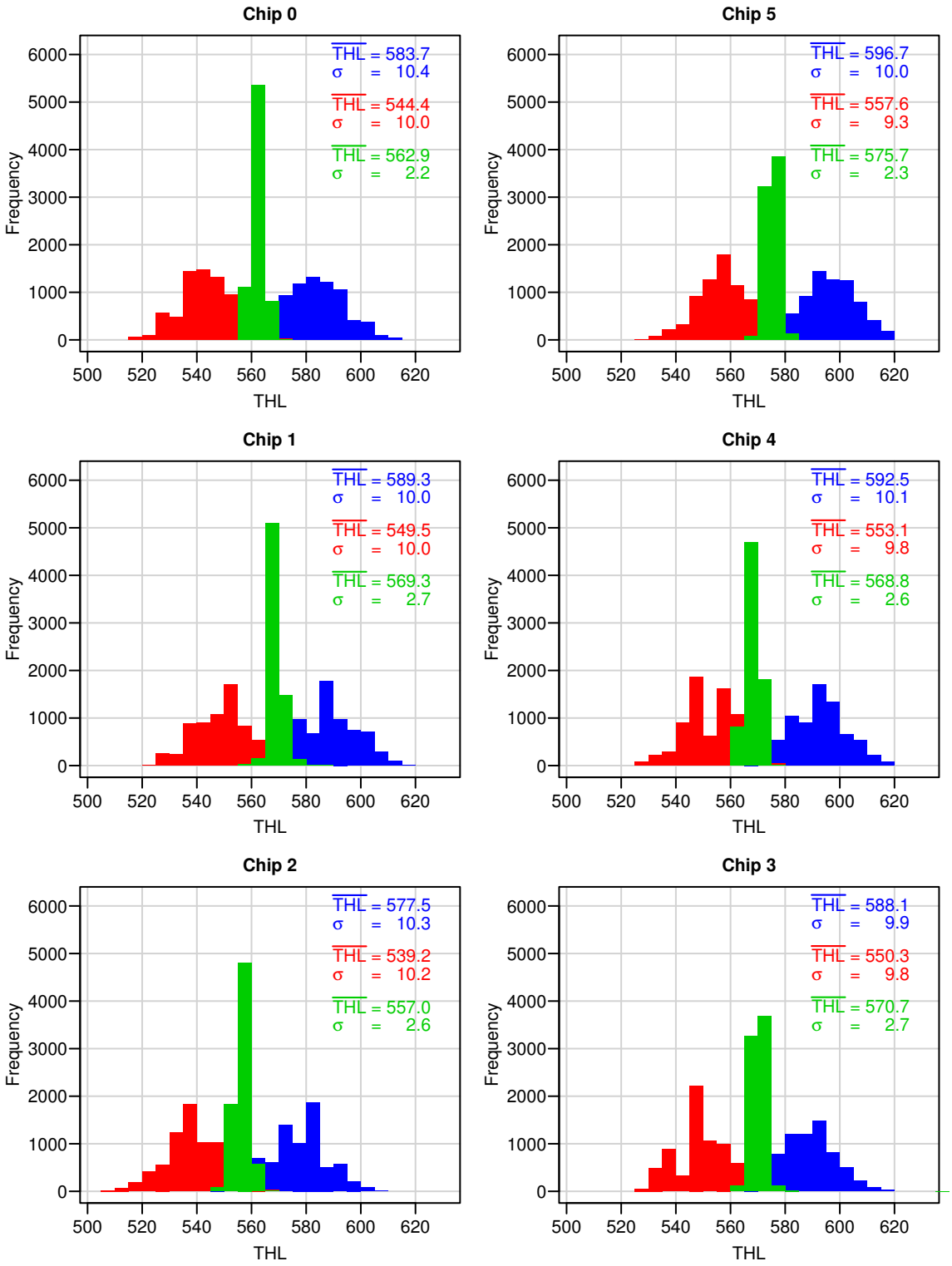

Figure 4.5 Results of a threshold equalisation performed with fluorescences excited in a silver foil by means of an X-ray tube. The red data correspond to setting all adjustment values to 7, the blue ones to values of 0. The green distribution represents a recording with optimised adjustment bits. It is important to note here that the standard deviations shown do not correspond to peak widths, but to the deviations of the fluorescence maxima among all the pixels of a chip.

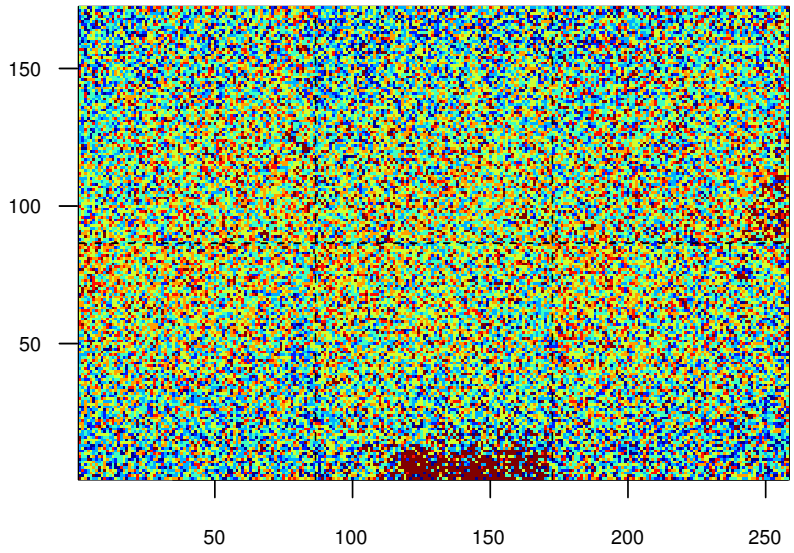

Figure 4.6 Adjustment values obtained from the measurements shown in Fig. 4.5 (red colour: 7, blue colour: 0). On average, the adjustment values decrease with increasing distance to the central axis. Defective pixels like those at the bottom were set to 7 by default.

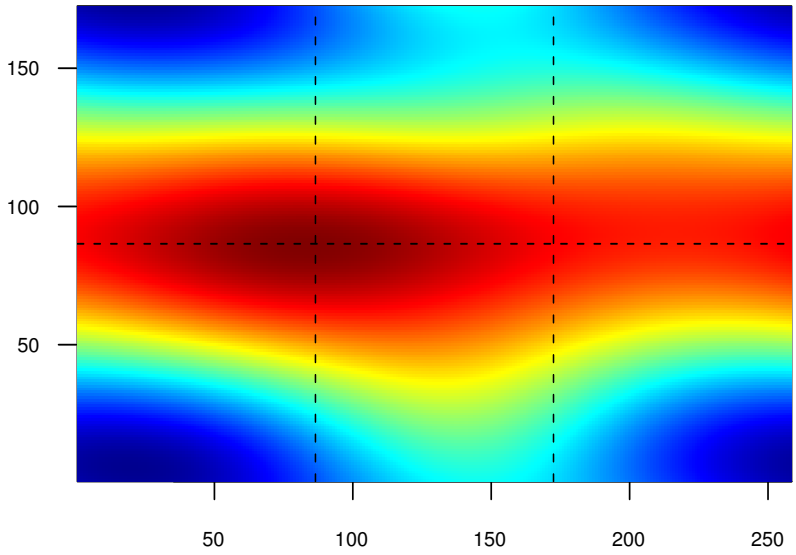

Figure 4.7 As in Fig. 4.6, but heavily lowpass filtered with periodic boundary conditions.

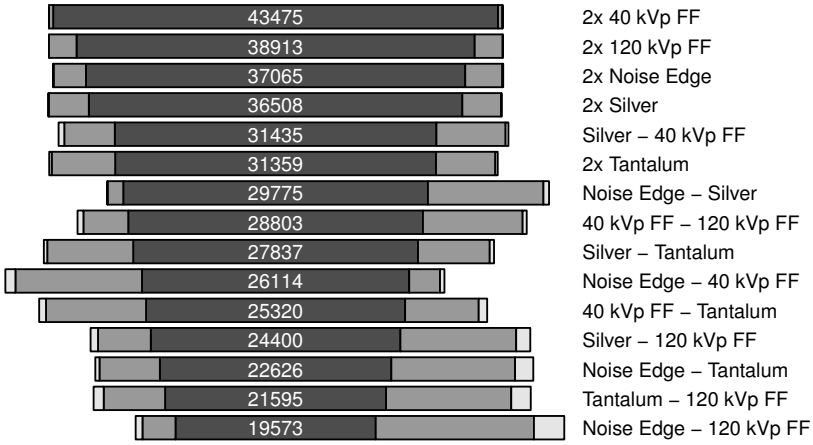

Figure 4.8 Differences between adjustment values for the various methods (FF: flat-field). Those that were assigned the same value are given in the centre. Note that some of the distributions are highly asymmetric. Other differences than those shown were found for only a very small number of pixels. The three shades correspond to 0, ±1, and ±2, respectively.

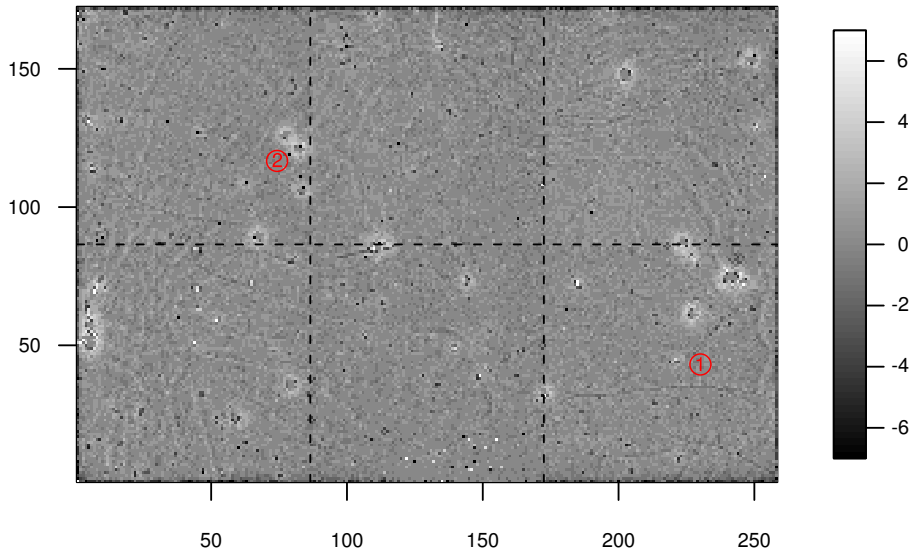

Figure 4.9 Differences between the silver and 120 kVp flat-field adjustment values. The chip boundaries are indicated. Various sensor defects can be spotted such as the one below the mark labeled (1), along with some halos around non-working areas (2). While images acquired with the spectral equalisation methods leave these features intact, those based on homogeneity will remove them from the resulting images as far as permitted by the 8-bit accuracy. The occurrence of these defects is responsible for the asymmetric distributions shown in Fig. 4.8.

any leakage current influencing the measurements). Whether its origin has to be attributed to the Medipix ASICs themselves or electrical glitches on the circuit boards employed is currently unclear. During a Medipix collaboration meeting in November 2010 at CERN, it was controversly discussed whether the component density of the Medipix2 ASICs is already small enough to make thresholds jump to different values if a charge is trapped by a defect present at a transistor's gate, and attributing this to our findings here remains a hypothesis.

The comparison of the various techniques is depicted in Fig. 4.8. It shows the number of pixels that differ in their adjustment values by a certain amount[3]. In general, the numbers of those deviating by ±3 or more were found to be very low and are therefore not shown.

It can be seen that the adjustment values produced by the flat-fields exhibit the highest agreement between two measurements, followed by those obtained by scanning over the K_α peak of silver (22.4 keV). It is striking that the measurements employing the tantalum line (57.5 keV) are less reproducible, although a similar SNR was measured.

Concerning the role of the noise measurements, it can be stated that only about one third of the pixels exhibit different adjustment values when compared to those obtained using silver K_α X-rays. This number increases to about one half when a comparison with tantalum K_α X-rays is performed, and is also well above the difference between the two tantalum measurements. We can therefore observe an energy dependence in the adjustment values, which is also visible for the two flat-field measurements. However, whether this discrepancy is relevant in imaging applications has yet to be determined.

The choice a user has to make should be the choice between spectral and image homogeneity equalisation. As can be seen in Fig. 4.8, the differences between the two groups is larger than within them, which is not surprising given the fact that the latter aims at removing the influence of assembly defects from the resulting images. This can be illustrated by considering the difference between the adjustment values obtained for the silver and the 120 kVp flat-field measurements, where crystal inhomogeneities become visible (Fig. 4.9). Even then, more than one half of the total number of pixels (24 K out of 44 K) exhibit the same values, and so the effect of the two equalisation strategies should not have an overwhelming effect on the overall spectral resolution per chip and mostly be concentrated around macroscopic defects.

4.6.6 Recommendations

As X-ray imaging applications with Medipix assemblies mainly concentrate around small animal imaging and mammography so far - both employing rather low photon energies - it will probably be sufficient for most users to perform a threshold equalisation with a photon energy roughly located at the average of the energies considered. For these kinds of applications, it is also typical to perform flat-field corrections. As our investigations have shown, even images using one of the homogeneity equalisation methods will require an additional, conventional flat-field correction performed in software in addition to the one used for choosing the adjustment values, since their 3-bit accuracy is too coarse to make this step obsolete. The question then arises if homogeneity equalisation should be performed at all. In our opinion, this question deserves an affirmative answer for imaging applications as the adjustment values produced hereby can be obtained much quicker and their stability was found to be significantly higher than for the spectral equalisation methods.

4.7 High Threshold Equalisation

4.7.1 Determining Adjustment Values

Lacking a mode where only the high threshold is active, the means by which it has to be equalised differ from the ones above by the fact that a value for the low threshold needs to be set at all times. Again, we can think of three methods:

[3] Measurements performed by Marcus Zuber.

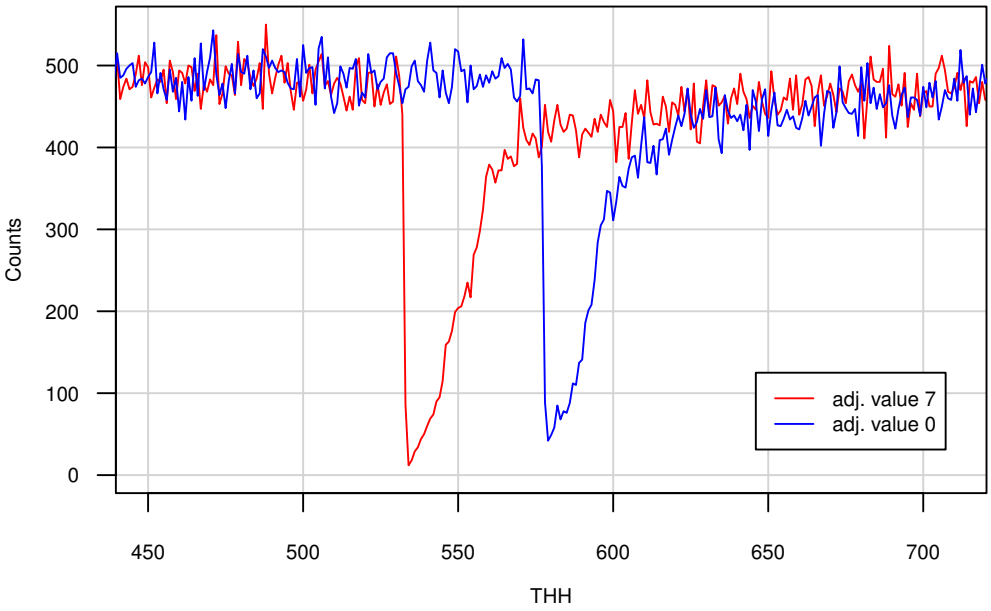

Figure 4.10 Raw data obtained for a single pixel when scanning the high threshold over the mode change point for adjustment values 0 & 7. Upon switching from single to dual threshold mode, the count number drops rapidly and then increases again, as the growing energy window records more and more photons.

- By setting the low threshold below an X-ray peak, scanning the high threshold over this peak and differentiating the resulting data again gives rise to some form of spectral equalisation. Unfortunately, this requires extremely long acquistion times to gain a high enough SNR, and hence this approach will not be followed here.
- Scanning the high threshold over the low one will cause a pixel to switch between single and dual threshold modes, which will be visible as a sudden drop in intensity at the mode change point (Fig. 4.10). Adjustment values can then be set to achieve homogeneous mode change points across the chip.
- Equalisation through image homogeneity (as before).

4.7.2 Differences between the Various Techniques

We have already explained that the window mode cannot be used to properly acquire high resolution spectra, and so its only use is the acquisition of images. Consequently, optimising image homogeneity seems the method of choice here. We were therefore interested in how well equalisation via mode change could keep up with homogeneity equalisation, i.e. how the standard deviations of flat-fields would be affected by either of the two methods.

The answer to this question can be found in Fig. 4.11, where it becomes very obvious that equalisation using the mode change will produce a high amount of image noise[4]. Note, however, that even homogeneity equalisation will produce standard deviations that are about two to three times higher than what would be expected from Poisson statistics (cf. chip 2, for instance, which shows an only small number of outliers). This is again a result from residual threshold dispersion and can be further reduced by performing a conventional flat-field correction in software.

[4]Measurements performed by Marcus Zuber.

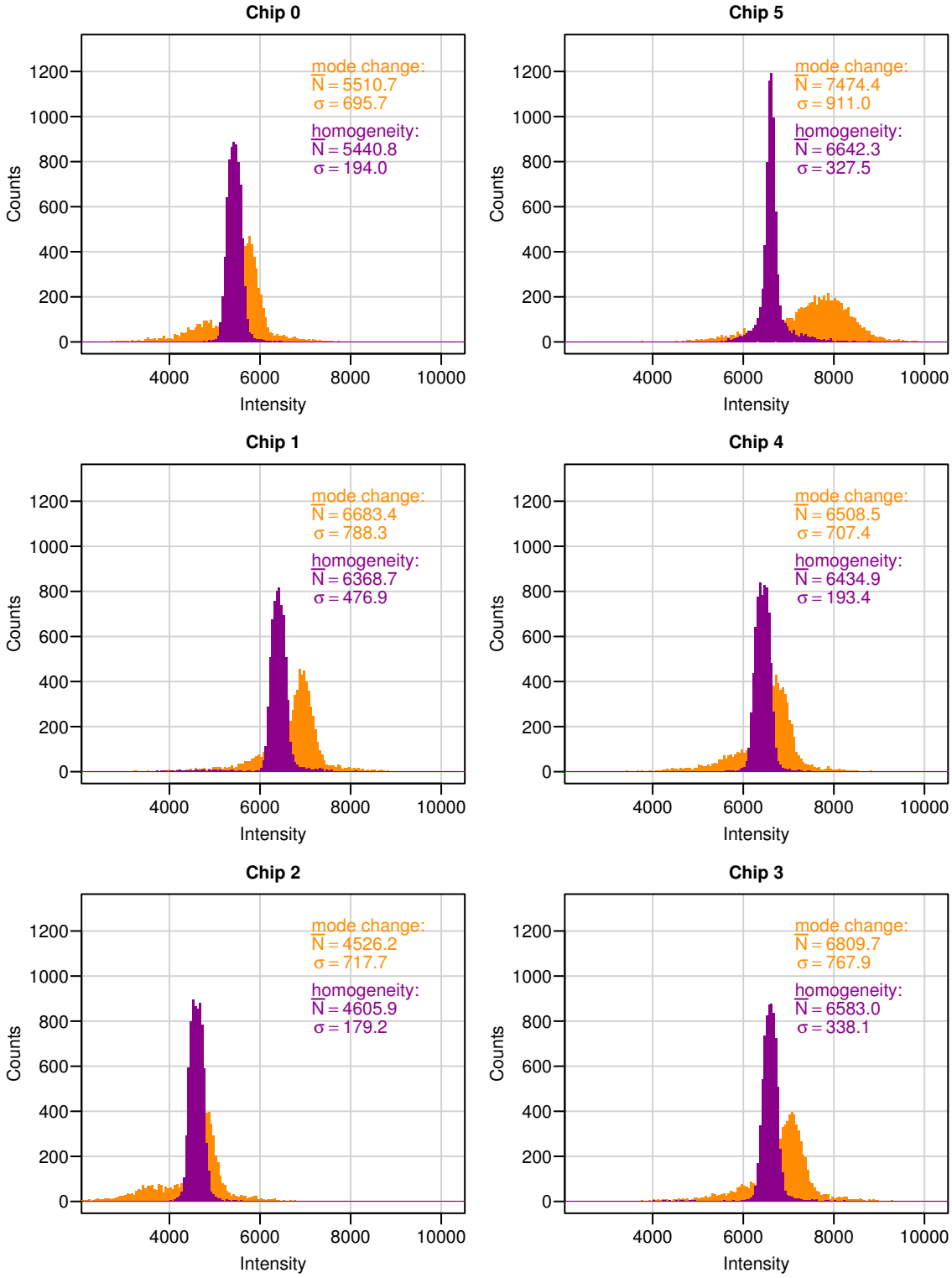

Figure 4.11 Comparison of two methods to equalise the high thresholds: optimising image homogeneity or equalising the switching point between single and dual threshold modes. No defective pixels were excluded to allow a fair comparison, and hence the standard deviations vary significantly among the six chips. However, by looking at the distributions it becomes clear that the mode change method cannot be used to produce images with a high SNR. The different appearance of the distributions of chip 5 is due to the same glitch already encountered in Fig. 4.3.

Sidebar 4.3 Kernel Density Estimation
Fitting a linear relationship between threshold value and photon energy, we can consider each pixel's calibration curve $\boldsymbol{x}_i = (b_i, m_i)$ with intercept b_i and slope m_i as a manifestation of a random variable $X = (B, M)$. We now seek an estimate $\hat{f}_X(\boldsymbol{x})$ of the the unknown probability density function (PDF) $f_X(\boldsymbol{x})$ generating all these calibration curves. The way this is done in kernel density estimation is by modelling $\hat{f}_X(\boldsymbol{x})$ as the convolution of the empirical distribution $\hat{F}$ with a kernel ϕ_λ:

$$\hat{f}_X(\boldsymbol{x}) = \frac{1}{N}\sum_{i=1}^{N}\phi_\gamma\left(\boldsymbol{x}-\boldsymbol{x}_i\right) = \left(\hat{F}\star\phi_\lambda\right)(\boldsymbol{x})\ , \tag{4.23}$$

where N is the number of pixels and λ denotes a parametrisation of the kernel ϕ_λ. In the very popular choice of a Gaussian for ϕ_λ, λ represents the standard deviation. In other words, the estimated PDF at point $\boldsymbol{x}$ is simply a weighted mean of the distribution measured (Hastie et al. 2001).

4.8 Energy Calibration

Energy calibration can be performed using a variety of methods, all of which have in common that photon spectra with well defined peak energies are recorded. For a pixelated detector, one has to bear in mind that, in principle, every pixel needs to be calibrated on its own. However, for any system known to this author, energy thresholds can only be set globally (i.e. per chip for the Medipix2) rather than on a single pixel level. Then, two methods can be distinguished:

- calibration per pixel and taking some representative values for intercept and slope of the resulting calibration curve as the calibration per chip, or
- calibration on the average spectra per chip.

Below, we will take a look at both of these methods, but before we do so, we have to point out a peculiarity affecting the energy calibration for pixelated anode geometries: Due to charge sharing (section 4.2.7), peaks are shifted to lower energies depending on pixel size, bias voltage and photon energy. These shifts have to be determined in Monte Carlo simulations (Durst et al. 2008) and are typically in the order of 0.5 - 1 keV (Koenig et al. 2010).

However, one might wonder if this approach is really the way to go. Setting energy thresholds, one probably would like to assign those threshold values to the events recorded that actually represent the corresponding photons, rather than those that one would get from a hypothetical detector calibration with charge sharing "switched off". Consequently, proceeding without the correction of peak energies seems more reasonable, and this is what we will do throughout this thesis. Due to the dependence of charge sharing on X-ray energies, however, it introduces non-linearities into the calibration curves. As the underlying deviations are small, we will neglect them and use linear relationships for detector calibration. Readers looking for a highly precise energy response function should keep this in mind, though.

With the lack of means to set thresholds for individual pixels, we need to develop a way to combine calibrations from individual pixels to one that gives reliable data for whole chips. Taking the average parameters from the calibration curves can be a bad idea in the presence of a lot of defective pixels, but before we will introduce alternatives, we will first discuss a way to properly visualise all these parameters. While plotting individual data points in two dimensions might be feasible for a small number of pixels, this certainly does not result in descriptive figures for the

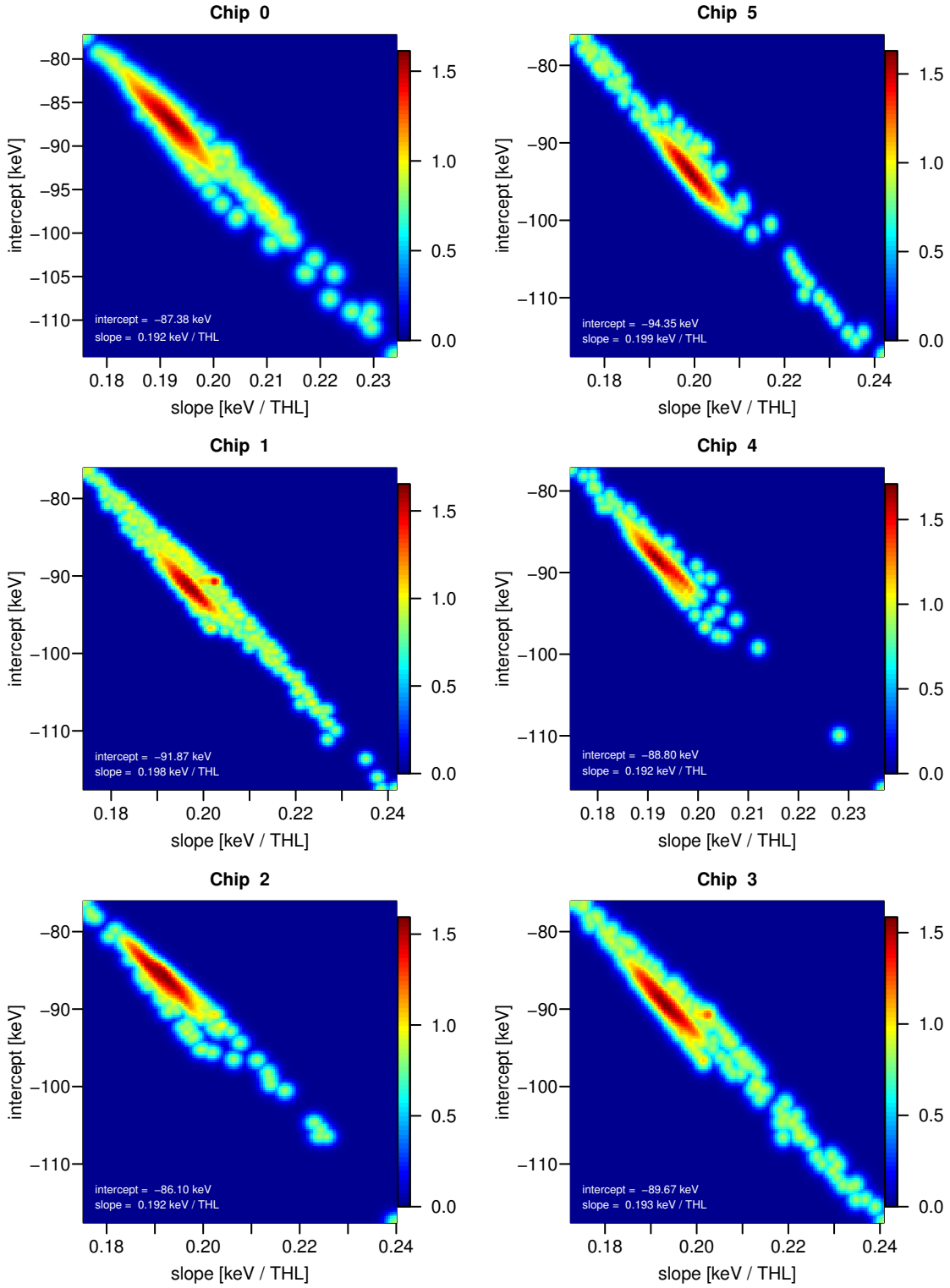

Figure 4.12 Kernel density estimation of the intercept-slope pairs obtained when performing an energy calibration on individual pixels. The well separated dots represent outlier pixels. Obviously, the two parameters are not statistically independent. The colour scale codes for the value of the PDFs (sidebar 4.3), and the positions where the PDFs are at their maximum values are indicated in the figures. The defective bump bonds from chip 1 and 3 can be clearly recognised if one compares them to chip 4, for instance.

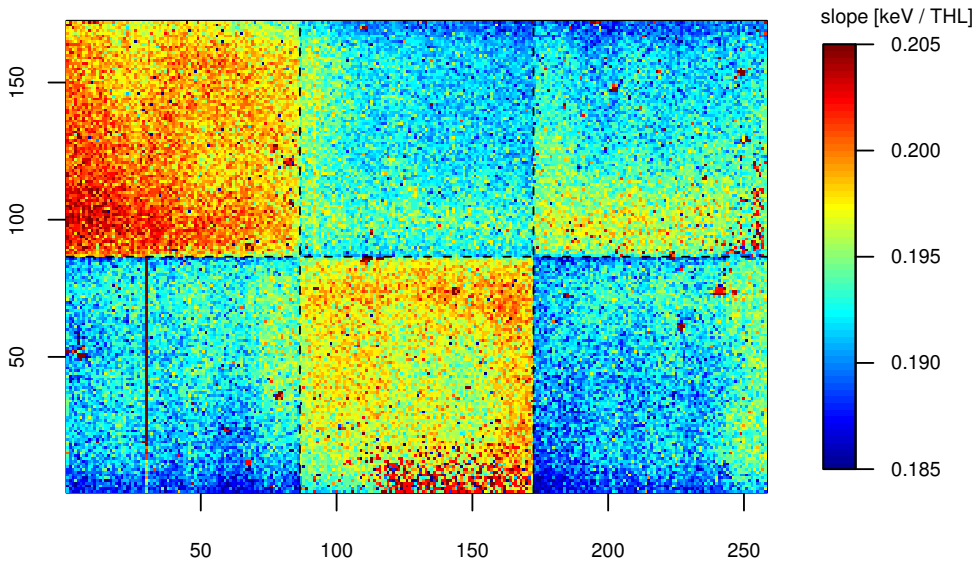

Figure 4.13 Map of the calibration curve's slope. The deviations present among the chips are likely to be caused by residiual variations in the preamplifier gain.

7396 pixels we encounter in a single chip of the Hexa detector. A way to solve this is to perform a Gaussian kernel density estimation (KDE, sidebar 4.3), that is an estimation of the probability density that a pixel x_i will be calibrated with intercept b_i and slope m_i.

The KDE of a calibration using the fluorescene peaks of molybdenum (17.5 keV), silver (22.2 keV) and the photopeak of an ^{241}Am source (59.6 keV) is shown in Fig. 4.12, where it can be seen that healthy pixels cluster around a well defined centre[5]. Defective pixels lie further off and can severly bias the average values of intercept and slope if present at a high number. A more robust way to obtain reliable calibration data is by taking those pairs of (b, m) where the maximum of the PDF occurs, as this is way less affected by outliers. Consequently, the respective values for the slope indicated in the figure are very similar. The small differences here are due to tiny variations in the preamplifier gain. The values for the intercept depend on the voltage set by FBK and thus vary stronger.

A very clear indication that these deviations are determined by the readout electronics rather than the sensor is given in Fig. 4.13, since the spatial patterns visible in it basically end at chip borders. As we have seen, calibration on a single pixel level can give interesting insights into how all the pixels behave. From a practical point of view, however, this method offers no advantage to calibration on average chip spectra. Our investiagations have shown that this second method gives calibration curves comparable to the ones above, and unless data such as those from Fig. 4.13 are required, it should be preferred for simplicity. Thus, for all the following analyses, we will pursue this approach instead, and rely on three peaks present in the spectrum from an ^{241}Am source: the photopeak itself (59.57 keV), the Cd K_{α_1} line (23.17 keV) and its associated escape peak (36.40 keV). The corresponding K_{α_2} transition is about half as intense and in a very close vicinity to the K_{α_1} line. Given the finite energy resolution that we will determine in the next section, they cannot be resolved, shift the measured peak positions insignificantly and can therefore be safely ignored. The Te K_α peaks are situated right after the Cd absorption edge, are thus only poorly visible (Table 4.1) and hence their escape peaks are also weaker. Therefore, we will not use these peaks for energy calibration.

[5] Code implemented by Patrick Schünke.

Sidebar 4.4 The Fano Factor
A detector's spectral resolution crucially depends on the fluctuations in the free charge generated by an ionising event. Naively, one would expect that these fluctuations are determined by Poisson statistics, yielding a variance $\sigma_Q = \sqrt{N_Q}$. However, this does not take into account the fact that phonon excitations also play a role in these interactions, and hence σ_Q is actually *smaller* than in the previous relation. Denoting the average phonon excitation energy by W_x, the average ionisation energy again by W and the minimum by $W_{\min}$, a photopeak's FWHM is given by the following relation:

$$\Delta E = 2.35\sqrt{kW} \cdot \sqrt{\frac{W_x}{W_{min}}\left(\frac{W}{W_{\min}} - 1\right)} \equiv 2.35\sqrt{kWF}\ , \tag{4.24}$$

where the expression under the second square root is called the Fano factor F. It is about 0.1 for Si and Ge (Spieler 2006) and about 0.15 for CdTe (Takahashi et al. 2002). The lower bound for the peak width is therefore smaller than what would be expected when ignoring phonon excitations. For CdTe and a photon energy of 60 keV, we obtain a FWHM of about 0.47 keV, assuming $W = 4.4$ eV (Sellin et al. 2006).

4.9 Energy Response Functions

We will now discuss the effect of the pixel size on the ERF, starting with the 165 µm of the Hexa detector and continuiung with the 110 µm of the Quad. Along with this, we will determine the effect of the bias voltage using settings of 200, 300, 400 and 500 V. Given a sensor thickness of 1 mm as used on both detectors and assuming the sensors to represent ideal parallel plate capacitors, these voltages correspond to maximum field strengths of $2{\cdot}10^5$ to $5{\cdot}10^5$ V/m. Due to sensor defects, polarisation effects and electrode configuration, the actual field shapes are of course more complicated.

ERFs were measured using a strong ^{241}Am source with a nominal activity of 1.11 GBq (Eckert & Ziegler, Berlin, Germany). It was additionally embedded in a Cr-Ni stainless steel housing (material code 1.4301), which was chosen to exhibit no absorption edges above 10 keV to avoid any impact on the ERF recorded. ^{241}Am additionally emits photons with an energy of 26.4 keV, which lie very close to the Te K_α line, but which are absorbed much stronger in the thin source containment made from tungsten than the relevant 59.6 keV peak. The tungsten shielding emits L-series peaks, with significant intensities occuring only below 10 keV. These photons are again mostly absorbed in the tungsten itself.

165 µm Pixel Pitch

We begin with discussing single pixel spectra, which are shown for a 3 × 3 neighbourhood and a bias voltage of 500 V in Fig. 4.14. It shows pixel spectra that were normalised to equal count number and aligned with respect to each other. While the photopeak around 60 keV is clearly visible, other effects depending on the pixel pitch severly distort the energy response: these are mostly the fluorescences along with their escape peaks, but also the combined charge sharing & hole tailing background. This means, whatever energy window is chosen during imaging, photons having energies within that window will partially split up into multiple events registered at lower energies, and the energy window set will also receive these pseudo-events caused by higher energy photons.

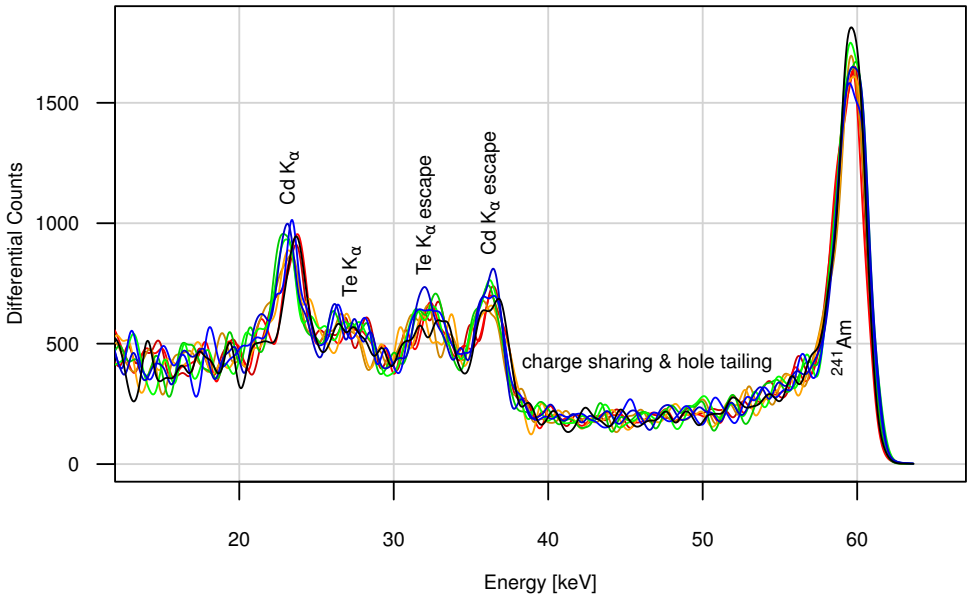

Figure 4.14 Single pixel spectra in a 3× 3 neighbourhood for a pixel pitch of 165 µm and a bias voltage of 500 V, aligned and normalised to equal integral count number. The curves show spline interpolants to lowpass-filtered data.

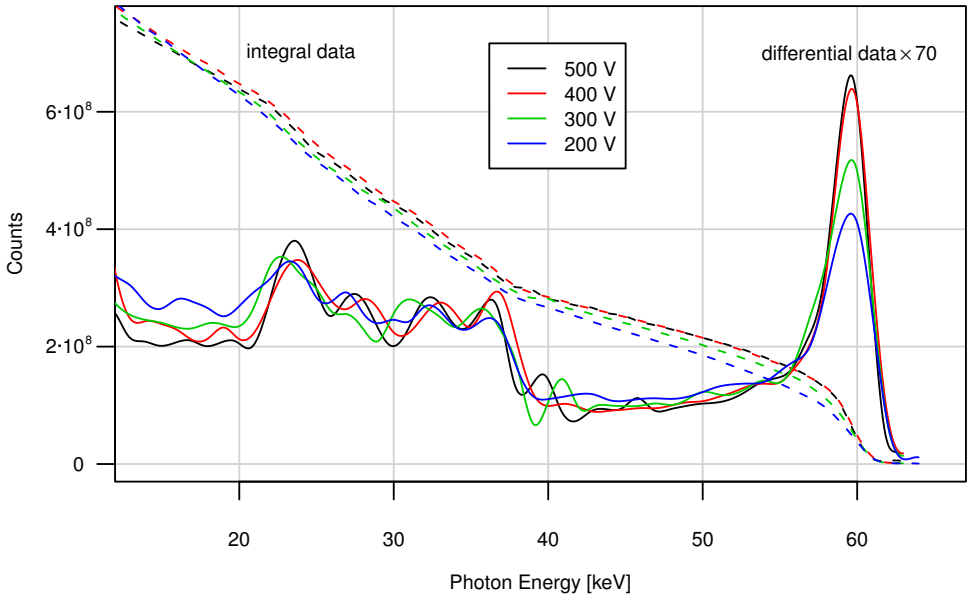

Figure 4.15 ERF obtained when summing up all pixel spectra for chip 4 as a function of the bias voltage. Note that these curves depend on the outcome of the low threshold equalisation.

pixel pitch	$FWHM_{200V}$ (keV)	$FWHM_{300V}$ (keV)	$FWHM_{400V}$ (keV)	$FWHM_{500V}$ (keV)
165 µm	2.57 ± 0.45	2.25 ± 0.26	2.22 ± 0.26	2.17 ± 0.22
110 µm	3.65 ± 0.39	2.49 ± 0.28	2.37 ± 0.22	2.28 ± 0.20

Table 4.2 Medians and standard deviations of the photopeaks' FWHMs obtained for individual pixels at a photon energy of 59.6 keV as a function of the bias voltage.

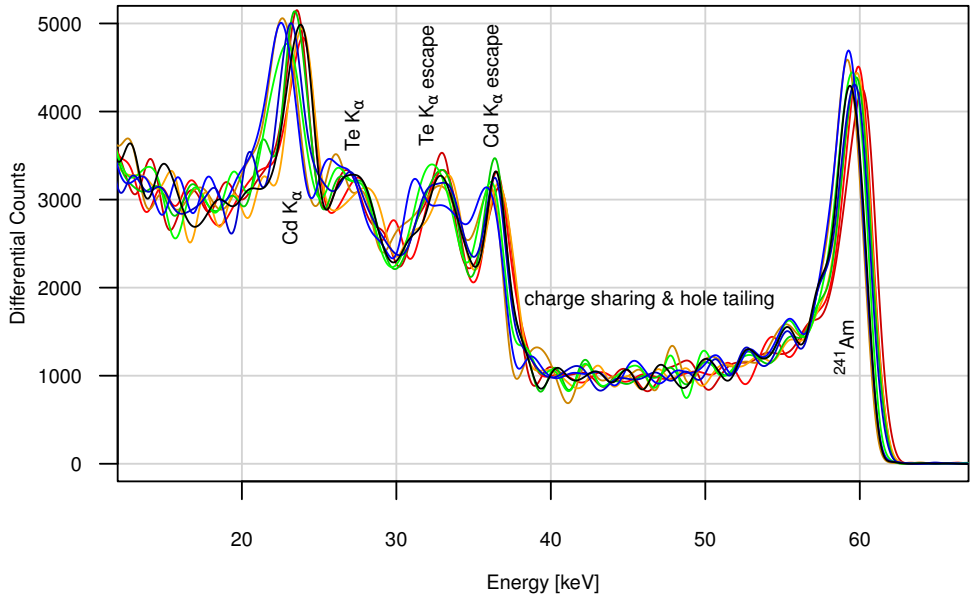

Figure 4.16 As in Fig. 4.14, but for a pixel pitch of 110 µm.

In order to investigate the effects of different bias voltages on the ERF, Gaussians were fitted to the ^{241}Am photopeaks of every single pixel to obtain their full widths at half maximum (FWHM). The results are shown in Table 4.2, where we find that a bias voltage of 300 V should be the minimum to operate these kinds of detectors if the photopeak is of relevance. For the maximum bias voltage chosen (500 V), the FWHM is about 5 times larger than the theoretical minimum (sidebar 4.4).

The same can be done for the average chip spectra depicted in Fig. 4.15, but here the results are less reliable due to the dependence on the threshold equalisation, i.e. the residual threshold dispersion illustrated in Fig. 4.5. For the measurements shown here, the adjustment values were determined separately for each voltage setting and hence they may vary in their quality. The deterioration of the photopeak at 300 V in Fig. 4.15 is probably due to this effect, as it is not confirmed by the peak widths listed in Table 4.2. The values we found for the FWHMs here range from about 2.9 keV at 200 V to roughly 2.5 keV at 400 V and 500 V.

110 µm Pixel Pitch

The results determined for the 110 µm pixel pitch of the Quad detector are very much in line with what has been reported in the last section for 165 µm, although the average peak widths are slightly larger (Table 4.2). Again, using a bias voltage of 200 V results in a comparably broad photopeak. The corresponding ERF is shown in Fig. 4.16, and as expected, the height of the photopeak decreases at the cost of fluorescences and charge sharing when compared with the larger pixel pitch.

Although it is tempting to explain the increase in the low energy tail by charge sharing, the occurance of fluorescences is probably responsible for most of the deterioration of the photopeak. Hence, we cannot tell from the present measurements if hole tailing is indeed negligible (cf. section 4.2.5).

Both pixel pitches investigated exhibit a strong distortion of the ideal Gaussian photopeaks due to charge sharing, hole tailing and sensor fluorescences. This is indeed a severe problem for quantitative spectroscopic imaging as illustrated in Fig. 4.17, where a measured spectrum of a

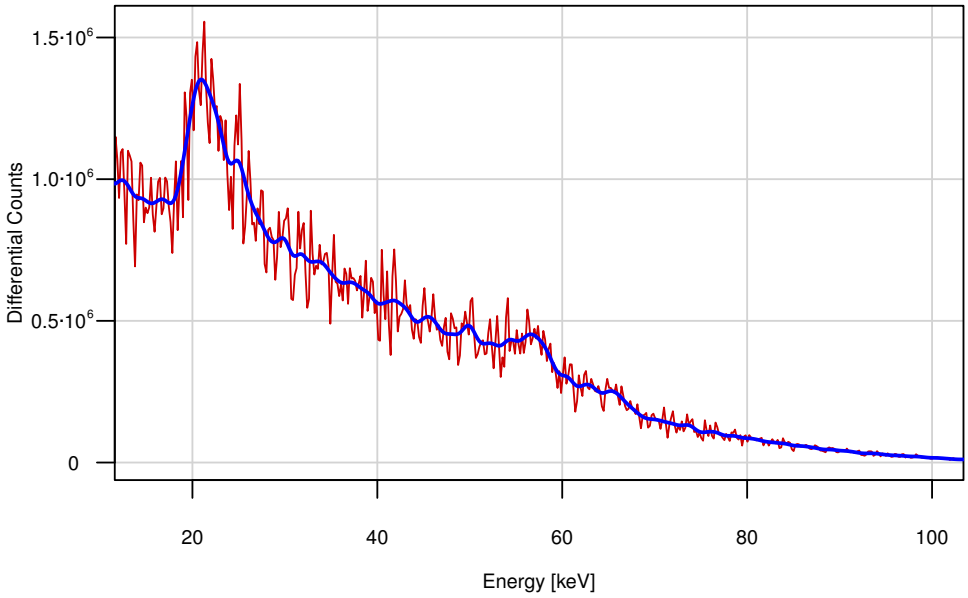

Figure 4.17 Spectrum of a Siemens Powerphos X-ray tube operated at 110 kVp, measured with a pixel pitch of 165 µm and obtained by summing up all pixel spectra for one of the six chips of the Hexa detector. Red line: Raw data after differentiation, sampled in 0.2 keV steps; blue line: low-passed filtered version ($\sigma \approx 2$ keV).

medical X-ray tube is shown. It clearly demonstrates that the charge sharing background and the CdTe fluorescences distort the actual spectrum predominantly at lower energies, where almost no X-rays pass the aluminium filter (2.5 mm) built into our medical X-ray tube, but where a large pseudo-fluence is measured. The tungsten K_α line can be found just below 60 keV, whereas the K_β line is barely visible at about 67 keV. The escape peaks encountered before are now a continuum due to the broad X-ray spectrum.

Given the above results, a charge summing logic, as implemented in the Medipix3, is clearly necessary for the small pixel sizes studied here (or an inverse filtering in software). Larger pixel pitches give better spectral response, but introduce spatial aliasing, as we will see in the next section.

4.10 Presampling Modulation Transfer Functions

The spatial resolution of a detector is not just determined by its pixel pitch, but also by the charge transport properties of the sensor employed, much like a digital camera does not profit from a high megapixel number if its optics produces rather blurry pictures. The effect of this blurring is most commonly described in terms of the point spread function (PSF), which, in linear systems theory, describes the response of a system to a point-like input, for instance a photon interacting with our sensors, creating a cloud of electron-hole pairs. The broader the PSF, the more blurred an image will be. In order to assess by how much each spatial frequency ν is affected by the PSF, the modulation transfer function (MTF) is introduced as the modulus of the Fourier transform of the PSF (normalised to unity at zero frequency), giving the factor by which a certain spatial frequency is attenuated.

We are mainly interested in the MTF of the CdTe sensor without any sampling present. Determining this so-called presampling MTF ($\mathrm{MTF_{pre}}$) via the presampling point spread function ($\mathrm{PSF_{pre}}$) is non-trivial because of the large amount of material that is needed to ensure an almost

100% absorption of the photons beyond a central aperture, which introduces unavoidable geometrical distortions into measuring the $\mathrm{PSF}_{\mathrm{pre}}$. The same applies to the presampling line spread function $\mathrm{LSF}_{\mathrm{pre}}$ determined using a slit collimator.

An alternative is to measure the presampling edge spread function $\mathrm{ESF}_{\mathrm{pre}}$. The $\mathrm{ESF}_{\mathrm{pre}}$ is the response of a sensor to a an input corresponding to a Heavyside step function, which can be implemented much easier. The way this was done at DKFZ was by embedding a tungsten wedge into a plexiglass phantom[6]. The important trick to circumvent the finite pixel size is to tilt at least one border of the wedge such that it is not aligned with a pixel column or row, but crosses a number of them. This leads to an oversampling of the $\mathrm{ESF}_{\mathrm{pre}}$, since every pixel near the edge will be shaded to a different degree (Fig. 4.18). One can then obtain the $\mathrm{LSF}_{\mathrm{pre}}$ as the derivative of the $\mathrm{ESF}_{\mathrm{pre}}$, which, for homogeneous media, has the same cross-section as the $\mathrm{PSF}_{\mathrm{pre}}$. Consequently, the Fourier transform of the $\mathrm{LSF}_{\mathrm{pre}}$ is the $\mathrm{MTF}_{\mathrm{pre}}$.

There are two methods to deal with the measured $\mathrm{ESF}_{\mathrm{pre}}$: performing the above operations directly, or fitting an analytical function to the $\mathrm{ESF}_{\mathrm{pre}}$ and using the fitting parameters in analytical versions of the $\mathrm{LSF}_{\mathrm{pre}}$ and $\mathrm{MTF}_{\mathrm{pre}}$. While the first method can result in rather noisy results, the second one is model-based and may therefore not capture every detail of the $\mathrm{ESF}_{\mathrm{pre}}$. Below, we choose the latter approach to avoid noise due to the limited pixel number of our Hexa detector.

The model that we used to fit the $\mathrm{ESF}_{\mathrm{pre}}$ to our measurements (Fig. 4.18) was first proposed by Boone (1994). The model basically consists of describing the $\mathrm{LSF}_{\mathrm{pre}}$ as a linear combination of a Gaussian and a symmetrised exponential distribution:

$$\mathrm{LSF}(x) \sim 2c\sqrt{d/\pi}\,\mathrm{e}^{-d(x-x_0)^2} + a\,b\,\mathrm{e}^{-b|x-x_0|}\ . \tag{4.25}$$

Here, a, b, c d and x_0 are the parameters obtained from fitting the $\mathrm{ESF}_{\mathrm{pre}}$, which requires two additional parameters e and f:

$$\mathrm{ESF}^{\dagger}\ (x) = a\left(1-\mathrm{e}^{-b|x-x_0|}\right) + c\ \mathrm{erf}\left(d^{1/2}\,|x-x_0|\right)\ , \tag{4.26}$$

$$\mathrm{ESF}\quad (x) = \begin{cases} \mathrm{ESF}^{\dagger}(x) & \text{if } \mathrm{x} \geq \mathrm{x}_0 \\ -\mathrm{ESF}^{\dagger}(x) & \text{if } \mathrm{x} < \mathrm{x}_0 \end{cases}\ , \tag{4.27}$$

$$\mathrm{ESF}_{\mathrm{fit}}(x) = e + f\ \mathrm{ESF}(x)\ . \tag{4.28}$$

The $\mathrm{MTF}_{\mathrm{pre}}$ is then expressed as a function of the spatial frequency ν as follows:

$$\mathrm{MTF}(\nu) = \frac{c\,\mathrm{e}^{-\pi^2\nu^2/d} + a/\left(1+4\pi^2\nu^2/b^2\right)}{c+a}\ . \tag{4.29}$$

The analyitcal $\mathrm{ESF}_{\mathrm{pre}}$ depends on seven free parameters and is thus non-unimodal, so a genetic optimisation was used to obtain reliable parameter estimates. The measurements were again performed with bias voltages of 200 V - 500 V, a tube voltage of 120 kV and low thresholds set to 10, 25 and 50 keV. In order to make the results more representative, the measurements were performed at four positions distributed across the sensor surface. For each threshold value, these four measurements were interpreted as the 0%, 33%, 66% and 100% percentiles of the underlying unknown probability distributions and the central 68% intervals were determined by interpolation[7] to give an estimate of the errors involved. The tungsten wedge was placed about 5 cm in front of the sensor, 1.1 m away from the X-ray tube, to reduce the effects of a finite focal spot size (~ 0.5 mm) on the measurements as much as possible.

[6] Done by Martin Steinke.

[7] Interested readers are referred to the help on the *quantile*-function (method 8) in the statistics software package R for details (R Development Core Team 2009).

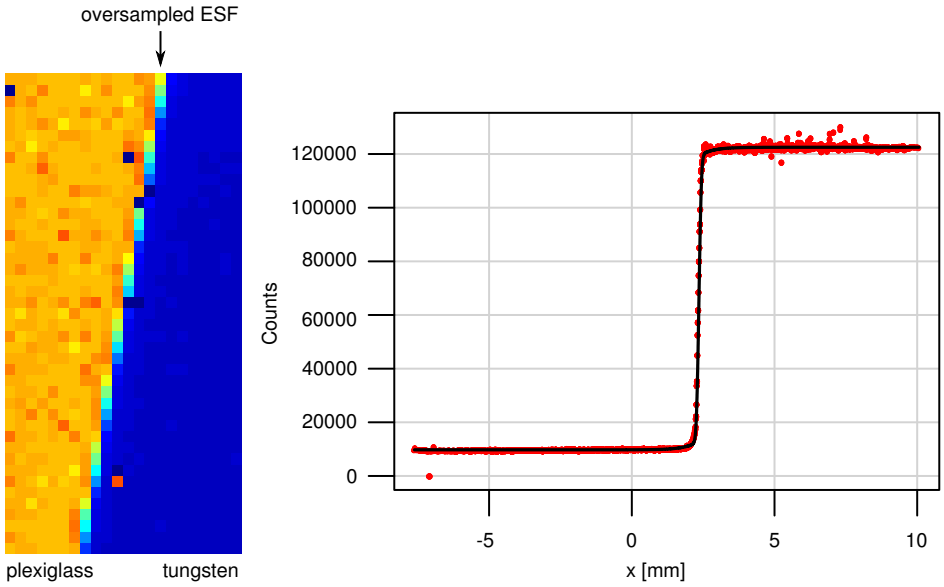

Figure 4.18 Illustration of the measurements performed to obtain the $\mathrm{ESF}_{\mathrm{pre}}$. Left: Flat-field corrected part of an image showing the tilted tungsten wedge. Right: Measured (red) and fitted (black) $\mathrm{ESF}_{\mathrm{pre}}$ according to algorithm 4.4, which also describes the edge detection procedure used here.

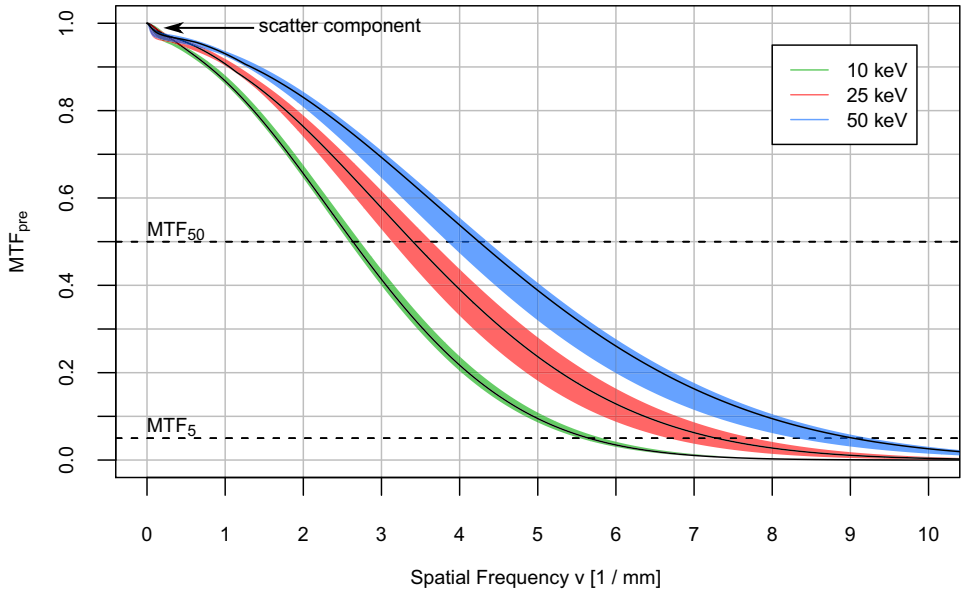

Figure 4.19 $\mathrm{MTF}_{\mathrm{pre}}$ for three values of the low threshold, a bias voltage of 500 V and a tube voltage of 120 kVp. Black lines: medians; shaded areas: 68% confidence interval of the errors in y-direction.

The results of these measurements are depicted in Fig. 4.19. They show a clear increase of the spatial resolution when the low threshold is raised. This is particular due to the removal of sensor fluorescences. Interestingly, we did not find any significant dependence on the bias voltage within the range investigated. This leads us to the conclusion that charge sharing only has a weak effect on the spatial resolution. Being unaffected by the bias voltage, fluorescences appear as the limiting factor instead, a finding that we will further support in the next section.

Algorithm 4.4 Determining the Presampling Modulation Transfer Function

1. For a number of images taken at various wedge positions, perform a flat-field correction.
2. Assume that both parts (wedge and surrounding plastic) of the image I exhibit Poisson noise with means λ_w and λ_p. For each row R_i with counts I_{ij} find the border b_i of the wedge such that it optimally separates these two Poisson distributions from each other in a maximum likelihood fashion, i.e. by minimising the negative log-likelihood $-\mathcal{L} = -\log\left[P\left(I_{ij}|b_i\right)\right]$:

$$\begin{aligned} b_i &= \arg\min_{b_i}(-\mathcal{L}) \\ &= \arg\min_{b_i}\left[\sum_{j\in\text{wedge}}\Big(\lambda_\mathrm{w} + \log(I_{ij}) - I_{ij}\log(\lambda_\mathrm{w})\Big) + \sum_{j\in\text{plastic}}\Big(\lambda_\mathrm{p} + \log(I_{ij}) - I_{ij}\log(\lambda_\mathrm{p})\Big)\right] \end{aligned}$$

3. For each pixel (i, j) in R_i, determine its distance d_{ij} to b_i. Create a two column matrix with the first column containing d_{ij} and the second one I_{ij}, both collapsed to a vector. Sort this matrix ascendingly with respect to the first column, i.e. the distances. The result contains the measured edge spread function ESF_m.
4. Fit the analytical edge spread function (4.28) to ESF_m.
5. Use the fitting parameters to obtain the presampling LSF (4.25) and MTF (4.29).

The curves also consistently show a decrease at low spatial frequencies. This can be caused by either broad-angle backscatter or scattering by the tungsten wedge itself. Control measurements with 40 kVp X-ray spectra, which are almost completely absorbed in the sensor, still showed this artifact, and therefore we can exclude backscatter as an explanation. As this effect is not very pronounced and the high frequency part of the $\mathrm{MTF}_\mathrm{pre}$ contains the information more relevant to imaging, we will now concentrate on this region in Fig. 4.19. There, we find that the MTF_5, i.e. the point where the MTF drops to 5%, is about 5.7 mm^{-1} for the 10 keV setting of the low threshold, which is very close to the noise edge of the readout electronics. The corresponding curve shows the smallest errors, because only few events are cut-off by the low threshold. Hence, it is not surprising that the above model for the $\mathrm{ESF}_\mathrm{pre}$ - which does not account for this effect - works best in this case. For the higher treshold settings, the MTF_5 increases to 7.2 mm^{-1} and 9.0 mm^{-1}, respectively. The curves show larger errors bars here due to insufficient model complexity. Still, the increase in spatial resolution is significant, and the MTF_5 increases by more than 50% when the low threshold is raised to 50 keV. Of course, this comes at the cost of a higher radiation dose to the object to be imaged, but has no analogy with conventional, energy integrating detectors.

From a sampling theory point of view, a pixel pitch of 165 µm, implying a Nyquist frequency of about 3.0 mm^{-1}, seems too large, at least for the higher values of the low threshold, where the $\mathrm{MTF}_\mathrm{pre}$ can exceed 70%. That this is indeed not only a theoretical obstacle can be seen very clearly when looking at the aliasing artifacts present in Fig. 4.3. A pixel pitch of 110 µm with a Nyquist frequency of 4.5 mm^{-1} is probably the more appropriate choice here.

All in all, we see that demanding both a good spectral and spatial resolution are conflicting interests. This becomes especially important for small animal imaging, where a high spatial resolution is a requirement and where one would like to image small blood vessels filled with a contrast agent, which in turn relies on a good ERF. Studies that aim at reconstructing pixel

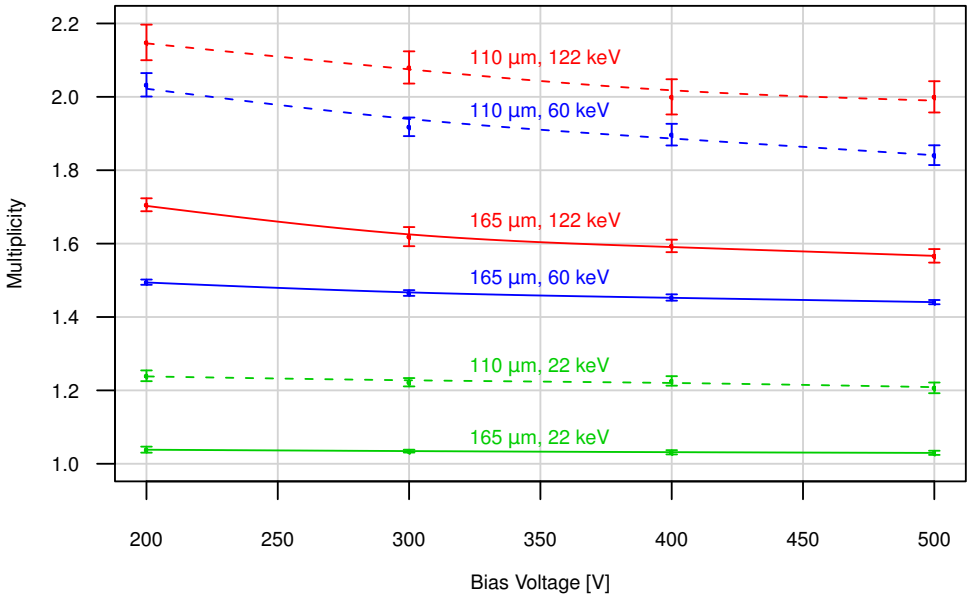

Figure 4.20 Medians of the average multiplicities per pixel as a function of the bias voltage, measured for three photon energies. The error bars denote the 95% confidence intervals, and the points were fitted with smoothing splines to guide the eye. Note that the low threshold was set to about 12 keV for these measurements.

spectra by inverse filtering (Firsching et al. 2009) suggest that indeed a small pixel pitch can be employed successfully without jeopardising spectral resolution, but to this author's knowledge the effects of this technique on the MTF and DQE (see next section) has not been studied in detail yet. The same applies to the charge summing logic introduced by the Medipix3, which inevitably leads to image distortions.

The situation is less critical when the imaging of human subjects is the main field of interest. Here, the spatial resolution can be chosen coarser, and due to the higher photon energies needed the sensor is required to be thicker (about 3 mm), potentially leading to a quicker decrease of the $\mathrm{MTF}_{\mathrm{pre}}$ due to charge sharing.

Of course, in most imaging applications the object to be imaged is not placed directly in front of the detector, but somewhere half way between X-ray tube and sensor. Due to the geometrical magnification that comes with this, the smallest structures that can still be resolved are smaller than the values reported above. Eventually, the spatial resolution obtainable in actual imaging systems delicately depends on the interplay of focus size, magnification, sensor and geometrical calibration, whose study is beyond the scope of this thesis.

4.11 Average Multiplicities & Detective Quantum Efficiencies

A figure of merit to describe the imaging performance of a detector is the detective quantum efficiency (DQE), which is a function of the spatial fequency ν and is defined as the ratio between the output $\mathrm{SNR}_{\mathrm{out}}$ and the $\mathrm{SNR}_{\mathrm{in}}$ of the incoming signal:

$$\mathrm{DQE}(\nu) \equiv \frac{\mathrm{SNR}_{\mathrm{out}}(\nu)}{\mathrm{SNR}_{\mathrm{in}}(\nu)} = \frac{q^2 G(q)^2\,\mathrm{MTF}^2(\nu)}{\mathrm{NPS}(\nu, q)} \,. \tag{4.30}$$

Here, $G(q)$ is the system gain, which relates the detector output signal to the photon density q and which can be assumed to be one in the case of photon counting detectors for photon fluxes not too high (cf. section 4.2.6). $\mathrm{NPS}(\nu, q)$ represents the noise power spectrum.

Algorithm 4.5 Determining Multiplicities

1. Record a number N of frames using an X-ray source of well defined photon energies, and choose the exposure time such that the number of events is much smaller than the number of pixels.
2. Discard all pixels with a count number greater than one.
3. For a frame interval $\mathcal{F}$ containing F frames discard all pixels showing more than f events within $\mathcal{F}$.
4. For each remaining event:
   (a) Has the event already been assigned to a cluster? If yes, proceed with the next event.
   (b) Assign the event to a new cluster. Within a radius r, assign any event to this newly created cluster, and proceed recursively with all events within r.
5. For each cluster, calculate the multiplicity and the pixel pertaining to it.
6. Remove all pixels with zero average multiplicity, as these belong to sensor defects.

For the results presented in this chapter, the following values were chosen: $N \geq 5000$, $r = 330\,\mu\text{m}$, $F = 100$ and $f = 20$.

Determining the DQE is non-trivial, as q and hence the output of the X-ray tube have to be known very precisely. Furthermore, by definition, it is a quantity defined by the noise present in an image, and hence one basically is free to choose settings such as exposure time, number of frames to be averaged and flat-field corrections. Technical standards exist, but were developed for conventional imaging devices and hence do not account for aspects like energy thresholds. Determining q in this case has to rely on simulations, which introduces a source of error. Also, estimating the NPS can be done by a variety of methods, each producing different results, and it is difficult to quantify the errors associated with these techniques.

Because of all these reasons, we will reduce the measurement of the DQE to determining its value at zero spatial frequency, i.e. $\nu = 0$. This value is often used as a single quantity to describe a detector and is called the effective quantum efficiency. Luckily, it can be measured much simpler than the full DQE. As was shown by Michel et al. (2006), it is sufficient to know the first and second order moments of the multiplicity m, that is the number of pixels responding to a single event, in order to determine the zero frequency DQE:

$$\text{DQE}(0) = \frac{\langle m \rangle^2}{\langle m^2 \rangle} \epsilon \ . \tag{4.31}$$

Here, ϵ denotes the detection efficieny, which, for very low discriminator settings, can be estimated by the percentage of photons absorbed in the sensor. Consequently, we will present the results obtained from measuring the multiplicity factor in (4.31) at a value of the low threshold set to about 12 keV[8], but we will alter the energy of the photons by again choosing the ^{241}Am used for determining the ERF, supplemented by a ^{57}Co source (122 keV) and characteristic radiation from a silver foil (22.2 keV). The detection efficiencies for ^{241}Am and ^{57}Co can be estimated using the

[8]This particular value was chosen to avoid any of the healthy pixels' thresholds to be situated below the noise edge.

110 µm			165 µm		
photon energy [keV]	$\langle m \rangle^2 / \langle m^2 \rangle$	DQE(0)	photon energy [keV]	$\langle m \rangle^2 / \langle m^2 \rangle$	DQE(0)
60	0.79	0.77	60	0.86	0.84
122	0.80	0.37	122	0.82	0.38

Table 4.3 Comparison of the ratio between first and second order moments of the measured muliplicities for the two pixel pitches studied, along with the zero frequency DQEs according to (4.31). The low threshold was set to about 12 keV and the bias voltage chosen to be 400 V.

respective absorption coefficients. For the silver fluorescence, this is not a valid strategy due to its low photon energy in combination with the threshold value chosen. It leads to a discarding of a significant amount of those events that are affected by charge sharing, and hence a detection efficiency lower than what would be expected from the corresponding attenuation coefficient. Hence, we determine the DQEs only for the higher energies provided by the two radioactive sources, using detection efficiencies of $\epsilon_{\mathrm{Am}} \approx 0.98$ and $\epsilon_{\mathrm{Co}} \approx 0.46$. The procedure[9] employed to obtain the multiplicities m is given in algorithm 4.5.

Fig. 4.20 shows the multiplicities measured for the two pixel pitches studied, where we see that the higher the photon energy and the smaller the pixels, the larger the multiplicity will be. Also, the higher the multiplicity, the greater the influence of the bias voltage. Taking the 122 keV measurements as an example, the multiplicities are less affected by photoelectric absorption than at lower energies, but show increased ranges of Compton and photoelectrons, whose trajectories are influenced by the bias voltage.

In total, the multiplicities change only slightly with the bias voltage, which confirms our finding from before that the change in the MTFpre is insignificant when the bias voltage is altered.

Table 4.3 gives the zero-frequency DQEs determined for the 400 V setting. Naturally, they decrease with increasing photon energy. What surprises at first glance is the larger value of the factor $\langle m \rangle^2 / \langle m^2 \rangle$ for the smaller pixel pitch and higher photon energy. Since this factor relates the mean multiplicity to its statistical spread, the increase just means that the multiplicities follow are relatively narrower distribution, yet centred on a higher value (Fig. 4.20).

4.12 Photon Counting Megavoltage Imaging

The discussion of MV imaging in chapter 3 suggests to investigate the performance of photon counting detectors in this energy regime, where the mass absorption coefficient is about two orders of magnitude smaller than in the energy range of medical X-ray tubes, and where photoelectric absorption can be neglected. We can disinguish two scenarios here:

- Using the full photon spectra for imaging.
- Setting an energy window in the diagnostic range and discarding all the higher energy photons.

In both cases, the MV photons will have to be detected as such, but, unfortunately, the Compton electrons exhibit a much higher kinetic energy here. As a consequence, their range will be drastically increased, and larger pixels are required than those that were studied before.

Although detectors with larger pixels were not available to us, we can give an estimate of a reasonable pixel size by again considering multiplicities. These were measured with the Hexa

[9] Implemented by Marcus Zuber.

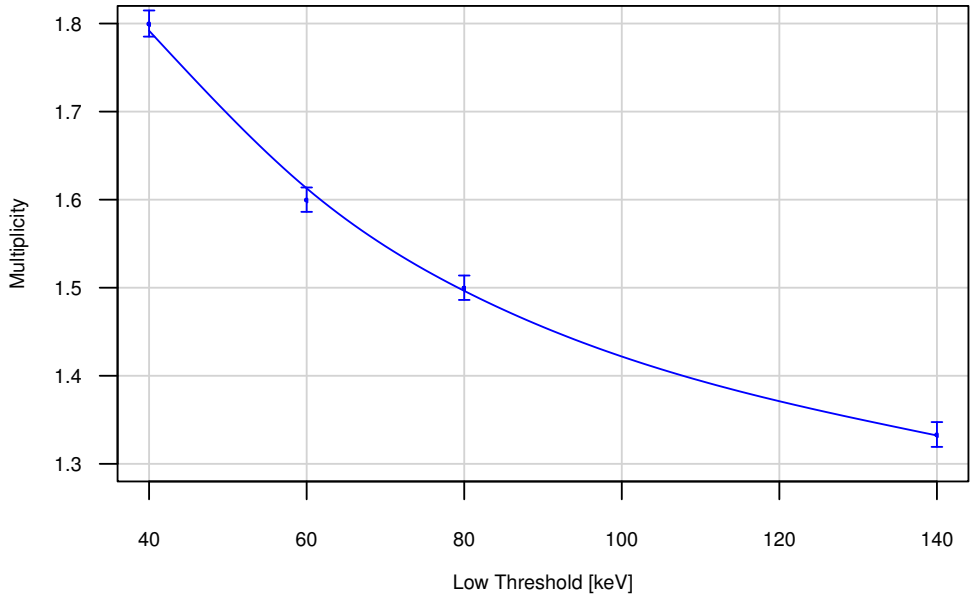

Figure 4.21 Medians of the average multiplicities per pixel as a function of the low threshold, measured for a ^{60}Co source (1.17 & 1.33 MeV photons). The error bars denote the 95% confidence intervals.

detector ($U = 400$ V) and a ^{60}Co source, which emits photons with energies of 1.17 and 1.33 MeV. Low thresholds were set to 40, 60, 80 & 140 keV to study the energy of the pseudo-events that arise from the stopping of Compton electrons. The results are shown in Fig. 4.21, where we find that these events are indeed of low energy, since the mutliplicities rapidly decrease when the low threshold is increased. From the underlying data we found that 95% of the events exhibit a multiplicity of 5 or less for the 40 keV setting, corresponding to an average diameter of 0.5 mm for each event. Hence, a pixel pitch of not much less than 1 mm would have to be chosen to properly "catch" most of the ionising events caused by the Compton electrons within a single pixel. Of course, also the sensor thickness would have to be increased to at least 3 mm.

For Medipix detectors, these two requirements pose a problem, as the remaining bump bonds would probably not be enough to hold the sensor. Still, developing detectors with a larger intrinsic pixel pitch seems an interesting option to greatly enhance the quality of MV images, because in contrast to energy integrating detectors, the contribution of the MV photons would not be weighted by their dose, but just like every other photon (or not at all by setting an appropriate energy window).

4.13 Bias Voltage Dependent Image Artefacts

Since CdTe is a material much less understood than Si, its fabrication is a lot more difficult (section 4.4). As a result, commercially available wafers are not as homogeneous as desired, and we have already encountered in Fig. 4.3 that this leads to areas that show biased or even vanishing count rates. Unfortunately, the size of these areas increases with the bias voltage, an effect which is depicted in Fig. 4.22, where we can also spot an increase of the counts at the boundaries of the dead areas. Apparently, the underlying sensor defects partially act as a dispersing lens on the charge carriers as these travel towards the readout electronics. Furthermore, the fact that the counts in the interior of these regions are zero suggest that the transport properties of the CdTe sensor, i.e. the mobility or lifetime of the charge carriers, completely break down, leading to catastrophic device failure.

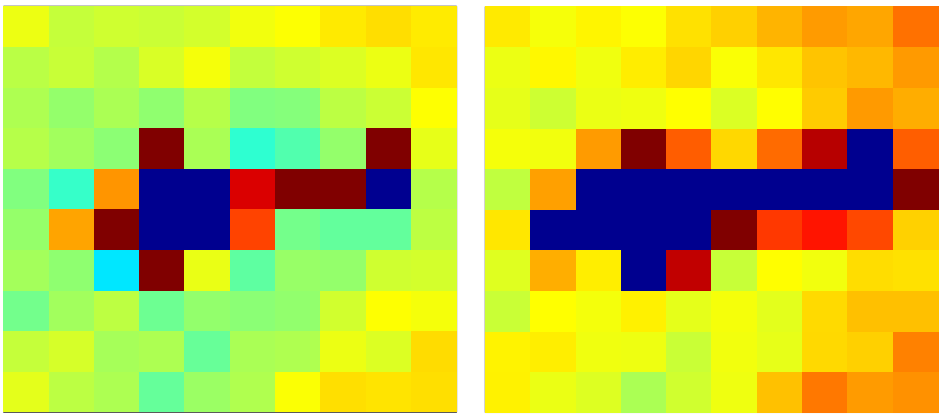

Figure 4.22 Illustration of how the magnitude of the bias voltage influences dead areas (blue: low, red: high count number).

Defects of similar appearance like those shown were reported by Sellin et al. (2008) to be caused by Te inclusions in the sensor. However, their findings indicated a *decrease* of the defect size when the bias voltage was increased, in contrast to our results. Furthermore, an analysis of a decommissoned detector performed at FMF by means of infrared spectroscopy found no correlation between Te inclusions and dead areas[10], which makes a connection between these two phenomena highly unlikely.

These dead areas are accompanied by other artefacts that also depend on the bias voltage and which can be seen in Fig. 4.23. It shows an image that has been recorded with the Hexa detector at a bias voltage of 500 V using a threshold equalisation performed at 200 V. Besides the dead areas we already encountered, it shows pronounced structures that must be caused by sensor inhomogeneities. Readers looking closely at these structures will spot a strange effect: They are formed by a pair of a black and white lines, with the white lines always being closer to the sensor boundaries. Obviously, these artefacts must stem from under- and overcompensations in the threshold equalisation, caused by some form of distortion of sensor properties when the bias voltage is altered. It is even more puzzling that these areas are much less visible in the centre of the image. Because of these two observations, we can infer that the underlying reason must be a global one rather than simple local distortions of the electric field, which would be random and unlikely to explain the clear orientation towards sensor boundaries.

One reason we could think of that would at least qualitatively explain all these artefacts is the deformation of the crystal structure by means of the piezoelectric effect. CdTe, exhibiting a diatomic basis, indeed shows such a behaviour, and it appears as an interesting hypothesis to assume that this deformation would be more chaotic around larger lattice defects, resulting in a dramatically decreased $\mu\tau$-product around them[11]. Then, the pairs of under- and overcompensated pixels would be related to a physical motion of defects across pixels, which would be zero in the centre, but more and more pronounced at outer parts, which is exactly in line with our observations. This mechanical explanation would also be compatible to our finding that there is some form of hysteresis visible in the images: Reducing the bias voltage from 500 V to 200 V was found to show more anomalies in the resulting images than increasing it from 0 to 200 V.

No matter the true origin of this behaviour, we can conclude the following: Threshold equalisation

[10] Private communication with Michael Fiederle, FMF Freiburg.

[11] As an exmaple, the reader is referred to amorphous Si here, whose $\mu\tau$-product is at least seven orders of magnitude smaller than that of crystalline Si (Spieler 2006).

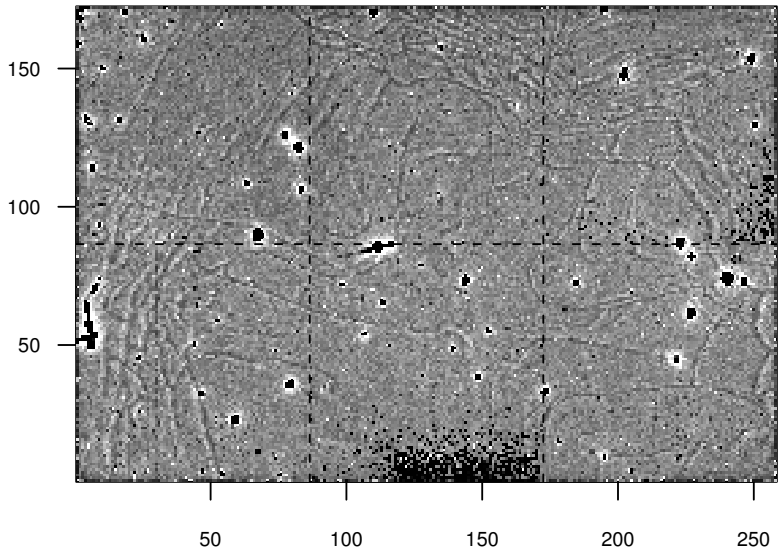

Figure 4.23 Visualisation of piezoelectric sensor deformation, obtained when performing a homogeneity equalisation of the low threshold at a bias voltage of 200 V and taking an image at 500 V. The bright and dark lines are caused by over- and undercompensations of the count rates caused by some form of distortion. Note that the contrast in this image has been enhanced.

and image acquisition should always be performed at the same bias voltage, and the bias voltage should be chosen as low as possible to avoid the growth of insensitive sensor regions, but high enough to give satisfaying charge transport properties.

4.14 Remarks on Count Rate Linearity

During our studies, the shaping time of the detector turned out to be the limiting factor on the count rate rather than detector polarisation. How can we know? When increasing the output of our X-ray tube, we found the resulting images to exhibit both the expected non-linearity of the count rate as well as fixed pattern noise, which got stronger and stronger until the number of counted events eventually broke down. The exact tube current where both phenomena were observed could be effectively shifted to higher values by increasing the IKrum DAC, responsible for controlling the return-to-zero time of the preamplifier[12]. This rules out sensor polarisation as the main cause for this saturation effect. We conclude: When the detectors that we studied are operated in their default configuration (only for this case all the above results are valid) it is signal pile-up instead of sensor polarisation that limits the maximum achievable count rates.

4.15 A First Application: Spectral CT

The heavily biased ERF (section 4.9) for both pixel pitches studied raises the question whether the performance of a CdTe sensor will be sufficient for spectral CT. While this is certainly not true for any quantitative measurements without further processing of the spectra, qualitative results, e.g. indicating the presence of an absorption edge caused by a contrast agent in a certain tissue volume may be enough for many applications. For this reason, a phantom was constructed[13] to

[12] Increasing this value implies broader photopeaks, which we have not investigated further so far.
[13] Joint work with Armin Runz and Julia Schulze.

Sidebar 4.5 Principal Component Analysis
Principal component analysis (PCA) performs a transformation into a coordinate system where no covariances (or correlations) exist between the random variables (e.g. the spectral channels shown in Fig. 4.24) of a dataset. This essentially reduces to finding a coordinate transformation which diagonalises the corresponding covariance matrix. The resulting principal components (images in our case), sorted by their variances, allow to assess the relevance of the different processes contributing to image formation. In other words, PCA helps to find so-called latent images (among many other methods). Principal components with smaller variances often only contain noise, and hence PCA can be considered a form of dimensionality reduction (Hastie et al. 2001).

contain conrast agents made from iodine (I) and gadolinium (Gd). These two materials exhibit absorption edges at 33 and 50 keV. Being able to see both edges hence requires a tube voltage significantly exceeding 50 kVp, which means that a large part of the recorded photon spectrum will not only be affected by charge sharing, but also by the escape continuum. It is therefore interesting to study if the iodine K-edge will still be visible.

The phantom constructed had a thickness of 1.4 mm and exhibited inserts for six concentrations of both I and Gd, each again for two diameters (0.8 and 1.6 mm). The tube voltage was set to 70 kVp and all measurements were performed with the Hexa detector, i.e. a pixel pitch of 165 µm. The concentrations chosen were 472.8 µmol/ml, 236.4 µmol/ml, 118.2 µmol/ml, 47.3 µmol/ml, 23.6 µmol/ml and 11.8 µmol/ml. The phantom was placed about 50 cm from the detector and 86 cm from the X-ray focus. 150 projections were recorded at angular intervals of 1.2° in window mode at energies set to 25-30 keV, 35-40 keV, 42-47 keV and 52-57 keV.

The corresponding CT reconstructions[14] are shown in the first two rows of Fig. 4.24. They exhibit some artefacts supposedly stemming from beam hardening, non-constant pixel responses and a poor geometric calibration, but the main message is very clear: Despite the ERF, both the K-edges are visible very clearly for the higher concentrations. What surprises is the fact that apparently iodine seems to be more visible at low concentrations despite the lower absorption; whether this is due to some odd effect of the ERF or because of an erroneous choice of the agent's concentration could not be resolved so far. Still, the very good visibility of both edges is almost surprising given all the charge sharing and escape events.

The first two components of a principal component analysis (sidebar 4.5) are depicted in the last row of Fig. 4.24. The first component, showing the similarity of the contrast agents below any absorption edge, exhibits even less noise than the original images. This changes for the second component, which clearly disinguishes the two substances.

The reconstructed absorption coefficients for the plexiglass part, which are essentially equal to that of water, are all significantly smaller than the expected values[15]. This implies that more events seem to enter an energy window by means of charge sharing, fluorescences and escape than actually leave it towards lower energies. This is consistent with the multiplicity measurements from section 4.11 and means that - despite energy discrimination - a Hounsfield calibration will still be necessary when relying on raw data.

[14] Measurements performed with Julia Schulze.
[15] http://physics.nist.gov/PhysRefData/XrayMassCoef/ComTab/water.html

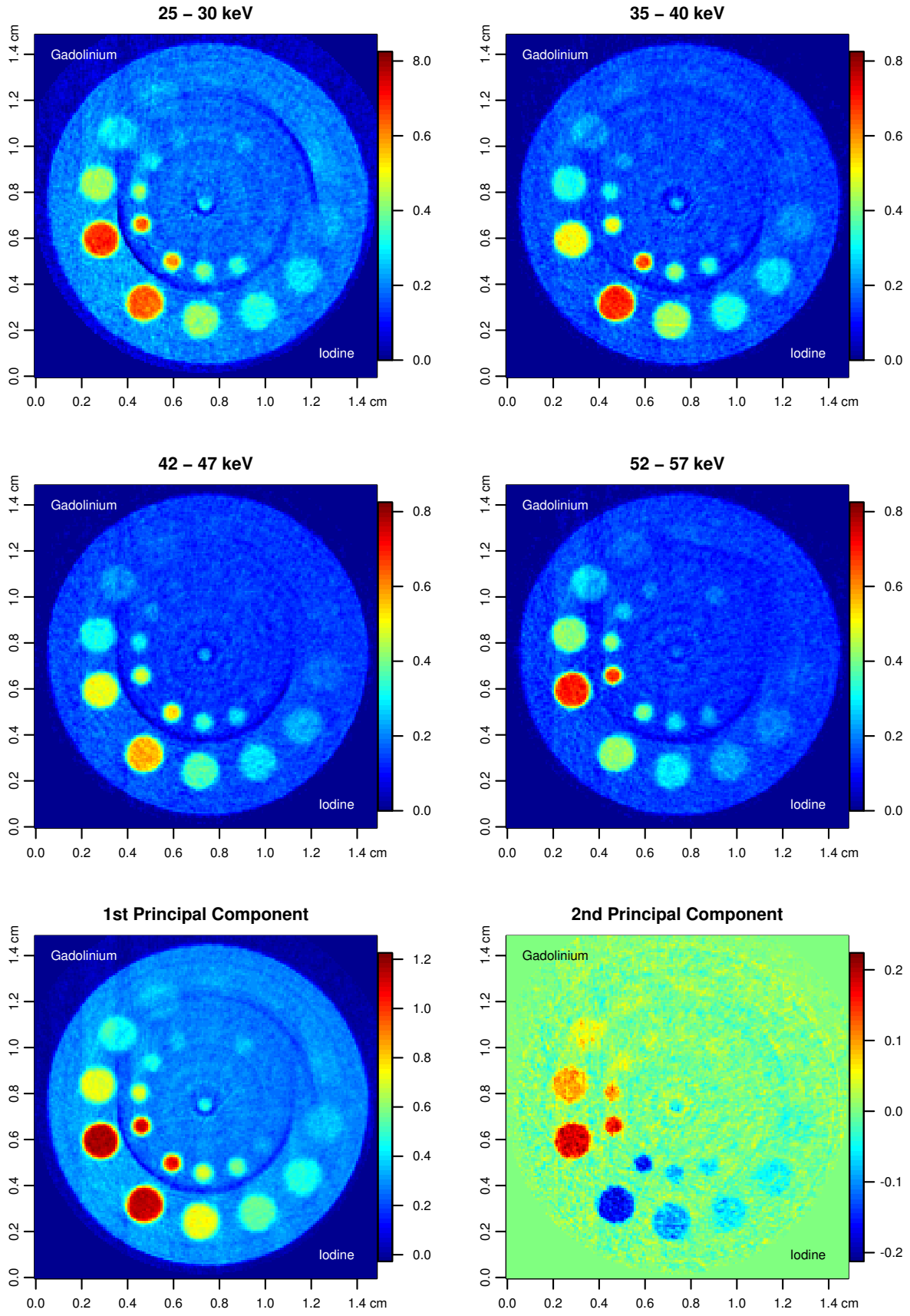

Figure 4.24 Upper and middle rows: Spectrally resolved CT reconstruction of a phantom filled with I and Gd contrast agents. The colour scale gives the reconstructed absorption coefficients in cm^{-1}. The ring structures are artefacts. Bottom row: First two principal components.

4.16 Discussion & Outlook

In this chapter, we have learned about photon counting X-ray imaging, the problems as well as the opportunities that come with this new technology, which we studied using the Medipix2 readout combined with cadmium telluride sensors.

Commissioning

The detectors employed come with a built-in correction to equalise the responses of all the pixels on a chip. This is implemented in hardware and hence goes beyond a traditional flat-field correction performed in software. It works by adjusting each pixel's low and high thresholds and requires additional measurements. For imaging applications, we found that these adjustments are most easily obtained using flat-fields generated by an X-ray tube. Competing techniques, such as those employing characteristic X-rays, were found to preserve image artefacts caused by sensor defects.

Spatial & Spectral Resolution

We found that achieving both a high spatial and spectral resolution are conflicting goals that cannot be achieved at the same time given the present level of technology: While for a high spatial resolution a high pixel density is required to avoid aliasing, this will lead to highly biased energy response functions due to charge sharing and sensor fluorescences. Only the latter can be avoided by choosing low-Z sensor materials like silicon or maybe germanium. Cadmium telluride, on the contrary, shows a distinct photopeak that is in fact extended by a very long and significant tail caused by the effects stated. Although the photopeak's width can be determined reliably, giving this number will by no means tell anything about the detector's energy response. Instead, the whole package has to be considered, and with this in mind, it is questionable if, for small pixels, the careful equalisation of the chips' energy thresholds will be necessary.

Cadmium Telluride in Imaging Applications and its Drawbacks

Two scenarios need to be distinguished here. Imaging of human subjects or of small animals, both of which can be performed spectroscopically or by simply exploiting the superior noise characteristics of a photon counting detector.

For X-ray imaging in human medicine, a very high spatial resolution is often not necessary and also hard to achieve, since the required X-ray fluxes imply comparably large focal spots, leading to a deterioration of the whole system's point spread function due to penumbra effects. Then, the resolution potential of the sensor becomes negligible, and a pixel pitch of more than 300 µm - which is considered by experts to be necessary to suppress the above effects - seems possible. Hence, a good spectroscopic performance can be expected.

Given the small size of the detectors described in this chapter, the imaging of small animals for biomedical research seems to be more within reach in the near future. Here, both fluxes and tube voltages can be chosen much smaller. X-ray tubes with relatively small focal spots are common in this context, and so sensor resolution becomes important. Cadmium telluride has a number of weaknesses here.

One of these weaknesses is the comparably poor sensor resolution due to absorption edges at 23 and 27 keV, leading to the emission of characteristic X-rays with mean free paths in the order of 100 µm, hence deteriorating both spatial and spectral resolution. A reduction of photon energies below these absorption edges only seems justified for very small animals such as mice.

Another weakness is the presence of sensor defects in state-of-the-art cadmium telluride. Areas with zero count rate were observed, which for larger pixels would just be responsible for intensity variations easily correctable, but which dominate for small pixels and hence obscure any image detail coinciding with them. These defective areas even grow with the bias voltage. This being said, cadmium telluride has received increased interest during the last decade, and it seems more than likely that future improvements in manufacturing techniques will be able to mitigate these issues.

The third drawback that especially applies to human medicine and which cannot be neglected either is sensor polarisation. Previous work on this field has shown that the count rates achievable with the cadmium telluride available so far are at least two orders of magnitudes lower than what modern medical diagnostics demands, and it is impossible to predict if future advancements in fabrication will be able to get rid of this problem. However, the operation of the Medipix2 detectors presented here with their default parameters was shown to be limited by signal pile-up in the readout electronics rather than polarisation. This means that polarisation is only of secondary importance for cadmium telluride sensors as thin as 1 mm.

Alternative Sensor Materials

Although not studied in this thesis, silicon also appears as a promising sensor material for small animal imaging. With X-ray fluorescences posing no problem, only charge sharing remains to determine spatial and spectral resolution. In the energy range relevant here ($< 30\,\mathrm{keV}$), silicon still exhibits good absorption, yet not as good as higher-Z sensors.

Germanium, also not discussed in detail, is normally not considered for room temperature detectors due to its small bandgap. However, some people argue that the leakage current compensation integrated into every pixel of the Medipix2 chips will be able to deal with this, and corresponding efforts are already undertaken by the community. Unfortunately, the maximum process temperatures allowed for the bonding of detector and sensor are even lower than with cadmium telluride, which makes this a difficult task.

Compensating for the Adverse Effects of Small Pixels

Two basic approaches have been proposed in the literature to correct for charge sharing and fluorescences. The first one is based on a deconvolution of the acquired spectra in software, knowing the detectors energy response function in the energy range of interest from either Monte Carlo simulations or measurements with synchrotron radiation. This approach decouples the energy response function from the point spread function and also relies on the detector's response being stable.

The second approach corrects for the described phenomena in hardware and is implemented in the Medipix3 chips by establishing communication between neighbouring pixels. This charge summing mode assigns a hit to the pixel with the largest charge, and hence a decoupling of spectral and spatial resolution does not take place. Instead, this is likely to cause small image deformations, and it will be interesting to see how the average point spread function will be affected by this.

Verdict

Without any corrections, the raw spectra recorded are heavily biased, but it was shown in this thesis that for a pixel pitch of 165 µm the K-edges of iodine and gadolinium can be clearly distinguished. At the current level of technology, this suggests the use of CdTe for many applications for

which a qualitative statement is already sufficient, and where an exact quantification of contrast agent concentration is not necessary.

The reader may now have got an impression of how much more complexity is introduced when making the step from conventional digital to spectroscopic X-ray imaging. It remains an open question whether the advantages of photon counting will justify the additional costs in a large scale medical context. Yet, these systems have stimulated new exciting developments in the field of X-ray diagnostics, which has relied on energy integration since its first days more than a hundred years ago.

Chapter 5

Energy Dispersive Coherent Scatter Imaging: First Steps

5.1 Motivation & Overview

Coherent scattering is widely known as the process enabling X-ray crystallography and was already introduced in chapter 2. There, we pointed out that the underlying Thomson cross-section is affected by both the atomic form factor, representing the influence of the electronic charge distribution, and the structure factor, taking account of the ordering and interatomic distances present in (poly-) crystals and amorphous matter. Since both of these factors are functions of the momentum transfer $\boldsymbol{q}$, which in turn can be expressed in terms of the scattering angle θ, they lead to a scattering process that can be highly emission angle specific. Depending on the structure of the material passed by a photon beam, the patterns appearing on a detector can be

- distinct peaks, as in the case of X-ray crystallography,
- sharp rings, as seen in power diffraction, caused by the random alignment of powdered crystals, or
- broad rings for amorphous materials.

An example of how a resulting image can look like is depicted in Fig. 5.1, which was acquired using parts of a drill core supplied by a mining company[1] (Fig. 5.2, we will come back to it later). It shows both the ring structures and some single-crystal reflexes mentioned before. In all cases, the patterns are caused by a modulation of the Thomson cross-section by the product of form and structure factors, and using (2.24), (2.12) and (2.13), we can easily derive the joint differential cross-section:

$$\frac{d\sigma_R}{d\Omega} = \left[\mathrm{e}^{-q^2\langle u^2\rangle/3} \, \frac{1}{N} \left| \sum\nolimits_{\boldsymbol{L}} \mathrm{e}^{i\boldsymbol{q}\cdot\boldsymbol{L}} \right|^2 + \left(1 - \mathrm{e}^{-q^2\langle u^2\rangle/3} \right) \right] \frac{r_\mathrm{e}^2}{2} \left(1 + \cos^2\theta \right) F^2(q, Z) \; . \tag{5.1}$$

As in the case of coherent bremsstrahlung discussed in chapter 3, we see that this expression is again influenced by thermal motion, and we find ourselves running into conceptual problems, dealing with a coherent scatter cross-section that now also exhibits an incoherent part, which is not to be mixed up with (incoherent) Compton scattering.

It was proposed already in the 1980s (Harding 1987, Harding & Schreiber 1999) to exploit coherent scatter for imaging purposes. Using (sufficiently) monochromatic radiation collimated to

[1] Courtesy of David Jaffray, Princess Margaret Hospital, Toronto, Canada.

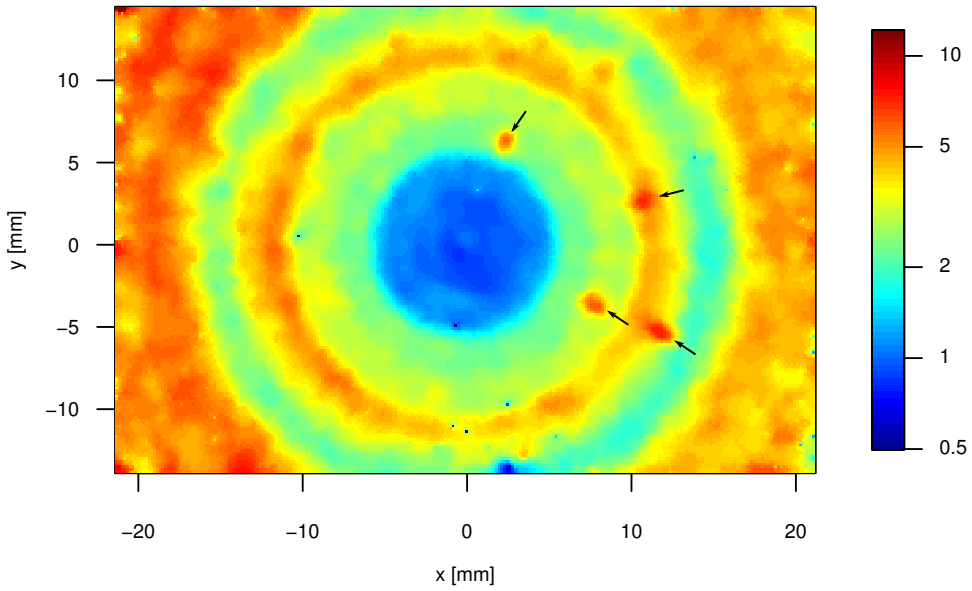

Figure 5.1 Coherent scattering from a drill core sample shown in Fig. 5.2, flat-field corrected, denoised and log-transformed. It was acquired with the Hexa detector described in the previous chapter. The tube voltage was 60 kVp and the energy window was set to 50-55 keV. The distance between the object and the sensor surface was about 9 cm. Larger single-crystal compartments are indicated with arrows.

Figure 5.2 Macro photography of the drill core sample.

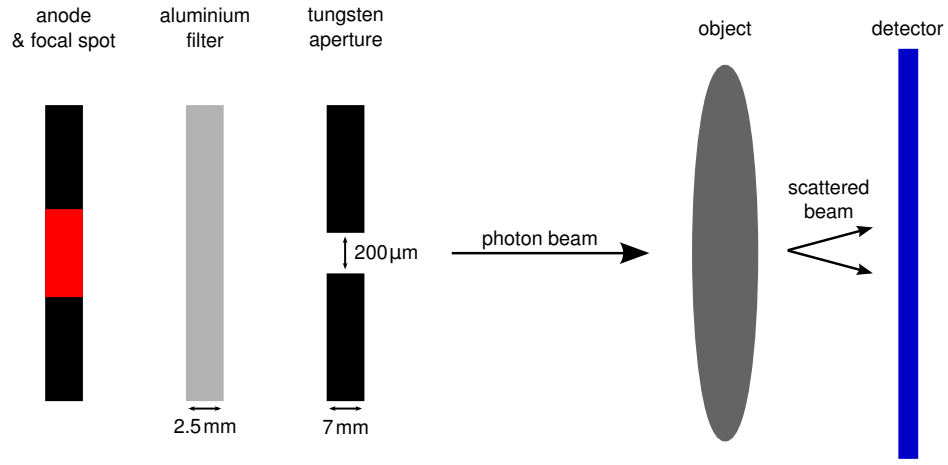

Figure 5.3 Experimental setup used for obtaining the coherent scatter images shown in this chapter (objects and lengths not to scale).

a pencil beam and scanned across an object slice, it was demonstrated that a form of computed tomography, based on scattering cross-sections, could be established, and it was also shown that the resulting images could provide information complementary to conventional, absorptive X-ray imaging. With a scattering behaviour highly depending on the photon energy and the lack of spectroscopic pixel detectors, this approach relied on the strong filtering of X-ray tube spectra or on arrays of monolithic detectors for a long time, and hence it never became very popular.

Recently, the advent of photon counting pixel detectors brought some new motion into the field of coherent scatter imaging (Thran et al. 2006), since now energy discrimination can be easily performed on the detector, rather than on the source side. Consequently, the availability of the Medipix2 detectors (described in chapter 4) to DKFZ suggested performing studies on coherent scatter imaging. Hence, this chapter is dedicated to presenting some of our initial measurements, and the results shown therefore have to be considered only qualtitative, while quantitative measurements will have to be the subject of further studies.

This chapter is structured as follows: In the next section, we will briefly describe the experimental setup employed, and continue with our results in section 5.3. A brief discussion and outlook will be given in section 5.4.

5.2 Experimental Setup

The images presented in this chapter were acquired as follows (Fig. 5.3): A tungsten collimator of thickness 7 mm including an aperture with a diameter of 200 µm (manufactured by means of electrical discharge machining) was placed in front of the exit window of a Siemens Powerphos X-ray tube and arranged in a way to make the collimated beam (the "pencil beam") hit the Hexa detector roughly at its centre. Objects were placed in the pencil beam at various distances from the detector. In contrast to scintillating detectors, no blocking of the primary beam after its passage through the object was necessary due to the photon counting capabilities of our setup. Energy windows were adjusted based on the methods described in the previous chapter. Two separate objects were used:

- the drill core sample (Fig. 5.2), about 3 - 4 mm thick; and
- a 2.5 mm thick piece of cured ham.

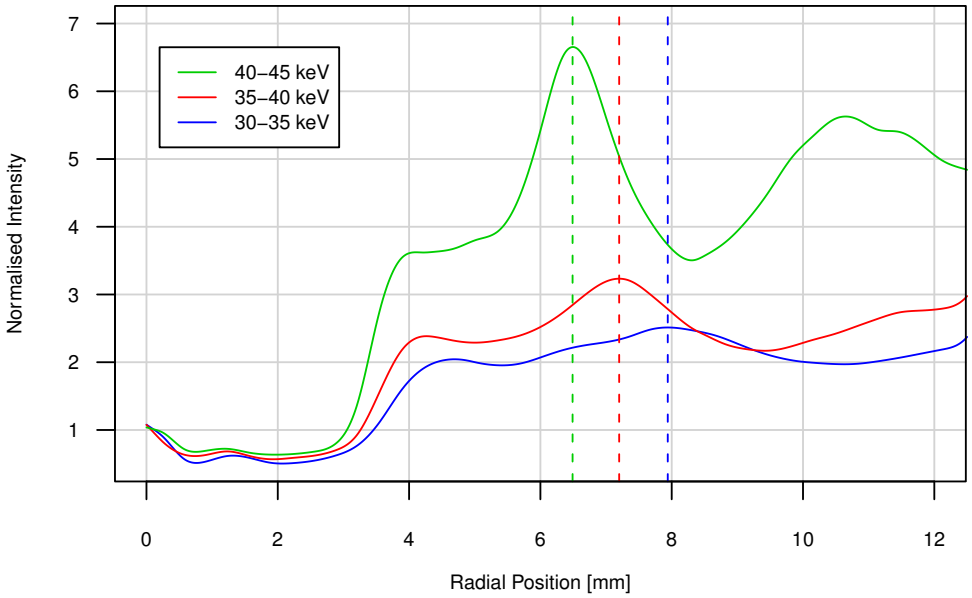

Figure 5.4 Radial coherent scatter profiles for the pencil beam hitting the drill core at one randomly chosen position, normalised to unity at zero radius. The curves correspond to three nominal energy windows. The dip at small distances is due to absorption. Note that the curves shown represent smoothing splines fitted to denoised data. Also, the position of the pencil beam is different to the one shown in Fig. 5.1, and the object to sensor distance was reduced to 5 mm here.

Each measurement was supplemented with a reference acquisition without any objects present in the pencil beam. The resulting images (cf. Fig. 5.1) were divided by this reference image and denoised. The centre of the primary beam was determined in order to compute the radial profiles of the scattered radiation as an average over the polar angle[2]. Due to geometrical effects and since the diameter of the aperture was only about half the one of the focal spot, comparably long exposure times were necessary, depending on the scattering strength of the material in the beam. For the drill core sample, 10 minutes were chosen, whereas the ham required about 30 minutes to give an acceptable SNR.

5.3 Results

Fig. 5.4 shows a radial profile obtained for one random position of the drill core, which was placed at about 5 mm from the sensor surface. What is clearly visible is the fact that the higher the photon energy, the smaller the radius of the rings. This is of course expected from (2.13), which predicts $\theta \approx q/k$ for small scattering angles. Unfortunately, the complicated ERF (section 4.9) of the Hexa detector, caused by the small pixel pitch used (165 µm), leads to poorer contrast at lower energies. Still, the shift of the maxima, indicated by the dashed lines, is clearly visible.

Measuring coherent scatter does not rely on a small pixel pitch as much as absorptive imaging. From Fig. 5.1, we see that an increase of the pixel pitch to 300 - 400 µm seems easily possible, and this increase is very likely to provide a much better contrast of the ring structures shown.

In Fig. 5.5, we see two radial profiles for the piece of ham. The shift of the maxima is only slightly indicated here, and we can conclude that the product of form and structure factors only has a

[2]Code implemented with Marcus Zuber.

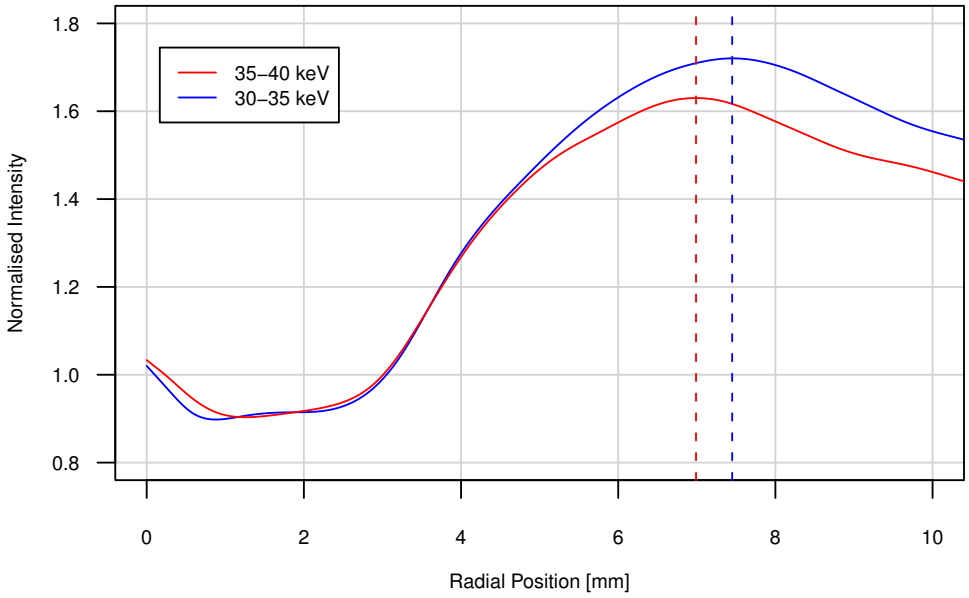

Figure 5.5 As in Fig. 5.4, but for a piece of cured ham.

very broad peak compared to the drill core sample. Because of this, imaging biological tissues suggests much a larger distance between object and sensor than the 5 cm employed here, which also requires larger detectors. The expected smaller cross-section for higher energies can actually be observed in this case, which is in contrast to the drill core sample. The reason for this is probably the lower absorption of low energy photons in the ham due to its smaller average atomic number Z.

5.4 Discussion & Outlook

The results shown above were obtained for single positions of the pencil beam. In order to obtain actual images, it would have to be scanned over the object, or a translation of the object would be necessary (for more sophisticated imaging geometries, cf. Thran et al., 2006). Hence, for each position of the pencil beam, "spectra" like those shown in Figs. 5.4 and 5.5 are obtained, and through the use of energy discimination, a multitude of these spectra results in matrix-like data structures, containing a lot more information than conventional X-ray images.

Besides being the input for CT reconstruction, these data, representing the line integral over $\Delta\Omega\ d\sigma/d\Omega$ times the density of the scattering centres, also carry the potential to serve as input for data mining and machine learning strategies that could be used for tissue classification. This is due to the fact that, in contrast to absorptive imaging, scattering naturally leads to a separation of overlapping structures on the detector, a characteristic which even more profits from energy discrimination. Hence, a reconstruction of 3D information seems to be possible from using a single or only a few projections, which could compensate for the rather long acquisition times. These reconstructions could also be performed on a higher level: instead of reconstructing cross-sections, one could think of going directly for tissue types. As all the scatter components from different depths and materials are linearly superposed on the detector, the strategy would be to use methods from sparse regression (Hastie et al. 2001) to explain the detector signals with as few components as possible. These components, mathematically represented as basis functions spanning the vector space of possible detector images, could be obtained from both measurements or Monte Carlo simulations. This approach appears especially promising for materials reasearch,

where a broader variety of materials with a high atomic number is usually present, very often in the form of poly-crystals, which gives a better and less ambiguous signal on the detector than for biological (soft) tissues.

The use of "conventional" coherent scatter CT suggests itself especially for small animal imaging, where low X-ray energies can be used, implying a larger coherent scatter cross-section. Although this has been described earlier, to this authors' knowledge no study investigated the use of coherent scatter imaging in cancer research so far, and it appears interesting to delve deeper into this subject, now that energy discriminating detectors are available.

Chapter 6

Summary

This thesis focused on two main topics: coherent scattering processes of both electrons and photons as well as photon counting X-ray imaging.

The coherent scattering of electrons lead us to propose the use of coherent bremsstrahlung in image guided radiotherapy. We were able to find initial theoretical evidence that this special kind of bremsstrahlung, relying on single-crystal targets, could potentially provide increased soft tissue contrast and reduce beam hardening artefacts in megavoltage imaging. These conclusions arose from the fact that coherent bremsstrahlung from megavoltage electrons can exhibit an increased kilovoltage component especially around the centre of a field of view, depending on the target orientation angle, thickness, and material.

We went on to study energy disciminating pixel detectors, for which we chose those of the Medipix2 type and which we operated with cadmium telluride sensors. Here, we found that the step from conventional, energy integrating to photon counting detectors introduces additional challenges, most of which are caused by the small pixels we employed. Despite this, it was demonstrated that it is possible to clearly separate iodine and gadolinium contrast agents at a single tube voltage using a pixel pitch of 165 µm.

We finally took a quick look at energy dispersive coherent scatter imaging using these sensors and, with the example of a piece of a drill core, we found that energy discrimination is a desirable extension to this technique.

The ideas and concepts presented here are either completely new to medical physics (coherent bremsstrahlung) or are not available as commercial products yet (energy discrimination and coherent scatter imaging). All have in common that they have the potential to bring some new motion into the field of X-ray imaging, which, since the invention of computed tomography and digital imaging systems, has remained in a somewhat dormant state on the hardware side, experiencing only gradual, yet nonetheless important improvements.

Appendix A

Derivation of the Coherent Bremsstrahlung Cross-Section

A.1 Overall Cross-Sections

We will base our calculations on formula 1BS given by Koch & Motz (Koch & Motz 1959) corresponding to the original cross-section by Bethe & Heitler (Bethe & Heitler 1934) carried out in first order born approximation. However, we will treat all energies in Planck units rather than in units of the electron mass, so we have to multiply the cross-section by the electron mass m^2. Using the definitions from table 3.1, we start with some minor transformations of the original formula:

$$
\begin{aligned}
d^5\sigma &= Z^2\alpha\left(\frac{r_0}{2\pi}\right)^2 m^2\left[1-F(q^2,Z)\right]^2\frac{dk}{k}\frac{p}{p_0}\frac{d\Omega_k d\Omega_p}{q^4}\\
&\left(\frac{p^2\sin^2\theta}{(E-p\cos\theta)^2}\left(4E_0^2-q^2\right)+\frac{p_0^2\sin^2\theta_0}{(E_0-p_0\cos\theta_0)^2}\left(4E^2-q^2\right)\right.\\
&\quad-\frac{2\,p\,p_0\sin\theta\sin\theta_0\cos\phi\left(4EE_0-q^2\right)}{(E-p\cos\theta)\,(E_0-p_0\cos\theta_0)}\\
&\quad\left.+\frac{2k^2\left(p^2\sin^2\theta+p_0^2\sin^2\theta_0-2\,p\,p_0\sin\theta\sin\theta_0\cos\phi\right)}{(E-p\cos\theta)\,(E_0-p_0\cos\theta_0)}\right) \qquad \text{(A.1)}\\
&= Z^2\alpha\left(\frac{r_0}{2\pi}\right)^2 m^2\left[1-F(q^2,Z)\right]^2\frac{k^2dk}{k}\frac{p}{p_0}\frac{d\Omega_k d\Omega_p}{q^4}\\
&\quad\times\left(\frac{p^2\sin^2\theta(4E_0^2-q^2)}{(Ek-\boldsymbol{p}\cdot\boldsymbol{k})^2}+\frac{p_0^2\sin^2\theta_0(4E^2-q^2)}{(E_0k-\boldsymbol{p}_0\cdot\boldsymbol{k})^2}\right.\\
&\qquad\left.-\frac{2\left[p\,p_0\sin\theta\sin\theta_0\cos\phi\left(4EE_0-q^2+2k^2\right)-k^2\left(p^2\sin^2\theta+p_0^2\sin^2\theta_0\right)\right]}{(Ek-\boldsymbol{p}\cdot\boldsymbol{k})(E_0k-\boldsymbol{p}_0\cdot\boldsymbol{k})}\right)
\end{aligned}
$$

Next we will make use of an integration trick which will later allow us to carry out the relevant integrations analytically without any approximations. It consists of adding the differential dp to (A.1), which is, due to energy conservation reasons, only possible by simultaneously introducing a delta distribution. Neglecting kinetic energy transfer onto the whole crystal as well as phonon excitations, we first add $\delta(E_0-E-k)dE$, and then perform a change of variable in the differential dE, but leave the distribution unchanged. This results in the additional factor $\delta(E_0-E-k)\frac{p}{E}dp$ that has to be added to the above cross-section (A.1). Note that this operation just represents a transformation of the original cross-section without adding characteristics of a regularly spaced

lattice yet.
By introducing the transversal momenta $p_{0\perp} = p_0 \sin\theta_0$ and $p_\perp = p \sin\theta$ into (A.1), we then obtain the following form of the Bethe-Heitler cross-section:

$$\frac{d^6\sigma}{d^3p\; d^3k} = Z^2\alpha \left(\frac{r_0}{2\pi}\right)^2 \delta(E_0 - E - k)\; \frac{m^2}{p_0 E k} \frac{(1 - F(q^2, Z))^2}{q^4}$$
$$\times \left(\frac{p_\perp^2 (4E_0^2 - q^2)}{(Ek - \boldsymbol{p}\cdot\boldsymbol{k})^2} + \frac{p_{0\perp}^2 (4E^2 - q^2)}{(E_0 k - \boldsymbol{p}_0\cdot\boldsymbol{k})^2} - \frac{2\left[p_{0\perp} p_\perp \cos\phi \left(4EE_0 - q^2 + 2k^2\right) - k^2\left(p_\perp^2 + p_{0\perp}^2\right)\right]}{(Ek - \boldsymbol{p}\cdot\boldsymbol{k})(E_0 k - \boldsymbol{p}_0\cdot\boldsymbol{k})} \right) \tag{A.2}$$

We can now move on to investigating the Bethe-Heitler cross-section in the presence of a periodic potential. In this case, as was shown by Überall (Überall 1956), the cross-section per unit-cell is affected by the additional factor

$$\frac{1}{N}\left\langle \left| \sum_{\boldsymbol{L}} \mathrm{e}^{\,i\boldsymbol{q}\cdot(\boldsymbol{L}+\boldsymbol{u_L})} \right| \right\rangle^2 = \frac{1}{N}\mathrm{e}^{-q^2\langle u^2\rangle/3} \left| \sum_{\boldsymbol{L}} \mathrm{e}^{\,i\boldsymbol{q}\cdot\boldsymbol{L}} \right|^2 + \left(1 - \mathrm{e}^{-q^2\langle u^2\rangle/3}\right) , \tag{A.3}$$

where $\boldsymbol{L}$ denotes the position of an atom within a regular lattice, $\boldsymbol{u_L}$ represents a small thermal displacement of this atom, $\langle u^2\rangle$ the mean square displacement and N the total number of unit cells in the crystal.
The first part of (A.3) represents a Laue-Bragg diffraction factor that will turn out to correspond to the coherent part, whereas the second one is responsible for an incoherent background. Both expressions are functions of the Debye - Waller factor $\mathrm{e}^{-q^2\langle u^2\rangle/3}$. It is interesting to see that, because of this, the incoherent background does not just correspond to the single-atom cross-section.. Also note that the diffraction factor is given per unit cell rather than for the whole crystal and that $\langle u^2\rangle$ is the mean square displacement in *three* dimensions.

Coherent Part

The derivation of the diffraction factor for a periodic potential was presented in detail by Diambrini Palazzi (Palazzi 1968). It is given by

$$\frac{1}{N}\left| \sum_{dia} \mathrm{e}^{\,i\boldsymbol{q}\cdot\boldsymbol{L}} \right|^2 = \frac{(2\pi)^3}{v_0} \sum_{\boldsymbol{\tau}} |S|^2 \delta\left(\boldsymbol{p}_0 - \boldsymbol{p} - \boldsymbol{k} - \boldsymbol{\tau}\right), \tag{A.4}$$

where v_0 is the volume of the fundamental unit cell, $\boldsymbol{\tau}$ represents a reciprocal lattice vector multiplied by 2π, $\boldsymbol{\tau} = \frac{2\pi}{a}\sum_{i=1}^{3} \hat{e}_i n_i$, with coordinates n_i and unit vectors $\hat{e}_i$. For simplicity, we will refer to $\boldsymbol{\tau}$ as reciprocal lattice vector as well, despite the factor of 2π. Note that (A.4) implies that the momentum transfer $\boldsymbol{q} = \boldsymbol{p}_0 - \boldsymbol{p} - \boldsymbol{k}$ is equal to a reciprocal lattice vector $\boldsymbol{\tau}$.
The structure factors $|S|^2$ for bcc, fcc and diamond crystals are given as follows (Palazzi 1968):

$$|S_{bcc}|^2 = \begin{cases} 4, & \text{if the sum of the } n_i \text{ is even,} \\ 0 & \text{otherwise;} \end{cases}$$
$$|S_{fcc}|^2 = \begin{cases} 16, & \text{if all the } n_i \text{ are either even or odd,} \\ 0 & \text{otherwise;} \end{cases} \tag{A.5}$$
$$|S_{dia}|^2 = \begin{cases} 64, & \text{if all the } n_i \text{ are even and their sum is a multiple of four,} \\ 32, & \text{if all the } n_i \text{ are odd,} \\ 0 & \text{otherwise.} \end{cases}$$

The usefulness of formulating our problem with structure factors is given by the fact that one can implement the reciprocal lattice in computer programs with simple for-loops iterating over the elements of a cubic grid having a lattice constant $2\pi/a$, with weights for the contributions of different elements according to (A.5). These expressions are valid for perfect single-crystals. Inserting (A.4) into (A.2), we now obtain

$$\begin{aligned}\frac{d^6\sigma_{coh}}{d^3p\ d^3k} = \frac{2\pi r_0^2\, Z^2\alpha m^2}{p_0 E k v_0}\ \delta(E_0 - E - k)\ \sum_{\boldsymbol{\tau}} \delta(\boldsymbol{p}_0 - \boldsymbol{p} - \boldsymbol{k} - \boldsymbol{\tau})\ \mathrm{e}^{-\tau^2\langle u^2\rangle/3}|S|^2\ \frac{(1-F(\tau^2,Z))^2}{\tau^4} \\ \times \left(\frac{p_\perp^2(4E_0^2-\tau^2)}{(Ek - \boldsymbol{p}\cdot\boldsymbol{k})^2} + \frac{p_{0\perp}^2(4E^2-\tau^2)}{(E_0 k - \boldsymbol{p}_0\cdot\boldsymbol{k})^2} \right. \\ \left. - \frac{2\left[p_\perp\, p_{0\perp}\cos\phi\left(4EE_0 - \tau^2 + 2k^2\right) - k^2\left(p_\perp^2 + p_{0\perp}^2\right)\right]}{(Ek - \boldsymbol{p}\cdot\boldsymbol{k})(E_0 k - \boldsymbol{p}_0\cdot\boldsymbol{k})} \right).\end{aligned} \tag{A.6}$$

We would like to stress that some of the signs in (A.6) are different to the expression given by Sáenz & Überall (1982).

Incoherent Part

The thermal motion amplitudes $\langle u^2\rangle$ appearing in (A.3) lead to the fact that a part of the incoming electron beam interacts without the restriction of the momentum transfer being equal to a reciprocal lattice vector, similar to the case of an amorphous target. It is intuitively clear that the summation over lattice vectors obtained for the coherent part (A.6) then has to be replaced by an integration over $\boldsymbol{\tau}$. In order to derive this in a more formal way, we will make use of a trick similar to the one already employed above, namely adding the factor $\delta(\boldsymbol{p}_0 - \boldsymbol{p} - \boldsymbol{k} - \boldsymbol{q})d^3q$ that just represents momentum conservation. By renaming $\boldsymbol{q}$ as $\boldsymbol{\tau}$ and switching to spherical coordinates, we then obtain the factor $\delta(\boldsymbol{p}_0 - \boldsymbol{p} - \boldsymbol{k} - \boldsymbol{\tau})\ \tau^2 d\tau \sin\theta_\tau d\theta_\tau d\phi_\tau$ which has to be added to the cross-section. Doing so expresses the incoherent part in a way very similar to the coherent one, with the additional differentials over $\boldsymbol{\tau}$:

$$\begin{aligned}\frac{d^6\sigma_{inc}}{d^3p\ d^3k} = \nu\frac{r_0^2\, Z^2\alpha m^2}{4\pi^2 p_0 E k}\delta(E_0 - E - k)\delta(\boldsymbol{p}_0 - \boldsymbol{p} - \boldsymbol{k} - \boldsymbol{\tau})\ \tau^2 d\tau \sin\theta_\tau d\theta_\tau d\phi_\tau \\ \times \left(1 - \mathrm{e}^{-\tau^2\langle u^2\rangle/3}\right)\frac{(1-F(\tau^2,Z))^2}{\tau^4} \\ \times \left(\frac{p^2\sin^2\theta(4E_0^2-\tau^2)}{(Ek - \boldsymbol{p}\cdot\boldsymbol{k})^2} + \frac{p_0^2\sin^2\theta_0(4E^2-\tau^2)}{(E_0 k - \boldsymbol{p}_0\cdot\boldsymbol{k})^2} \right. \\ \left. - \frac{2\left[p\, p_0\sin\theta\sin\theta_0\cos\phi\left(4EE_0 - \tau^2 + 2k^2\right) - k^2\left(p^2\sin^2\theta + p_0^2\sin^2\theta_0\right)\right]}{(Ek - \boldsymbol{p}\cdot\boldsymbol{k})(E_0 k - \boldsymbol{p}_0\cdot\boldsymbol{k})} \right).\end{aligned} \tag{A.7}$$

This expression enables us to compute the photon spectra of the incoherent part with arbitrary expressions for the Debye - Waller and form factors. It has been obtained without any assumptions as to energy or angle and therefore replaces (3BS(a)) of (Koch & Motz 1959), which was derived for the extreme relativistic case. The integrations over τ and θ_τ, which remain after the ones over $\boldsymbol{p}$ and $\boldsymbol{\Omega}_k$ that are to be detailed below, still have to be carried out numerically, which makes this cross-section unsuitable for being used in Monte Carlo codes. The only work known to the authors performing a similar integration of the Bethe Heitler cross-section without any further approximations was presented by Borie (1972). It pursues a different approach and also ends up with two numeric integrations to be carried out. We see an advantage of our result in the similarity to the coherent cross-section (A.6).

A.2 Spectra

Coherent Part

In order to determine the spectrum, one has to integrate (A.6) over the outgoing electron momentum $\boldsymbol{p}$ and the direction of the bremsstrahlung photon $\boldsymbol{\Omega}_k$. This calculation will be carried out in detail on the following pages.

First of all, we will perform the integration over p, expressing the energy of the outgoing electron in the first δ-distribution by its momentum imposed by the second one, which now vanishes:

$$\begin{aligned}\frac{d^3\sigma_{coh}}{d^3k} = \frac{2\pi r_0^2\, Z^2\alpha m^2}{p_0 E k v_0} \sum_{\boldsymbol{\tau}} |S(\boldsymbol{\tau})|^2 \, \frac{(1-F(\tau^2,Z))^2}{\tau^4} \, \mathrm{e}^{-\tau^2\langle u^2\rangle/3} \\ \times \; \delta\left(E_0 - E\left(\boldsymbol{p}_0 - \boldsymbol{k} - \boldsymbol{\tau}\right) - k\right) \left(\frac{p_\perp^2(4E^2-\tau^2)}{(Ek - \boldsymbol{p}\cdot\boldsymbol{k})^2} + \frac{p_{0\perp}^2(4E_0^2-\tau^2)}{(E_0 k - \boldsymbol{p}_0\cdot\boldsymbol{k})^2} \right. \\ \left. - \frac{2\left[p_\perp\, p_{0\perp}\cos\phi\left(4EE_0 - \tau^2 + 2k^2\right) - k^2\left(p_\perp^2 + p_{0\perp}^2\right)\right]}{(Ek - \boldsymbol{p}\cdot\boldsymbol{k})(E_0 k - \boldsymbol{p}_0\cdot\boldsymbol{k})} \right) .\end{aligned} \tag{A.8}$$

This now requires us to transform the remaining δ-distribution by change of variable:

$$\begin{aligned}&\int d\Omega_k \; \delta\left((E_0 - k) - \sqrt{m^2 + (\boldsymbol{p}_0 - \boldsymbol{\tau})^2 - 2\,(\boldsymbol{p}_0 - \boldsymbol{\tau})\cdot\boldsymbol{k} + k^2} \right) \\ &= 2E \int d\Omega_k \; \delta\Big(\underbrace{E^2 - \left(m^2 + (\boldsymbol{p}_0 - \boldsymbol{\tau})^2 + k^2\right)}_{=:a} + 2\,(\boldsymbol{p}_0 - \boldsymbol{\tau})\cdot\boldsymbol{k} \Big) \; .\end{aligned}$$

We have introduced the variable a for convenience. By defining θ_γ as the angle between $\boldsymbol{p}_0 - \boldsymbol{\tau}$ and $\boldsymbol{k}$ (notice the negative sign in contrast to (Sáenz & Überall 1982)) and by introducing ϕ_γ as an azimuthal angle to be defined below, we can further simplify the integral:

$$= 2E \int_0^{2\pi} d\phi_\gamma \int_0^{\pi} d\theta_\gamma \, \sin\theta_\gamma \, \delta\left(a + 2\,|\boldsymbol{p}_0 - \boldsymbol{\tau}|\, k \cos\theta_\gamma\right) \; .$$

By substituting $x := \cos\theta_\gamma$, we transform the integral into

$$= 2E \int_0^{2\pi} d\phi_\gamma \int_{-1}^{1} dx \, \delta\left(a + 2\,|\boldsymbol{p}_0 - \boldsymbol{\tau}|\, kx\right) \quad ,$$

and by performing once more a change of variable within the delta function and by swapping the position of the integrals, we get:

$$= \frac{E}{|\boldsymbol{p}_0 - \boldsymbol{\tau}|\, k} \int_{-1}^{1} dx \; \delta\left(x + \frac{a}{2|\boldsymbol{p}_0 - \boldsymbol{\tau}|\, k}\right) \int_0^{2\pi} d\phi_\gamma \; .$$

Thus, (A.8) transforms into:

$$\begin{aligned}\frac{d^3\sigma_{coh}}{d^3k} = \frac{2\pi r_0^2\, Z^2\alpha m^2}{p_0 k^2 v_0} \sum_{\boldsymbol{\tau}} |S(\boldsymbol{\tau})|^2 \, \frac{(1-F(\tau^2,Z))^2}{\tau^4\,|\boldsymbol{p}_0 - \boldsymbol{\tau}|} \, \mathrm{e}^{-\tau^2\langle u^2\rangle/3} \delta\left(x + \frac{a}{2|\boldsymbol{p}_0 - \boldsymbol{\tau}|\, k}\right) \\ \times \left(\frac{p_\perp^2(4E^2-\tau^2)}{(Ek - \boldsymbol{p}\cdot\boldsymbol{k})^2} + \frac{p_{0\perp}^2(4E_0^2-\tau^2)}{(E_0 k - \boldsymbol{p}_0\cdot\boldsymbol{k})^2} \right. \\ \left. - \frac{2\left[p_\perp\, p_{0\perp}\cos\phi\left(4EE_0 - \tau^2 + 2k^2\right) - k^2\left(p_\perp^2 + p_{0\perp}^2\right)\right]}{(Ek - \boldsymbol{p}\cdot\boldsymbol{k})(E_0 k - \boldsymbol{p}_0\cdot\boldsymbol{k})} \right) .\end{aligned} \tag{A.9}$$

By defining

$$\epsilon_b = \frac{p_0^2 - (\boldsymbol{p}_0 - \boldsymbol{\tau})^2}{2k} \ , \tag{A.10}$$

we can express a as follows:

$$\begin{aligned} a &= (E_0 - k)^2 - m^2 - (\boldsymbol{p}_0 - \boldsymbol{\tau})^2 - k^2 \\ &= -2E_0 k + p_0^2 - (\boldsymbol{p}_0 - \boldsymbol{\tau})^2 = -2k \left(E_0 - \frac{p_0^2 - (\boldsymbol{p}_0 - \boldsymbol{\tau})^2}{2k} \right) \\ &= -2k \left(E_0 - \epsilon_b \right) \ . \end{aligned} \tag{A.11}$$

We insert this expression into (A.9) and finally obtain:

$$\begin{aligned} \frac{d^3\sigma_{coh}}{d^3k} = \frac{2\pi r_0^2 \, Z^2 \alpha m^2}{p_0 k^2 v_0} \sum_{\boldsymbol{\tau}} |S(\boldsymbol{\tau})|^2 \, \frac{(1 - F(\tau^2, Z))^2}{\tau^4 \, |\boldsymbol{p}_0 - \boldsymbol{\tau}|} \, \mathrm{e}^{-\tau^2 \langle u^2 \rangle / 3} \delta \left(x - \frac{E_0 - \epsilon_b}{|\boldsymbol{p}_0 - \boldsymbol{\tau}|} \right) \\ \times \left(\frac{p_\perp^2 (4E^2 - \tau^2)}{(Ek - \boldsymbol{p} \cdot \boldsymbol{k})^2} + \frac{p_{0\perp}^2 (4E_0^2 - \tau^2)}{(E_0 k - \boldsymbol{p}_0 \cdot \boldsymbol{k})^2} \right. \\ \left. - \frac{2 \left[p_\perp \, p_{0\perp} \cos\phi \left(4EE_0 - \tau^2 + 2k^2 \right) - k^2 \left(p_\perp^2 + p_{0\perp}^2 \right) \right]}{(Ek - \boldsymbol{p} \cdot \boldsymbol{k})(E_0 k - \boldsymbol{p}_0 \cdot \boldsymbol{k})} \right) . \end{aligned} \tag{A.12}$$

Carrying out the integration involves computing an expression of the form $\int_{-1}^{1} dx \ \delta \left(x - \frac{E_0 - \epsilon_b}{|\boldsymbol{p}_0 - \boldsymbol{\tau}|} \right)$ which imposes the following restriction on the summation variable $\boldsymbol{\tau}$:

$$|E_0 - \epsilon_b| \leq |\boldsymbol{p}_0 - \boldsymbol{\tau}| \ . \tag{A.13}$$

If this condition is not fulfilled for a specific value of $\boldsymbol{\tau}$, the simultaneous conservation of energy and momentum will violated and the cross-section will be zero for this value.

Before we finally come to solving the four integrals contained in (A.12), we will compute some frequently occuring expressions and define a suitable coordinate frame.

Scalar Products with $\boldsymbol{k}$

The following equations are imposed by the argument of the δ-distribution:

$$(\boldsymbol{p}_0 - \boldsymbol{\tau}) \cdot \boldsymbol{k} = -\frac{a}{2} = k \left(E_0 - \epsilon_b \right) \tag{A.14}$$

$$\boldsymbol{p} \cdot \boldsymbol{k} = (\boldsymbol{p}_0 - \boldsymbol{\tau}) \cdot \boldsymbol{k} - k^2 = -\frac{a}{2} - k^2 = k \left(E_0 - \epsilon_b \right) - k^2 \tag{A.15}$$

$$\boldsymbol{p}_0 \cdot \boldsymbol{k} = (\boldsymbol{p}_0 - \boldsymbol{\tau}) \cdot \boldsymbol{k} + \boldsymbol{k} \cdot \boldsymbol{\tau} = -\frac{a}{2} + \boldsymbol{k} \cdot \boldsymbol{\tau} = k \left(E_0 - \epsilon_b \right) + \boldsymbol{k} \cdot \boldsymbol{\tau} \tag{A.16}$$

Azimuthal Angle

An azimuthal angle ϕ_γ requires being defined with respect to an arbitrary direction perpendicular to $\boldsymbol{p}_0 - \boldsymbol{\tau}$. The clue to such a definition lies in the scalar product $\boldsymbol{k} \cdot \boldsymbol{\tau}$. We will now express it as a function of $\cos\phi_\gamma$.
ϕ_γ can be defined as the angle between two planes as illustrated in Fig. A.1. Thus, it can be written as the angle between the two normal vectors of these planes:

$$\cos\phi_\gamma = \frac{\Big[(\boldsymbol{p}_0 - \boldsymbol{\tau}) \times \boldsymbol{p}_0 \Big] \Big[(\boldsymbol{p}_0 - \boldsymbol{\tau}) \times \boldsymbol{k} \Big]}{\sqrt{\tau^2 p_0^2 - (\boldsymbol{\tau} \cdot \boldsymbol{p}_0)^2} \sin\theta_\gamma |\boldsymbol{p}_0 - \boldsymbol{\tau}| k} \ . \tag{A.17}$$

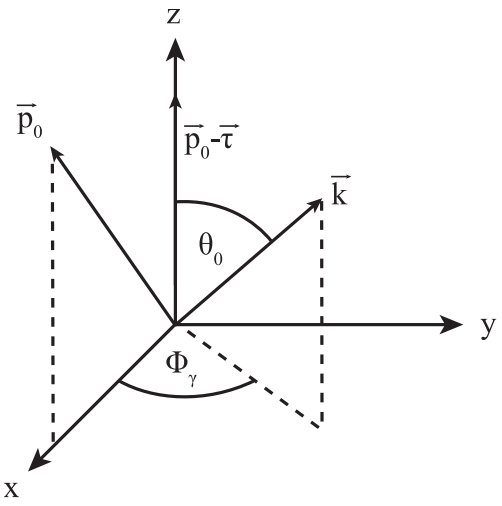

Figure A.1 Definition of ϕ_γ as the angle between two planes.

With $x := \cos\theta_\gamma$, $\sin\theta_\gamma = \sqrt{1-x^2}$ and the first intermediate result of (A.16) we obtain

$$\begin{aligned}\frac{\boldsymbol{k}\cdot\boldsymbol{\tau}}{k} &= x\,\underbrace{\frac{\boldsymbol{\tau}\cdot(\boldsymbol{p}_0-\boldsymbol{\tau})}{|\boldsymbol{p}_0-\boldsymbol{\tau}|}}_{=:b} + \sqrt{1-x^2}\,\underbrace{\sqrt{\frac{\tau^2 p_0^2-(\boldsymbol{\tau}\cdot\boldsymbol{p}_0)^2}{|\boldsymbol{p}_0-\boldsymbol{\tau}|^2}}}_{=:c}\cos\phi_\gamma \\ &= xb+\sqrt{1-x^2}\,c\cos\phi_\gamma\ .\end{aligned} \tag{A.18}$$

Transversal Momenta

We exploit the definitions of the components of $\boldsymbol{p}$ and $\boldsymbol{p}_0$ being perpendicular to $\boldsymbol{k}$:

$$\begin{aligned}p_\perp^2 &= p^2-\left(\frac{\boldsymbol{p}\cdot\boldsymbol{k}}{k}\right)^2 \overset{(A.15)}{=} (\boldsymbol{p}_0-\boldsymbol{\tau})-\boldsymbol{k})^2-\frac{\left((\boldsymbol{p}_0-\boldsymbol{\tau})\cdot\boldsymbol{k}-k^2\right)^2}{k^2} \\ &= (\boldsymbol{p}_0-\boldsymbol{\tau})^2-2\,(\boldsymbol{p}_0-\boldsymbol{\tau})\cdot\boldsymbol{k}+k^2-\frac{((\boldsymbol{p}_0-\boldsymbol{\tau})\cdot\boldsymbol{k})^2-2k^2\,(\boldsymbol{p}_0-\boldsymbol{\tau})\cdot\boldsymbol{k}+k^4}{k^2} \\ &= (\boldsymbol{p}_0-\boldsymbol{\tau})^2-\frac{((\boldsymbol{p}_0-\boldsymbol{\tau})\cdot\boldsymbol{k})^2}{k^2} \overset{(A.14)}{=} (\boldsymbol{p}_0-\boldsymbol{\tau})^2-\left(\frac{a}{2k}\right)^2 \\ &= (\boldsymbol{p}_0-\boldsymbol{\tau})^2-(E_0-\epsilon_b)^2\end{aligned} \tag{A.19}$$

$$\begin{aligned}p_{0\perp}^2 &= p_0^2-\left(\frac{\boldsymbol{p}_0\cdot\boldsymbol{k}}{k}\right)^2 \overset{(A.16)}{=} p_0^2-\left(E_0-\epsilon_b+\frac{\boldsymbol{k}\cdot\boldsymbol{\tau}}{k}\right)^2 = p_0^2-\left(E_0-\left(\epsilon_b-\frac{\boldsymbol{k}\cdot\boldsymbol{\tau}}{k}\right)\right)^2 \\ &\overset{(A.18)}{=} p_0^2-\left(E_0-\left(\epsilon_b-xb-\sqrt{1-x^2}\,c\cos\phi_\gamma\right)\right)^2\end{aligned} \tag{A.20}$$

Resonance Denominators

$$Ek - \boldsymbol{p}\cdot\boldsymbol{k} \overset{(A.15)}{=} Ek - \left(-\frac{a}{2} - k^2\right) = E_0 k + \frac{a}{2} \overset{(A.11)}{=} E_0 k - k\left(E_0 - \epsilon_b\right) = k\epsilon_b \tag{A.21}$$

$$E_0 k - \boldsymbol{p}_0\cdot\boldsymbol{k} \overset{(A.16)}{=} E_0 k - \left(-\frac{a}{2} + \boldsymbol{k}\cdot\boldsymbol{\tau}\right) = E_0 k + \frac{a}{2} - \boldsymbol{k}\cdot\boldsymbol{\tau} \overset{(A.11)}{=} E_0 k - k\left(E_0 - \epsilon_b\right) - \boldsymbol{k}\cdot\boldsymbol{\tau} \tag{A.22}$$

$$\overset{(A.18)}{=} k\epsilon_b - k\left(xb + \sqrt{1-x^2}\, c\cos\phi_\gamma\right) \tag{A.23}$$

First Integral

Since we were able to express $p_\perp^2$ as a function of known constants in (A.19) ($\boldsymbol{\tau}$ is considered fixed within each summation step), this integration becomes trivial:

$$\tilde{I}_1 \;:=\; \int_{-1}^{1} dx\; \delta\left(x - \frac{E_0 - \epsilon_b}{|\boldsymbol{p}_0 - \boldsymbol{\tau}|}\right) \int_0^{2\pi} d\phi_\gamma\; \frac{p_\perp^2\left(4E_0^2 - \tau^2\right)}{\left(Ek - \boldsymbol{p}\cdot\boldsymbol{k}\right)^2} \tag{A.24}$$

Thus:

$$\boxed{\tilde{I}_1 = 2\pi \frac{p_\perp^2\left(4E_0^2 - \tau^2\right)}{k^2\epsilon_b^2}} \tag{A.25}$$

Second Integral

$$\begin{aligned}
\tilde{I}_2 \;&:=\; \int_{-1}^{1} dx\; \delta\left(x - \frac{E_0 - \epsilon_b}{|\boldsymbol{p}_0 - \boldsymbol{\tau}|}\right) \int_0^{2\pi} d\phi_\gamma\; \frac{p_{0\perp}^2\left(4E^2 - \tau^2\right)}{\left(E_0 k - \boldsymbol{p}_0\cdot\boldsymbol{k}\right)^2} \\
&=\; \int_{-1}^{1} dx\; \delta\left(x - \frac{E_0 - \epsilon_b}{|\boldsymbol{p}_0 - \boldsymbol{\tau}|}\right) \int_0^{2\pi} d\phi_\gamma\; \frac{p_{0\perp}^2\left(4E^2 - \tau^2\right)}{\left(E_0 k - \boldsymbol{p}_0\cdot\boldsymbol{k}\right)^2} \\
&\overset{(A.20)}{=} \frac{4E^2 - \tau^2}{k^2} \int_{-1}^{1} dx\; \delta\left(x - \frac{E_0 - \epsilon_b}{|\boldsymbol{p}_0 - \boldsymbol{\tau}|}\right) \int_0^{2\pi} d\phi_\gamma\; \frac{p_0^2 - \left(E_0 - \left(\overbrace{\epsilon_b - xb}^{=:d} - \overbrace{\sqrt{1-x^2}\, c\cos\phi_\gamma}^{=:e}\right)\right)^2}{\left(\underbrace{\epsilon_b - xb}_{=:d} - \underbrace{\sqrt{1-x^2}\, c\cos\phi_\gamma}_{=:e}\right)^2} \\
&=\; \frac{4E^2 - \tau^2}{k^2} \int_{-1}^{1} dx\; \delta\left(x - \frac{E_0 - \epsilon_b}{|\boldsymbol{p}_0 - \boldsymbol{\tau}|}\right) \int_0^{2\pi} d\phi_\gamma \left(-1 + \frac{2E_0}{d - e\cos\phi_\gamma} - \frac{m^2}{\left(d - e\cos\phi_\gamma\right)^2}\right)
\end{aligned} \tag{A.26}$$

(A.26) gives rise to three sub-integrals which will be computed below. Before we come to that, we state a couple of identities which come in handy during the integration:

$$\boldsymbol{\tau}\cdot\left(\boldsymbol{p}_0 - \boldsymbol{\tau}\right) = \boldsymbol{p}_0\cdot\left(\boldsymbol{p}_0 - \boldsymbol{\tau}\right) - \left(\boldsymbol{p}_0 - \boldsymbol{\tau}\right)^2 \tag{A.27}$$

$$\tan^{-1}(-x) = -\tan^{-1}(x) \tag{A.28}$$

$$\int_0^{2\pi} d\phi_\gamma f\left(\cos\left(\gamma\right)\right) = \int_0^{\frac{\pi}{2}} d\phi_\gamma f\left(\cos\left(\gamma\right)\right) + \int_0^{\frac{\pi}{2}} d\phi_\gamma f\left(-\cos\left(\gamma\right)\right) + \int_0^{\frac{\pi}{2}} d\phi_\gamma f\left(\sin\left(\gamma\right)\right) + \int_0^{\frac{\pi}{2}} d\phi_\gamma f\left(-\sin\left(\gamma\right)\right) \ , \tag{A.29}$$

with f being an arbitrary integrable function. We are now able to carry out the integration:

$$\tilde{I}_2^a := \int_{-1}^{1} dx\ \delta\left(x - \frac{E_0 - \epsilon_b}{|\boldsymbol{p}_0 - \boldsymbol{\tau}|}\right) \int_0^{2\pi} d\phi_\gamma\ (-1) = -2\pi \tag{A.30}$$

$$\begin{aligned}
\tilde{I}_2^b &:= \int_{-1}^{1} dx\ \delta\left(x - \frac{E_0 - \epsilon_b}{|\boldsymbol{p}_0 - \boldsymbol{\tau}|}\right) \int_0^{2\pi} d\phi_\gamma\ \frac{2E_0}{d - e\cos\phi_\gamma} \\
&= 2E_0 \int_{-1}^{1} dx\ \delta\left(x - \frac{E_0 - \epsilon_b}{|\boldsymbol{p}_0 - \boldsymbol{\tau}|}\right) \\
&\times \left(\int_0^{\frac{\pi}{2}} d\phi_\gamma \frac{1}{d - e\cos\phi_\gamma} + \int_0^{\frac{\pi}{2}} d\phi_\gamma \frac{1}{d + e\cos\phi_\gamma} + \int_0^{\frac{\pi}{2}} d\phi_\gamma \frac{1}{d - e\sin\phi_\gamma} + \int_0^{\frac{\pi}{2}} d\phi_\gamma \frac{1}{d + e\sin\phi_\gamma}\right) \\
&= \frac{8E_0}{\sqrt{d^2 - \mathrm{e}^2}} \int_{-1}^{1} dx\ \delta\left(x - \frac{E_0 - \epsilon_b}{|\boldsymbol{p}_0 - \boldsymbol{\tau}|}\right) \left(\arctan\frac{d+e}{\sqrt{d^2 - \mathrm{e}^2}} + \arctan\frac{d-e}{\sqrt{d^2 - \mathrm{e}^2}}\right) \\
&= \frac{8E_0}{\rho_b}\left(\arctan\left(\frac{E_0 - \eta_b + \mu_b}{\rho_b}\right) + \arctan\left(\frac{E_0 - \eta_b - \mu_b}{\rho_b}\right)\right)
\end{aligned} \tag{A.31}$$

Here, we have introduced the quantities

$$\sigma_b := \boldsymbol{p}_0 \cdot (\boldsymbol{p}_0 - \boldsymbol{\tau}) \ , \tag{A.32}$$

$$\eta_b := \frac{\sigma_b \left(E_0 - \epsilon_b\right)}{|\boldsymbol{p}_0 - \boldsymbol{\tau}|^2} \ , \tag{A.33}$$

$$\mu_b := \sqrt{\frac{\tau^2 p_0^2 - \left(\boldsymbol{\tau} \cdot \boldsymbol{p}_0\right)^2}{|\boldsymbol{p}_0 - \boldsymbol{\tau}|^2}\left(1 - \frac{\left(E_0 - \epsilon_b\right)^2}{|\boldsymbol{p}_0 - \boldsymbol{\tau}|^2}\right)} \ , \tag{A.34}$$

$$\rho_b := \sqrt{\left(E_0 - \eta_b\right)^2 - \mu_b^2} \tag{A.35}$$

by applying the relations below,

$$\int_{-1}^{1} dx\ \delta\left(x - \frac{E_0 - \epsilon_b}{|\boldsymbol{p}_0 - \boldsymbol{\tau}|}\right) d(x) = E_0 - \eta_b \ , \tag{A.36}$$

$$\int_{-1}^{1} dx\ \delta\left(x - \frac{E_0 - \epsilon_b}{|\boldsymbol{p}_0 - \boldsymbol{\tau}|}\right) e(x) = \mu_b \ , \tag{A.37}$$

$$\int_{-1}^{1} dx\ \delta\left(x - \frac{E_0 - \epsilon_b}{|\boldsymbol{p}_0 - \boldsymbol{\tau}|}\right) \left(e(x) + d(x)\right) = \mu_b + \left(E_0 - \eta_b\right) \tag{A.38}$$

$$\int_{-1}^{1} dx\ \delta\left(x - \frac{E_0 - \epsilon_b}{|\boldsymbol{p}_0 - \boldsymbol{\tau}|}\right) \left(e(x) - d(x)\right) = \mu_b - \left(E_0 - \eta_b\right) \tag{A.39}$$

$$\int_{-1}^{1} dx\ \delta\left(x - \frac{E_0 - \epsilon_b}{|\boldsymbol{p}_0 - \boldsymbol{\tau}|}\right) \sqrt{d^2(x) - \mathrm{e}^2(x)} = \sqrt{\left(E_0 - \eta_b\right)^2 - \mu_b^2} = \rho_b \ . \tag{A.40}$$

Notice, in particular, the square in the denominator of η_b, in contrast to Sáenz & Überall (1982). In order to further simplify (A.31) we write one of the inverse tangents as a limit and then

transform their sum by using $\arctan(x)+\arctan(y)=\arctan((x+y)/(1-xy))$:

$$\begin{aligned}
&\arctan\left(\frac{E_0-\eta_b+\mu_b}{\rho_b}\right)+\arctan\left(\frac{E_0-\eta_b-\mu_b}{\rho_b}\right)= \\
&\arctan\left(\frac{E_0-\eta_b+\mu_b}{\rho_b}\right)+\lim_{\epsilon\to 1}\arctan\left(\frac{E_0-\eta_b-\epsilon\mu_b}{\rho_b}\right)= \\
&\lim_{\epsilon\to 1}\arctan\left(\frac{2\left(E0-\eta_b\right)+\mu_b-\epsilon\mu_b}{\rho_b-\left(E0-\eta_b+\mu_b\right)\left(E0-\eta_b-\epsilon\mu_b\right)/\rho_b}\right)=\lim_{\epsilon\to 0}\arctan(\frac{1}{\epsilon})=\frac{\pi}{2}
\end{aligned} \tag{A.41}$$

Thus:

$$\tilde{I}_2^b{=}2\pi\frac{2E_0}{\rho_b}\ . \tag{A.42}$$

We proceed similarly with the third sub-integral:

$$\begin{aligned}
\tilde{I}_2^c\ :=\ & \left(-m^2\right)\int_{-1}^{1}dx\ \delta\left(x-\frac{E_0-\epsilon_b}{|\boldsymbol{p}_0-\boldsymbol{\tau}|}\right)\int_0^{2\pi}d\phi_\gamma\ \frac{1}{\left(d-e\cos\phi_\gamma\right)^2} \\
=\ & \left(-m^2\right)\int_{-1}^{1}dx\ \delta\left(x-\frac{E_0-\epsilon_b}{|\boldsymbol{p}_0-\boldsymbol{\tau}|}\right)\left(\int_0^{\frac{\pi}{2}}d\phi_\gamma\frac{1}{\left(d-e\cos\phi_\gamma\right)^2}\right. \\
+\ & \left.\int_0^{\frac{\pi}{2}}d\phi_\gamma\frac{1}{\left(d+e\cos\phi_\gamma\right)^2}+\int_0^{\frac{\pi}{2}}d\phi_\gamma\frac{1}{\left(d-e\sin\phi_\gamma\right)^2}+\int_0^{\frac{\pi}{2}}d\phi_\gamma\frac{1}{\left(d+e\sin\phi_\gamma\right)^2}\right) \\
=\ & \frac{-4m^2d}{\left(d^2-\mathrm{e}^2\right)^{3/2}}\int_{-1}^{1}dx\ \delta\left(x-\frac{E_0-\epsilon_b}{|\boldsymbol{p}_0-\boldsymbol{\tau}|}\right)\left(\arctan\frac{d+e}{\sqrt{d^2-\mathrm{e}^2}}+\arctan\frac{d-e}{\sqrt{d^2-\mathrm{e}^2}}\right) \\
=\ & \frac{-4m^2\left(E_0-\eta_b\right)}{\rho_b^3}\left(\arctan\frac{E_0-\eta_b+\mu_b}{\rho_b}+\arctan\frac{E_0-\eta_b-\mu_b}{\rho_b}\right) \\
=\ & -2\pi\frac{m^2\left(E_0-\eta_b\right)}{\rho_b^3}
\end{aligned} \tag{A.43}$$

Combining the results, we obtain the following solution to the second integral:

$$\boxed{\begin{aligned}
\tilde{I}_2{:=}\ & \frac{4E^2-\tau^2}{k^2}\left(\tilde{I}_2^a+\tilde{I}_2^b+\tilde{I}_2^c\right) \\
=\ & 2\pi\frac{4E^2-\tau^2}{k^2}\left(-1+\frac{2E_0}{\rho_b}-\frac{m^2\left(E_0-\eta_b\right)}{\rho_b^3}\right)
\end{aligned}} \tag{A.44}$$

Third Integral

We need to express $\cos\phi$ as a function of $\cos\phi_\gamma$ in order to solve the third integral, since the latter is the integration variable. For this purpose, we will make use of the definition of ϕ as the angle between the normal vectors of two planes:

$$
\begin{aligned}
\cos\phi \quad &:= \quad \frac{(\boldsymbol{p}_0 \times \boldsymbol{k})\,(\boldsymbol{p} \times \boldsymbol{k})}{|\boldsymbol{p}_0 \times \boldsymbol{k}||\boldsymbol{p} \times \boldsymbol{k}|} \quad = \quad \frac{(\boldsymbol{p}_0 \cdot \boldsymbol{p})\,k^2 - (\boldsymbol{p}_0 \cdot \boldsymbol{k})\,(\boldsymbol{p} \cdot \boldsymbol{k})}{p_0 k \sin\theta_0\, pk \sin\theta} \\
&= \quad \frac{p_0^2 k^2 - (\boldsymbol{p}_0 \cdot \boldsymbol{\tau})\,k^2 - (\boldsymbol{p}_0 \cdot \boldsymbol{k})\,k^2 - (\boldsymbol{p}_0 \cdot \boldsymbol{k})\,(\boldsymbol{p} \cdot \boldsymbol{k})}{k^2 p p_0 \sin\theta \sin\theta_0} \\
&\overset{(A.15,A.16)}{=} \frac{p_0^2 k^2 - (\boldsymbol{p}_0 \cdot \boldsymbol{\tau})\,k^2 + \frac{a}{2}k^2 - (\boldsymbol{k} \cdot \boldsymbol{\tau})\,k^2 + \left(-\frac{a}{2} + \boldsymbol{k} \cdot \boldsymbol{\tau}\right)\left(k^2 + \frac{a}{2}\right))}{k^2 p p_0 \sin\theta \sin\theta_0} \\
&= \quad \frac{p_0^2 k^2 - (\boldsymbol{p}_0 \cdot \boldsymbol{\tau})\,k^2 + \frac{a}{2}k^2 - (\boldsymbol{k} \cdot \boldsymbol{\tau})\,k^2 - \frac{a}{2}k^2 - \frac{a^2}{4} + (\boldsymbol{k} \cdot \boldsymbol{\tau})\,k^2 + (\boldsymbol{k} \cdot \boldsymbol{\tau})\,\frac{a}{2}}{k^2 p p_0 \sin\theta \sin\theta_0} \\
&= \quad \frac{p_0^2 k^2 - (\boldsymbol{p}_0 \cdot \boldsymbol{\tau})\,k^2 - \frac{a^2}{4} + (\boldsymbol{k} \cdot \boldsymbol{\tau})\,\frac{a}{2}}{k^2 p p_0 \sin\theta \sin\theta_0} \\
&\overset{(A.11)}{=} \frac{p_0^2 k^2 - (\boldsymbol{p}_0 \cdot \boldsymbol{\tau})\,k^2 - k^2\,(E_0 - \epsilon_b)^2 - (\boldsymbol{k} \cdot \boldsymbol{\tau})\,k\,(E_0 - \epsilon_b)}{k^2 p p_0 \sin\theta \sin\theta_0} \\
&\overset{(A.18)}{=} \frac{p_0^2 - \boldsymbol{p}_0 \cdot \boldsymbol{\tau} - (E_0 - \epsilon_b)^2 - \left(bx + c\sqrt{1-x^2}\cos\phi_\gamma\right)(E_0 - \epsilon_b)}{p p_0 \sin\theta \sin\theta_0} \\
&= \quad \frac{p_0^2 - \boldsymbol{p}_0 \cdot \boldsymbol{\tau} - (E_0 - \epsilon_b)^2 - bx\,(E_0 - \epsilon_b) - c\sqrt{1-x^2}\,(E_0 - \epsilon_b)\cos\phi_\gamma}{p p_0 \sin\theta \sin\theta_0}
\end{aligned}
\tag{A.45}
$$

Using (A.45), we can now perform the integration. Note that the transversal momenta will completely cancel out.

$$
\begin{aligned}
\tilde{I}_3 \quad &:= \quad -\int_{-1}^{1} dx\;\delta\left(x - \frac{E_0 - \epsilon_b}{|\boldsymbol{p}_0 - \boldsymbol{\tau}|}\right)\int_0^{2\pi} d\phi_\gamma\;\frac{2 p p_0 \sin\theta \sin\theta_0 \cos\phi\left(4EE_0 - \tau^2 + 2k^2\right)}{(Ek - \boldsymbol{p} \cdot \boldsymbol{k})\,(E_0 k - \boldsymbol{p}_0 \cdot \boldsymbol{k})} \\
&\overset{(A.18,A.21,A.22,A.45)}{=} -2\left(4EE_0 - \tau^2 + 2k^2\right)\int_{-1}^{1} dx\;\delta\left(x - \frac{E_0 - \epsilon_b}{|\boldsymbol{p}_0 - \boldsymbol{\tau}|}\right)\int_0^{2\pi} d\phi_\gamma \\
&\qquad \times \frac{\overbrace{p_0^2 - \boldsymbol{p}_0 \cdot \boldsymbol{\tau} - (E_0 - \epsilon_b)^2 - bx\,(E_0 - \epsilon_b)}^{=:f} - \overbrace{c\sqrt{1-x^2}\,(E_0 - \epsilon_b)}^{=:g}\cos\phi_\gamma}{\underbrace{\epsilon_b^2 k^2 - \epsilon_b k^2 bx}_{=:h} - \underbrace{\epsilon_b k^2 c\sqrt{1-x^2}}_{=:j}\cos\phi_\gamma} \\
&= \quad -2\left(4EE_0 - \tau^2 + 2k^2\right)\int_{-1}^{1} dx\;\delta\left(x - \frac{E_0 - \epsilon_b}{|\boldsymbol{p}_0 - \boldsymbol{\tau}|}\right)\int_0^{2\pi} d\phi_\gamma\left(\frac{f}{h - j\cos\phi_\gamma} - \frac{g\cos\phi_\gamma}{h - j\cos\phi_\gamma}\right)
\end{aligned}
\tag{A.46}
$$

Again, we will consider the sub-integrals separately. The ϕ_γ-part of the first one is completely analogous to $\tilde{I}_2^b$ in (A.42), so its computation will not be repeated here.

$$
\tilde{I}_3^a = \frac{4f}{\sqrt{h^2 - j^2}}\int_{-1}^{1} dx\;\delta\left(x - \frac{E_0 - \epsilon_b}{|\boldsymbol{p}_0 - \boldsymbol{\tau}|}\right)\left(\arctan\frac{h + j}{\sqrt{h^2 - j^2}} + \arctan\frac{h - j}{\sqrt{h^2 - j^2}}\right) \tag{A.47}
$$

Carrying out the x-integration over the individual quantities provides

$$
\begin{aligned}
\int_{-1}^{1} dx\;\delta\left(x - \frac{E_0 - \epsilon_b}{|\boldsymbol{p}_0 - \boldsymbol{\tau}|}\right) f(x) \quad &= \quad p_0^2 - \boldsymbol{p}_0 \cdot \boldsymbol{\tau} - (E_0 - \epsilon_b)^2 - \frac{\boldsymbol{\tau} \cdot (\boldsymbol{p}_0 - \boldsymbol{\tau})\,(E_0 - \epsilon_b)^2}{|\boldsymbol{p}_0 - \boldsymbol{\tau}|^2} \\
&\overset{(A.27)}{=} \sigma_b - \eta_b\,(E_0 - \epsilon_b)
\end{aligned}
\tag{A.48}
$$

$$\begin{aligned}\int_{-1}^{1} dx\ \delta\left(x-\frac{E_0-\epsilon_b}{|\boldsymbol{p}_0-\boldsymbol{\tau}|}\right)h(x) &= \epsilon_b^2k^2-\epsilon_bk^2\frac{\boldsymbol{\tau}\cdot(\boldsymbol{p}_0-\boldsymbol{\tau})\,(E_0-\epsilon_b)}{|\boldsymbol{p}_0-\boldsymbol{\tau}|^2} \\ &\overset{(A.27)}{=} \epsilon_bk^2\,(E_0-\eta_b)\end{aligned} \tag{A.49}$$

$$\int_{-1}^{1} dx\ \delta\left(x-\frac{E_0-\epsilon_b}{|\boldsymbol{p}_0-\boldsymbol{\tau}|}\right)j(x) = \epsilon_bk^2\mu_b \tag{A.50}$$

$$\int_{-1}^{1} dx\ \delta\left(x-\frac{E_0-\epsilon_b}{|\boldsymbol{p}_0-\boldsymbol{\tau}|}\right)(j(x)+h(x)) = \epsilon_bk^2\,(\mu_b+(E_0-\eta_b)) \tag{A.51}$$

$$\int_{-1}^{1} dx\ \delta\left(x-\frac{E_0-\epsilon_b}{|\boldsymbol{p}_0-\boldsymbol{\tau}|}\right)(j(x)-h(x)) = \epsilon_bk^2\,(\mu_b-(E_0-\eta_b)) \tag{A.52}$$

$$\int_{-1}^{1} dx\ \delta\left(x-\frac{E_0-\epsilon_b}{|\boldsymbol{p}_0-\boldsymbol{\tau}|}\right)\sqrt{h^2(x)-j^2(x)} = \epsilon_bk^2\sqrt{(E_0-\eta_b)^2-\mu_b^2}=\epsilon_bk^2\rho_b\ . \tag{A.53}$$

Inserting (A.48) - (A.53) into (A.47) finally yields

$$\begin{aligned}\tilde{I}_3^a &= 4\frac{\sigma_b-\eta_b\,(E_0-\epsilon_b)}{\epsilon_bk^2\rho_b}\left(\arctan\frac{E_0-\eta_b+\mu_b}{\rho_b}+\arctan\frac{E_0-\eta_b-\mu_b}{\rho_b}\right) \\ &= 2\pi\frac{\sigma_b-\eta_b(E_0-\epsilon_b)}{\epsilon_bk^2\rho_b}\ .\end{aligned} \tag{A.54}$$

Once more, the second part can be computed in a similar way:

$$\begin{aligned}\tilde{I}_3^b &:= -\int_{-1}^{1} dx\ \delta\left(x-\frac{E_0-\epsilon_b}{|\boldsymbol{p}_0-\boldsymbol{\tau}|}\right)\int_0^{2\pi} d\phi_\gamma\left(\frac{g\cos\phi_\gamma}{h-j\cos\phi_\gamma}\right) \\ &= -\int_{-1}^{1} dx\ g \\ &\times\left(\int_0^{\frac{\pi}{2}} d\phi_\gamma\frac{\cos(\phi_\gamma)}{h-j\cos\phi_\gamma}-\int_0^{\frac{\pi}{2}} d\phi_\gamma\frac{\cos(\phi_\gamma)}{h+j\cos\phi_\gamma}+\int_0^{\frac{\pi}{2}} d\phi_\gamma\frac{\sin(\phi_\gamma)}{h-j\sin\phi_\gamma}-\int_0^{\frac{\pi}{2}} d\phi_\gamma\frac{\sin(\phi_\gamma)}{h+j\sin\phi_\gamma}\right) \\ &= -2\frac{g}{j}\left(\frac{2h}{\sqrt{h^2-j^2}}\arctan\frac{h+j}{\sqrt{h^2-j^2}}+\frac{2h}{\sqrt{h^2-j^2}}\arctan\frac{h-j}{\sqrt{h^2-j^2}}-\pi\right)\ .\end{aligned} \tag{A.55}$$

With (A.49), (A.50) and

$$\int_{-1}^{1} dx\ \delta\left(x-\frac{E_0-\epsilon_b}{|\boldsymbol{p}_0-\boldsymbol{\tau}|}\right)g(x) = \mu_b\,(E_0-\epsilon_b) \tag{A.56}$$

we obtain

$$\begin{aligned}\tilde{I}_3^b &= -2\frac{E_0-\epsilon_b}{\epsilon_bk^2}\left(\frac{2\,(E_0-\eta_b)}{\rho_b}\arctan\frac{E_0-\eta_b+\mu_b}{\rho_b}+\frac{2\,(E_0-\eta_b)}{\rho_b}\arctan\frac{E_0-\eta_b-\mu_b}{\rho_b}-\pi\right) \\ &= -2\pi\frac{E_0-\epsilon_b}{\epsilon_bk^2}\left(\frac{E_0-\eta_b}{\rho_b}-1\right)\ .\end{aligned} \tag{A.57}$$

By combining (A.54) with (A.57), we get the following solution to the third integral:

$$\boxed{\begin{aligned}\tilde{I}_3 &:= -2\left(4EE_0-\tau^2+2k^2\right)\left(\tilde{I}_3^a+\tilde{I}_3^b\right)\\ &= -2\pi\frac{2\left(4EE_0-\tau^2+2k^2\right)}{\epsilon_b k^2}\left(\frac{\sigma_b}{\rho_b}-(E_0-\epsilon_b)\left(\frac{E_0}{\rho_b}-1\right)\right)\end{aligned}} \tag{A.58}$$

Fourth Integral

$$\begin{aligned}\tilde{I}_4 &:= 2k^2\int_{-1}^{1}dx\;\delta\left(x-\frac{E_0-\epsilon_b}{|\boldsymbol{p}_0-\boldsymbol{\tau}|}\right)\int_0^{2\pi}d\phi_\gamma\;\frac{p_\perp^2+p_{0\perp}^2}{(Ek-\boldsymbol{p}\cdot\boldsymbol{k})\,(E_0k-\boldsymbol{p}_0\cdot\boldsymbol{k})}\\
&= 2k^2\int_{-1}^{1}dx\;\delta\left(x-\frac{E_0-\epsilon_b}{|\boldsymbol{p}_0-\boldsymbol{\tau}|}\right)\int_0^{2\pi}d\phi_\gamma\;\left(\frac{p_\perp^2}{\epsilon_b k^2\left(\epsilon_b-\frac{\boldsymbol{k}\cdot\boldsymbol{\tau}}{k}\right)}+\frac{p_{0\perp}^2}{\epsilon_b k^2\left(\epsilon_b-\frac{\boldsymbol{k}\cdot\boldsymbol{\tau}}{k}\right)}\right)\\
&\overset{(A.18)}{=} 2k^2\int_{-1}^{1}dx\;\delta\left(x-\frac{E_0-\epsilon_b}{|\boldsymbol{p}_0-\boldsymbol{\tau}|}\right)\int_0^{2\pi}d\phi_\gamma\;\left(\frac{p_\perp^2}{\epsilon_b k^2\left(\epsilon_b-\left(xb-\sqrt{1-x^2}\,c\cos\phi_\gamma\right)\right)}\right.\\
&\qquad\left.+\frac{p_{0\perp}^2}{\epsilon_b k^2\left(\epsilon_b-\left(xb-\sqrt{1-x^2}\,c\cos\phi_\gamma\right)\right)}\right)\\
&= \frac{4\pi k^2p_\perp^2}{\epsilon_b k^2\rho_b}+2k^2\int_{-1}^{1}dx\;\delta\left(x-\frac{E_0-\epsilon_b}{|\boldsymbol{p}_0-\boldsymbol{\tau}|}\right)\int_0^{2\pi}d\phi_\gamma\;\left(\frac{p_{0\perp}^2}{\epsilon_b k^2\left(\epsilon_b-\left(xb-\sqrt{1-x^2}\,c\cos\phi_\gamma\right)\right)}\right)\\
&\overset{(A.20)}{=} \frac{4\pi\left(p_\perp^2+p_0^2\right)}{\epsilon_b\rho_b}-\frac{2}{\epsilon_b}\int_{-1}^{1}dx\;\delta\left(x-\frac{E_0-\epsilon_b}{|\boldsymbol{p}_0-\boldsymbol{\tau}|}\right)\int_0^{2\pi}d\phi_\gamma\\
&\qquad\times\left(\frac{E_0^2-2E_0\left(\epsilon_b-xb+\sqrt{1-x^2}\,c\cos\phi_\gamma\right)+\left(\epsilon_b-xb+\sqrt{1-x^2}\,c\cos\phi_\gamma\right)^2}{\epsilon_b-xb+\sqrt{1-x^2}\,c\cos\phi_\gamma}\right)\\
&= \frac{4\pi\left(p_\perp^2-m^2\right)}{\epsilon_b\rho_b}-\frac{2}{\epsilon_b}\int_{-1}^{1}dx\;\delta\left(x-\frac{E_0-\epsilon_b}{|\boldsymbol{p}_0-\boldsymbol{\tau}|}\right)\int_0^{2\pi}d\phi_\gamma\\
&\qquad\times\left(\frac{-2E_0\left(\epsilon_b-xb+\sqrt{1-x^2}\,c\cos\phi_\gamma\right)+\left(\epsilon_b-xb+\sqrt{1-x^2}\,c\cos\phi_\gamma\right)^2}{\epsilon_b-xb+\sqrt{1-x^2}\,c\cos\phi_\gamma}\right)\\
&= \frac{4\pi\left(p_\perp^2-m^2\right)}{\epsilon_b\rho_b}+\frac{8\pi E_0}{\epsilon_b}-\int_{-1}^{1}dx\;\delta\left(x-\frac{E_0-\epsilon_b}{|\boldsymbol{p}_0-\boldsymbol{\tau}|}\right)\int_0^{2\pi}d\phi_\gamma\left(\epsilon_b-xb+\sqrt{1-x^2}\,c\cos\phi_\gamma\right)\\
&= \frac{4\pi\left(p_\perp^2-m^2\right)}{\epsilon_b\rho_b}+\frac{8\pi E_0}{\epsilon_b}-\frac{4\pi E_0}{\epsilon_b}+\frac{4\pi\eta_b}{\epsilon_b}\end{aligned} \tag{A.59}$$

Therefore, we obtain

$$\boxed{\tilde{I}_4=\frac{4\pi\left(p_\perp^2-m^2\right)}{\epsilon_b\rho_b}+\frac{4\pi}{\epsilon_b}\left(E_0+\eta_b\right)} \tag{A.60}$$

as a solution to the fourth integral.

Combined Solution

We finally obtain the following expression for the coherent cross-section, into which the expressions for the individual integrals (A.25, A.44, A.58 and A.60) need to be inserted:

$$\frac{d\sigma_{coh}}{dk} = \frac{2\pi r_0^2 \, Z^2 \alpha m^2}{p_0 v_0} \sum_{\boldsymbol{\tau}} |S|^2 \mathrm{e}^{-\tau^2 \langle u^2 \rangle / 3} \, \frac{(1 - F(\tau^2, Z))^2}{\tau^4 \, |\boldsymbol{p}_0 - \boldsymbol{\tau}|} \sum_i \tilde{I}_i \left(\boldsymbol{\tau} \right) \ . \tag{A.61}$$

Photon Collimation: the Mozley - de Wire Effect

We now consider the constraints imposed by the two δ-functions representing energy and momentum conservation, and remember the substitution $\cos\theta_\gamma = x$, where $\cos\theta_\gamma$ was defined as the angle between $\boldsymbol{p}_0 - \boldsymbol{\tau}$ and $\boldsymbol{k}$. This leads to a form of the evaluated integrals given below:

$$\int_{-1}^{1} dx \ \delta \left(x - \frac{E_0 - \epsilon_b}{|\boldsymbol{p}_0 - \boldsymbol{\tau}|} \right) = \int_{-1}^{1} d\cos\theta_\gamma \ \delta \left(\cos\theta_\gamma - \frac{E_0 - \epsilon_b}{|\boldsymbol{p}_0 - \boldsymbol{\tau}|} \right) \ . \tag{A.62}$$

Due to the Debye - Waller factor we have $\tau \ll p_0$, and so we can identify θ_γ with θ_0, the angle between $\boldsymbol{p}_0$ and $\boldsymbol{k}$. The effects of collimation around the electron axis can then be investigated simply by adjusting the integration limits in (A.62). Of particular interest is the case where the lower limit is increased, corresponding to a narrowing of the central aperture from 180° down to a smaller angle.

Incoherent Part

The fact that we have brought the cross-section of the incoherent part (A.7) into a form very similar to the coherent one (A.6) permits us to recycle all the integrations carried out before. The only thing that will still need our attention is the summation constraint (A.13) that now needs to be transformed into boundaries for the θ_τ-integration. The corresponding calculation is a bit tricky, but relies on straightforward mathematics, so we will only roughly point out our approach.

The main idea to transfer all the integration steps to the incoherent part is to introduce spherical coordinates $(\tau, \theta_\tau, \phi_\tau)$ by defininig θ_τ as the angle between $\boldsymbol{p}_0$ and $\boldsymbol{\tau}$. We can then rewrite the omnipresent expression $\boldsymbol{p}_0 \cdot \boldsymbol{\tau}$ accordingly and note that the angle ϕ_τ does not appear anywhere in the cross-section, leading to a constant factor of 2π. Now we transform (A.13) into boundaries for the θ_τ-integration that are still dependent on τ, so one must not interchange the order of the two integrals. We then obtain (A.65).

Here we note that the assumption $\tau \ll p_0$ is no longer valid because now, in contrast to the above considerations, we have 1 minus the Debye - Waller factor in the incoherent cross-section. Therefore, an adjustment of the integration boundaries does no longer correspond to a change in the collimation angles. The cases where one can still work with this assumption are discussed in the main article; the situations when the square-root becomes imaginary in (A.80) and (A.81) (see next page) can be "rescued" to some extent by introducing the case differentiations in these expressions, as a comparison with the Schiff cross-section (Schiff 1951) reveals.

Note that the derivation for the full solid angle is still perfectly valid as the integration boundaries remain unchanged here.

A.3 Final Cross-Sections

We pull out a factor of $2\pi/k^2$ in the $\tilde{I}_i$ to obtain the final expressions:

$$\frac{d\sigma_{coh}}{dk} = \frac{4\pi^2 r_0^2\, Z^2 \alpha m^2}{p_0 v_0\, k^2} \sum_{\boldsymbol{\tau}'} |S|^2 \mathrm{e}^{-\tau^2\langle u^2\rangle/3}\ \frac{(1-F(\tau^2,Z))^2}{\tau^4\,|\boldsymbol{p}_0-\boldsymbol{\tau}|} \sum_i I_i\,(\boldsymbol{\tau}) \tag{A.63}$$

$$\boldsymbol{\tau}'\text{: subject to } \cos(\psi_o)\,|\boldsymbol{p}_0-\boldsymbol{\tau}| \le E_0-\epsilon_b \le \cos(\psi_i)\,|\boldsymbol{p}_0-\boldsymbol{\tau}| \tag{A.64}$$

$$\frac{d\sigma_{inc}}{dk} = \nu \frac{r_0^2\, Z^2 \alpha m^2}{p_0 k^2} \int_{\tau_{min}}^{\tau_{min}} d\tau \int_{\theta_{\tau,min}(\tau)}^{\theta_{\tau,max}(\tau)} d\theta_\tau\ \sin\theta_\tau\ \left(1-\mathrm{e}^{-\tau^2\langle u^2\rangle/3}\right)\ \frac{(1-F(\tau^2,Z))^2}{\tau^2\,|\boldsymbol{p}_0-\boldsymbol{\tau}|} \sum_i I_i\,(\boldsymbol{\tau}) \tag{A.65}$$

$$I_1 = \frac{p_\perp^2\left(4E_0^2-\tau^2\right)}{\epsilon_b^2} \tag{A.66}$$

$$I_2 = \left(4E^2-\tau^2\right)\left(-1+\frac{2E_0}{\rho_b}-\frac{m^2\,(E_0-\eta_b)}{\rho_b^3}\right) \tag{A.67}$$

$$I_3 = \frac{2\left(4EE_0-\tau^2+2k^2\right)}{\epsilon_b}\left[(E_0-\epsilon_b)\left(\frac{E_0}{\rho_b}-1\right)-\frac{\sigma_b}{\rho_b}\right] \tag{A.68}$$

$$I_4 = \frac{2k^2}{\epsilon_b}\left(\frac{p_\perp^2-m^2}{\rho_b}+E_0+\eta_b\right) \tag{A.69}$$

$$p_\perp^2 = (p_0-\boldsymbol{\tau})^2-(E_0-\epsilon_b)^2 \tag{A.70}$$

$$\epsilon_b = \frac{p_0^2-(\boldsymbol{p}_0-\boldsymbol{\tau})^2}{2k} \tag{A.71}$$

$$\sigma_b = \boldsymbol{p}_0\cdot(\boldsymbol{p}_0-\boldsymbol{\tau}) \tag{A.72}$$

$$\eta_b = \frac{\sigma_b\,(E_0-\epsilon_b)}{|\boldsymbol{p}_0-\boldsymbol{\tau}|^2} \tag{A.73}$$

$$\mu_b = \sqrt{\frac{\tau^2 p_0^2-(\boldsymbol{\tau}\cdot\boldsymbol{p}_0)^2}{|\boldsymbol{p}_0-\boldsymbol{\tau}|^2}\left(1-\frac{(E_0-\epsilon_b)^2}{|\boldsymbol{p}_0-\boldsymbol{\tau}|^2}\right)} \tag{A.74}$$

$$\rho_b = \sqrt{(E_0-\eta_b)^2-\mu_b^2} \tag{A.75}$$

$$\tau_{min} = p_0-p-k \tag{A.76}$$

$$\tau_{max} = p_0+p+k \tag{A.77}$$

$$\theta_{\tau,min}(\tau) = \arccos\frac{p_0^2+\tau^2-|\boldsymbol{p}_0-\boldsymbol{\tau}|_{min}^2}{2p_0\tau} \tag{A.78}$$

$$\theta_{\tau,max}(\tau) = \arccos\frac{p_0^2+\tau^2-|\boldsymbol{p}_0-\boldsymbol{\tau}|_{max}^2}{2p_0\tau} \tag{A.79}$$

$$|\boldsymbol{p}_0-\boldsymbol{\tau}|_{min} = \begin{cases} k\cos\psi_o+\sqrt{k^2\cos^2\psi_o-2kE_0+p_0^2}, \text{ if } k^2\cos^2\psi_o-2kE_0+p_0^2>0 \\ k\cos\psi_o, \text{ if } k^2\cos^2\psi_o-2kE_0+p_0^2<0 \end{cases} \tag{A.80}$$

$$|\boldsymbol{p}_0-\boldsymbol{\tau}|_{max} = \begin{cases} k\cos\psi_i+\sqrt{k^2\cos^2\psi_i-2kE_0+p_0^2}, \text{ if } k^2\cos^2\psi_i-2kE_0+p_0^2>0 \\ \text{undefined otherwise } \left(\text{i.e. } \frac{d\sigma_{inc}}{dk}(\boldsymbol{\tau})\equiv 0\right) \end{cases} \tag{A.81}$$

Appendix B

Coherent Pair Production

B.1 Cross-Sections

It is a well known fact that bremsstrahlung is very similar to pair production on a quantitative level, that is, the Feynman diagrams describing the two processes are related closely (Figs. 3.2 and B.1). As a consequence, the corresponding differential cross-sections can be derived analogously, which was already recognized by Bethe & Heitler (1934), who published their cross-sections for the two processes in a single article. Since both involve interactions with a target's atomic nuclei, it is easy to predict that also coherent pair production (CPP) should exist, and the interference should now happen between electron or positron particle waves. Indeed, much of the early work on CB was also dedicated to this effect, and readers are referred to the literature cited in chapter 3 for ultrarelativistic versions of the CPP cross-section.

With the similarities in the cross-sections of the two processes, the integration to obtain the differential cross-section with respect to energy (of the bremsstrahlung photons or electrons/positrons) is analogous in both cases, but leads to even lengthier expressions here. For this reason, we will only give the final cross-sections. As before, the following discussion will be based on the first-order Born approximation (sidebar 3.2). Note that we will not detail any emission angle specificity of the generated pair as this is not of interest here.

Figure B.1 First-order Feynman diagrams for the generation of an electron-positron pair by a photon γ. Note the similarity to the bremsstrahlung process depicted in Fig. 3.2.

$$\frac{d\sigma_{coh}}{dE_+} = \frac{4\pi^2 m^2 \alpha r_0^2}{v_0 k^3} \sum_{\boldsymbol{\tau}'} |S|^2 e^{-\tau^2\langle u^2\rangle/3} \frac{(Z - F(\tau^2, Z))^2}{\tau^4 \left|\boldsymbol{p}_0 - \boldsymbol{\tau}\right|} \sum_i I_i\left(\boldsymbol{\tau}\right) \tag{B.1}$$

$$\boldsymbol{\tau}'\text{: subject to } |k - \epsilon_p| \leq \frac{p_+}{E_+}|\boldsymbol{k} - \boldsymbol{\tau}| \tag{B.2}$$

$$\frac{d\sigma_{inc}}{dE_+} = \nu \frac{r_0^2 Z^2 \alpha m^2}{k^3} \int_{\tau_{min}}^{\tau_{min}} d\tau \int_{\theta_{\tau,min}(\tau)}^{\theta_{\tau,max}(\tau)} d\theta_\tau \ \sin\theta_\tau \ \left(1 - e^{-\tau^2\langle u^2\rangle/3}\right) \ \frac{(Z - F(\tau^2, Z))^2}{\tau^2 \left|\boldsymbol{p}_0 - \boldsymbol{\tau}\right|} \sum_i I_i\left(\boldsymbol{\tau}\right) \tag{B.3}$$

$$I_1 = \left(4E_-^2 - \tau^2\right)\left(1 + \frac{2\mu_p^2 E_+ k - \left(E_+ k - \eta_p\right)\left(E_+^2 k^2 - 2E_+ k\eta_p + k^2 p_+^2\right)}{\rho_p^3}\right) \tag{B.4}$$

$$I_2 = \left(4E_+^2 - \tau^2\right)\left(1 + \frac{2\mu_p^2 E_- k - \left(\eta_p + \boldsymbol{\tau}\cdot\boldsymbol{k} - E_+ k\right)\left(E_+ k\left[E_+ k - 2\eta_p - 2\boldsymbol{\tau}\cdot\boldsymbol{k}\right]\right)}{\chi_p^3}\right.$$
$$\left. - \frac{k^2\left[k^2 - 2\boldsymbol{\tau}\cdot\boldsymbol{k} - 2\eta_p - p_-^2\right]}{\chi_p^3}\right) \tag{B.5}$$

$$I_3 = 4\left(4E_- E_+ - 2k^2 + \tau^2\right)\left(1 - \frac{k^2\left(\lambda_p - p_+^2\right) + \left(E_+ k\right)\left(\boldsymbol{\tau}\cdot\boldsymbol{k} - E_- k\right)}{\rho_p\, \boldsymbol{\tau}\cdot\boldsymbol{k}}\right.$$
$$\left. - \frac{k^2\left(\lambda_p - p_+^2 + \boldsymbol{\tau}\cdot\boldsymbol{k}\right) - E_+ k\left(E_- k + \boldsymbol{\tau}\cdot\boldsymbol{k}\right)}{\chi_p\, \boldsymbol{\tau}\cdot\boldsymbol{k}}\right) \tag{B.6}$$

$$I_4 = 2k^2\left(2 - \frac{\left(k^2 - \boldsymbol{\tau}\cdot\boldsymbol{k}\right)^2 - 2E_+ k\left(\boldsymbol{\tau}\cdot\boldsymbol{k} - E_- k\right) - k^2\left(p_+^2 + p_-^2\right)}{\rho_p\, \boldsymbol{\tau}\cdot\boldsymbol{k}}\right.$$
$$\left. - \frac{\left(k^2 - \boldsymbol{\tau}\cdot\boldsymbol{k}\right)^2 - 2E_+ k\left(\boldsymbol{\tau}\cdot\boldsymbol{k} + E_- k\right) - k^2\left(p_+^2 + p_-^2 - 2\boldsymbol{\tau}\cdot\boldsymbol{k}\right)}{\chi_p\, \boldsymbol{\tau}\cdot\boldsymbol{k}}\right) \tag{B.7}$$

$$\epsilon_p = \frac{k^2 - \left(\boldsymbol{k} - \boldsymbol{\tau}\right)^2}{2E_+} \tag{B.8}$$

$$\sigma_p = \boldsymbol{k}\cdot\left(\boldsymbol{k} - \boldsymbol{\tau}\right) \tag{B.9}$$

$$\lambda_p = E_+\left(k - \epsilon_p\right) \tag{B.10}$$

$$\eta_p = \frac{\sigma_p \lambda_p}{|\boldsymbol{k} - \boldsymbol{\tau}|^2} \tag{B.11}$$

$$\mu_p = p_+ \sqrt{\frac{\tau^2 k^2 - \left(\boldsymbol{\tau}\cdot\boldsymbol{k}\right)^2}{\left(\boldsymbol{k} - \boldsymbol{\tau}\right)^2}\left(1 - \frac{\lambda_p^2}{p_+^2\left(\boldsymbol{k} - \boldsymbol{\tau}\right)^2}\right)} \tag{B.12}$$

$$\rho_P = \sqrt{\left(E_+ k - \eta_P\right)^2 - \mu_P^2} \tag{B.13}$$

$$\chi_P = \sqrt{\left(\eta_p + \boldsymbol{\tau}\cdot\boldsymbol{k} - E_+ k\right)^2 - \mu_p^2} \tag{B.14}$$

$$\tau_{min} = k - p_- - p_p \tag{B.15}$$

$$\tau_{max} = k + p_- + p_p \tag{B.16}$$

$$\theta_{\tau,min}(\tau) = \arccos\frac{k^2 + \tau^2 - |\boldsymbol{k} - \boldsymbol{\tau}|_{min}^2}{2k\tau} \tag{B.17}$$

$$\theta_{\tau,max}(\tau) = \arccos\frac{k^2 + \tau^2 - |\boldsymbol{k} - \boldsymbol{\tau}|_{max}^2}{2k\tau} \tag{B.18}$$

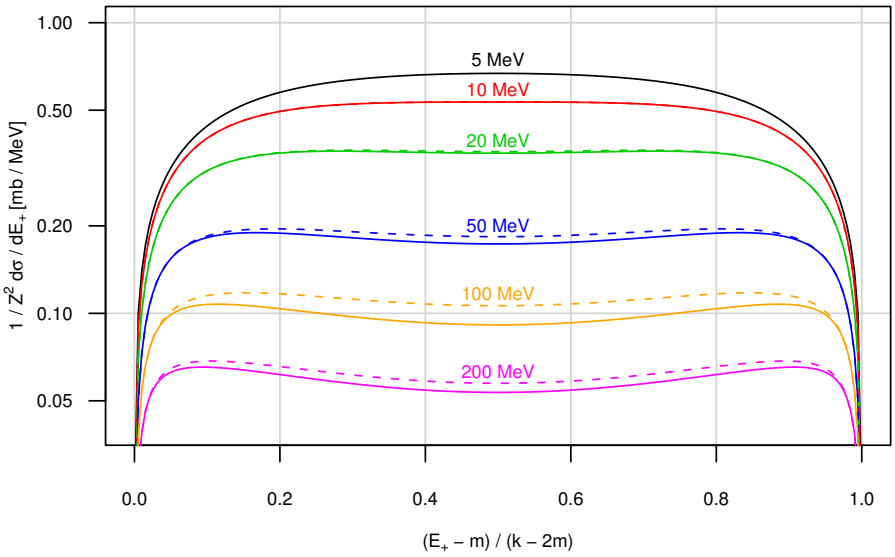

Figure B.2 Positron energy spectra produced by photons with various energies. Solid lines: Incoherent part in a tungsten single-crystal; dashed lines: spectrum from amorphous tungsten. Note the normalisation on the x-axis.

$$|\boldsymbol{k} - \boldsymbol{\tau}|_{min} = |p_+ + p_-| \tag{B.19}$$
$$|\boldsymbol{k} - \boldsymbol{\tau}|_{max} = |p_+ - p_-| \tag{B.20}$$

B.2 Discussion

Incoherent Part

Again, we start with the incoherent part, which we now discuss for the case of a tungsten single crystal ($Z = 74$) at a temperature of 300 K (remember the Z^2 dependence of the cross-section).

Introducing the electron and positron total energies E_- and E_+, the resulting positron energy spectra are depicted in Fig. B.2 for some energies k of the incident photon. Below 20 MeV, there is hardly any difference between amorphous and single-crystalline tungsten, which already tells us that the coherent fraction in this energy range will be negligible.

The positron energy spectra shown are symmetric and thus equal to the electron energy spectra, which is a consequence of the first-order Born approximation. Actually, attracting and repelling forces between the atomic nucleus and the produced leptons lead to a suppression of the positron wave function near the nucleus and a corresponding enhancement of the electron wave function in its vicinity (a fact which is obviously not captured by the plane waves the Born approximation is based on). A very detailed discussion of this behaviour was given by Motz et al. (1969). Here, we only state that as a consequence the energy spectra will be asymmetric, but symmetry gets more and more restored with increasing photon energies or lower atomic numbers Z. Thus, the results for the 5 MeV photons in Fig. B.2 can already be considered quite reliable.

Coherent Part

As can be seen in Fig. B.3 the coherent part of the cross-section exhibits a peak structure similar to that of CB. A comparison of the magnitudes with those shown in Fig. B.2 reveals that the

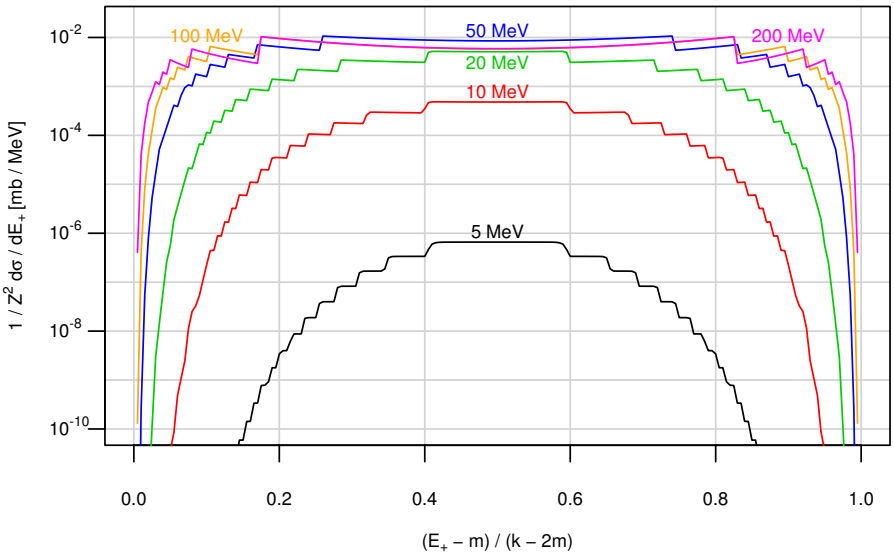

Figure B.3 Coherent part of the pair production cross-section for photons of various energies incident on a tungsten single-crystal along the 110-direction. For photon energies relevant to medical physics ($k < 25\,\text{MeV}$), its magnitude is tiny compared with the incoherent part (Fig. B.2).

change in the total cross-section by using a tungsten target is insignificant for the photon energies considered. Both a notable increase as well as a decrease would have had interesting implications for the design of photon filters. While an increase would have allowed to filter out high energy photons more efficiently, resulting in a narrower spectrum for instance in the case of treatment beams, a decrease would have allowed for a larger thickness of flattening filters, yielding a more efficient removal of low energy photons and again a sharper spectrum. Unfortunately, the change in the total cross-section is far too small to be exploited in any of these ideas.

The situation changes if one increases the photon energy above 10 GeV, where indeed a notable change in the cross-section occurs (data not shown). Clearly, this energy range is of no interest in medical physics.

Acknowledgements

This work relied on the help of many people. I would like to express my gratitude to my supervisor and principal investigator Prof. Dr. Uwe Oelfke, who has been very open to initiating projects off the beaten track and whose initial idea led to the introduction of coherent bremsstrahlung into image guided radiotherapy. My thanks also go to the head of our department, Prof. Dr. Schlegel, who readily provided the funding for the Medipix detectors, and to Dr. Simeon Nill, who supported much of the experimental work. I would like to acknowledge Prof. Dr. Jan Wilkens and Prof. Dr. Peter Bachert, too, for being members of my advisory commitee at DKFZ.

Many of the results presented in this thesis were initially obtained in student projects. I would like to thank Irene Marco Rius for elaborating differences between the cross-sections derived in this work and those previously published. A big "thank you" goes to Marcus Zuber for spending endless hours in our basement laboratory, where he carried out most of the measurements required for the threshold equalisation comparisons. He also implemented the code for determining multiplicities and many other useful computer programs. Thanks very much to Julia Schulze, too, who carried out the CT measurements presented here, to Patrick Schünke, for implementing the pixel-wise energy calibration, and to Dr. Sönke Bartling and Jan Kuntz for providing the contrast agents.

I am indebted to Gernot Echner and Armin Runz for designing many of the experimental devices used to hold X-ray tube, stepper motors and detectors, and to the staff of the mechanical workshop at DKFZ for constructing these items. My thanks also go to the radiation protection team, in particular Dr. Wolfgang Kuebler for designing the shielding and mount for the americium source, as well as to Mechthild Kämmer and Barbara Kahn for helpful advice and the provision of other radioactive sources.

I would like to thank the staff from the technology transfer office at DKFZ, in particular Dr. Frieder Kern, for managing the patent application describing the use of coherent bremsstrahlung in clinical LINACs. Furthermore, my thanks go to patent attorney Martin Abel for preparing the actual application.

The part of my work concerning the Medipix detectors would not have been possible without the collaboration with the Freiburg Materials Research Center, and I would like to thank PD Dr. Michael Fiederle for being very open to establishing this project. The commissioning of the two detector systems heavily relied on the support of Andreas Zwerger, who did not hesitate to visit DKFZ during weekends in order to make things work, and who designed the necessary electronics. I would also like to thank Dr. Alex Fauler for helpful discussions concerning the properties of cadmium telluride.

I would like to acknowledge help from the Erlangen Centre for Astroparticle Physics. In particular, my thank goes to Prof. Dr. Gisela Anton, Dr. Thilo Michel and Ewald Guni for lots of advise and the opportunity to perform initial measurements with their americium source when ours was not ready yet. Also, I am grateful to the people of the Medipix community for performing all the years of work that led to the opportunity to work with their detectors.

I am grateful to Prof. Dr. David Jaffray from the Princess Margaret Hospital in Toronto for directing my attention to coherent scatter imaging, for providing the drill core samples and for an invitation to give a talk at his department.

Last but not least, I would like to thank all the people I shared an office with at DKFZ, for many discussions, lots of proofreading and making my stay at DKFZ enjoyable. In particular, these are Mark Bangert, Malte Frese, Martin Fast, Prof. Dr. Emily Heath and Dr. Martin Tacke.

Bibliography

Adishev, Y. N., Zabaev, V. N., Kaplin, V. V., Razin, S. V., Uglov, S. R., Kuznetsov, S. I. & Kunashenko, Y. P. (2003). Parametric x-ray radiation generated by 5.7-MeV electrons in a pyrolytic-graphite crystal, *Phys. Atom. Nuclei* **66**(2): 420–422.

Alig, R. C. & Bloom, S. (1975). Electron-Hole-Pair creation energies in semiconductors, *Phys. Rev. Lett.* **35**(22): 1522.

Alvarez, R. E. & Macovski, A. (1976). Energy-selective reconstructions in x-ray computerised tomography, *Phys. Med. Biol.* **21**(5): 733–744.

Amsler, C. (2008). Review of particle physics, *Physics Letters B* **667**(1-5): 1–6.

Andersen, J. & Laegsgaard, E. (1988). Coherent bremsstrahlung and sidebands for channeled electrons, *Nucl. Instrum. Methods Phys. Res. B* **33**(1-4): 11–17.

Andersen, J. U., Eriksen, K. R. & Laegsgaard, E. (1981). Planar-Channeling radiation and coherent bremsstrahlung for MeV electrons, *Phys. Scr.* **24**: 588–600.

Bale, D. S. & Szeles, C. (2008). Nature of polarization in wide-bandgap semiconductor detectors under high-flux irradiation: Application to semi-insulating Cd(1-x)Zn(x)Te, *Phys. Rev. B* **77**(3): 35205.

Ballabriga, R., Campbell, M., Heijne, E. H. M., Llopart, X. & Tlustos, L. (2007). The medipix3 prototype, a pixel readout chip working in single photon counting mode with improved spectrometric performance, *Nuclear Science Symposium Conference Record, 2006. IEEE*, Vol. 6, p. 3557–3561.

Barrett, H. H., Eskin, J. D. & Barber, H. B. (1995). Charge transport in arrays of semiconductor gamma-ray detectors, *Phys. Rev. Lett.* **75**(1): 156–159.

Bethe, H. & Heitler, W. (1934). On the stopping of fast particles and on the creation of positive electrons, *Proc. R. Soc. London A* **146**(856): 83–112.

Bilokon, H., Bologna, G., Celani, F., Piazzoli, B., Falcioni, R., Mannocchi, G. & Picchi, P. (1983). Coherent bremsstrahlung in crystals as a tool for producing high energy photon beams to be used in photoproduction experiments at CERN SPS, *Nucl. Instr. and Meth.* **204**(2-3): 299–310.

Binder, N., Matthäus, L., Burgkart, R. & Schweikard, A. (2005). A robotic c-arm fluoroscope, *Int. J. Med. Rob. Comput. Assist. Surg.* **1**(3): 108–116.

Bissonnette, J., Moseley, D. J. & Jaffray, D. A. (2008). A quality assurance program for image quality of cone-beam CT guidance in radiation therapy, *Med. Phys.* **35**(5): 1807–15.

Bloch, F. (1933). Ionization of matter by charged particles, *Ann. Physik* **16**: 285–293.

Bonham, R. A. & Strand, T. G. (1963). Analytical expressions for potentials of neutral Thomas—Fermi—Dirac atoms and for the corresponding atomic scattering factors for x rays and electrons, *J. Chem. Phys.* **39**(9): 2200–2204.

Boone, J. M. (1994). An analytical edge spread function model for computer fitting and subsequent calculation of the LSF and MTF, *Med. Phys.* **21**(10): 1541.

Borie, E. (1972). Screening and second born corrections to bremsstrahlung at intermediate energies, *Nuovo Cimento A* **11**(4): 969–982.

Campbell, M., Heijne, E. H. M., Meddeler, G., Pernigotti, E. & Snoeys, W. (1998). Readout for a 64 x 64 pixel matrix with 15-bit single photon counting, *IEEE Trans. Nucl. Sci* **45**(3): 751–753.

Casnati, E., Tartari, A., Baraldi, C. & Napoli, G. (1984). Experimental k-shell fluorescence yield of monocrystalline germanium, *J. Phys. B* **17**: 2413.

Chouffani, K., Überall, H., Genz, H., Stascheck, P. H., Nething, U. & Richter, A. (1999). Low energy channeling radiation experiments in a germanium crystal, *Nucl. Instrum. Methods Phys. Res. B* **152**(4): 479–493.

Cuello, G. J. (2008). Structure factor determination of amorphous materials by neutron diffraction, *J. Phys.: Condens. Matter* **20**(24): 244109.

Durst, J., Bartl, P., Kreisler, B., Michel, T. & Anton, G. (2008). Monte carlo simulation of pixelated photon counting x-ray detectors like the medipix2 and the medipix3 using high-Z sensor materials, *IEEE Nuclear Science Symposium Conference Record, 2008*, p. 4990–4994.

Faddegon, B. A., Wu, V., Pouliot, J., Gangadharan, B. & Bani-Hashemi, A. (2008). Low dose megavoltage cone beam computed tomography with an unflattened 4 MV beam from a carbon target, *Med. Phys.* **35**(12): 5777–5786.

Firsching, M., Butler, A. P., Scott, N., Anderson, N. G., Michel, T. & Anton, G. (2009). Contrast agent recognition in small animal CT using the medipix2 detector, *Nucl. Instr. and Meth. A* **607**(1): 179–182.

Flampouri, S., Evans, P. M., Verhaegen, F., Nahum, A. E., Spezi, E. & Partridge, M. (2002). Optimization of accelerator target and detector for portal imaging using monte carlo simulation and experiment, *Phys. Med. Biol.* **47**(18): 3331–3349.

Gemmell, D. S. (1974). Channeling and related effects in the motion of charged particles through crystals, *Reviews of Modern Physics* **46**(1): 129.

Greiffenberg, D., Fauler, A., Zwerger, A. & Fiederle, M. (2011). Energy resolution and transport properties of CdTe-Timepix-Assemblies, *J. Inst.* **6**(01): C01058–C01058.

Harding, G. (1987). X-ray diffraction computed tomography, *Med. Phys.* **14**(4): 515.

Harding, G. & Schreiber, B. (1999). Coherent x-ray scatter imaging and its applications in biomedical science and industry, *Rad. Phys. Chem.* **56**(1-2): 229–245.

Hastie, T., Tibshirani, R., Friedman, J. H. & Robert Tibshirani, J. H. F. (2001). *The Elements of Statistical Learning*, Springer.

Holy, T., Jakubek, J., Pospisil, S., Uher, J., Vavrik, D. & Vykydal, Z. (2006). Data acquisition and processing software package for medipix2, *Nucl. Instr. and Meth. A* **563**(1): 254–258.

Hunklinger, S. (2009). *Festkörperphysik*, 2nd, revised edition. edn, Oldenbourg.

Jaffray, D. A. & Siewerdsen, J. H. (2000). Cone-beam computed tomography with a flat-panel imager: Initial performance characterization, *Med. Phys.* **27**(6): 1311–1323.

Jenkins, R., Manne, R., Robin, R. & Senemaud, C. (1991). IUPAC-nomenclature system for x-ray spectroscopy, *X-Ray Spectrometry* **20**(3): 149–155.

Kane, P. P., Kissel, L., Pratt, R. H. & Roy, S. C. (1986). Elastic scattering of gamma-rays and x-rays by atoms, *Phys. Rep.* **140**(2): 75–159.

Koch, H. W. & Motz, J. W. (1959). Bremsstrahlung Cross-Section formulas and related data, *Rev. Mod. Phys.* **31**: 920–955.

Koenig, T., Zwerger, A., Zuber, M., Schuenke, P., Nill, S., Guni, E., Fauler, A., Fiederle, M. & Oelfke, U. (2010). On the energy response function of a CdTe medipix2 hexa detector, *Nucl. Instr. and Meth. A* **in press**.

Kraus, V., Holik, M., Jakubek, J., Kroupa, M., Soukup, P. & Vykydal, Z. (2011). FITPix — fast interface for timepix pixel detectors, *J. Inst.* **6**(01): C01079–C01079.

Llopart, X. (2007). Design and characterization of 64K pixels chips working in single photon processing mode, *Mid Sweden University* .

Llopart, X., Ballabriga, R., Campbell, M., Tlustos, L. & Wong, W. (2007). Timepix, a 65k programmable pixel readout chip for arrival time, energy and/or photon counting measurements, *Nucl. Instr. and Meth. A* **581**(1-2): 485–494.

Llopart, X., Campbell, M., Dinapoli, R., Segundo, D. S. & Pernigotti, E. (2002). Medipix2: A 64-k pixel readout chip with 55-m square elements working in single photon counting mode, *IEEE Trans. Nucl. Sci.* **49**(5): 2279.

Lohmann, D., Peise, J., Ahrens, J., Anthony, I., Arends, H. J., Beck, R., Crawford, R., Hünger, A., Kaiser, K. H. & Kellie, J. D. (1994). Linearly polarized photons at MAMI (Mainz), *Nucl. Instrum. Methods Phys. Res. A* **343**(2-3).

Michel, T., Anton, G., Böhnel, M., Durst, J., Firsching, M., Korn, A., Kreisler, B., Loehr, A., Nachtrab, F. & Niederlöhner, D. (2006). A fundamental method to determine the signal-to-noise ratio (SNR) and detective quantum efficiency (DQE) for a photon counting pixel detector, *Nucl. Instr. and Meth. A* **568**(2): 799–802.

Motz, J. W., Olsen, H. A. & Koch, H. W. (1969). Pair production by photons, *Rev. Mod. Phys.* **41**(4): 581–639.

Mozley, R. & De Wire, J. (1963). Monochromatic bremsstrahlung from thin crystals, *Nuovo Cimento* **27**(5): 1281–1285.

Mueller, K., Chang, J., Amols, H. & Ling, C. (2000). Cone-beam computed tomography (CT) for a megavoltage linear accelerator (LINAC) using an electronic portal imaging device (EPID) and the algebraic reconstruction technique (ART), *Eng. Med. Biol.* **4**: 2875–2878.

Nasonov, N., Pokhil, G., Voronov, V. & Zhukova, P. (1998). X-ray coherent bremsstrahlung by low energy electrons, *Nucl. Instrum. Methods Phys. Res. B* **145**: 150–154.

Ostapiak, O. Z., O'Brien, P. F. & Faddegon, B. A. (1998). Megavoltage imaging with low z targets: Implementation and characterization of an investigational system, *Med. Phys.* **25**(10): 1910–1918.

Palazzi, G. D. (1968). High-Energy bremsstrahlung and electron pair production in thin crystals, *Rev. Mod. Phys.* **40**(3): 611.

Peng, L. M., Ren, G., Dudarev, S. L. & Whelan, M. J. (1996). Debye-Waller factors and absorptive scattering factors of elemental crystals, *Acta Cryst. A* **108**: 7673.

Pouliot, J., Bani-Hashemi, A., Chen, J., Svatos, M., Ghelmansarai, F., Mitschke, M., Aubin, M., Xia, P., Morin, O., Bucci, K., Roach, M., Hernandez, P., Zheng, Z., Hristov, D. & Verhey, L. (2005). Low-dose megavoltage cone-beam CT for radiation therapy, *Int. J. Radiat. Oncol. Biol. Phys.* **61**(2): 552–60.

Procz, S., Lubke, J., Zwerger, A., Mix, M. & Fiederle, M. (2009). Optimization of medipix-2 threshold masks for spectroscopic X-Ray imaging, *IEEE Trans. Nucl. Sci.* **56**: 1795–1799.

R Development Core Team (2009). R: A language and environment for statistical computing. **URL:** *http://www.R-project.org*

Ruchala, K. J., Olivera, G. H., Kapatoes, J. M., Schloesser, E. A., Reckwerdt, P. J. & Mackie, T. R. (2000). Megavoltage CT image reconstruction during tomotherapy treatments, *Phys. Med. Biol.* **45**(12): 3545–3562.

Salvat, F., Fernández-Varea, J. M., Acosta, E. & Sempau, J. (2001). *PENELOPE: A code system for Monte Carlo simulation of electron and photon transport*, http://www.nea.fr/dbprog/penelope.pdf.

Salvat, F., Martinez, J. D., Mayol, R. & Parellada, J. (1987). Analytical Dirac-Hartree-Fock-Slater screening function for atoms(Z=1–92), *Phys. Rev. A* **36**(2): 467–474.

Sarfehnia, A., Jabbari, K., Seuntjens, J. & Podgorsak, E. B. (2007). Experimental verification of beam quality in high-contrast imaging with orthogonal bremsstrahlung photon beams, *Med. Phys.* **34**(7): 2896–906.

Schiff, L. I. (1951). Energy-Angle distribution of thin target bremsstrahlung, *Phys. Rev.* **83**(2): 252.

Schlomka, J., Roessl, E., Dorscheid, R., Dill, S., Martens, G., Istel, T., Bäumer, C., Herrmann, C., Steadman, R., Zeitler, G., Livne, A. & Proksa, R. (2008). Experimental feasibility of multi-energy photon-counting k-edge imaging in pre-clinical computed tomography, *Phys. Med. Biol.* **53**(15): 4031–4047.

Sellin, P., Davies, A., Gkoumas, S., Lohstroh, A., Özsan, M., Parkin, J., Perumal, V., Prekas, G. & Veale, M. (2008). Ion beam induced charge imaging of charge transport in CdTe and CdZnTe, *Nucl. Instr. and Meth. B* **266**(8): 1300–1306.

Sellin, P. J., Davies, A. W., Lohstroh, A., Ozsan, M. E. & Parkin, J. (2006). Drift mobility and mobility-lifetime products in CdTe:Cl grown by the travelling heater method, *IEEE Trans. Nucl. Sci* **52**(6): 3074–3078.

Shul'ga, N. & Syshchenko, V. (2007). Contribution of the second-order born approximation to the coherent bremsstrahlung cross section by relativistic electrons and positrons in crystals, *J. Surf. Invest.* **1**(2): 141–146.

Spieler, H. (2006). *Semiconductor Detector Systems*, Oxford University Press.

Strassburg, M., Schroeter, C. & Hackenschmied, P. (2011). CdTe/CZT under high flux irradiation, *J. Inst.* **6**(01): C01055–C01055.

Stützel, J., Oelfke, U. & Nill, S. (2008). A quantitative image quality comparison of four different image guided radiotherapy devices, *Radiother Oncol* **86**(1): 20–24.

Sáenz, A. W. & Überall, H. (1982). Coherent bremsstrahlung at low energies, *Phys. Rev. B* **25**(7): 4418.

Takahashi, T., Mitani, T., Kobayashi, Y., Kouda, M., Sato, G., Watanabe, S., Nakazawa, K., Okada, Y., Funaki, M., Ohno, R. & Mori, K. (2002). High-resolution schottky CdTe diode detector, *IEEE Trans. Nucl. Sci.* **49**(3): 1297–1303.

Thran, A., Barschdorf, H., Martens, G., van Stevendaal, U. & Schlomka, J. P. (2006). Performance improvements of energy-resolved fan-beam coherent scatter computed tomography, *SPIE Conference Series*, Vol. 6318, p. 43.

Tlustos, L. (2005). Performance and limitations of high granularity single-photon processing x-ray imaging detectors, *Vienna University of Technology* .

Vykydal, Z., Jakubek, J. & Pospisil, S. (2006). USB interface for medipix2 pixel device enabling energy and position-sensitive detection of heavy charged particles, *Nucl. Instr. and Meth. A* **563**(1): 112–115.

Wambersie, A., Inokuti, M. & Seltzer, S. (2007). Multiple-Scattering angular deflections, *J. ICRU* **7**: 105–115.

Williams, E. (1935). Correlation of certain collision problems with radiation theory, *Mat.-Fys. Medd.* **13**: 38–38.

Überall, H. (1956). High-Energy interference effect of bremsstrahlung and pair production in crystals, *Phys. Rev.* **103**(4): 1055.

sapere aude